A SUPERCONDUCTING-SOLENOID ISOTOPE SPECTROMETER FOR PRODUCTION OF NEUTRON-RICH NUCLEI ($^{136}Xe +^{nat} C,\ E/A = 30MeV/u$)

by

Thomas W. O'Donnell

A dissertation submitted in partial fulfillment
of the requirements for the degree of
Doctor of Philosophy
(Physics)
in The University of Michigan
2000

Doctoral Committee:

Professor Frederick D. Becchetti, Chairperson
Professor Fred Adams
Professor David Gidley
Professor Henry Griffin
Professor Joachim Janecke
Dr. Donald A. Roberts

"One is always a long way from solving a problem until one actually has the answer." — Stephen Hawking[1]

---

[1] Op Cit, National Superconducting Cyclotron Laboratory's weekly "Green Sheet," 30 July 1999

For Tina, Danny and Leah

Love
Tom/Dad

ACKNOWLEDGEMENTS

Tina
My love, my friend, and comrade in endeavors both arduous and earnest

Danny
Junior NYU, psychology, who strives to help others and for what is just

Leah
Junior Pioneer/Community HS, dancer, writer, and lover of stories who has an exuberance for life

∞

Who suffered and gave the most for this achievement,
but supported and loved me always.

¶

My Dad and Mom

Who always had complete confidence in me,
loved me and patiently listened to my ideas.

¶

My Grandfathers who shared their
enthusiasm of knowledge, science, machines, history and politics
and my Grandmothers who were kind and loving.
My Mother- and Late-Father-in-Law for their enduring love and support.

- **My advisor**

Who stuck with me through thick and (plenty of)
thin with constant enthusiasm for physics:

Fred Becchetti*

¶

- **Colleagues in Physics at Michigan and elsewhere, and collaborators(*) on my thesis experiments:**

Don Roberts* – who always made things work during my experiments, commiserated in friendship over beer; and who spent many days and nights of long hours proofreading, discussing and helping me to correct and prepare the final text of this dissertation—without which this dissertation would have been a much poorer document

Quin Jänecke* – for his confidence in me and constant example of patient, careful research, and for his constant willingness to patiently explain the fundamentals of nuclear physics

Roy Clarke – for his confidence in me, friendship, intrepid support, collegiality and mentoring in solid state physics

Reg Ronningen* – for his constant hands-on assistance into the early morning hours with my experimental work at the NSCL, for his constant encouragement and interest in my work, and for his friendship and the many sessions at the *Peanut Barrel* in East Lansing,

Henry Griffin* – for his collegiality, confidence in my work, encouragement and sound advice

Muyoung Lee* – for his constant unstinting experimental assistance, friendship and graduate-student commiseration

Khai Pham* and Thillina Annakkage* – for their friendship and help in experiments as fellow graduate students

and my other collaborators and friends **Bob Tickle*, Rich Raymond*, Jim Brown*** (Milliken College).

- **The many physicists in the small international community of basic research in nuclear physics** who welcomed and initiated a newcomer into this engrossing and satisfying field of natural science at innumerable conferences and experiments at national and university laboratories both here and abroad. Most particularly, to **Walter Loveland** (Oregon State), **Gordon Wozniak** (LBNL), **Jim Kolata** (UND) and **Bob Warner** (Oberlin) who offered their insights, advice and collegial encouragement at crucial times in my work
- **Fred Adams and Dave Gidley** for giving their time to be on my doctoral committee and supporting my efforts.
- **Dearest friends and intrepid allies:**
  - **Sanjiv Gupta** (UMichigan, Amherst U, Demographics)
  - **Pat Pranke** (UMichigan, Buddhist Studies)
  - **Vahid Sattaray** (UMichigan, San Francisco, Civil Engineering)
  - **Charo Montoya** (UMichigan, Anthropology/History)
  - **Chandra Raman** (UMichigan, MIT, Physics)
  - **Najeeb, Aneela Jan** (UMichigan, History)

  - **Tom Abowd** (UMichigan, Columbia U, Anthropology)
  - **Tracy Edwards** (UWisconsin, UMichigan, Philosophy)
  - **The Friday night friends** and (again) ...
  - **Tina Meltzer-O'Donnell** (UMichigan, Anthropology, ...).

- **-Favorite physics teachers:**

  Jean Krisch (modern physics), Ted Hecht (quantum mechanics, E&M), Bob Lewis (quantum mechanics, mathematical methods), Bill Ford (statistical mechanics), Duncan Steel (practical quantum mechanics), Jim Allen (solid state) & Bob Savit (advanced statistical mechanics).

- **-Friends and special supporters through the years:**

  Dave Norton, Ron Dankert, Larry Henkel

- **-My eight younger brothers and sisters,** whom I left so young and for so long on my quest for social justice and scientific understanding, and who are always close to me though they are far away.

TABLE OF CONTENTS

CHAPTER

LIST OF FIGURES

Figure

LIST OF TABLES

Table

LIST OF APPENDICES

Appendix

ABSTRACT

A SUPERCONDUCTING-SOLENOID ISOTOPE SPECTROMETER FOR PRODUCTION OF NEUTRON-RICH NUCLEI

$({}^{136}Xe +^{nat}C,\ E/A = 30MeV/u)$

by
Thomas W. O'Donnell

Chairperson: Professor Frederick A. Becchetti

This dissertation in experimental nuclear physics describes the production of exotic, neutron-rich isotopes towards to the limits of particle stability—the "neutron-dripline"—in the region of the periodic table from neon to zinc ($10 \leq Z \leq 30$). Isotopes up to and beyond the most neutron-rich known at the time were produced (e.g. ${}^{80}_{29}$Cu, ${}^{76}_{28}$Ni, ${}^{68}_{27}$Mg and ${}^{66}_{26}$Cr).

The reaction studied was a mass-asymmetric collision: ^{136}Xe^{+24} on a thick (114 mg/cm^2) ^{nat}C target at an energy of E/A = 30 MeV/u, conducted at the National Superconducting Cyclotron Laboratory (NSCL) in E. Lansing, MI, USA.

A novel superconducting-solenoid spectrometer, "BigSol Isotope Spectrometer," was built to collect, separate and identify the neutron-rich isotopes. This device is based on the University of Michigan's seven-Tesla superconducting magnet, "BigSol." The device features a large-bore (40 cm), long time-of-flight path length (6.31 m), and position-sensitive detectors at the entrance and focal-plane. Reaction-product fragments were collected over an angular range from $0.7^\circ \leq \theta_{lab} \leq 6^\circ$ with respect to the primary-beam direction. Particle-by-particle identification of isotopes was achieved through software limitation of magnetic dispersion ($\Delta(B\rho)/B\rho \approx 1.6\%$) of the fragments analyzed, together with high-resolution silicon focal-plane detectors ($\Delta E/E < 10^{-3}$), and by time-of-flight measurements taken between the entrance parallel-plate gas avalanche counter (2D-PPAC) and a silicon focal-plane ΔE detector.

Isotopic separation was achieved for some 200 distinct isotopes collected at magnetic rigidities of $B\rho = 1.36$ and 1.76 T-m, despite the large distribution of the isotopes' ionic charge states. Novel data reduction techniques which avoid placing any restrictive cuts whatsoever on the data were developed. Solenoid-specific methods of achieving reliable isotopic identifications using calibration beams of isotopes which were mass-to-charge analogs of the cyclotron's primary beam were developed.

This device and type of reaction provide novel means for mapping the region of the table of isotopes toward the neutron dripline, beyond the current experimental limit at neon ($Z = 10$), and for producing new radioactive nuclear beams (RNBs) for secondary experiments. This would provides stringent tests of nuclear mass-model predictions which extrapolate from knowledge derived mainly from stable isotopes. In addition one can anticipate the appearance of new magic-number shell closings, shell quenchings, new regions of nuclear deformity and isomerism, diffuse and extended neutron 'halos' and other exotic structures in the vicinity of the neutron dripline. This information is important for understanding the astrophysical 'r-process' of nucleosynthesis of the heavy elements in supenovae.

CHAPTER I

Introduction

1.1 Overview

This dissertation in experimental nuclear physics describes the construction and development of "BigSol-Isotope-Spectrometer" and a series of experiments using it to produce very neutron-rich (heavy) isotopes of elements from neon to zinc ($10 \leq Z \leq 30$) in the table of isotopes. This work demonstrates a novel means to produce and study extremely heavy (i.e. neutron-rich) isotopes. This pertains both to the novelty of the nuclear reaction employed and to the experimental methods and device which were developed.

1.1.1 Neutron-rich nuclei produced

For example, in one particular experimental run lasting just over three hours, isotopes near to and beyond the most neutron-rich ever produced at that time[1] were produced, including small numbers of the isotopes $^{66}_{24}\mathrm{Cr}$, $^{68}_{25}\mathrm{Mn}$, $^{69}_{26}\mathrm{Fe}$, $^{71}_{27}\mathrm{Co}$, $^{76}_{28}\mathrm{Ni}$ and $^{80}_{29}\mathrm{Cu}$. [O'Donnell 1999] These isotopes were emitted as fragments from a beam of $^{136}\mathrm{Xe}$ having a kinetic energy of 30 MeV/u[2] impinging on a thick, natural carbon

---

[1] This experiment was from a set conducted over 72 hours in April, 1993. A second 72-hour set was conducted in July, 1993. A test run was also conducted in November, 1992 while the spectrometer construction was still not completed.

[2] 30 MeV/u: 30 million electron Volts per each nucleon within the projectile's nucleus. For $^{136}\mathrm{Xe}$ this is a *total* kinetic energy of 4 GeV (billion electron Volts), and a velocity of $0.25c$: 25% the

target (114 mg/cm^2 ^{nat}C). Fragments were collected over an angular range of $0.7^\circ \leq \theta_{lab} \leq 3.1^\circ$ with respect to the primary beam, as measured in the laboratory reference frame. The magnetic rigidity setting of the spectrometer for this run was $B\rho = 1.36$ Tesla-meters and the fragments were analyzed with a narrow acceptance setting of $\Delta(B\rho)/B\rho \approx 1.7\%$ so as to insure the highest accuracy in isotopic identifications.

Experimental progress in producing neutron-rich isotopes towards the limits of nuclear stability (the "neutron-dripline") has proven to be quite difficult for a number of reasons, regardless of the reaction mechanism(s) or experimental device employed.[3] The review by [Mueller & Sherrill 1993] summed up the general situation in the following terms:

> "Mapping of the neutron drip-line remains an experimental challenge. Indeed very large neutron-excesses are possible, owing to the fact that neutron matter itself is almost bound. The major difficulty is that far from stability, a very rough, but useful rule of thumb says that the production cross-sections fall by one order of magnitude for each step further away (regardless of the mechanism actually used). It is clear that ... at least for the foreseeable future, (certain) nuclei ... predicted to be particle stable by mass formulae, are beyond any experimental possibilities.
>
> "The minute quantities in which the isotopes on the neutron drip-line are made in nuclear reactions call for efficient, fast and selective

---

speed of light.

[3] Recently the low-excitation fission of a relativistic uranium projectile [Bernas 1994] [Bernas 1997] has been very successful in producing over 100 new neutron-rich isotopes for a region centered at significantly higher Z than the present experiments, but including isotopes in some cases as low as $Z = 20$ These lower-Z yields are reported to be from a multifragmentation reaction component [Bernas 1998], though this component is not as neutron rich as were the fission yields. These experiments were conducted at the GSI in Darmstadt. A similar, but *much* lower energy (20 MeV/u), *nuclear* sequential fissioning of uranium, conducted at the NSCL in East Lansing [Souliotis 1997], has since reproduced many of the new, higher-Z isotopes reported from GSI. See the chapter, "Results and Conclusions" in this thesis for further discussion.

> experiments. This is because of the short lifetimes of these weakly bound species and the huge background induced by the more stable reaction products."

The design of "BigSol-Isotope-Spectrometer" and the data reduction methods described in this dissertation were developed specifically with these difficulties in mind.

1.1.2 A novel isotope spectrometer

The device built as part of this thesis project, which we call "BigSol-Isotope-Spectrometer," is shown in an artist's rendition in Figs. 1.1 and 1.2. It is a novel seven-Tesla, superconducting solenoid spectrometer designed to collect and identify exotic neutron-rich *isotopes* emitted at small angles. It is designed for nuclear reactions involving the fragmentation of massive projectiles having low-to-intermediate kinetic energies.

The main features of the device, which permit event-by-event isotopic identification of in excess of 200 different isotopes, include:

1. Position-sensitive entrance- and focal-plane detectors which allow off-line software limitation of the fractional magnetic dispersion ($\Delta(B\rho)/B\rho$) of the events being analyzed;
2. Time-of-flight (ToF) measured between two fast detectors over a flight path of 6.4m;
3. High-resolution Si detectors at the focal plane providing thick-multiple-ΔE-E-ToF-XY signals, and;
4. A highly asymmetric image/object ($i/o = 5.3/1.4m$) setup.

The high level of resolution and the multi-parameter character of the data which was collected allowed methods of data reduction to be employed which eliminated all charge-state ambiguity as to isotopic (Z, A) identification.

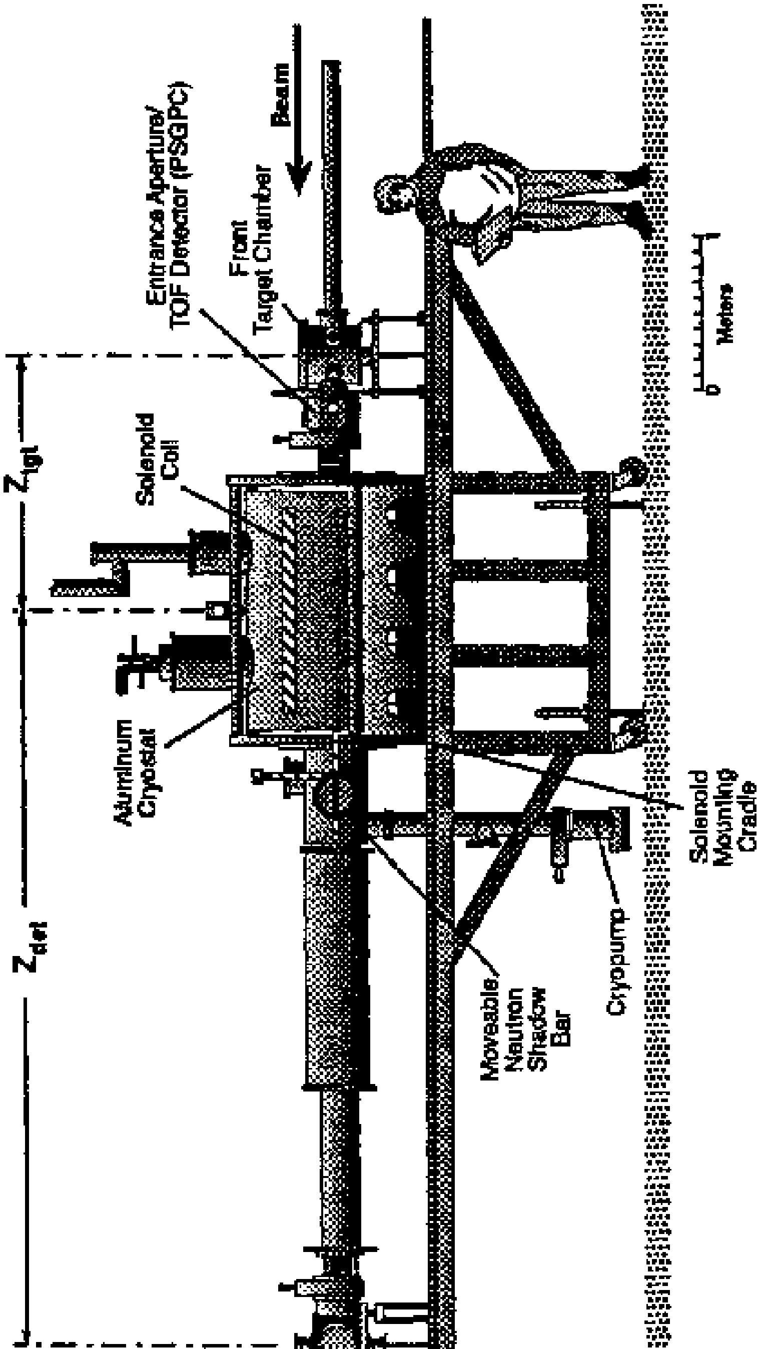
Entrance Aperture/
TOF Detector (PSGPC)
Front
Target Chamber
Beam
0
Meters
Z_{tgt}
Solenoid
Coil
Z_{det}
Aluminum
Cryostat
Solenoid
Mounting
Cradle
Moveable
Neutron
Shadow
Bar
Cryopump
Back Chamber
ΔE_1-ΔE_2-E-xy
TOF
Moveable
Mount

Figure 1.1: (Page 5) Artist's rendition, University of Michigan's "BigSol Isotope Spectrometer" at the NSCL. Shown in its completed long-flight-path mode.

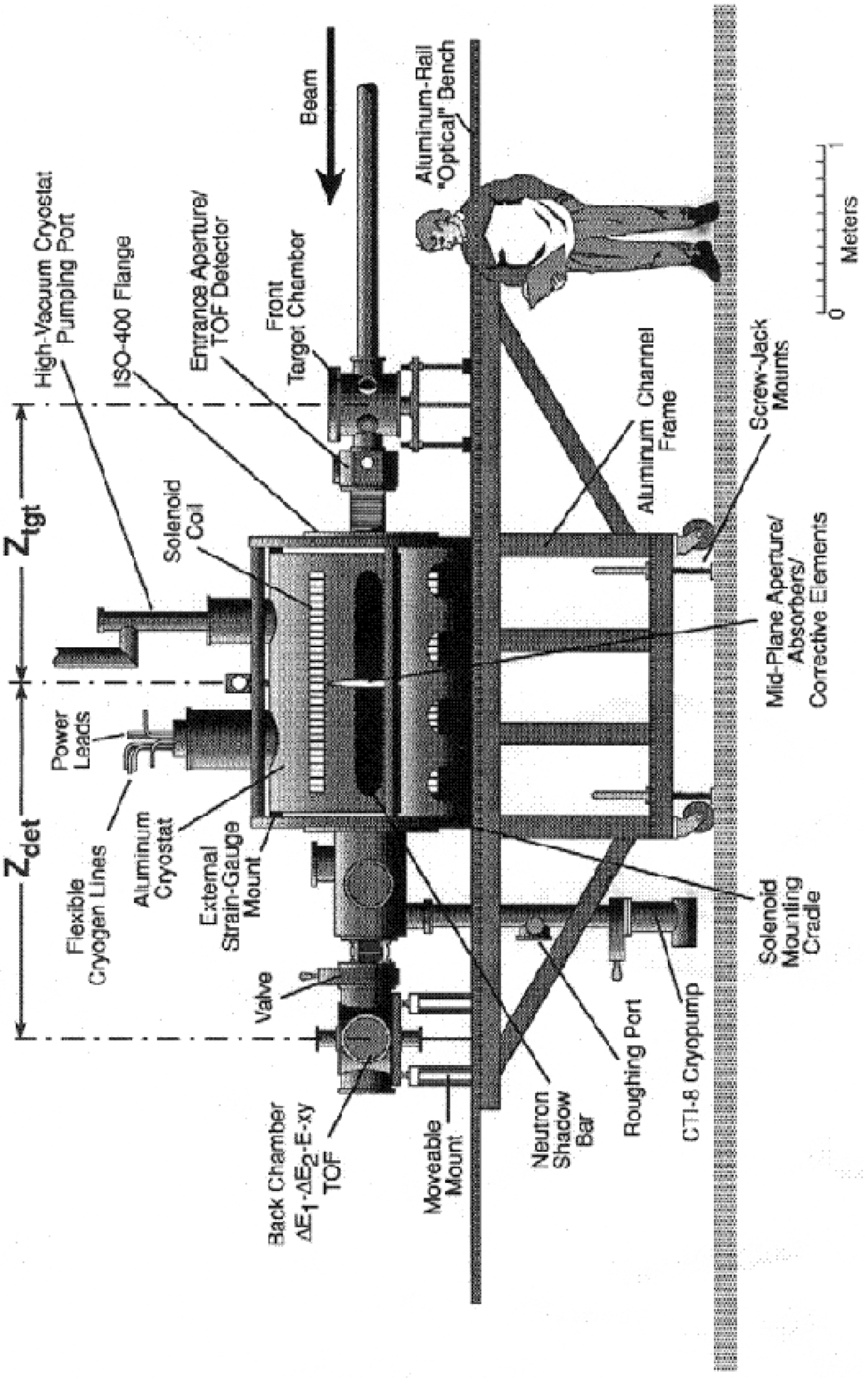
Z_det
Z_tgt
Flexible Cryogen Lines
Power Leads
High-Vacuum Cryostat Pumping Port
Aluminum Cryostat
Solenoid Coil
ISO-400 Flange
External Strain-Gauge Mount
Entrance Aperture/ TOF Detector
Valve
Back Chamber ΔE1-ΔE2-E-xy TOF
Front Target Chamber
Beam
Moveable Mount
Aluminum-Rail "Optical" Bench
Neutron Shadow Bar
Roughing Port
Aluminum Channel Frame
CTI-8 Cryopump
Screw-Jack Mounts
Solenoid Mounting Cradle
Mid-Plane Aperture/ Absorbers/ Corrective Elements
0
1
Meters

Figure 1.2: (Page 7.) "BigSol Isotope Spectrometer" shown in process of construction, as configured during initial test run, before long-flight path completed (see previous figure). Additional instrumentation and detector details are shown here.

1.2 Producing exotic nuclei

1.2.1 In the past

In the past, the principal means of searching for new, exotic isotopes was to examine daughter products emitted from the fission of long-lived terrestrial isotopes. At first these investigations were limited to studying the products emitted in the *spontaneous* radioactive decay of rare, heavy elements found in nature including uranium, radium, thorium, etc. Eventually it was discovered that one could induce fission and transmutations in some of these elements by exposing them to the radioactive emissions of others. By the 1930's *artificial* sources of these emissions were invented. Machines which could accelerate light charged particles allowed nuclear physicists and chemists to systematically excite and/or transmute even stable elements. In the early 1940's the first nuclear reactor was built, after which intense beams of neutrons became available to systematically induce uranium and other heavy elements to fission. Many exotic, short-lived isotopes were soon discovered by using these light charged-particle and neutron beams.

1.2.2 Today

Today, however, after about seven decades of the development of particle accelerators and their attendant ion-optical systems, and six decades since the development of the first reactor neutron source, the three principal means used to produce very neutron-rich or proton-rich exotic isotopes include the methods of: i) projectile fragmentation (PF) [Mueller & Sherrill 1993], ii) isotope-separator-on-line (ISOL) [Nolan 1998], and iii) fission or photo-fission of relativistic uranium. [Mueller 1998]

1.3 The place of a solenoidal collector/spectrometer

1.3.1 Instrumental advantages

The results of the present thesis, and recent results by other workers [Souliotis, 1997], indicate that low-to-intermediate energy fragmentation of very massive beams observed at small angles (in the case of this thesis $\geq \theta_{grazing} \approx 0.7°$—the classical grazing angle of the reaction) may become a fourth, and highly accessibly way, to produce exotic isotopes. Many existing facilities can produce such beams, and generally at much higher intensities than can higher-energy facilities [ibid.] and a solenoid's characteristics are well-matched to such reactions. This dissertation explains the basis of these optimistic assertions regarding the reaction(s) employed here and regarding solenoid spectrometers. In general, the instrumental basis of these experiments where *only* a *single-element* ion-optical device was employed, is *far less complex and expensive* than those of the three well-established, complimentary methods of producing exotic nuclei listed above.

1.3.2 Care in methods and analysis

However, the experimental methods employed and the reduction of the experimental data for a solenoid device for this type of low-to-intermediate energy, require *particular care and attention.* In this regard, this thesis demonstrates the realization of i) the complete removal all charge-state ambiguities in the identification of multiple-charge-state-distributed data, and ii) the realization of complete avoidance of placing *any restrictive cuts whatsoever* on the data (aside from at the focal plane to limit the fractional magnetic dispersion of the set of analyzed ions). Thus *all* data is retained and accounted for *throughout the analysis process*, in strict accordance with the standard, best-practises of modern multi-dimensional statistical science.

1.4 Increasing use of solenoid-based devices

1.4.1 Current and new facilities

Magnetic-selection devices based on dipoles, quadrupoles, sextapoles, etc. have long been ubiquitous in methods of producing and separating exotic isotopes. However, in recent years, superconducting solenoid magnets such as BigSol have been introduced, or are planned for use, at a number of facilities. They are especially being employed for the production of radioactive nuclear beams (RNBs) and/or to increase beam-line transmissions of traditional-type fragment analyzers. The advantages of solenoid magnets include a full-2π azimuthal acceptance, relatively simple ion optics [Stern 1987], and a good matching of solenoid-focused ions to the acceptance of traditional ion-optical beamlines. [Anne 1996]

The list of nuclear research facilities where solenoid devices, of various types, are now available worldwide includes:

1. In the USA:
    (a) TwinSol, a new double-solenoid device [Becchetti & Kolata 1997] [Lee 1997] [Kolota 1998], and
    (b) the older LilSol (the prototype for BigSol) both of which are located at the University-Notre-Dame/University-of-Michigan Radioactive Beam Facility at UND in South Bend, Indiana, and
    (c) a new solenoid device at Argonne National Labs near Chicago, Illinois [Pardo 1998] [Harss 1999]. In addition, devices were recently being considered at
    (d) Oak Ridge National Laboratories in Tennessee, and

   (e) at Lawrence Berkeley National Laboratories in California [Lee3 1998].

2. In France: The double solenoid device SISSY used to enhance the acceptance of RNBs into the LISE3 beam analysis system at the Grand Accelerator National d'Ions Lourdes (GANIL) at Caen [Anne 1996] [Baron 1995].
3. In Italy: At the cyclotron facility in Catania, Sicily.
4. In Brazil: At the University of Sao Palo a device similar to TwinSol but with a higher field, has been designed, and construction is planned to begin soon. [Hussein 1998][4]
5. In Australia: A device is being considered at the Canberra University Laboratories to be used with the 18 megavolt (MV) tandem and linac facility.

1.4.2 Previous solenoid work

This list represents a significant development in the application of solenoids to nuclear physics research. This period began with the pioneering work of Schapira [Schapira 1984] [Laurent 1979] at Orsay, France, where the 'SOLENO' device was developed as a nuclear spectrometer for research with stable nuclear beams. The University of Michigan group of F.D. Becchetti has been extremely active in this field in the subsequent decades, specifically in the applications of solenoid technology in radioactive nuclear beam (RNB) research. This work has involved the development of *superconducting* devices including: LilSol, [Stern 1987] [Liu 1990], BigSol [Brown 1993]; and TwinSol [Lee 2000] in pursuit of intense, low-mass and low-energy radioactive nuclear beams.

---

[4] Also, private communications, Dr. Valdir Guimaraes, Universidade Paulista (UNIP), São Palo, Brazil & U Notre Dame, 1999.

This thesis is a continuation of this work, using the BigSol device. However, for the present thesis research it has been completely reconfigured and adopted to a new application as a collector and isotope spectrometer for neutron-rich fragments emitted at small angles from the collisions of *massive* projectiles at low-to-intermediate energies. This a very different application as compared to BigSol's earlier use.

1.5 Two modes of recent solenoid use in nuclear physics

The BigSol-Spectrometer, a type of solenoidal isotope spectrometer or fragment mass analyzer (FMA)), differs significantly from the heretofore-typical use of BigSol at the NSCL for the production of *light* heavy-ion (HI) RNBs using transfer reactions at low-to-intermediate energies. [Becchetti2 1994] [Brown2 1995] [Roberts 1995]

In the *light* heavy-ion (HI) mode, BigSol had been configured quite differently, [O'Donnell 1994] having a nearly symmetric image-to-object ratio ($i/o \approx 1$), a short flight path ($\approx$ 3m), fixed (mechanical) apertures, and, when ToF was used, the cyclotron's RF was taken as a timing signal. In contrast, in the present "isotope-spectrometer" mode, BigSol is configured with a highly asymmetric i/o (image/object) ratio (1.37/5.25m), and a long time-of-flight path length (6.4m)—over which fast timing is done between two detectors. In addition, position-sensitive detectors are located at *both* the entrance and, especially, at the focal plane, to control magnetic dispersion in software. The setup can thus, as will be shown later, successfully accomplish particle-by-particle identification in an statistically correct and unbiased manner.

The *light* HI transfer-reaction mode is that which has also been used with the "LilSol" and "TwinSol" devices located at the University of Michigan-University of Notre Dame (UM-UND) RNB facility at UND's 9 Mega Volt (MV) tandem accelerator laboratory.[5]

These devices produce very intense RNBs at low *total* kinetic energies (5-30 MeV), principally for experiments of astrophysical interest.[6]

1.6 Specific ion-optical challenges

The adaptation of BigSol for fission, fusion-fission and similar reactions induced by very massive HI projectiles presented several new ion-optical problems as compared to the previous *light* HI work at MSU-NSCL with BigSol:

1. Transfer-type reactions used with the *light* HI RNB solenoid devices at UND and NSCL typically yield a total of only 3-to-10 distinct transfer-reaction products (isotopes). In contrast reactions examined in this thesis with the BigSol-Spectrometer device typically yield over 200 distinct isotopic species;

2. for any magnetic selection device, resolution of heavy, n-rich isotopes is intrinsically more difficult than resolving lighter and stable (or proton-rich) isotopes;[7]

3. beam energies for the heavy projectile reactions studied with the BigSol-Spectrometer are insufficient to achieve full stripping of electrons from all of the reaction-product ions in the $10 \leq Z \leq 35$ range of interest, causing most of the isotopes produced to be found in a distribution of discrete charge states.

The major experimental challenge, therefore, in doing physics in the regime examined in this thesis with the BigSol-Spectrometer device, is *to resolve and correctly identify*

---

[5] See [Becchetti3 1989] [Liu2 1989] [Becchetti4 1990] [Becchetti5 1990] [Brown3 1991] [Becchetti6 1991] [Smith 1991] [Smith2 1991] [Becchetti7 1992] [Caussyn 1993] [Becchetti8 1993] [Becchetti9 1993] [Balbes 1995] [Warner 1995] [Gu 1995] [Becchetti & Kolata2 1997] [Kolata2 1998] [Becchetti10 1999] [Becchetti11 1999].

[6] For example, ^{8}Li or ^{6}He RNBs at fluxes of $\geq 10^5$ are produced from inverse-kinematics transfer reactions using ^{7}Li or ^{9}Be or other *light*-HI beams at primary beam currents of $\leq 1.7\mu$ A.

[7] The fractional separation of reaction products in energy as a function of mass at constant magnetic rigidity decreases with the inverse square of the isotopic mass: $dE/dA = -1/2(qB\rho/A)^2$.

a plethora of multiple-charge-state isotopes.[8]

The results of the present experiments demonstrate that it is both possible, and practical, to overcome this problem using an simple, single element superconducting solenoid. Such a solenoid is relatively inexpensive, has a relatively high-acceptance, and may be fitted with appropriate position-sensitive entrance-and focal-plane detection systems.

1.7 Physics and astrophysical motivations

The physics motivation for developing a solenoid-based, low-to-intermediate energy, massive-projectile isotope spectrometer, is to search for and study new neutron-rich nuclei in the region of the chart of nuclides comprising atomic numbers $10 \leq Z \leq 35$. The development of neutron-rich RNB's is a further motivation in this region. The development of neutron rich RNB's would allow decay and reaction studies of these isotopes, and thus extend our knowledge of nuclear structure beyond the valley of stability in the chart of nuclides. It is notable that the limits of particle stability for nuclei with respect to increasing neutron number—known as the "neutron-dripline"—has only been reached experimentally up to Z $\approx$ 10 (neon).

It is quite difficult to determine theoretically exactly how many neutrons may be added to an element before there is no room left in the nuclear potential well to bind another. The di-neutron (a system of two bound neutrons), does not exist in nature. Nor do larger clusters of pure neutron matter, with the exception of neutron stars, which will be discussed below. Yet, neutron matter *is* very nearly bound. [Ogloblin

---

[8] This difficulty arises from the basic magnetic-selection relation governing any magnetic ion-optical device:

$$B\rho = p/q \propto A/q, \tag{1.1}$$

where p is the ion's momentum and q is its electronic charge state. Equation 1.1 indicates that any uncertainty as to an ion's q-state—the well-known "charge-state ambiguity"— will preclude certainty as to its mass (A) identification.

& Penionzhkevich 1984] The result is that as one proceeds up through the elements in the table of isotopes, the limits of stability quickly move very far distant in mass from the isotopes which have been produced to date in the laboratory (this will be discussed quantitatively in the following chapters). In fact, in neutron stars, where the extra binding energy is provided by the gravitational force, neutrons indeed comprise a bound system.[9] Understanding the precise limits of nuclear stability for elements beyond neon with respect to neutron number has been a matter of considerable interest and research in both nuclear physics and astrophysics for at least the past three decades [Boyd 1993]. [Arnold 1989] [Mathews 1990] [Wallace & Woosley 1981]

In astrophysics, the interest is primarily in understanding the 'r-process'—the explosive nucleosynthesis which occurs in supernova explosions and is believed to be responsible for the production of elements beyond iron in the periodic table. The earth, which is a "rocky" planet with an iron and nickel core, is itself thought to be the product of the remnants of thousands of supernovae [Siemens & Jensen 1987, p. 5] which coalesced to form not only our planet, but everything on it—author and reader included.

In particular, theorists carry out complex nucleon-reaction "network" calculations which give predictions of the abundances of isotopes (or their abundance ratios) in the universe after many generations of supernovae. In these network calculations the temperature and pressure of neutrons during the course of the explosion are modeled. In addition, it is imperative to know the beta-decay half lives and neutron capture cross sections of all the isotopes involved in the reaction network throughout the astrophysical r-process. These network calculations start from a low mass "seed"

---

[9] Though they are not *purely* composed of neutrons—they likely include a certain small fraction of protons.

isotope, typically near $Z = 28$, leading from the lighter elements (near Ni) up to the very heaviest elements (uranium and perhaps transuranic elements). Producing the very neutron-rich isotopes which participate in this process and determining their half lives would provide valuable input to such calculations. In general, the research for this thesis involved producing elements in the table of isotopes which are below the astrophysical r-process.

From the standpoint of nuclear physics our primary interest is to test and develop better theoretical understanding of the nucleus and its stability.

1.8 Criteria for discovery, half-life and structure determination of dripline isotopes

Production and identification of ≈ 10 counts of a very n-rich isotope is generally sufficient to confirm its stability. Typically, systematic experiments are performed to produce and detect a series of ever-heavier isotopes of a given element. When such a search *unambiguously* identifies a significant number of counts of a given isotope but *not* any heavier isotopes of that same element, this presents a strong case to conclude that the heavier isotopes are unstable against decay by the strong force (i.e., they decay with a characteristic lifetime of about 10^{-22} s). An example of such an experiment is shown in Fig 1.3 taken from [Mueller2 1993]. This figure shows a Z-identifier plotted against time of flight (which, for technical reasons, runs "backwards" in this figure) through GANIL's LISE [Anne 1987] magnetic spectrometer. In this figure the time of flight axis is *inversely* proportional to the A/q (atomic mass/ionic charge) of the ions detected (see Eqn. 1.1). Because of their high kinetic energies, the q-states of the ions shown are equal to their atomic numbers, Z (i.e. they are "fully stripped" of electrons).

Note the trend along the curving, vertical line of n-rich isotopes having neutron numbers of $N = 2Z + 2$. These are labeled with: ^{20}C, ^{23}N, (^{26}O is conspicuously missing), ^{29}F and ^{32}Ne. In addition, the line connecting a plot of the counts collected for each of these isotopes, shown in the inset, reveals that, by systematics, some 30 counts of ^{26}O 'should have' been produced— *if it were stable.* Such experiments are a sensitive test for distinguishing between various competing mass models [Sherrill & Mueller 1993]. Some models, for example, do, and some of models do not (or, did not) predict the stability of ^{26}O. Such 'null result' experiments put a strict limit on the strength (depth) of the nuclear potential for additional neutrons for a given element.

It is important to note that, quite generally, great effort is required to produce neutron-dripline isotopes, and to unambiguously *not* produce the next heavier isotope.[10] Indeed, despite the prodigious efforts to date of many experimental groups around the world, the neutron-dripline has only been mapped out unambiguously up to about neon ($Z = 10$). In this circumstance, there is clearly little hope of being able to make many *mass* measurements of nuclei in the vicinity of the neutron-dripliine for some time to come. [Mittig 1997]

In general, such measurements would be the only way one could check the validity and predictive power of the nuclear theories underlying the various mass model predictions which have been made. However, there is indeed a way to to "jump ahead," and test mass models right *at* the dripline. The later method is to do an experiment as shown in Fig. 1.3 and prove that a given n-rich isotope does or does

---

[10] To be more precise, one really has to show that not only the next heavier isotope isn't produced, but, also that the next *two* are not produced. Due to the lower energy (greater binding energy) caused by nucleon pairing, it is expected that there are likely many situations where every other n-rich isotope of a given element is found to be stable just before the dripline is encountered and no more neutrons can be bound by its nuclear well. See discussion of the semi-empirical mass model, below.

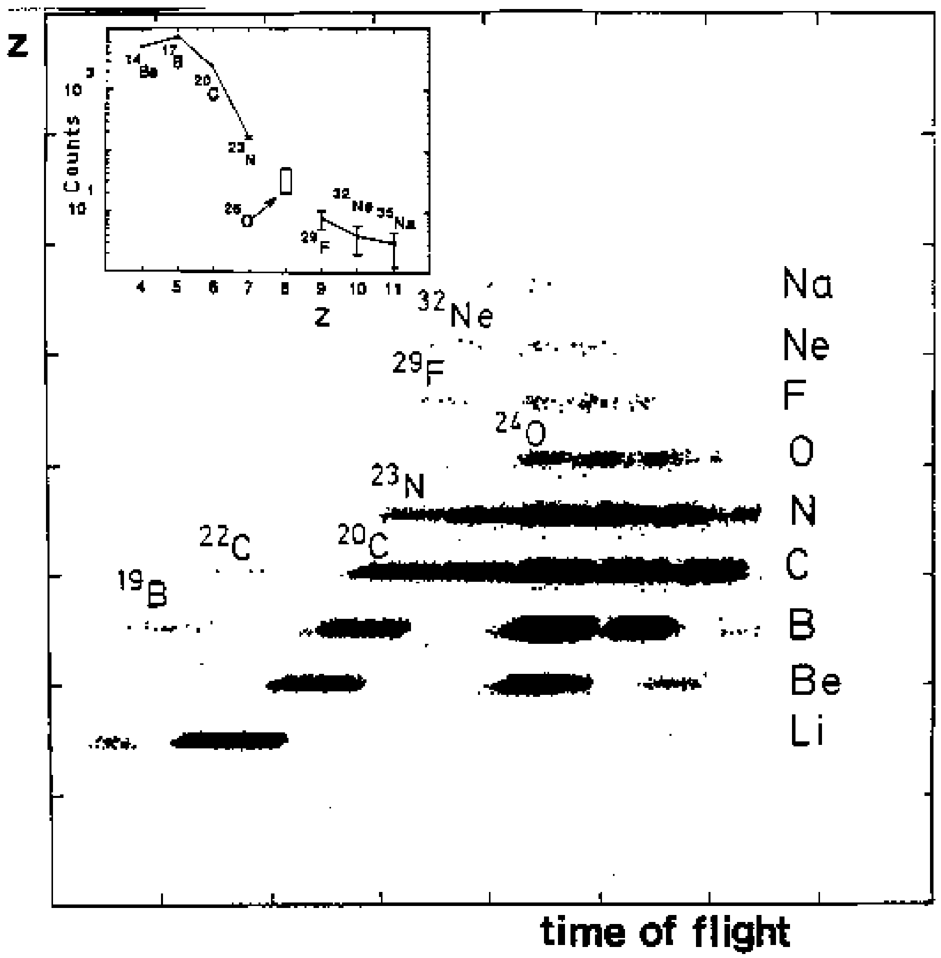

Figure 1.3: Experimental evidence for the non-existence of ^{26}O. Figure is explained in text. Plot is from [Guillemaud-Mueller 1990]. See also [Sherrill & Mueller 1993], pp. 26-30 and [Mueller2 1993], p. 8, for discussions of this experiment.

not "exist." Indeed, further information requires more than simply the ≈ 10 particle identified events required for a statistically valid claim to have produced a new isotope. To determine the isotope's half life through beta-decay spectroscopy (the *stable* neutron-dripline isotopes generally decay via a characteristic electroweak beta-delayed neutron emission) requires ≈ 100 particle identified events. To explore the excited states of the exotic nucleus (spectroscopy) requires on the order of thousands of events.[11]

1.9 Scientific and social perspective

To date, the great abundance of nuclear theory has been derived from elements which are found naturally in our terrestrial environment. Given that the age of the earth is approximately 4.6 billion years [Sagan 1980][12] the distribution of radioisotopes found on earth in the present era is such that only the most long-lived radioisotopes generated by supernovae or, in other astrophysical events, are still present. Starting at the end of the 19th and in the early 20th centuries, with the pioneering work of Curie, Becquerel, and many others, the first available samples of uranium, thorium, radium, radon and other radioactive elements were laboriously separated and concentrated from pitch-blend and other ores. The study of these trace terrestrial sources paved the way for the development of the entire edifice of present-

---

[11] These "order-of-magnitude" rules-of-thumb for the count rates required for various measurements are taken from a paper by Dominique Guillemaud-Mueller, Institute de Physique Nucléare, Orsay, Fr., presented at a conference in the 1980's which unfortunately we have not been able to relocate.

[12] The teaching of a 10,000 year-old earth ("Creationism") as taught in various States in the US has led to widespread popular misconceptions of issues of evolution not only as pertains to biology (the origin of the species as arising from natural selection [Darwin, 1859]) but, also as pertains to the physical sciences of astronomy, cosmology, geology, and nuclear physics. Creationism also opposes the "Big Bang" theory of cosmogenesis [Wagoner, Fowler and Hoyle 1967] and, to a lesser degree, modern theories of stellar evolution which explain the abundances of the elements in the universe, plate tectonics and other physical theories, and which all give an age for the earth greatly exceeding the biblically derived figure of 10,000 years.

day nuclear and quantum theory. This knowledge was paid for with considerable sacrifice, including the untimely death of Mdm. Curie, and others, from radiation exposure.

CHAPTER II

The research goals of this thesis

With a modern version of the continuing quest to explore the limits of nuclear stability in mind, a set of studies were performed at the NSCL to develop the Big-Sol Isotope Spectrometer device. These experiments employing a 30 MeV/u (4 GeV) $^{136}Xe^{+24}$ primary beam incident on a ^{nat}C target. The ^{136}Xe beam was chosen for its relatively high A/Z ratio (2.52), nearly identical to that of ^{235}U (2.55). This choice of a highly asymmetric entrance-channel reaction and intermediate primary-beam energy, is known to produce reactions at the boundary between complete and incomplete fusion of target and projectile. Fission fragments were then expected to be sequentially emitted from a massive and excited moving source. It was expected that the yield of such a reaction might be peaked not at $\theta_{lab} = 0°$, as with higher-energy 'sudden' projectile fragmentation reactions, but near the classical grazing angle. In contrast, the very commonly utilized sudden 'projectile fragmentation' (PF) reactions are typically conducted with beam energies above the Fermi energy levels of nucleons within the target nucleus, at about 40-70 MeV/u. It is generally those fragments which are emitted at zero degrees, and at the same velocity as the incident beam, which are of interest for the production of neutron-rich isotopes with this higher-energy method. In contrast, the lower-energy fission, fusion-fission and fragmentation reactions pursued in the present case were examined at small, but *non-zero* values of θ_{lab} consistent with the reaction's classical grazing angle. This emission pattern is particularly well-matched to a solenoid's acceptance characteristics. In the present experiments, a particular effort was also made to magnetically select and identify the highest-rigidity reaction products possible. The hypothesis being that, in the partition of reaction energy between internal excitation modes and kinetic energy, the *fastest* products should exhibit the *least internal excitation per nucleon* (and/or lowest temperatures). Thus, these isotopes should be favored to retain whatever neutron excess may have been fortuitously produced for some fragments during the breakup/fissioning reaction.[1] There are similarities between these expectations and the results of a reaction conducted by [Souliotis 1997]—which was sucessful in producing many very neutron-rich isotopes in a region of higher Z than that explored in the present experiments. The strategy of selecting the fastest isotopes as having the least internal excitation is similar to that successfully demonstrated by [Bernas 1994] for low-excitation fission of relativistic U.

---

[1] This is a highly selective cut in the momentum phase space of the reaction products, and therefore not designed to be particularly well-suited to characterization of the *overall* reaction mechanism.

CHAPTER III

Nuclear Stability: Historical Perspective

3.1 The beginnings of exotic nuclei research

3.1.1 The advent of charged-particle and neutron beams

A significant portion of 20th Century—as well as present-day nuclear research—has involved efforts to accurately measure the size of the microscopic, unseen world of atoms, nuclei and subatomic particles. Perhaps the first serious experimental effort to actually extract a quantitative measurement of the atomistic constituents of matter was devised and conducted by the early American scientist, Benjamin Franklin.[1]

Franklin sought to determine the limiting, smallest size of the particles of which he believed all substances to be made. His experiment consisted of standing on a small bridge over the very still waters of a pond on his property. He then gently poured a small vile of oil whose volume he had carefully measured onto the surface of the pond. He then determined as accurately as possible the great extent to which the oil spread out upon the surface of the pond. He hypothesized that the oil would spread to cover an ever greater area until the point at which it reached the limit of its single-particle thickness. Hence, by dividing the volume of the original vile by the area over which the oil slick had spread, he made one of the earliest measurements

---

[1] This story was related some years ago on PBS by a professional historian who studied Franklin's life, and showed the footbridge from which it was conducted.

of the diameters of what we now know to be hydrocarbon molecules.

However, the atomistic theory of nature was not firmly established for almost another 125 years. Boltzman, the 'father' of modern statistical mechanics went to his grave convinced in the validity of the unseen atomistic constituents of matter but without the proof yet having been established.

Not until 1905, with the appearance of the earliest papers of Albert Einstein on the foundations of molecular physics, and especially those explaining Brownian motion, was the atomistic theory firmly established. After writing a series of papers on the foundations of statistical mechanics in 1902-1903 (two-to-three years before his Doctoral Exams) he wrote the paper [Einstein 1905], wherein he makes the assertion as regards Brownian motion:

> "If the movement discussed here can actually be observed (together with the laws relating to it that one would expect to find), then classical thermodynamics can no longer be looked upon as applicable with precision to bodies even of dimensions distinguishable in a microscope: *an exact determination of actual atomic dimensions is then possible.* On the other hand, had the prediction of this movement proved to be incorrect, a weighty argument would be provided against the molecular-kinetic conception of heat." (emphasis added - T.O'D.)

Einstein rapidly produced four important papers on Brownian movement [Einstein2 1906] [Einstein3 1906] [Einstein4 1907] [Einstein5 1908].[2] This period marked the beginning of the modern era in which the atomistic view of nature became very firmly established in science, and in the popular consciousness. Einstein's explana-

---

[2] These are available in English in *Investigations on the Theory of the Brownian Movement*, A. Einstein, Ed. R. Fürth. Dover, New York 1956.

tion of the quantal theory of light, which followed soon thereafter, undoubtedly was both philosophically and scientifically primed by his earlier work on the atomistic explanation of the Brownian motion. His quantal theory of light is one of the foundations upon which arose the entire quantum-mechanical revolution and the modern (post-classical) conception of nature.

Much of the earliest experimentation conducted to understand the nucleus was contemporary, and even somewhat earlier, than even these earliest theoretical efforts by Einstein on the foundations of statistical mechanics and the atomistic theory of matter. Early nuclear work was at first limited to observing the *spontaneous* emissions and decay of naturally occurring radioactive elements. But, it soon became apparent that the radioactive emissions from these events (especially energetic alpha particles) could in turn be used as probes to investigate the nature of other nuclei, to artificially induce nuclear reactions in other nuclei, albeit at low rates and energies.

These investigations using naturally occurring "beams" of subatomic particles spurred the quest to develop intense and energetic *artificial* beams which would be capable of inducing other, more fundamental nuclear transformations, and which would enable systematic studies of nuclear structure to be conducted.

There were two possibilities in this regard: charged particle beams and beams of neutrons. On the one hand, three different types of accelerators for light, *charged* particles—protons (^{1}He), deuterons (^{2}H) and He-alphas (^{4}He)—were invented in the 1930's. On the other hand, years of work by Enrico Fermi and others irradiating samples with neutron emissions from uranium and other radio-isotopes, directly led to the first controlled fission reaction, at the University of Chicago in 1943. [Fermi1 1947] With this later advance, reactor-produced, high-intensity neutron beams became available— just eleven years after Chadwick had discovered the neutron in

1932. [Chadwick 1932] These two developments—artificially produced charged particle beams and beams of neutrons—led to a plethora of new information about the structure and transformations of nuclear systems, and about the limits of nuclear stability.

There are fundamentally three directions research into the limits of nuclear stability might proceed: in the directions of i) adding neutrons onto a given element, ii) removing neutrons from a given element, and, iii) adding, in some fashion, additional protons onto the heaviest naturally available element, uranium.

Early experimental work led to significant theoretical advances in understanding the strong nuclear force and nucleonic systems, and motivate further and more refined programs of experimentation. To contextualize the modern state of affairs in this continuing quest, a general overview of this historical development will be given before proceeding to elaborate the experimental work and results of this thesis project.

3.1.2 Neutron activation and fission

It was found in the early 20th century that uranium nuclei which are irradiated by neutrons are induced to emit further radioactive particles. In the early 1930's in Italy, Fermi conducted systematic studies of beta decay (the emission of positrons and/or electrons, and the subsequent change of the product's atomic number) of many elements activated in this manner and of their products. He deduced from chemical tests of the products produced by the irradiation of uranium and other elements in 1934 that by irradiating uranium with neutrons he had produced an element of *higher* atomic number.[3] Such an element is known as a 'transuranic'—an element with an atomic number *greater* than $Z = 92$ found in a uranium nucleus.

---

[3] For this work Enrico Fermi received the Nobel Prize in 1938.

However, the positive identification of the daughter products of this proposed element had presented Fermi and his co-workers with difficulties. Eventually, these daughters were positively identified by Hahn and Strassmann in 1939, nuclear chemists working in Berlin, thus leading to the discovery of nuclear fission. Almost immediately thereafter, Meitner and Frisch (1939), continuing along the lines suggested by earlier workers, realized that the fission[4] fragment products of uranium would in turn be neutron-rich and that they should undergo beta decay. With this insight they realized that fission could release a great deal of energy—about 200 MeV per uranium fission event. This is an amount 18 times the energy released in the most exothermic known non-fission reaction $^{6}\mathrm{Li}(d,\alpha)^{4}\mathrm{He}$.

In addition, it was predicted by Fermi that beta-delayed neutron emission would take place from the fission products. Later, it was observed that an average of 2.5 "prompt" neutrons were *also* emitted *at the moment* when the initial uranium fission event took place. [Burge 1988]

This excess prompt-neutron production was realized to be extremely significant, in that the excess neutrons could be used, in turn, to trigger additional uranium nuclei to fission and perhaps begin a chain reaction. This possibility was investigated by Fermi in the US, Halban in France, and many others.

In general terms, if one were able to have two fission-event neutrons per each neutron initially introduced into a sample of $^{235}\mathrm{U}$ weighing about 10 kg, then, in 80 generations of reactions there would be on the order of 10^{24} effective neutrons. About $5\mathrm{x}10^{6}$ kilowatt-hours of energy (equivalent to about 5000 tons of TNT) would be released in about 10^{-6} seconds (a microsecond). [ibid] Aside from the military possibilities, it was proposed that this chain reaction could perhaps be controlled to

---

[4] This term was borrowed by nuclear chemists and physicists from the term used by cell biologists for spontaneous cell division [Krane 1988].

provide a new source of energy. In late 1939, with the advent of WWII, work along these paths of investigation were recognized to be extremely sensitive/dangerous in their implications, and all such work was soon subjected to military censorship (and direction).

The systematic understanding of the landscape of the table of isotopes had rapidly developed through this and other work (e.g., see below on charged-particle beam experiments), and the quest for a comprehensive, overall theory, produced a very useful model of the nucleus as an entity akin to a liquid drop. A particular version of this theory is known as the Bethe-von Weizsäcker *Semi-Empirical Mass Model* (SEMM). [Bethe & Bacher 1936] This version of the liquid drop model is particularly useful in describing the fission process —though it does *not* explain the overall shell closures, excitation spectra and many other systematics seen in specific nuclear systems. The predictions of this model (SEMM) as regards the limits of stability of nuclear systems will be explored in detail below.

3.1.3 Early charged-particle accelerator work

The first electro-static (DC) particle accelerator was introduced by Cockcroft and Walton [Cockcroft & Walton 1932] and their machine eventually reached a potential energy of 800 keV.[5] This machine was used for the first accelerator-based nuclear reaction experiment, performed at the Cavendish Laboratories of Cambridge. The experiment carried out was $^{7}\mathrm{Li}(p,{}^{4}\mathrm{He})^{4}\mathrm{He}$ at 125 keV.

This type of accelerator was later supplanted by the Van de Graaff [Van de Graaff 1931] generator. Over about twenty-years' time, this evolved into the modern *tandem* Van de Graaff accelerator. The Van de Graaff generator avoided the problem of DC

---

[5] This historical discussion draws especially on the expositions of [Krane 1988, pp. 559-599] and [Burge 1988, pp. 32-71].

ripple in the potential of the Cockcroft-Walton, and was capable of significantly higher energies.[6] Modern 'tandems' attain energies of 30-40 MeV (e.g., Oak Ridge National Labs' 'pelletron,' University Notre Dame, etc.), and became very common in the 1960's at university-based laboratories in the US and abroad.

Higher energies became feasible only with the development of cyclotrons of various types, beginning with the first cyclotron, built at Berkeley by [Lawrence 1931].[7] This has led to the modern superconducting cyclotrons of the AVS-type, such as that at the NSCL [Sherrill 1991] which was used for the present thesis research.

Early 1930's and 1940's era electro-static accelerators allowed experimenters to conduct elastic Coulomb (Rutherford) and inelastic (Coulomb excitation) scattering experiments to study the excited states of nuclei. They could also be used to induce fission of heavy elements with energetic proton beams – which could easily penetrate the coulomb barrier. This work complimented continuing studies of neutron-induced and spontaneous fission. Such experiments led to the identification of many new and short-lived fission products, especially neutron-rich ones, from europium to, eventually, nickel. Observation of gamma and alpha decay energies, has lead to an understanding of the shell and excited-state structure of isotopes in this region of the periodic table.

The general trend was that, as the energy of accelerators increased, the beams

---

[6] This is not to say that Cockroft-Walton generators do not still find a place in modern devices. A Cockcroft-Walton with low DC voltage ripple was successfully (re)developed for use in the electrostatic portion of the Fragment Mass Analyzer at the Nuclear Division of Argonne National Laboratories by [Davids 1992], while [Becchetti10 1999] has indicated plans for a Cockcroft-Walton-based electrostatic separator element to be located *between* the two TwinSol devices recently built at U. Notre Dame RNB laboratory. In addition, these devices can be used to produce neutron beams from, for example, ^{2}H(^{2}H,n)^{3}He (which requires only a few hundred keV), as injectors into linacs, etc.

[7] For which Lawrence won the 1939 Nobel Prize in Physics. The famous 82-inch cyclotron in use at Orlando Lawrence National Laboratories at Berkeley (LBNL), California, for some 40 years now, is identical in construction to a cyclotron formerly in use here, at the University of Michigan. A picture of the UM device is presented in [Tippler 1978, p. 398], along with the original Cambridge Cockcroft-Walton, and LBNL's 27-in cyclotron in 1934.

of protons, deuterons and alphas produced by these accelerators were able to get ever closer to the nucleus (i.e. to smaller impact parameters). When the incident beam energy exceeds the Coulomb barrier, the projectile-target system will undergo *nuclear* elastic scattering, and *nuclear* inelastic reactions. These nuclear (as opposed to Coulomb) interactions led to either i) *indirect*, compound nucleus reactions, which were first discussed by [Bohr & Klackar 1937] (see also [Wigner 1955], and references therein), or ii) *direct* reactions such as nucleon stripping, which was first discussed by [Oppenheimer & Phillips 1935] for (d, p) reactions,[8] and pickup reactions such as (p, d).

At bombarding nucleon energies of 10 or 20 MeV compound reactions are quite likely as there is a large chance that the incident particle and its energy can be absorbed by a more-massive target nucleus which, after some brief time, will then emit nucleons isotropically.[9] As the beam energy increases, the projectile's de Broglie wavelength becomes small enough that the incident particle begins to interact with objects of a size comparable to that of the individual nucleons within the nuclei; these individual nucleons having an extent of about 1 fm within the target nucleus. When the de Broglie wavelength is comparable to the size of the individual constituents within the nucleus the aforementioned *direct* transfer reactions such as stripping and nucleon pickup, become operative. These reactions provide detailed information on

---

[8] Originally analyzed using the Born approximation which neglected the nuclear interaction effects and was improved by using the optical-model potential to get the wave functions which include the motion of incident and final particles, i.e. the Distorted Wave Born Approximation (DWBA), [Tobocman 1959].

[9] Isotropic emission is characteristic for *light* projectiles, as is generally the case with reactions at tandems. With heavy ion projectiles, a large amount of angular momentum is transferred to the target nuclei in any peripheral collision. When this rotating compound system emits de-exciting nucleons, they are generally emitted in a plane perpendicular to the angular momentum axis, dissipating the angular momentum. Since this axis is perpendicular to the incident projectile's direction, the heavy-ion compound nucleus preferentially emits particles at 0° and 180°. Much is learned from studying such high angular momentum systems, but, here we concentrate rather narrowly on issues immediately relevant to the limits of stability of nuclei against decay by the strong force.

the energies of excited states, and, through studying angular distributions, about their spins and parities. Higher-energy, light-ion-projectile reactions then began to probe the strong, nuclear force as opposed to probing solely the longer-range Coulomb force.

One striking change which occurs with this transition, is the flattening-out in the angular distribution *of cross sections* when going from Rutherford elastic scattering[10] to nuclear elastic scattering. This occurs at impact parameters less than or equal to the radii of the two interacting nuclei (i.e., the classical grazing angle in Rutherford scattering). Crossing this threshold produces pronounced interference effects in the cross section as a function of the emission angle of the scattered particle in the laboratory. These effects were shown to be explained strikingly well by the Optical Model (OM) which was first proposed by [Feshbach, Porter & Weisskopf 1953]. The degree to which these models match a large body of data for light-ion projectiles is illustrated by [Becchetti & Greenless 1969].[11]

The Optical Model has a close analogy to the index of refraction in light optics, in that the real portion of the potential of the interaction describes the elastic scattering of nuclei, while the imaginary portion describes the degree to which nuclei are "absorbed" by the target nucleus via inelastic, nuclear reactions. From the optimum adjustment of the parameters of the optical model so as to fit nuclear scattering data, the nuclear radius, potential well depth and other information is extracted, as well as wave functions for DWBA direct reactions calculations.

---

[10] The angular dependence of *electromagnetic* Rugherford elastic scattering (σ_{Rfrd} goes like the fourth-power of the scattering angle (θ),

$$\sigma_{Rfrd}(\theta) \propto \frac{1}{\sin^4(\frac{\theta}{2})}. \tag{3.1}$$

[11] See also reproduction of figures of [Becchetti & Greenless 1969] in [Krane 1988, p. 416].

By the mid-20^{th} Century, the collection of a large body of reaction data and the now-routine transmutation of stable and long-lived terrestrial isotopes produced a more systematic picture of the landscape of the table of isotopes (excited states, beta decay, neutron separation energies, binding energies, and, especially, of close shells and "magic numbers," etc.). The degree of this development can be seen in the paper by [Mayer 1948], where she summarized data collected through the 1930's and 40's which "show(ed) that nuclei with 20, 50 82 or 126 neutrons or protons are particularly stable."[12]

After many attempts a model of nuclear interactions was developed which would reproduce the magic numbers for closed proton and neutron shells of 2, 20, 28, 50, 82, and, for protons 114, and for neutrons 126. This solution was finally found independently by [Mayer 1949] and by [Haxel, Hans, Suess & Jensen2 1949], in the Independent-Particle Shell Model (IPSM). Their key addition relative to previously proposed models, which had only been able to reproduce the lower shell-closing numbers, was the inclusion of a strong spin-orbit coupling ($\vec{L} \cdot \vec{S}$) term – a term which is much stronger than that of atomic-electron systems and of opposite sign. In the succinct assessment of [deShalit & Feshbach 1974, p. 192] the "*very radical assumptions*" of this theory consist in

> "*asserting* that the nucleus can be described to some approximation in the following way: The nucleons are assumed to move in a single-particle potential $U(r)$, which depends on the nucleon's spatial, spin, and charge coordinates; in addition, one takes into account an *effective residual interaction* ν_{ij}, limiting oneself to first, or sometimes second, order perturbation theory only. ..." (all emphasis in original).

---

[12] See also [Haxel, Jensen & Suess 1949].

The "physical idea" here is simply that, because the nucleons are mutually interacting fermions, their collisions in low-lying states within the nucleus will not deflect their motion and, so, they will rarely be excited by such interactions. Thus "the residual effective interaction is 'weak' and can be treated as a small perturbation." [ibid.]

Suffice it to say, for the purposes of this very general overview, that the Single-Particle Shell Model, and its many extensions, have been extraordinarily successful in explaining a broad range of phenomena across the entire table of isotopes.[13] This model is as fundamental a tool for the nuclear researcher, as is Fermi's theory of conductivity for the solid-state researcher, if not more so.

3.2 Heavy-ion reaction physics

The theories discussed above have been around for some time during which they have continued to be developed and refined. Further, these nuclear models have broad and significant predictive power. Nevertheless, a recent survey of physicists [Physics World 1999] at the end of the 20th century, listed the number two problem to be resolved in physics as being "understanding the nucleus!" Indeed, for all the successes of nuclear theory,[14] many important properties of the nucleus: its quantum states and collective excitations, its limits of stability and even such basic properties such as density and radius, the character of the nuclear force and the origin of the spin of the neutron and proton, etc. face difficulties to greater or lesser degrees. In general, the nucleus presents a problem which is significantly more complex and less

---

[13] Such overviews are a central feature of many standard textbooks in nuclear physics such as [Krane 1988] [Enge 1966] as well as of advanced texts including [de Shalit & Feshbach 1974] [Siemens & Jensen 1987] [Bertsch 1972]. This eclectic list is given principally because these have been found to be enormously useful in this thesis work, and quite stimulating.

[14] Some of which, (viz.: nuclear power and weapons), unfortunately have been and remain, at the center of of social, political and environmental concerns worldwide.

well understood than are the atomic-electron systems and chemistry, where QED[15] can, at least in principle, provide answers to fundamental problems to ten or more decimal-places (e.g., [Bjorken & Grotch 1987, p. 302]) in accuracy(!). Indeed, the modern shell and liquid drop models do not provide the satisfaction which would be derived from a theory which starts from the fundamental, elementary particle interactions on the level of the quark constituents of protons and neutrons, and from the quark constituents of the π mesons (long-range, attractive) and ρ mesons (short-range, repulsive) which mediate the strong nuclear forces between protons and neutrons. Extensive observations of elastic and inelastic scattering reactions, low-energy nucleon transfer reactions, compound nucleus and other relatively *low-energy* reactions involving beams of neutrons, protons and other *light*-ion beams (e.g., d and He) had been accumulated by the 1960's. These models are extraordinarily successful in explaining much of the behavior of nuclei throughout the entire table of isotopes. However, this understanding is based on a limited—and one might even say, biased—sample of all possible nuclear systems. The terrestrially available isotopes whose study has thus far been so intensively pursued, involves some 2700 known isotopes to date. However, extrapolations of nuclear theory predict that perhaps some seven-to-ten thousand [Mueller & Sherrill 1993] nuclear systems should be stable and therefore possible (i.e. 'stable' against decay via the strong, *nuclear* force, though not necessarily the electroweak). The problem with studying these non-terrestrial isotopes, and thereby checking and extending nuclear theory, is that it has been possible in the past to artificially produce only several hundred of the thousands of theoretically possible exotic isotopes. This problem has begun to be

---

[15] Quantum Electro Dynamics (QED), developed independently by Feynman, Tomonaga and Schwinger, and for which they jointly received the Nobel Prize in 1965.

addressed by the development of radioactive nuclear beams (RNBs)[16] over the past 20-25 years.

As the technology of building ever more powerful accelerators has advanced– especially superconducting cyclotrons and synchrotrons – and of building high-intensity ion sources capable of producing high charge-state ions for these to accelerate, it has became possible to accelerate not just protons and helium beams, but very heavy nuclei, up to and including uranium. There were many fundamental advantages to this development of "heavy-ion" beams (see e.g.[Bromley 1985]). One consequence of these is that now reactions involving both a massive projectile and target could be arranged and studied. Others advantages involve the possibilities of inverse-kinematics studies, in which a heavy ion beam impinges a light ion target, and consequently produces kinematic focusing of reaction products.

3.2.1 Inverse-kinematics studies and kinematic focusing

A reaction induced by a proton beam on a heavy target might cause, besides elastic or inelastic scattering and few-nucleon transfer reactions, the target to fission or otherwise emit one of more quite massive products. However, these massive products will have gained very little momentum from the proton. These massive reaction products will therefore either remain embedded in the target material, or be feebly ejected and, so, produce a very low-quality signal in detector systems beyond the target. However, if we do the *same* reaction, but in "inverse kinematics," where the heavy ion is accelerated to form a particle beam, which then impinges onto a proton-like (e.g. plastic or gaseous hydrogen) target, the same nuclear interactions will take place. However, now any projectile-like, compound-nucleus or breakup reaction products, will be emitted from the target much nearer to the velocity of the

---

[16] Sometimes also called RIBs, Radioactive Ion Beams.

original heavy projectile (and, perhaps, with *more* energy/nucleon, if the reaction has a positive Q-value [is exothermic]). Such reaction products can be expected to trigger significantly larger and better-resolved signals in detector systems located beyond the target.

Very complicated magnetic "recoil mass spectrometers" or "fragment mass analyzers" were constructed beginning especially in the 1970's [Symons 1979] [Westfall 1979] to analyze such reaction products. An added bonus of the higher momentum of the emitted reaction products produced with HI-accelerators, besides improved detector responses, is that, as the reaction products' momenta increase, they are increasingly "kinematically focused" in angle when they emerge from the target. Rather than being spread over a large angular range in the laboratory frame, they become focused into a relatively narrow, very forward-peaked cone. Thus, a large percentage of the reaction products can enter the entrance apertures of a magnetic fragment analyzer or spectrometer.

3.2.2 High-energy heavy ion reaction mechanisms

In HI reactions, all of the same reactions which occur at lower bombarding energies for lighter projectiles, will *still* occur at *peripheral* nuclear impact parameters (peripheral incidences). However, a new development with HI's is that central collisions between nuclei—each having a sizeable Coulomb barrier—can now occur (i.e., collisions involving *small* nuclear impact parameters). These interactions may form compound nuclei much as at lower incident energies, but other phenomena begin to occur as well.

As a rule-of-thumb, above 20 MeV/u it becomes impossible for two heavy ions to completely fuse, as the excitation energy of the compound system will cause it to undergo particle emission and/or fission [Gross 1993]. In such a reaction the energy deposited into the compound system may have time (in some manner) to "thermalize" such that an effective "temperature" can be assigned to the system. The system may also fission and produce exotic isotopes which are very proton- or neutron-rich. If the fission products themselves are highly excited (or 'hot'), neutron emission will be strongly favored over charged-particle emission. The "boiling off" of neutrons operates as a mechanism to dissipate the daughter nuclei's excitation energies and begins to dominate over charged particle emission, as the Coulomb barrier suppresses the latter. As a result, the compound nuclear systems in this energy regime tend to produce proton-rich nuclei, *not* exotic neutron-rich nuclei. In addition, unless special, neutron-rich projectiles and/or targets are chosen for the reaction, the n-to-Z ratio of participating nuclei will strongly favor the production of heavy systems which are again *proton* rich.

3.2.3 Multi-fragmentation

Above 20 MeV/u we enter the regime of incomplete fusion of target and projectile, while, at about 30 MeV/u we approach velocities near to the Fermi energy of the nucleons within the nucleus.[17] Here other phenomena begin; multi-fragmentation and projectile fragmentation.

Above the Fermi energy, the incident HI may pass through the target nucleus – or some portion of it – so rapidly, that the effect of the interaction does not have time to completely propagate across either nucleus. If the two HI nuclei overlap incompletely, a section of both the target and projectile may undergo "abrasion-ablation." The overlap region may be a region of nuclear matter so hot as to form a so-called

---

[17] The concept of a Fermi energy and level are explained in detail in the chapter "The Limits of Nucleon Stability."

"nuclear fireball." Additionally, if the impact parameter is quite small a maximally violent collision occurs with the projectile striking the target head on (head on collision). Experimental apparatus which can detect the charged particle multiplicities of reaction products emitted into the full 4π solid angle in the lab have been developed (e.g., the "4π Detector" at the NSCL, and several others elsewhere). Studies of such multi-fragmentation phenomena may reveal the appropriate equation of state for nuclear matter under extreme conditions. If the energy (or temperature) of the resultant system in these collisions is above the average binding energy for stable nuclei (about 8.0-8.5 MeV/u) a type of (perhaps dynamical) phase transition is thought to occur, involving a transition from a 'liquid drop'-like nucleus, to a gaseous-like, completely disassociated state. Experimenters seek to extract the critical exponents of this nuclear phase transition, in complete analogy to atoms in condensed-matter systems, though using the statistical mechanics of relatively small as opposed to infinite systems. The intermediate shapes of nuclei formed when a very energetic HI passes through another, knocking out a large, central portion, have been shown to include quite exotic nuclear shapes, including 'rings' and 'bubbles,' etc. In addition, depending on the temperature of the source which undergoes multi-fragmentation, some degree of re-formation into, cooled nuclei may take place, resulting in large nuclear fragments. Another area of interest in such studies, is search for signs of unusual 'collectivity' in the reaction products indicating new, collective modes of excitation of nuclear matter.

3.2.4 Projectile fragmentation

For the production of very neutron-rich nuclei, 'fireballs' and violent multi-fragmentation reactions would seem to be obviously *not* the way one should proceed. However, at these energies, there are indeed other interactions (reaction mechanisms) which have been very successful in producing exotic nuclei, and in particular neutron-rich isotopes.

The principal interactions of interest are:

1. Projectile fragmentation. [Mueller & Sherrill 1993] This mechanism has been used intensively to produce 100's of new isotopes and RNB's, especially since the 1980's starting with the first such experiments at Berkeley's Bevalac. This mechanism starts at about 30 MeV/u but, is especially productive at energies of $\approx$ 70 MeV/u. Also of recent, renewed interest is;

2. Sequential nuclear fission of the projectile beam and/or certain deep inelastic interactions at about 20 or 30 MeV/u leading to fissioning systems [Souliotis 1997] and;

3. Virtual photon-induced Coulomb fission of U at relativistic energies which is a low-excitation-energy process [Bernas 1998] [Bernas 1994] [Bernas 1997].

3.2.5 Fission from neutron-rich, very massive beams

A striking difference occurs for fissioning nuclei which have additional excitation energy above that acquired when bombarded with thermal neutrons and low-energy protons.[18] When spontaneous or low-energy induced-fission-product yields are displayed against atomic number, a characteristic "double hump" often appears. In the case of ^{235}U with an excitation energy of about 6 MeV, after thermal neutron capture, the peak-to-valley (P/V) ratio of the fission products is about 400, see for example [Bernas 1998, p. 665]. This is characteristic of *asymmetric* fission, where one daughter is strongly constrained by shell closings and other factors to remain at

---

[18] For an exhaustive treatment see [Vanderbosch & Huizenga 1973].

or above a certain mass. However, for greater excitation energies of the parent, or 'mother' nucleus, the fission products can loose their characteristic double hump and become quite symmetrically distributed. Recent experiments at GSI in Darmstadt which produced many new neutron-rich nuclei observed, for example, report P/V ratios of 2.5 or 6.0 [ibid.] and *much more spread out wings* of the distributions in mass (and Z). In these experiments 56 new neutron-rich isotopes were produced by relativistic U on Pb [Bernas 1995], an another 61 new neutron-rich nuclei were produced in 1995, between Ca and Nd—up to and including the r-process path from Ni to Br, and in the region of Te— with n/Z ratios extending to 2.8 [Bernas 1997].

These results were produced by *relativistic* beams of ^{238}U accelerated to 750 MeV/u on Pb and Be targets. At these beam velocities, the virtual photons of the large Coulomb field of the Pb (target) nucleus ($Z = 82$) cause a sharp Coulomb excitation of the U projectile, which then undergoes fission. For the light Be target, Coulomb excitations are only a small contribution; in this case the U projectiles are excited predominately via the strong, nuclear force which induces it to fission, as did the Coulomb excitation from the Pb target.

Another set of experiments, were conducted at a significantly lower beam energy of 20 MeV/u by [Souliotis 1997] at the NSCL, shortly after those at Darmstadt. These experiments reproduced a large number of the new n-rich isotopes first observed by the Darmstadt group at relativistic energies. The mass distribution was shown to be asymmetric, ruling out low-energy fission. This reaction mechanism was shown to be consistent with quasi-elastic or deep-inelastic scattering of the uranium, followed by *sequential* fission.

3.3 Radioactive nuclear beam production

With the proliferation of HI nuclear research, it was not long before beam energies and intensities became sufficient, and magnetic-selection systems sensitive enough, that not only could very short-lived nuclear systems be *detected*, but, in fact, sufficient fluxes of these could be produced and separated in-flight to form useful beams. Thus, relatively pure *secondary* RNB beams became available to experimenters. These exotic RNB isotopes were then, in turn, subjected to nuclear reactions such as elastic and inelastic scattering, transfer reactions, compound nucleus reactions, and fission. This research program mirrors the research undertaken with the mostly stable isotopes available when accelerators were first developed. This advent of secondary RNB reaction studies has greatly expanded the mapping of the theoretically possible nuclear systems over the past $\approx$ 20 years. In the case of some exotic nuclei this research has led to results which conflict with some of the heretofore most fundamental rules of thumb in nuclear physics. These include the observation of nuclei at the limits of nuclear stability having diffuse neutron 'skins' [Tanihata 1992] and in some cases diffuse, very spatially extended neutron 'halos' [Hansen 1995] [DeYoung 1998], and even proton 'halos.' [Warner2 1998]

This is in contradiction to the quite consistent observation of the saturation of nuclear matter (its constant density) and of the proportionality between the radii of nuclei and their atomic numbers (A's) for nuclei near stability. The outer neutrons of the halo nuclei orbit so far distant that, for example, the neutron halo nucleus, ^{11}Be has a diameter approximately equivalent to that of ^{208}Pb [Kelley 1995] even though it has only 5% the number of nucleons – a clear violation of the $r \approx r_0 A^{1/3}$ rule.

Other striking examples of neutron-halo systems include ^{6}He, ^{19}C and, especially ^{11}Li. ^{14}Be [Simon 1998] and ^{11}Li, [Hansen 1995] are examples of quantum-mechanical 'Borromean' systems. That is, these are a special type of three-body system (two-neutron-halo system) in which no combination of the three constituents can form a stable two-body system (e.g., neither ^{9}Li+n = ^{10}Li, nor the di-neutron, nn, are stable). In addition, other RNB work has established the quenching of shell closures (magic number) far from stability. Furthermore, in the light isotopes there is the quenching of the $n = 20$ magic number, and a "transition from spherical to deformed shapes in the so-called 'island of inversion'" [Allatt 1998]. And, at the $N = 40$ subshell, there is reported to be a vanishing of its closure at ^{66}Fe where a "new region of significant deformation" is reported [Wöhr 1998].

In general, the neutron-rich side of the valley of stability, a region mostly free of the strong, disruptive Coulomb forces present on the proton-rich side, appears to be fertile ground to investigate the *nuclear* force. The appearance of new regions of deformity and pseudo-magicity, isomers, halos, and other exotic phenomena present both rich material and a challenge to extant nuclear theory. A study of the neutron-rich nuclei presents an opportunity to extend our present knowledge of the nucleus and its constituents.

CHAPTER IV

The Limits of Nucleon Stability

4.1 Experimental facts—the curve of binding energy

Figure 4.1 is the 'curve of binding energy' for nuclei. This is undoubtedly the most important plot of experimental data to appear in the field of nuclear physics. Over the past ≈ 70 years some version of it has appeared in practically every nuclear physics text book, and in many seminal papers. This particular version plots the binding energy per nucleon, B/A, for the single most stable (i.e., most tightly bound) isotope *of each element* against its atomic number. It was generated using the table of isotope masses as compiled by [Audi & Wapstra 1995].[1] In the case of elements where there are no stable isotopes, for example in the 'actinide gap,' the most tightly bound isotope of each element was taken. The calculation made for each isotope selected is:

$$B/A = \frac{(Nm_n + Zm_z - m(A,Z))c^2}{A} \tag{4.1}$$

where $m(A,Z)$ is the mass of the isotope having atomic mass A and atomic number Z, N is its number of neutrons (i.e., $N = A - Z$), and m_n and m_z are the masses of

---

[1] This is their most recent version, which means that the recently discovered superheavy elements $Z = 109 - 112$ from Darmstadt in Germany, $Z = 116 - 118$ from Berkeley in the US, and $Z = 114$ from Dubna, in Russia are not included. In any case, the most tightly bound (most stable) isotope of each of these new elements is, of course, not yet known.

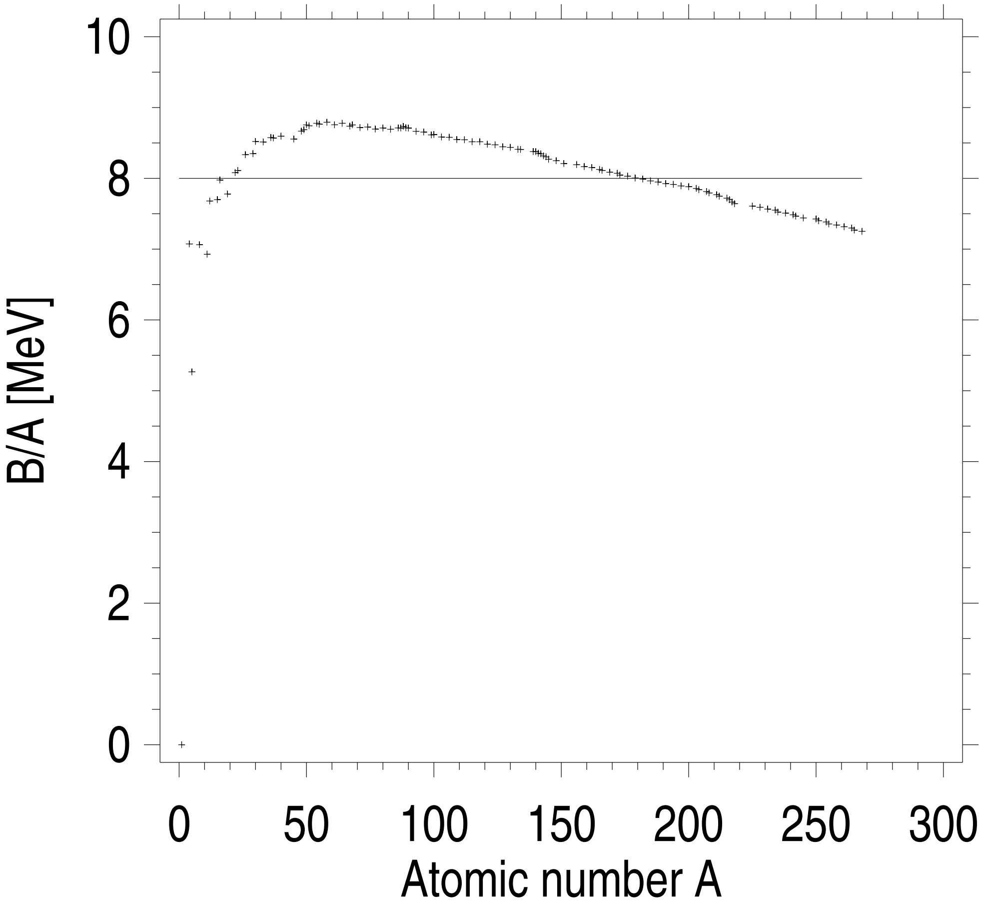

Figure 4.1: Curve of nuclear binding energy. Binding energy per nucleon as a function of atomic mass. Isotopes *above* mass 61 will have a positive Q value (are exothermic) if they fission. Elements below this yield a positive Q for fusion. Plotted is the single most tightly bound isotope of each element as found in [Audi & Wapstra 1995]. Note this selection is slightly different from some other plots.

a free neutron and proton respectively. All the masses are expressed as an equivalent energy, in MeV, using the Einstein mass-energy relationship $E = mc^2$.

To say that a system of nucleons with Z protons and N neutrons comprises a 'bound' system means that, when the system is somehow assembled, its constituent protons and neutrons actually *lose* some fraction of what their masses were as free, individual nucleons. This energy is released from the system as a radioactive emission in the form of gamma rays (electromagnetic energy), beta particles and neutrinos (electroweak decay), alpha or other energetic particle emission, etc. At the top of the curve of binding energy, for iron and cobalt isotopes having atomic masses of about 60, this missing mass fraction is about $\approx 0.9\%$ of what the total mass of 60 free protons and neutrons would be. At the other extremes of the curve—at the bottom left of the curve near helium, or at the bottom right near uranium—the missing fraction for these nuclei is $\approx 0.7\%$.

Being a bound system means that the neutrons and protons in any given nucleus cannot be disassembled and made free and independent again without this 'missing' binding energy somehow being restored. It turns out that there is an abundance of processes in nature and in the laboratory by which this restoration might somehow take place. Much of the history and current practice of nuclear physics and nuclear chemistry was, and remains, concerned with discovering, understanding and controlling such processes.

This thesis is concerned with producing and understanding exotic, neutron-rich nuclei. To make clear just what is and is not 'exotic' for nuclear matter, we have to have some general knowledge of the characteristics of 'ordinary' nuclear matter as reference point. A good place to start such an outline is with the curve of binding energy; much can be inferred from reflecting upon its characteristics.

4.2 Implications of a maximum in the binding energy curve

The curve of binding energy has a maxima at mass 61, for an isotope of nickel.[2] This is the most tightly bound isotope known.[3] One implication of the existence of this maxima is that, if any two of the lighter elements some distance to the left hand side of the curve were forced to combine, the resultant isotope would be farther up towards the peak of the curve, and the net process (reaction) would be exothermic. Similarly, if an isotope some distance to the right hand side of the maxima were to be induced to split apart—or if it were to do so spontaneously—the two daughters into which it split could also be farther up the curve and again the reaction would be exothermic. These two possible exothermic processes are known respectively as nuclear fusion and nuclear fission.

Of course, it is possible to force an element on the right-hand side of the maxima to 'fuse' with some other element, or to cause one on the left-hand side to 'fission.' However, these reactions would require a net *input* of energy to accomplish, and so these reactions are said to have a 'negative Q value.' In nuclear physics, endothermic and exothermic reactions are referred to respectively as 'negative-Q' and 'positive-Q' reactions.

As long as we are clarifying some nomenclature, it should be said that so-called

---

[2] Contrary to accounts which have often wrongly given this distinction to an isotope of iron.

[3] All which is being said here applies to 'ordinary' nuclear matter as it exists in isotopes found on earth, and, for that matter, in most of the universe. However, nuclear matter is also found in the interior of very massive stars, black holes and perhaps elsewhere under extreme conditions of pressure and temperature. Below we will discuss some newly developed experimental circumstances where some of the aspects of such exotic conditions may be briefly recreated. The properties of nuclear matter and elementary particles in these circumstances are expected to be very unlike those of 'ordinary' matter. In addition, nuclei composed of strange quarks are theoretically possible. It is believed that strange-matter would include nuclei which are more strongly bound than the peak in Fig. 4.1. Periodically there is concern raised that a high energy nuclear experiment could produce strange matter which might seed a phase transition of the earth from ordinary u and d quark-based nuclei to strange quark nuclei. This theorized catastrophic transition has yet to be observed by experimenters.

'atomic' bombs are actually 'fission' bombs, while so-called 'nuclear' and/or 'hydrogen' bombs are actually 'fusion' bombs. As both types quite evidently represent 'positive-Q' processes, it should be immediately clear from which sides of the maxima of Fig. 4.1 their respective nuclear fuels are taken. Controlled power production from a nuclear reaction has only been successfully accomplished here on earth using fission. The sun and stars, on the other hand, shine because they are naturally occurring fusion reactors.

4.3 Implications of a flat curve

Although Fig. 4.1 is indeed a 'curve,' nevertheless, if the first 12 - 20 isotopes are ignored, the remainder is otherwise often said to be remarkably flat. This perception of course depends on the aspect ratio used between the ordinate and abscissa. The important point, however, is that, as *compared* to a plot of the binding energy per particle for an object held together by gravity or by the Coulomb force, this curve is indeed quite 'flat.' These two forces obey an inverse-square force law, where the magnitude of the force between *each* pair of particles is written as

$$F_{ij} = k\frac{q_i q_j}{|\vec{r}_i - \vec{r}_j|^2} \tag{4.2}$$

In the case of the force of gravity, k would be Newton's universal gravitational constant, G, and this equation would be that described in [Newton, 1687][4] and q_i and q_j would be the masses of the ith and jth particles, while, in the case of Coulomb's law, k is $1/4\pi\epsilon_0$, and the q's are the electric charges of the ith and jth particles. In both cases, $|\vec{r}_i - \vec{r}_j|^2$ is the square of the distance between the two particles.

---

[4] See Proposition VII, Theorem VII, wherein Sir Issac Newton explains: *"That there is a power of gravity tending to all bodies, proportional to the several quantities of matter which they contain"*, and, further, Proposition VIII, Theorem VIII wherein *"In two spheres mutually gravitating each towards the other, if the matter in places on all sides round about and equidistant from the centers is similar, the weight of either sphere towards the other will be reciprocally as the square of the distance between their centers."* (emph. in original - T. O'D.)[Newton 1687]

Since these forces operate over an infinite distance, finding the potential energy involved in assembling a number A of such particles involves

$$\begin{pmatrix} A \\ 2 \end{pmatrix} = \frac{1}{2}A(A-1) \tag{4.3}$$

two-body interaction terms[5] and the potential energy of the assemblage would scale roughly like A^2. The binding energy *per* nucleon would then scale like A. However, Fig. 4.1 does not increase with A but, rather, bends over after mass 61 and starts a slow and steady descent. A horizontal line has been drawn over the figure at 8 MeV/u (i.e., MeV per nucleon). The median value of the binding energy per nucleon for isotopes above $A \approx 12$ or 20 is evidently about 8.0 MeV/u. This phenomenon, of there being a relatively flat (not linearly increasing) binding energy per nucleon, is known as the '*saturation* of nuclear matter.' In contradistinction to the electrostatic or gravitational force, this saturation is compelling evidence that the nuclear force *must be short-ranged*; it must be that each nucleon added to a nucleus primarily interacts only with a small number of nucleons in its immediate vicinity.

For example, in atomic electron systems, all across the periodic table, the *electronic* binding energy can be quite well represented by the Thomas-Fermi model [Foldy 1951] which gives $B_E(z) = 15.73\ Z^{7/3}$ eV, so that B/Z, the binding energy per electron for atoms, scales roughly like $Z^{4/3}$. This result for atomic electrons grows fractionally *faster* than linear and so is quite different than Fig. 4.1. For an inverse-square force to produce such a flat B/A curve for nuclear matter would require a *very* diffuse, extended nuclear system, but all experimental evidence contradicts such a picture.[6]

---

[5] This is the number of two-body interactions possible amongst A objects, or the number of ways to 'pick two out of A' without double-counting. This can be expressed (on the left-hand side of the equation) as a binomial coefficient.

[6] With the exception of the peripheral nucleons in some exotic nuclei at the very limits of nuclear

4.4 Constant density

In this aspect, it follows that the nuclear force is more reminiscent of something like a nearest-neighbor interaction familiar from the condensed-matter physics of metals, semi-conductors and other solids, or from the nearest neighbor (but spatially unstructured) interactions of molecules in a liquid. In such systems doubling the number of atoms of a sample simply doubles its total binding energy and volume, leaving the density unaffected (i.e., once the size of the assemblage goes beyond that of a small atomic cluster.[7]) As discussed above, elastic nuclear scattering experiments with neutrons, alphas and protons, analyzed with the optical model, have measured the radii of nuclei and their potential well depths. It is found that, quite generally, the radii can be written as

$$R = r_0 A^{1/3} \tag{4.4}$$

where $r_0 \approx 1.25$ fm. However, the surface is found to be diffuse. It has a lower-density 'skin thickness' of about the same magnitude as the range of the nuclear force and the distance between nucleons inside the nucleus [Siemens & Jensen 1987, pp. 48 and 52]. The distance over which the nuclear potential (the real potential of the optical model) falls off from 90% to 10% of its maximum height is taken as this skin thickness and measures typically about 2.9 fm. The information from optical model fits of nuclear scattering data, combined with a study of the most elementary nn and np interactions, reveals a great deal about the character of the nuclear potential (and force).

---

stability called 'halo nuclei,' which are discussed below.

[7] It is interesting to note that an effect similar to the odd-even staggering (OES) in nuclear binding energies attributed to the pairing interaction, has recently been observed in small metallic clusters and is believed to be due to similar 'superconducting' correlations. See [Black 1996] [Rossignoli 1998] [Nazarewicz 1998, and references therein].

4.5 Spin dependence of the nuclear force

The *nuclear* potential used in these optical model fits has a Woods-Saxon shape. It is of the form

$$U(r) = \frac{U_0}{1 + \exp\left(\frac{(r - r_0)A^{1/3}}{a_u}\right)} \tag{4.5}$$

where $a_u = 0.65$ fm and U_0 depends on the energy, E, of the particle used according to

$$U_0 \approx -50 - 48 \cdot t_3 \frac{(N - Z)}{A} + ... \tag{4.6}$$

in units of MeV. The "..." part left out depends on the Coulomb potential of the target nucleus and the energy of the incident particle. The term t_3 is the projection of the incident particle's isospin, defined as +1/2 for protons, and -1/2 for neutrons. This term reflects the fact that a neutron will interact (scatter) more weakly from another neutron than from a proton. This difference in nn vs. np nuclear interaction (or in pp vs. np when the Coulomb force is subtracted out) has its origin in the fact that there is no nn bound state (no di-neutron), found in nature, while there is indeed a bound np state, i.e., the deuteron ($^2_1\mathrm{H}_1$).

4.5.1 Unbound nn state: the di-neutron

The reasons for the nn system being unbound are of far reaching consequences. The argument against the nn bound state starts from i) the fact the any two neutrons are identical fermions and ii) the fact that, for nucleons, it is their total angular momentum $\vec{J}$ which is a 'good' quantum number. The later statement means that $\vec{L}^2$ and $\vec{S}^2$ do not *independently* commute with the Hamiltonian in nuclear interactions (are not independently conserved). However, their sum, $\vec{J} = \vec{L} + \vec{S}$ does commute, and the conservation of $\vec{J}^2$ must be respected in calculations.

Statement i) dictates that, if two neutrons are to be in a state of even-parity orbital angular momentum ($L = 0, 2$, etc.), then the spin portion of their wave function must be anti-symmetric in order to have the required totally anti-symmetric fermionic wave function. The only possibilities for combining two spin 1/2 fermions is for a net spin of $S = 0$ or $S = 1$. Of these only the first can produce an anti-symmetric spin wave function, and so $S = 1$ is not allowed for an nn system. The required $S = 0$ anti-symmetric spin wave function then must be

$$|SS_z\rangle = |00\rangle = \frac{1}{\sqrt{2}}\left(\,|\uparrow\rangle_1|\downarrow\rangle_2 - |\downarrow\rangle_1|\uparrow\rangle_2\,\right). \tag{4.7}$$

However, when an analysis of low-energy scattering cross sections is done which compares the interaction of two fermions with spins parallel ($S = 1$) to that of two fermions with their spins anti-parallel ($S = 0$), it turns out that these two different interactions have very different strengths, and thus very different potential well depths.[8] In the anti-parallel (singlet) case the mutual potential well is found to be too shallow to support a bound state, while the parallel (triplet) potential well is found to be deep enough to support a bound state. where $V_s = 54.7$ and $V_t = 74$ MeV. [Enge 1966, p. 64]

This explains why the di-neutron system is not bound: as identical fermions in a state of even orbital angular momentum, the spin state is required be the anti-symmetric singlet state—whose well depth is insufficient to support a bound state.

4.5.2 Bound np system: the deuteron

This reasoning also explains why the deuteron, however, *is* found to be bound—though just barely so, with a binding energy in Fig. 4.1 of only $2.23/2 = 1.11$ MeV/u.

---

[8] See [Enge 1966, pp. 61-64] and [Bohr & Mottelson 1965] comparing singlet and triplet scattering lengths and effective ranges. Enge gives a comprehensive overview of the nn and np system incorporating many references and explanations of the early experimental work on these systems.

It is because, as *non*-identical fermions, if they have an even (i.e., symmetric) orbital wave function, they cannot have an anti-symmetric spin wave function. So, they will have an $S = 1$ triplet spin state.

The total angular momentum and spin of nucleons is designated by J^π, where J is the total angular momentum, and π is the state's parity which depends on the orbital angular momentum L according to $(-1)^L$. Experimentally the deuteron turns out to have $J^\pi = 1^+$, but it is found to have a small quadrupole moment as well and the spherically symmetric S state cannot account for this. So, while the deuteron is made up of mainly a triplet $^3S_1$ wave function, there must be a small admixture (about 5%) of the only other possible $J = 1$ state-preserving choice for an even orbital angular momentum ($\pi = +$) state, the $^3D_1$. This small $L = 2$ (D state) portion of its total wave function accounts for the deuteron's small quadrupole moment without violating conservation of the total momentum quantum number $J = 1$ [Siemens & Jensen, 1987, p. 15] [Enge 1966 pp. 31-46]. Since neither L nor S need to be conserved separately, varying either or both is legal, so long as we preserve $J^\pi = 1^+$, which we have.

4.5.3 Tensor component of the nuclear force

So, returning to our initial point of departure, the term proportional to N-Z in Eqn. 4.6 reflects the difference in the np vs. nn nuclear interaction (or np vs. pp when the Coulomb interaction is subtracted out). In writing the nuclear interaction, it can be shown that the simplist manner to account for this difference is by a tensor component, with a nucleon-nucleon operator written as

$$S_{12} = \frac{12}{r^2}(\vec{s}_1 \cdot \vec{r})(\vec{s}_2 \cdot \vec{r}) - 4(\vec{s}_1 \cdot \vec{s}_2). \tag{4.8}$$

which can be rewritten in terms of the total spin as

$$S_{12} = \frac{6}{r^2}(\vec{S} \cdot \vec{r})^2 - 2\vec{S}^2. \tag{4.9}$$

4.6 Theoretical understanding

4.6.1 The Liquid Drop Model

Earlier we indicated that there is a macroscopic model which successfully reproduces the general appearance of the curve of binding energy, the Liquid Drop Model (LDM). In its most basic form it is written as

$$B \approx B_v V - B_s S - E_c. \tag{4.10}$$

Here the total binding energy, B, of any given nucleus is modeled as the sum of a volume-dependent part, B_v, a surface-tension-dependent part, B_s, and a part due to the Coulomb repulsion between its protons, E_c. Like the binding energy of any droplet of water, the surface tension here is a negative term while the volume energy is a positive term. This means that to minimize its energy in accordance with the first law of thermodynamics, the droplet is driven to minimize its surface area and maximize its volume. This favors spherical nuclei. [Landau & Lifshitz 1976, pp. 517-518] However, the addition of the long-range and repulsive Coulomb force between the protons in a nucleus lowers the total binding energy. This effect is mitigated if the distance between the protons can be increased. For large nuclei with many protons—in which the Coulomb force is greater—this leads to deformations. Heavy nuclei, especially the rare earths ($150 < A < 190$) and actinides ($A > 220$) often take on substantial static deformations of prolate (especially) or oblate, as opposed to spherical shapes. [Krane 1988, pp. 142-149] These nuclei are made more stable by this deformation.

If one considers the region of interest of this thesis, at much lower Z values than the rare earths and actinides, there is also a

> "...rapid onset of prolate deformation found in the ^{31}Na-^{32}Mg region, where one would normally expect to find a spherical shape for the ground state due to the completion of the $N = 20$ closed shell. The fact that $N = 20$ is no longer 'magic' came as a complete surprise—this deformation could not have been predicted from what as known about other nearby nuclei lying closer to β-stability. Because both strong and electroweak forces play important roles in the binding and decay of these nuclei, fundamental information about the very nature of these forces can be obtained." [Viera 1989, p. 408].

More recently, for example, a study conducted at GANIL in France, found that in the

> "...region of β-unstable nuclei, near $N = 28$" there is a "persistence of the shell closure for large neutron excess (compared to the experimental evidence for an *island* of deformed nuclei located near the closed shell $N = 20$ for $Z < 14$)" and "...an overbinding in the S_{2n}[9] for P, S and Cl isotopes between the two magic numbers $N = 20$ and $N = 28$, indicating a new region of deformed nuclei near $N = 28$. The measurement of the $N = 28$ nuclei like ^{43}P, ^{44}S and ^{45}Cl ...suggest the persistence of this magic gap, even if eroded by the large neutron excess." [Sarazim 1998]

In addition, a study by [Allatt 1998] indicated that the deformations in the $N = 20$ *island of inversion*

---

[9] I.E., S_{2n} are the two-neutron separation energies.

> "...can also result in the appearance of the isomeric states of very neutron-rich isotopes. Such effects may influence the decay properties of these nuclei, such as half-life, and neutron emission probability." This study "...suggests that the deformation phenomena, predicted and observed in the Mg-Na region, disappears below $Z = 11$."

In general, the farther ones goes from closed shells in the table of isotopes, the more likely and the more pronounced these deformations may become. However, the Liquid Drop Model, a collective, macroscopic model, cannot account for microscopic interactions leading to such phenomena as closed shell stabilization at magic numbers. From the viewpoint of the experimentalist, another way to look at this is that, if one subtracts out from measured isotopic masses the portions explained (predicted) by the liquid-drop or other mass models, that which remains are the *microscopic*, quantum-mechanical effects.

4.6.2 The Semi-Empirical Mass Model

A considerable improvement on the simple charged-liquid-drop model Eqn. 4.10 is achieved by the Semi-Empirical Mass Model, also known as the Bethe-von Weizsäcker mass model [Bethe & Bacher 1936], [Bohr & Mottelson 1969,] One form in which this model can be written [Siemens & Jensen, 1987, p. 92] is

$$\begin{aligned} B(N,Z) &= b_v A\left[1 - k_v\left(\frac{N-Z}{A}\right)^2\right] \\ &\quad - b_s A^{2/3}\left[1 - k_s\left(\frac{N-Z}{A}\right)^2\right] \\ &\quad - b_c\frac{Z^2}{A^{1/3}} + \delta[(-1)^N + (-1)^Z]A^{1/2} \end{aligned} \tag{4.11}$$

This formula is fit to the experimentally known binding energies of nuclei across the entire table of isotopes to find the optimum values of its six constants. In a fit done by [Green & Engler 1953] for isotopes with $A > 12$ they were determined to be

$$\begin{aligned} b_v &= 15.68\,\mathrm{MeV} \\ k_v &= 1.50 \\ b_s &= 17.2\,\mathrm{MeV} \\ k_s &= 0 \\ b_c &= 0.70\,\mathrm{MeV} \\ \delta &= 6\,\mathrm{MeV} \end{aligned} \tag{4.12}$$

Were the subscript 'v' stands for volume, 's' for surface and 'c' for Coulomb. Comparing Eqn. 4.1, to Eqn. 4.11 we have the correspondences: $V \rightarrow A$, $S \rightarrow A^{2/3}$ and the Coulomb energy dependence goes like $A^{1/3}$. This 'change of variables' to powers of A, is consistent with the saturation of nuclear matter discussed above, where $R = r_0 A^{1/3}$ as in Eqn. 4.4.

A perhaps more familiar form of the Bethe-von Weizsäcker mass model and its optimal fit parameters are given by Myers [Myers & Swiatecki 1966], as

$$\begin{aligned} B(N,Z) &= Zm_p + Nm_n - a_1 A + a_2 A^{2/3} \\ &\quad + a_3 \frac{Z^2}{A_{1/3}} \\ &\quad + a_4 \frac{(Z-N)^2}{A} + \delta(A) \end{aligned}$$

where

$$\begin{aligned} a_1 &= 15.68\,\mathrm{MeV}\ (\mathrm{volume}) \\ a_2 &= 18.56\,\mathrm{MeV}\ (\mathrm{surface}) \\ a_3 &= 0.717\,\mathrm{MeV}\ (\mathrm{Coulomb}) \\ a_4 &= 28.1\ \ \mathrm{MeV}\ (\mathrm{symmetry}) \end{aligned} \tag{4.13}$$

$$\delta(A) \;=\; \left\{ \begin{array}{lll} 34 & A^{-3/4} & \mathrm{MeV\ odd-odd\,nuclei} \\ 0 & & \mathrm{MeV\ odd-even\,nuclei} \\ -34 & A^{-3/4} & \mathrm{MeV\ even-even\,nuclei} \end{array} \right\} \mathrm{(pairing)}$$

4.6.3 Liquid drop vs. Bethe-von Weizsäcker model

There are two important differences between either of these two versions of the Bethe-von Weizsäcker mass model (Eqns. 4.11 and 4.13) on the one hand, and the simple Liquid Drop Model (Eqn. 4.10) on the other. First, note that the volume and surface terms of Eqn. 4.11 are no longer constants as was the case in Eqn. 4.10. Now each of these terms are mitigated by a factor of $(N-Z)^2/A$. Eqn. 4.13 collects these two $(N-Z)^2/A$ terms together and explicitly labels it as the "symmetry energy." Secondly, Eqn. 4.11 has two final terms which will each produce $\pm\delta A^{-1/2}$ depending on whether there are odd or even numbers of neutrons and protons in the nucleus. In Eqn. 4.10 the equivalent term has become '$\pm\delta A^{-3/4}$'. In both cases it is called the 'pairing energy.'

It remains to explain the rationales for these two new terms—the symmetry and pairing energies. Their origins are somewhat more subtle than are those of the volume, surface and Coulomb terms which appeared in the simple Liquid Drop Model, Eqn. 4.10, and they are particularly important in the details of our program of determining the stability of nuclei near the n-dripline.

4.7 Symmetry energy

There are two physical origins of the symmetry term(s) in the Semi-Empirical Mass Model. One contribution to this term is potential energy, the other kinetic. Both of these contributions cause a nucleus to be more strongly bound when it has equal numbers of neutrons and protons. In this sense this term is sometimes referred to as the '*asymmetry*' term (e.g. [Burcham 1979, p. 186]).

4.7.1 Potential contribution: Isospin

The first cause for a term proportional to $(N-Z)^2/A$ is as a consequence of the fact that the np two-body *nuclear* bond is stronger than either the nn or pp bonds due to the greater strength of the triplet $^3S_1$ vs. the singlet $^1S_0$ potential.

In Eqn. 4.13 the best-fit strength for the symmetry term is given as 28.1 MeV. We can make a numerical estimate[10] of what the Phenomenological Optical Model (POM) potential predicts for this term.

We do not want to delve with great detail here into the Optical Model, but rather intend to sketch out a plausibility argument as to the *physical* origins of the $(N-Z)^2/A$ term in the Semi-Empirical Liquid Drop Model.[11]

The POM Hamiltonian is

$$H_{POM} = \frac{\vec{p}^2}{2m} + U(r) + (\vec{l}\cdot\vec{s})U^{ls}(r) - iW(r). \tag{4.14}$$

From a choice for the potentials which has been very successful for fitting a very large amount of data [Perey & Perey 1976] we take the real potential term U(r)[12] in Eqn. 4.14 to be

$$U(r) = U_0 f((r-R(A))/a_u) + U_c(r) \tag{4.15}$$

Here the function $f((r-R(A))/a_u)$ is of Woods-Saxon shape and was previously

---

[10] This argument follows [Siemens & Jensen 1987] pp. 152-154 and, on the POM, pp. 50-54.

[11] Just to emphasize once more the state of affairs in nuclear physics vs. atomic physics we should point out that, if this were a discussion of atomic phenomena, at this point we would not be resorting to a "phenomenological" model, but would have a fundamental theory, quantum electrodynamics, which would supply the term U^{ls}.

[12] For this discussion we leave aside the spin-orbit portion of the real potential U^{ls} and the imaginary, absorptive term $W(r)$ as we are only interested in terms like $(N-Z)^2/A$.

given in Eqn. 4.5. The term of immediate interest, however, is

$$U_0(E) \approx -50 - 48 \cdot t_3 \frac{(N-Z)}{A} + 0.3(E - U_c(R)) \text{ MeV} \tag{4.16}$$

where the term with $U_c(R)$ is a Coulomb part used for protons and other charged-particle beams. E is the kinetic energy of the incoming beam particles, and the initial term (−50 MeV) is the basic depth of the nuclear well which emerges from fitting the POM to data.

The term t_3 is the isospin projection of a nucleon. In analogy to spin, where a fermion has its spin either "up" or "down," the projection of the isospin degree of freedom distinguishes protons from neutrons.[13] The total isospin, $\vec{t}$ is 1/2 for both a neutron or a proton. The convention in nuclear physics for these isospin operators when acting on a neutron (n) or on a proton (p) is:

$$\begin{aligned} t_3|p\rangle &= +1/2|p\rangle \qquad (4.17) \\ t_3|n\rangle &= -1/2|n\rangle \end{aligned}$$

The 'charge independence of the nuclear force' or the 'isospin projection independence of the nuclear force' means that the potential between nucleons does not depend on isospin *projection*, t_3, or the sum of these projections

$$T_3 = \sum_{nucleons} t_3 = -\frac{1}{2}(N-Z) \tag{4.18}$$

however it can, and does, depend on the total isospin of a nucleus

$$\vec{T} = \sum_{nucleons} \vec{t} \tag{4.19}$$

If we calculate the expectation value of a two-body nucleon interaction, where we represent the ground state determinant by $|gs\rangle$, and the total-isospin part of a

---

[13] For a discussion of isospin from the viewpoint of elementary particle physics, covering both the strong and electro-weak interactions, see [Ryder 1985] pp. 13 and 108.

transition matrix (effective interaction) by $\mathcal{T}^t$ it can be shown [Siemens & Jensen 1987, p. 152] that when the numerical values of Eqn 4.16 are used in this evaluation the result will be

$$\langle gs|\mathcal{T}^t|gs\rangle = \cdots = \frac{(N-Z)^2}{A} 12 \text{ MeV}. \tag{4.20}$$

We shall call this $b_{s,isospin}$ as it is the isospin-dependent part of the symmetry energy. However, if we compare this result with the values of the fit for the Bethe-von Weizsäcker mass model symmetry term (Eqn. 4.12), it is too small by

$$(b_v \cdot k_v) - b_{s,isospin} = (15.68 \cdot 1.50) - 12.0 \approx 11.5 \text{ MeV}. \tag{4.21}$$

The remainder will now be sought in a kinetic-energy contribution.

4.7.2 Kinetic energy contribution: Pauli exclusion

Consider a nucleus with equal numbers of neutrons and protons in the ground state. The uppermost neutron and proton are both at the Fermi energy level, ε_F. To replace a single neutron with a proton requires that the new proton be put into a state of greater energy than the original neutron it replaces—into a state *above* the Fermi level. This is due to the Pauli exclusion principle which dictates that no two identical fermions may be in the same quantum state.

When such a neutron is replaced by a proton[14] this new proton single-particle orbit will necessarily have more kinetic energy than the single-particle orbit which was vacated at the Fermi level by the neutron. All other factors being equal, energy is required to create the new system and the nucleus will have *less* binding energy than the original $N = Z$ *symmetric* system.

A rough estimate of this energy cost can be made using the Fermi degenerate-gas

---

[14] For example, through β decay, which will also produce an e^- and a $\bar{\nu}_e$—both of which leave the nucleus.

model applied to a nucleus. First we need to establish some basic characteristics of the nucleus as a degenerate Fermi gas.

4.7.3 Fermi gas model

If we say the energy needed for removal/separation of the uppermost neutron or proton is the chemical potential μ, then we have a nuclear well with a depth $-U_0$ ($U_0 \approx 50$ MeV) in which our particle orbits with a kinetic energy $\mu = \varepsilon_F$. The Fermi-level momentum is then

$$p_F = \sqrt{2m(\mu - U_0)} = \sqrt{2m\varepsilon_F}. \tag{4.22}$$

The number of states which are allowed (will fit) in the nucleus up to the Fermi level can then be calculated from [Fermi 1949, pp. 154-158] the size of the total six-dimensional phase space (3D configuration space times the 3D momentum space) available to the particles divided by the volume per microstate, which is given by Heisenberg's constant, h

$$N_{states} = \frac{[4/3\pi(Ar_0^3)] \cdot [4/3\pi(p_F^3)]}{h^3}. \tag{4.23}$$

But, there are four particles allowed per state due to their being two distinct spins orientations and two distinct isospins orientations per state. Hence there are actually $A = 4N_{states}$ particles allowed per nucleus. Taking this into account[15] in Eqn. 4.23

---

[15] We are following similar expositions from [de Shalit and Feshbach 1974, pp. 124-126], and from [Siemens & Jensen 1987, pp. 63 and 153]. While numerical results vary slightly between various authors depending on measured values and approximations taken, the numerical values used here are mostly in accord with [de Shalit and Feshbach 1974] who give the Fermi energy as 33 MeV. [Burcham 1979 p. 188] gives it similarly, as 38.3 MeV. However [Siemens & Jensen 1987] give this (and μ) a value of -17 MeV. The latter is evidently a distance measured *down* from the top of the nuclear well, which they take as having of a depth of -50 MeV. The distance, then, of a particle from the *bottom* of their well is ≈ 33 MeV. The discrepancy between these authors is apparently in which direction—from the top or from the bottom—of the well each measure the nuclear "Fermi energy." As we want the kinetic energy of the particle within the well, measurement from the bottom as reference point seems appropriate, as long as the identity of μ and ε_F is also kept in mind. In fact, when doing calculations of the "Fermi momentum," [Siemens & Jensen 1987] identify this with "$\sqrt{2m(\mu - U_0)}$," where $\mu - U_0$ is indeed the distance from the bottom of the well—the kinetic energy of the uppermost-orbiting particle in the ground state.

we can replace A by $4 \cdot N_{states}$, and then cancel out the N_{states} terms from each side of the equation. The highest momentum state is then

$$p_F = \left(\frac{h^3}{4(\frac{4}{3}\pi)^2 r_0^3} \right)^{1/3}. \tag{4.24}$$

But, the nuclear density is just

$$\rho = \left(\frac{4\pi r_0^2}{3} \right)^{-1} \approx 0.172 \, \text{particles/fm}^3. \tag{4.25}$$

This means that the momentum is a function of the density alone

$$p_F = \hbar \left(\frac{3\pi^2}{2} \rho \right)^{1/3}. \tag{4.26}$$

This dependence on the density is identical to the situation for a Fermi gas of electrons in a metal. However in nuclear matter *the density is quite constant for all(!) nuclei*, while in atomic systems the electron densities vary greatly from one element to another. From the de Broglie wave-particle duality relation, $p = \hbar k$ [de Broglie 1923, 1924] we can then also determine the value of k_F to be

$$k_F = \left(\frac{3\pi^2}{2} \rho \right)^{1/3} = 1.36 \, \text{fm}^{-1}. \tag{4.27}$$

The kinetic energy of the uppermost-orbital ground-state nucleon, the Fermi energy, is then

$$\varepsilon_F = \frac{(\hbar k_F)^2}{2m} \approx 38 \, \text{MeV}. \tag{4.28}$$

We will also need the *average* kinetic energy in this model taken over the entire fermion gas. This is, of course, the definition of a temperature of the gas. This is obtained [de Shalit & Feshbach 1974, pp. 126] from the integral

$$\begin{aligned} \langle T \rangle &= \frac{1}{A/4} \int_0^{\varepsilon_F} \varepsilon \frac{dn}{d\varepsilon} \\ &= \frac{3}{5} \varepsilon_F \\ &= 23 \, \text{MeV} \end{aligned} \tag{4.29}$$

4.7.4 Terms like $(N-Z)^2/A$

With these basic results for the Fermi gas model of the nucleus, we pursue the kinetic energy contribution to terms like $(N-Z)^2/A$ which are identified with the Semi-Empirical Mass Model's symmetry energy term(s). In analogy to Eqn. 4.20 which determined the isospin-potential contribution, we use the results of Eqn. 4.29 to write

$$\begin{aligned} \langle gs|K.E.|gs\rangle &= \langle T\rangle(N+P) \\ &= \frac{3}{5}(\varepsilon_N N + \varepsilon_P Z) \end{aligned} \tag{4.30}$$

where we have separated the nucleons up into two separate Fermi gasses, one of N neutrons, and the other of Z protons—each with their own Fermi energies. We assume each set moves within the full nuclear potential [Siemens & Jensen 1987, p. 153]. This gives the number of neutrons in terms of their Fermi momenta as

$$\begin{aligned} N(p_{F,N}) &= 2 * \frac{1}{h^3}2\left(\frac{4\pi R(A)^3}{3}\right)\cdot\left(\frac{4\pi p_F^3}{3}\right) \\ &\equiv \eta\, p_F^3 \end{aligned} \tag{4.31}$$

and a similar result for $Z(p_{F,Z})$. The factor of two in front the expression is to account for the spin degeneracy of the neutron (proton) gas.[16] Using the earlier result $\langle T\rangle = \frac{3}{5}\varepsilon_F$ we have

$$\langle gs|K.E.|gs\rangle = \frac{3}{5}\left(\frac{p^2}{2m_{proton}} + \frac{p^2}{2m_{neutron}}\right). \tag{4.32}$$

Using Eqn. 4.31 to put this in terms of N and Z produces

$$\langle gs|K.E.|gs\rangle = \frac{3}{m\eta^2 10}\left(N^{5/3} + Z^{5/3}\right). \tag{4.33}$$

---

[16] It is important to keep in mind that the factor of two for isospin and two for spin is *not* the determining factor in labeling this a '*degenerate*' Fermi gas. Rather, this specifically refers to the situation where the ambient temperature is much less than the temperature of the nucleons in the nucleus. The later is defined by the limiting energy ε^F. "The temperature defined by the relation $T_F \approx \varepsilon_F$ is called the *degeneracy temperature*." [Landau & Lifshitz 1976 p. 168 and, see also p. 165]. (emphasis in original).]

This can be Taylor expanded in terms of $(N-Z)/A$ and A to produce

$$\langle gs|K.E.|gs\rangle = \varepsilon_F \left(\frac{3}{5}A + \frac{1}{3}\frac{(N-Z)^2}{A}\right). \tag{4.34}$$

Using 38 MeV for ε_F we get

$$b_{s,Pauli} \approx 12.7\,\mathrm{MeV}. \tag{4.35}$$

Finally, combining this with the isospin-potential result of Eqn. 4.20 yields

$$b_{s,isospin} + b_{s,Pauli} \approx 12 + 12.7 = 24.7\,\mathrm{MeV}, \tag{4.36}$$

which compares rather favorably with the symmetry term in the Bethe-von Weizsäcker model

$$(b_v \cdot k_v) = (15.68 \cdot 1.50) = 23.5\,\mathrm{MeV}. \tag{4.37}$$

The conclusion then, is that the binding-energy-*lowering* symmetry term in the Semi-Empirical Mass Model is about one-half due to a potential-energy contribution having to do with the potential's isospin dependence, and about one-half due to kinetic energy gains which Pauli exclusion forces upon non-isospin-symmetric nuclei. The other term added to the Semi-Empirical Mass Model over and above the naive charged-liquid-drop model is the pairing energy.

4.8 Pairing energy

It is the pairing energy which is responsible for the observed very low number of stable odd-odd nuclei in the table of isotopes. In Table 4.8 we list the numbers of stable isotopes as a function whether A, Z and N are even or odd numbers.

The very low number of Z-N $\Rightarrow$ odd-odd stable isotopes, and the very high percentage of even-even stable isotopes, known as the odd-even staggering of binding energies (OES) [Heisenberg 1932] is a direct result of correlated nucleonic parings.

A	Z	N	Stable
odd	odd	even	50
odd	even	odd	55
even	odd	odd	4
even	even	even	165
		Sum:	274

Table 4.1: Numbers of stable isotopes by odd/even numbers of nucleons. Odd-even staggering (OES) effect due to pairing energy favors even-N and even-Z nuclei. Data from [Evans 1955].

[Bohr, Mottelson & Pines 1958] In particular the phenomena of β^+ and β^- decay into these stable isotopes is the result of a spontaneous, cascading chain of decays made energetically favorable by pairing-energy differences. These sequences of decays are said to go through 'isobaric analog' (constant-A) nuclei into the most tightly bound isotope in each isobaric multiplet.

The Pauli exclusion principle for a Fermi gas is also responsible for the pairing energy term in the Semi-Empirical Mass Model. The pairing phenomena can be explained[17] by starting from consideration of an effect of the relatively longer-distance, attractive portion of the nuclear potential, as opposed to the shorter, hard-core, repulsive portion. Two-body collision hard-core interactions near the Fermi surface may cause scattering of nucleons into a state above the Fermi level, leaving behind a particle-state 'hole' just below the Fermi level. The correlation between the particle and hole cause them to act effectively as though they were a single-particle entity, called a *quasi-particle*. It is extremely important to note that such scattering

---

[17] Here we are closely following the succinct exposition of [Burcham 1979, pp. 190-193]. Burcham's eigenvalue problem was calculated using the IDL^R language to produce Figure **??**.

is extremely unlikely for nucleons much *below* the Fermi level, as the possible energies one of them may gain in such a collision are extremely unlikely to allow either one to move to an unoccupied state *above* the Fermi level—the only place which Pauli exclusion would allow it to go. This extremely restrictive barrier to lower-lying nucleons scattering off one another, called ‘Pauli blocking,’ is the fundamental reason why the entire core of the nucleus may be treated as a single entity and approximated as a rather static mean field in which the remaining few incomplete-outer-shell nucleons move.

However, for two nucleons near the Fermi surface which interact under the influence of the longer-range attractive portion of the nuclear potential, an entirely different phenomenology results. Here we consider collisions in which the resultant angular momentum of the pair becomes zero. In this collision we will call the initial two-body state S_1, its internal momentum vector $\vec{k}_1$, the final two-body state S_2 and its momentum vector $\vec{k}_2$. The initial collision conserves momentum and subsequently, further interactions of the two particles will conserve energy and end up putting the two back into the relative state of motion S_1. Similar phenomena are found in Fermi electron gasses in metals, and, like these metals, if the force is attractive, the net result is that pairs found back in their S_1 states are lowered in energy. This lowering in energy opens up a gap for the ground state.

This may be seen in a general way as follows. Take the kinetic energy of each of the two particles to be a plane-wave state where

$$e_i = \frac{\hbar^2 ki^2}{2m} \qquad i = 1, 2. \tag{4.38}$$

If the complete set of wave functions of the *two*-body potential-free Schrödinger

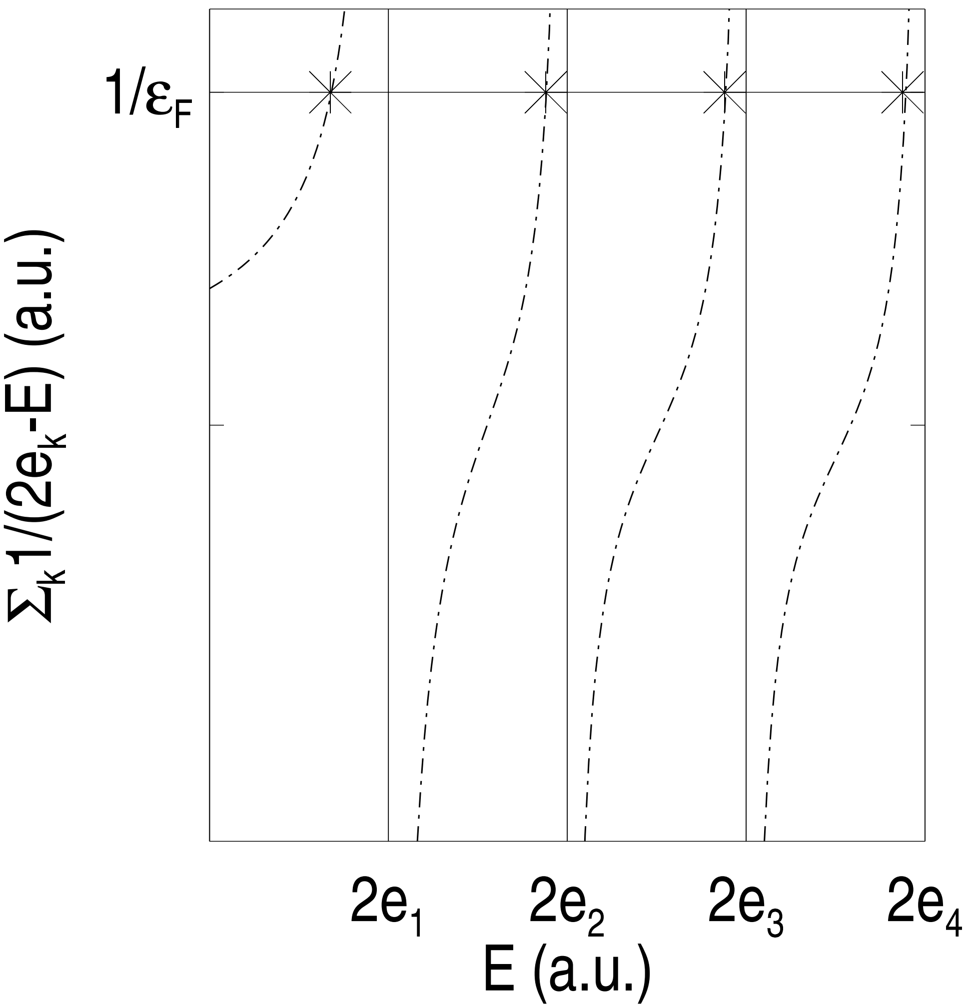

Figure 4.2: Energy gap due to lowering of 'ground state' for pairing interaction of two nucleons near Fermi surface. Figure shows graphical solution for the eigenvalue problem of Eqn. 4.44. The sum (dash-dotted lines) was performed over five lowest k values. The crosses show solutions. Vertical lines are unperturbed plane-wave states. Note the ground state is shifted lower than others, opening up a pairing-energy 'gap' like that responsible for the pairing term in Bethe-von Weizsäcker Semi-Empirical Mass Model."

equation are

$$\phi_1, \phi_1, ...\phi_n, \tag{4.39}$$

we then have

$$H_0\phi = E_0\phi \tag{4.40}$$

and a ground state energy where $E_0 = 2e_1$. Now, a potential is added to represent the collisions of the two particles and the new, perturbed Hamiltonian will have some wave function for its solution ψ. Then the Schrödinger equation is now

$$(H_0 + V)\psi = E\psi \tag{4.41}$$

where ψ is assumed to be able to be expanded in terms of the earlier set of ϕ's. This means that

$$\psi = \sum_i^n c_1\phi_1 \tag{4.42}$$

The solution for E is then [Burcham 1979, p. 192] found from

$$(2e_k - E)c_k + \sum_i^n = c_i\langle\phi_k^*|V|\phi_i\rangle = 0. \tag{4.43}$$

Assuming that this situation occurs only very near to the Fermi surface of the nucleus, we have the requirement that *all* the brackets on the right hand side of Eqn. 4.43 must be either equal to the Fermi energy, or are zero. Then Eqn. 4.43 leads to the eigenvalue equation

$$\frac{1}{\varepsilon_F} = \sum_k^n \frac{1}{(2e_k - E)} \ . \tag{4.44}$$

A graphical solution of this is plotted in Fig. 4.2. Here we plotted the $1/\varepsilon_F$ value from the left hand side of Eqn. 4.44 as a horizontal line, and overlaid the sum from the right hand side. Five values of k were numerically summed over to produce this plot. For comparison, the unperturbed, plane wave solutions are plotted as vertical, solid lines. The intersection of the terms representing the left- and right-hand sides of Eqn. 4.44 are the solutions of the eigenvalue equation. Note that the lowest energy solution is *displaced a greater distance below* the unperturbed ground state than are the other solutions with respect to their adjacent unperturbed states. This additional distance demonstrates the origin of the pairing energy gap between the ground state and first excited state of most even-even nuclei. These states have a high degree of coherence, akin to a superconducting state in low-temperature metals.

As a result of this *lowering* of even-even nucleis' ground states by a factor generally assigned a value of "2δ" [Burcham 1979, p. 193], those odd-odd nuclei having the same values of A will have dissimilar and therefore unpaired nucleons in their ground states. Since these will not experience this lowering, they are almost always energetically favored to β-decay into the even-even nuclei. This "2δ" difference in energies between 'isobaric-analog' even-even and odd-odd nuclei is represented in the Semi-Empirical Mass Formula by *raising* odd-odd nucleons' energies by "δ", and *lowering* the even-even by "δ". This '2δ' OES staggering of binding energies (and, as a consequence, frequently an odd-even staggering of particle yields in reactions—especially fission) becomes a major effect at the limits of stability, in very neutron-rich nuclei of the sort we are particularly interested in in this thesis research.

4.9 Mass and Stability Predictions

4.9.1 Neutron and proton dripline predictions from Bethe-von Weizsäcker model

Having sketched out the physical principles behind each term of the Semi-Empirical Mass Model, we will now see what this and other, more sophisticated models predict for the limits of nuclear stability in the region of interest of the experiments performed for this thesis.

The most straightforward approach would be to take partial derivatives of Eqn. 4.11.[18] with respect to N and A and set these equal to zero as with

$$\left.\frac{\partial B}{\partial N}\right|_{Z} = 0 \qquad \text{and} \qquad \left.\frac{\partial B}{\partial Z}\right|_{N} = 0. \tag{4.45}$$

This should reveal the limits of stability. That is to say, when the addition of a single neutron at constant Z no longer increases the binding energy, the additional neutron will not be bound, and we have arrived at the neutron 'dripline.'[19] This first 'failed' isotope is the first step *beyond* the limit of stability predicted by the Semi-Empirical Mass Model. A similar argument applies to the addition of protons at constant N, until the limits of stability are found at the proton dripline.

In practise, since N and Z (and the linear combination: $A = N + Z$) in Eqn. 4.11 are integers, it is appropriate to rewrite the partial derivatives above as difference equations. This is done by simply calculating $B(N, Z)$ for the entire table of isotopes and then calculating

$$\begin{aligned} S_N(N,Z) &= B(N,Z) - B(N-1,Z) \\ &\text{and} \\ S_P(N,Z) &= B(N,Z) - B(N,Z-1) \end{aligned} \tag{4.46}$$

The physical interpretation of this first differences is that S_N is the 'one neutron separation energy' and S_P is the 'one proton separation energy.' Earlier we said that,

---

[18] We start with Eqn. 4.11. However, as it stands it will actually yield the total mass-energy of nuclei. For our purposes we don't want this, but rather the *binding energy* Hence, we drop the terms in Eqn. 4.11 which represent the mass of the nucleons when they are free $(M_N \cdot N + (M_Z \cdot Z)$, and then reverse the sign of the remainder of the equation. The expression this produces will directly yield a curve such as the curve of binding energy, shown in Fig. 4.1. Various equations which all contain essentially the identical information are traditionally referred to as the nuclear 'binding energy.'

[19] This perhaps fanciful terminology is, however, consistent with the theoretical paternity of the prediction: When a single additional nucleon will not adhere to the 'liquid drop' nucleus, it 'drips off.' "Physics is nothing if it be not consistent." [Anon.]

if one wants to 'disassemble' a nucleus, the curve of binding energy tells us exactly how much energy must be somehow supplied to liberate the constituent neutrons and/or protons. Now, here, we have expressions (predictions) for how much energy would have to be supplied to free a single, *outermost* neutron or proton. For very neutron-rich isotopes this energy is supplied by the energetically favorable β decay of a neutron into a proton. The daughter isotope is still neutron rich and often may be in an excited state such that the β^- decay is followed by the ('β^--delayed') *direct* emission of one, two or even three neutrons. This is the source of the observed delayed neutrons from n-rich fission fragments. The β^-2n and β^-3n decay of the prototypical exotic (neutron-halo) isotope, ^{11}Li were discovered respectively in 1979 and 1980. [Hamilton 1980] From observations of these emissions S_N's of exotic isotopes can be determined and, indirectly, the $B(N, Z)$ predictions of different nuclear mass models can be tested.

We are particularly interested in predictions of the dripline in the region of $10 \leq Z \leq 30$. Fig. 4.3 shows two examples of calculations performed using the Bethe-von Weizsäcker Semi-empirical model. The upper case illustrates a calculation for the isotopes of the even-proton-number element calcium, $_{20}$Ca. The curve labeled "$B/10$" is the Bethe-von Weizsäcker binding energies, from Eqn. 4.11, in MeV (divided by 10). The curve labeled "B/A" are the predicted binding energies per nucleon (in MeV/u) for each isotope, and the jagged curve labeled "S_N" shows the predicted *one*-neutron separation energies calculated using Eqn. 4.46. The value of S_N is predicted to go to zero for $^{56}_{20}\mathrm{Ca}_{36}$,[20] meaning that this is the Bethe-von Weizsäcker dripline location for Ca. The effect of the pairing term in Eqn. 4.11 is

---

[20] The standard notation used here indicates the A, Z and N values for the isotope according to the scheme: $^{A}_{Z}\mathrm{Ca}_{N}$. The one remaining possibility, a superscript on the right hand side, $\mathrm{Ca}^{\pm q}$ is used when one wishes to indicate the ionic charge state (positive or negative) in which the isotope was found.

starkly visible in the jagged appearance of the S_N line. The greater binding energies of even-even nuclei in general is reproduced here, with the result that, had it not been for the paring contribution, $^{53}_{20}$Ca would have been the predicted location of the dripline. However, the pairing term is predicted to be sufficient to stabilize an additional two even-even isotopes beyond $^{53}_{20}$Ca. In fact, this every-other-one is stable phenomena has been observed in many elements just before the drip line.

The lower plot in Fig. 4.3 shows the same calculations for the odd-proton-number element vanadium, ^{23}V. Figures 4.4 and 4.5 are surface plots of, respectively, S_N and S_P for the entire region of interest (ROI) of the present experiments. While the S_N surface shows the profile of the model's predictions for the neutron dripline, obviously all the isotopes whose S_N values are shown to the left-hand side of this region are not stable nuclear systems as they become extremely proton-rich. The same can be said, albeit in reverse, for the S_P surface: it only indicates stability with respect to the proton dripline, etc. What is needed is the overlap of these two sets of calculations/predictions.

Fig. 4.6 is made by operating on an array of the $B(N,Z)/A$ calculations for isotopes in the ROI with the Boolean truth function

$$\mathrm{\Theta(N,Z) = (S(N,Z)_N > 0)and((S(N,Z)_P > 0)} \tag{4.47}$$

which identifies those isotopes in the ROI which are *between* the n- and p-driplines. Note that the vertical axis begins at a value of $B/A = 6.5$ MeV/u. The interpretation is that this is the the minimum energy/nucleon needed in this model to form a bound nuclear system in this ROI. The high ridge running just 'south' of the $N = Z$ line shows the location of the valley of stability; these nucleons have a B/A in excess of 8 MeV/u.[21]

---

[21] Note that these fits are claimed to be good only for isotopes of $Z \geq 12$.

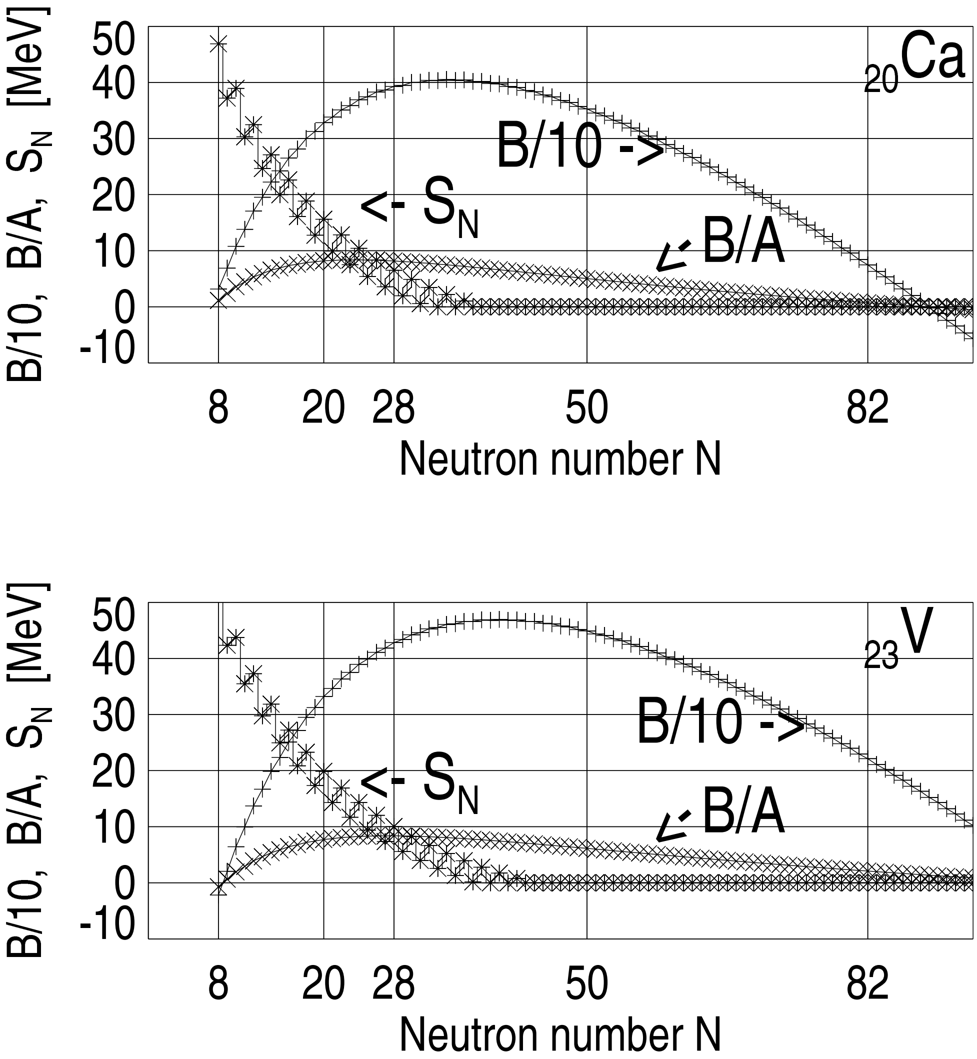

Figure 4.3: Calculations from the Semi-Empirical Mass Model for Ca and V. Shown are the total binding energy (divided by 10), $B/10$; the binding energy per nucleon, B/A; and the one neutron separation energies, S_n. Note the effect of pairing energy causing odd-even staggering (OES) in S_n values.

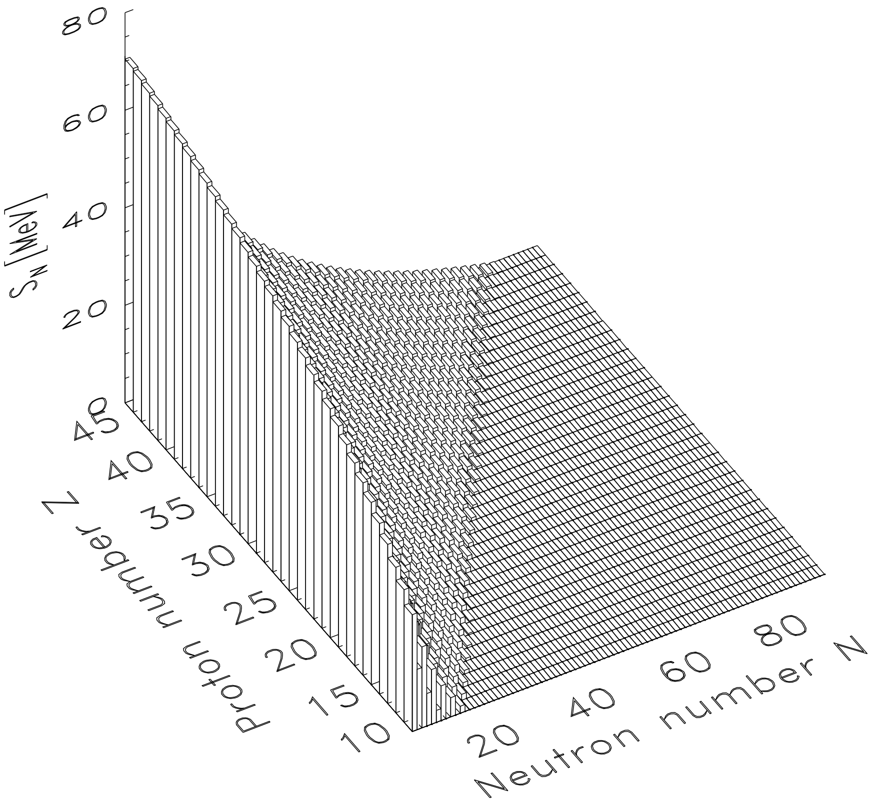

Figure 4.4: Calculated values for the neutron separation energy from Semi-Empirical Mass Model. The calculated neutron dripline is at the transition from the curved portion of the surface to the flat portion, where the neutron separation energies, S_n, go to zero. See text for further explanation.

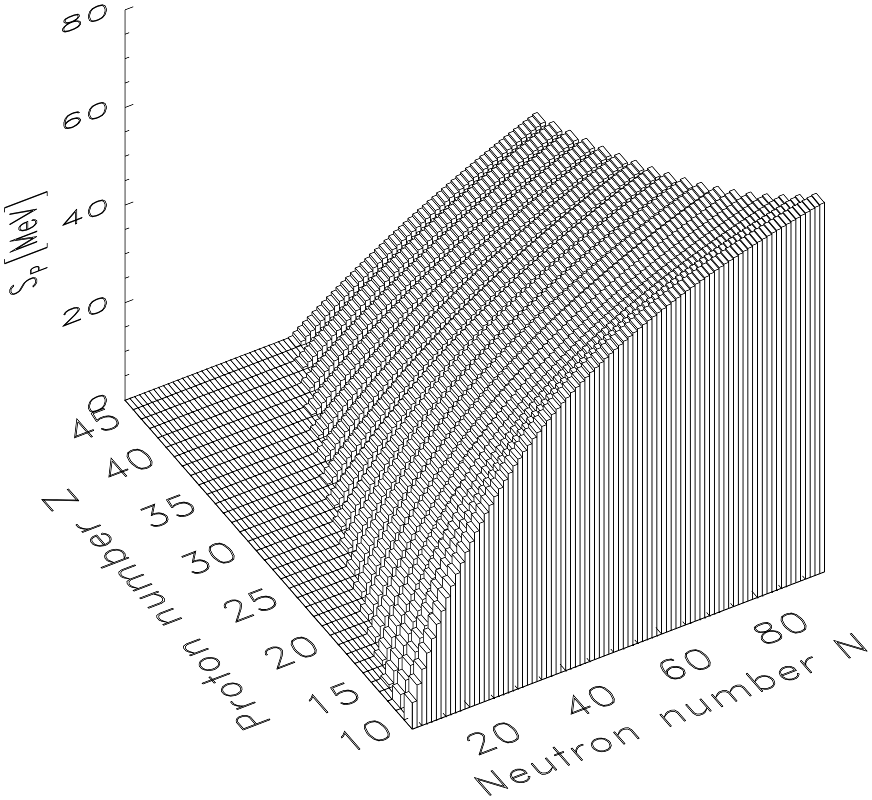

Figure 4.5: Calculated values for the proton separation energy, S_p, from Semi-Empirical Mass Model. The calculated proton dripline is at the transition from the curved portion of the surface to the flat portion, where the proton separation energies go to zero. See text for further explanation.

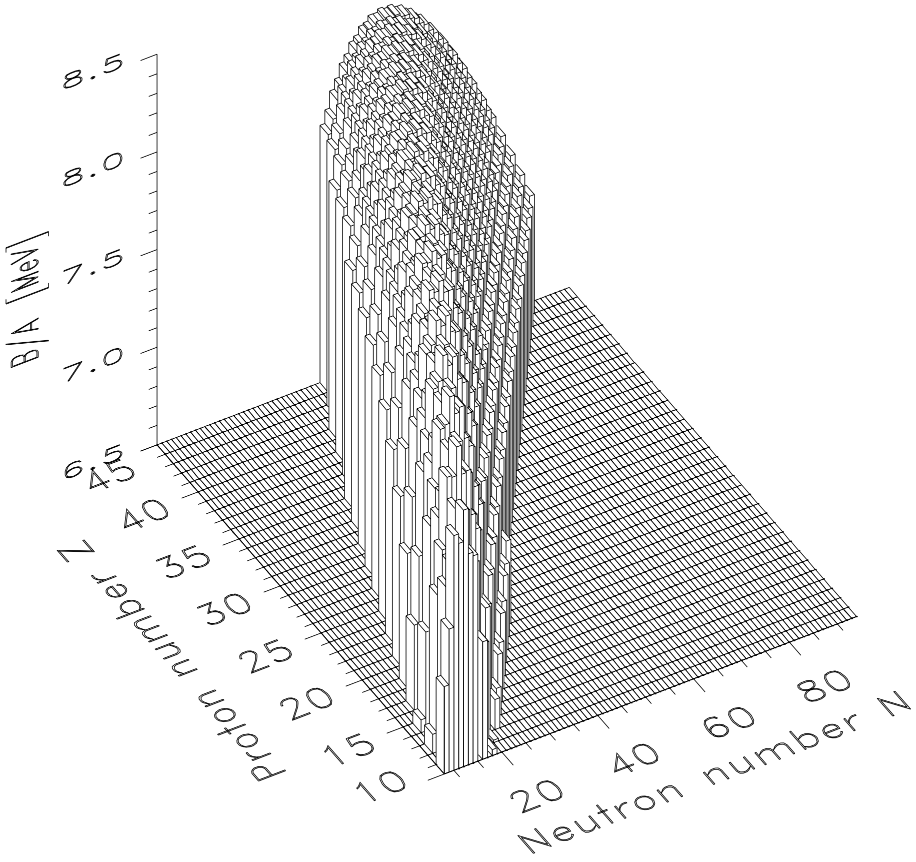

Figure 4.6: Calculated neutron and proton driplines from Semi-Empirical Mass Model. The neutron and proton driplines are at the right- and left-hand edges respectively of the lego surface. Note the lowest binding energies here is just above 6.5 MeV. See text for further explanation.

For later comparisons, the isotopes that are predicted to be stable in the Bethe-von Weizsäcker model are mapped out in a view of the table of isotopes in Fig. 4.7. In practise we know that this cannot be the entire story. Although this mass model is a great improvement over the naive charged-liquid-drop model, nevertheless we know that there are microscopic, quantum mechanical effects which no macroscopic, collective model can account for. The principal additional phenomenon which emerges from even the most rudimentary microscopic calculation is the emergence of closed shells. The more sophisticated the microscopic model, the more of these closed shells it accurately locates.

From Fig. 4.6 we can see that the predicted dripline and near-to-dripline nuclei are bound by as little as 100-300 keV. However, shell-closing effects produce ground-state energy gaps on the order of MeV. Clearly, then, microscopic calculations for nuclei in the vicinity of the driplines may significantly alter the semi-empirical collective-model predictions.

If we restate this last point in a more positive light—from the perspective of the experimentalist at least—we see that *actual laboratory measurements* which determine the location of the dripline will reveal the microscopic shell effects when compared to the predictions of macroscopic models.

4.10 Shell model levels

We shall not discuss in detail the single-particle or other shell model(s). However, it is important for later reference to give the results of a spherical single-particle shell model without static deformations. The convention in Table 4.10 is to label the single-particle quantum states as follows

$$\left({}^{n}l_{j=l+s}\right)^{2j+1} \tag{4.48}$$

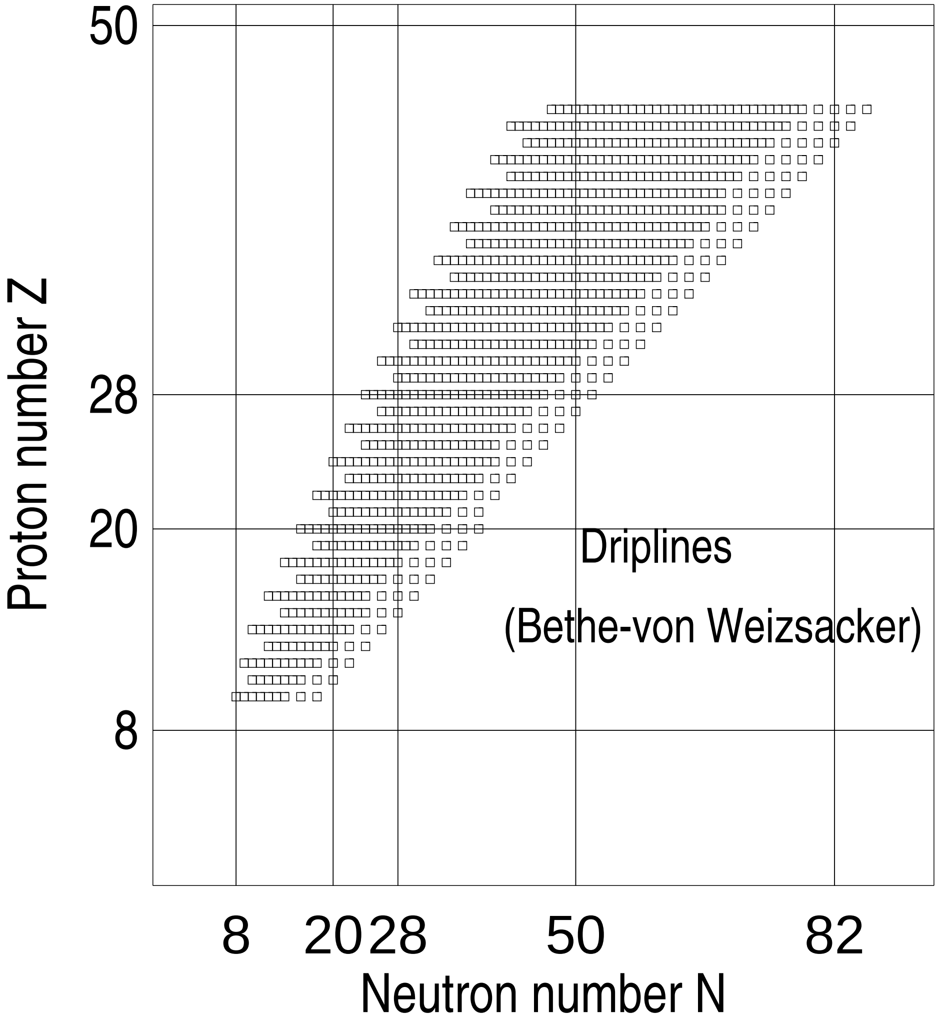

Figure 4.7: Neutron and proton driplines as predicted by the Semi-Empirical Mass Model, shown on a table of isotopes. The neutron- and proton-driplines are on the right- and left-hand edges of the chart respectively, and exhibit odd-even staggering due to the effects of the pairing-energy term.

where n is the radial quantum number, j is the total angular momentum. Here $j = l + s$, where l is the orbital quantum number: $[s, p, d, f, g, \ldots] = [0, 1, 2, 3, 4, \ldots]$, and s may be $\pm 1/2$ for any single neutron or proton. The parity of single particle states is determined by the value of its orbital angular momentum from $\pi = (-1)^l$.

The physical picture here is that of single-particle orbits of the outermost nucleon(s), moving in the mean field of *all* the other nucleons. The order of filling of the single-particle shell-model states for spherical nuclei is found by reading the levels given in Table 4.10 from the bottom to the top. When a shell is completely filled, at the numbers of nuclei indicated (2, 8, 20, etc.), the nucleus will be *perfectly* spherical and be in an *overall* J^π state of 0^+ (the states given in the table are those of the *outermost*, single proton and/or neutrons *only*).

The numbers at the right: 2, 8, 20, 28 and 50 (a complete table would include 82, and then also 126 for neutrons and 114 for protons), are the locations of shell closures, and these are called the 'magic numbers' in nuclear physics. The single-particle shell model was discovered independently by Maria Goeppert-Mayer and J.H.D. Jensen, for which they received the Nobel Prize jointly in 1963. [Mayer & Jensen 1955]

As one approaches the dripline, in general the behavior of the very loosely bound outermost nucleon(s) may become 'exotic,' in that they do not bind to the remaining core nucleons in the manner which is familiar from studying the stable nucleons. The Semi-Empirical Mass Model, for example, is derived largely from an understanding of the ≈ 270 isotopes which naturally occur here on earth. So too is the single-particle shell model. Suffice it to say, that the predictions of these models—including predictions of what the shell closures (magic numbers) are—will often break down as one considers isotopes at the limits of stability. This is a fundamental motivation of the present experimental research.

$\left({}^{n}l_{j=l+s}\right)^{2j+1}$	*Nucleons*	*Shell*
$\left({}^{1}g_{\frac{9}{2}}\right)^{10}$	$\boxed{50}$	fp shell
$\left({}^{2}p_{\frac{1}{2}}\right)^{2}$		
$\left({}^{1}f_{\frac{5}{2}}\right)^{6}$		
$\left({}^{2}p_{\frac{3}{2}}\right)^{4}$		
$\left({}^{1}f_{\frac{7}{2}}\right)^{8}$	$\boxed{28}$	dp shell
$\left({}^{1}d_{\frac{3}{2}}\right)^{4}$	$\boxed{20}$	pf shell
$\left({}^{2}s_{\frac{1}{2}}\right)^{2}$		
$\left({}^{1}d_{\frac{5}{2}}\right)^{6}$		
$\left({}^{1}p_{\frac{1}{2}}\right)^{2}$	$\boxed{8}$	sd shell
$\left({}^{1}p_{\frac{3}{2}}\right)^{4}$		
$\left({}^{1}s_{\frac{1}{2}}\right)^{2}$	$\boxed{2}$	

Table 4.2: Single-particle shell model levels (states) for lowest five proton or neutron shells. The systematics of the appearance of gaps between closed shells is completely ‘accidental’ in that the strong spin-orbit coupling term in the nuclear potential (propotional to $-\vec{L} \cdot \vec{S}$) lowers the energy of a given orbital angular momentum state inversely proportional to its total angular momentum, j. Thus, note the pf shell's $\left({}^{1}d_{\frac{3}{2}}\right)^{4}$ state is *higher* in energy than its $\left({}^{1}d_{\frac{5}{2}}\right)^{6}$ state. Adopted from [Enge 1966, pp. 154-155]. Note that, as nuclei deform, the distances between states are changed; some levels will be raised in energy while others will be lowered. Hence, some level-orderings will eventually cross at some level of deformation.

Figures 4.8 and 4.11 show the general state of affairs along the valley of stability and driplines. Note these compilations were taken from the mass tables of [Audi & Wapstra 1995]; these tables include *both* measured masses *and* extrapolations to as-yet unobserved/unmeasured isotopes.

4.11 The predictions of Jänecke and Masson

A number of macroscopic and microscopic mass models have been developed (see e.g. [Haustein 1988]) to calculate, and predict, nuclear binding energies. Here we present nuclear mass predictions from one contemporary mass model other than the early Bethe-von Weizsäcker SEMM (Semi-Empirical Mass Model). The mass model of Jänecke and Masson [Jänecke &Masson 1988] has been very successful in predicting nuclear masses.[22]

The basis of the Jänecke & Masson model and predictions are as follows: The effective n-p interaction, $I_{np}(N,Z)$, is defined as shown in the top line of Fig. 4.10. The grids shown in this figure represent arbitrary portions of the table of isotopes with neutron number increasing along the horizontal axis and proton number increasing along the vertical axis. The plus and minus signs represent the binding energies of the respective nuclei. The top line of the figure represents an operational definition for the quantity $I_{np}(N,Z)$ for a given isotope (that isotope which is located in the dark-outlined, upper-right-hand corner of the 4x4 grid)

$$I_{np}(N,Z) \equiv B(N,Z) - B(N-1,Z) - B(N,Z-1) + B(N-1,Z-1). \qquad (4.49)$$

Here, $B(N,Z)$ is the nuclear binding energy of the isotope with N neutrons and Z protons. Assuming that $I_{np}(N,Z)$ changes only little for neighboring isobars, one

---

[22] For example, a report on a recent measurement of the masses of 48 neutron-rich nuclei from ^{55}Sc to ^{75}Cu [Bai 1998, pp. 90-93.] at Los Alamos (TOFI spectrometer) observed: "Comparing experiment to a variety of mass models, we find that the predictions of Möller and Nix [Möller & Nix 1995] and Jänecke and Masson are generally the best overall."

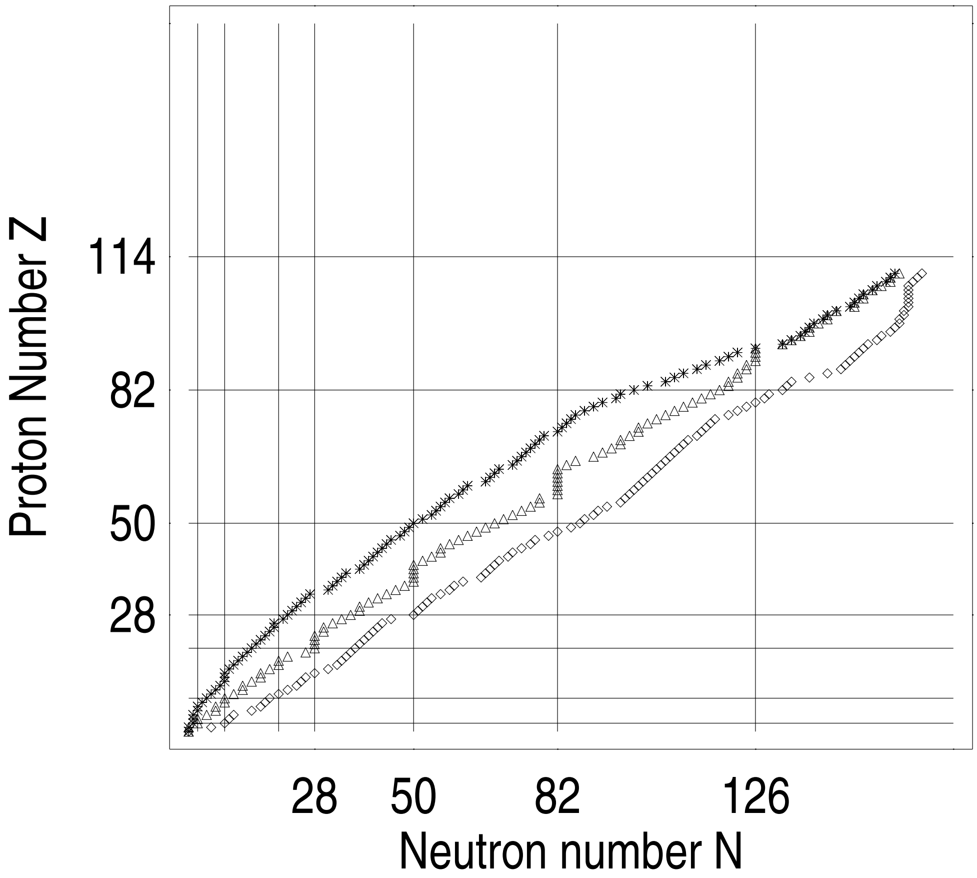

Figure 4.8: Plot of:(upper line) most proton-rich isotope of each element, (lower line) most neutron-rich isotope of each element, (middle-line) most tightly bound isotope for each element (i.e., the bottom of the 'valley of stability'). Note the grouping at magic numbers, especially in the valley of stability. Data taken from [Audi & Wapstra 1995]. Note this compilation includes both masses which have been measured, and also some extrapolations to as-yet unobserved/unmeasured nuclear masses.

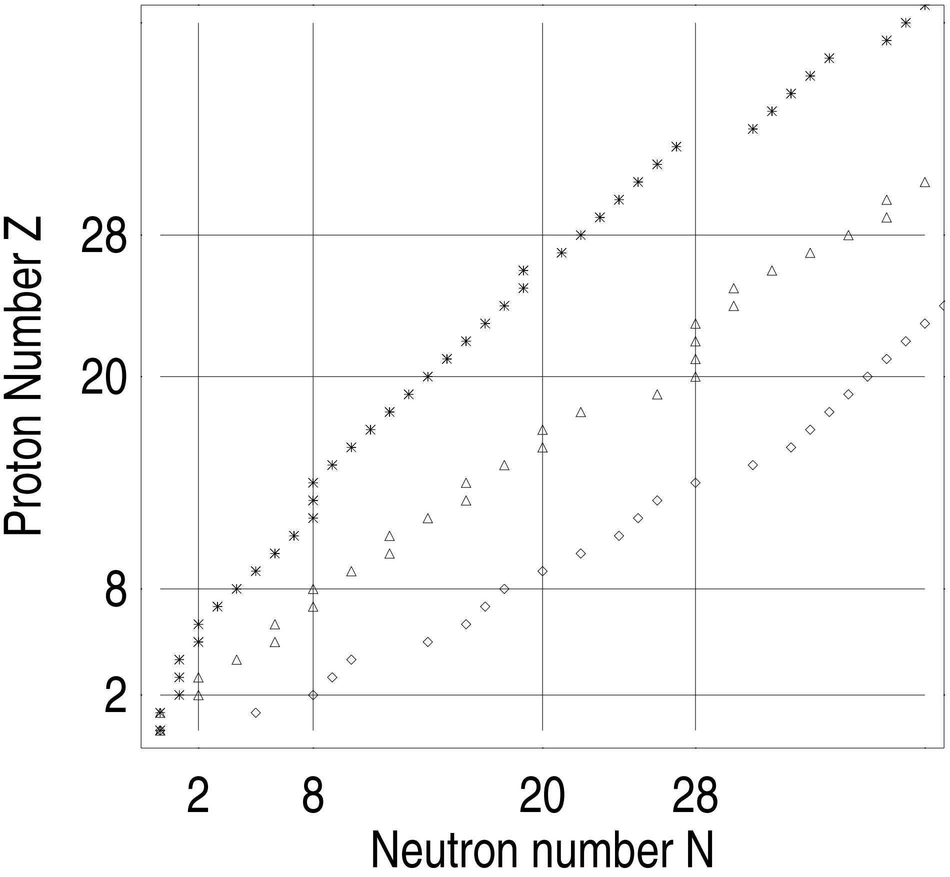

Figure 4.9: Identical to 4.8, but showing expanded low-atomic-number region. Data taken from [Audi & Wapstra 1995].

obtains the Garvey-Kelson relation [Garvey & Kelson 1966] [Garvey & Kelson 1969]. This is shown schematically in the second and third lines of Fig. 4.10. This relation represents a homogeneous partial difference (*pde*) equation for the nuclear binding energies.

In an extension of this approach of Garvey-Kelson, Jänecke and Masson introduced considerations related to the nuclear asymmetry energy which led to an *inhomogeneous* pde. This equation has then been used to obtain mass predictions. Shown in Fig. 4.11 are these predictions in the region of the Table of Isotopes which is of interest in this thesis research. In general, comparison with the Bethe-von Weizsäcker SEMM predictions shown in Fig. 4.3 shows that Jänecke and Masson generally predict the neutron-dripline to be more distant from the valley of stability, and also show more pronounced pairing-energy effects (an odd-even staggering of predicted-to-be-stable masses) along driplines.

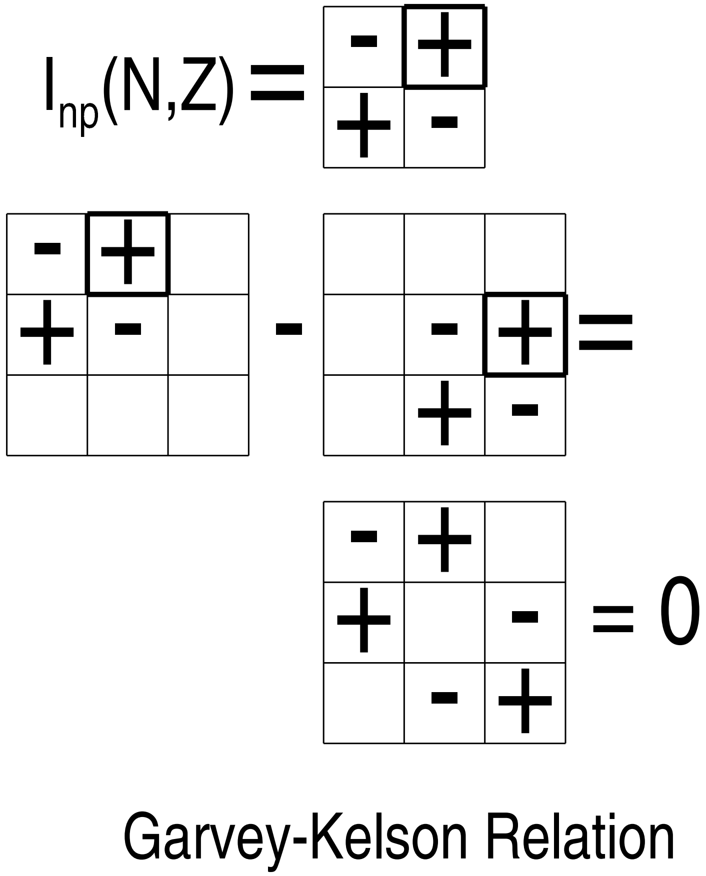

Figure 4.10: Top row: Operational definition for the quantity $I_{np}(N, Z)$. Second and third rows: The Garvey-Kelson relation: a *homogeneous* partial differential equation (pde). (An extension of this approach due to Jänecke & Masson introduces considerations related to the nuclear asymmetry energy and leads to an *inhomogeneous* pde.) See text.

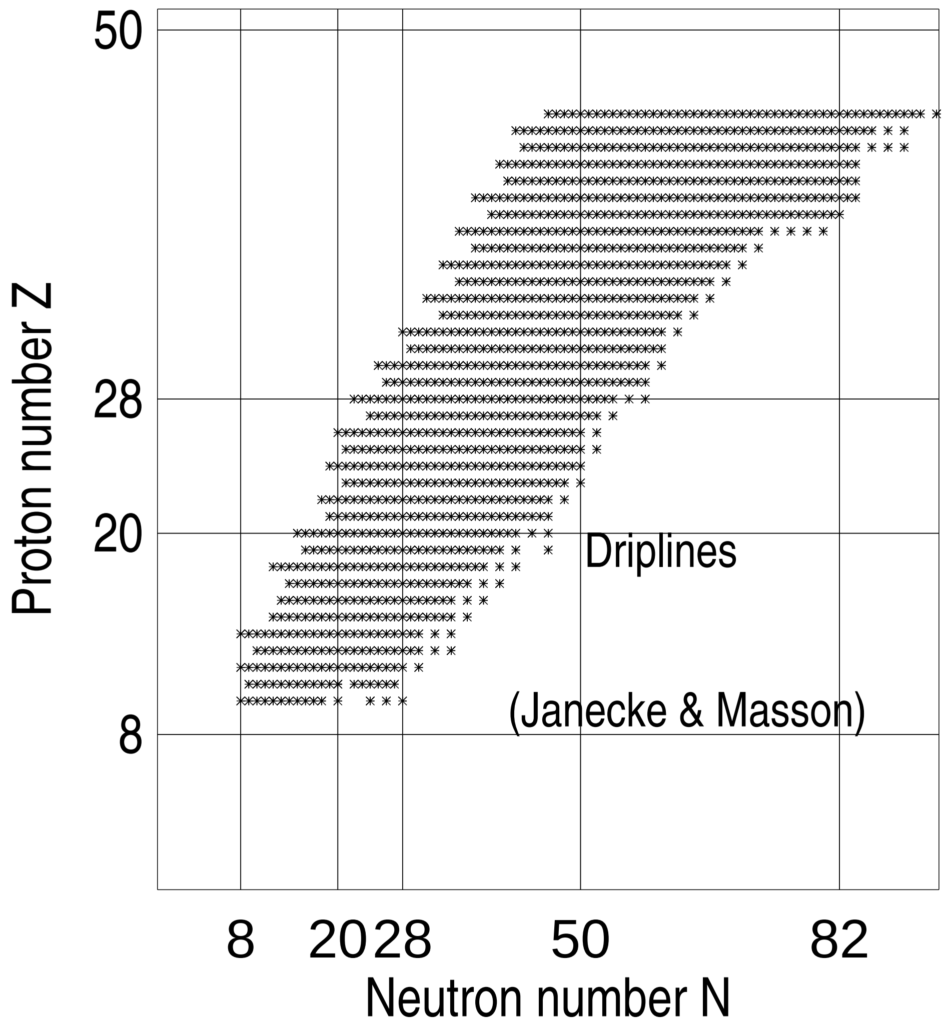

Figure 4.11: Predictions of nuclear stability for $10 \leq Z \leq 45$ isotopes against decay by the strong, nuclear force. Source: mass predictions of [Jänecke & Masson 1988] based on an Inhomogeneous Partial Difference Equation with Higher-Order Isospin Contributions. The right- and left-hand edges of the plotted isotopes represent the predictions for the neutron- and proton-driplines respectively. Compare to Fig. 4.7, which shows the Semi-Empirical Mass Model's predictions.

CHAPTER V

Solenoid Ion Optics and Magnetic Dispersion

5.1 Introduction

This chapter deals with the mathematical and phenomenological aspects of solenoid ion optics as applied to nuclear physics, while the next chapter describes the "BigSol-Isotope-Spectrometer" device itself. This order is taken because the mathematical details of solenoidal ion optics constrain both the engineering design of the device, and the experimental methods.

The technical objective of this work is to obtain heavy-ion (HI) particle resolution (isotope separation) on the order of $\Delta A/A \leq 1/90$ for reaction products having a broad range of A, Z, and q values, and which are emitted over continuous ranges in θ_{lab} and kinetic energy. More specifically, the interest is in exotic, especially neutron-rich, ions in the $Z \leq 35$ range. The kinetic energies of the reaction products are within what is commonly referred to in nuclear physics as the "low-to-medium-energy" range[1] of 5 to 35 MeV/u, and, they are emitted at relatively small — but

---

[1] These are imprecise concepts, of course. However, generally "low-energy" is less than 20 MeV/u, as this is about the limit for complete fusion of projectile and target, and much of traditional reaction studies take place in this regime as well. Once one is into the regime of incomplete fusion of projectile and target nuclei, above 20 MeV/u, and especially into the regime where the projectile has an energy equal to the Fermi energy level of nucleons in the target nuclei, the "intermediate-energy" regime has begun. In this regime sudden, projectile fragmentation, or abrasion-ablation interactions begin. The effects of the interaction may not have sufficient time to propagate across the nucleus during the brief interaction time. Optimal projectile fragmentation exotic-isotope (RNB)

non-zero — angles of emission in the laboratory frame measuring about $0.5^\circ \leq \theta_{lab} \leq 10^\circ$. The latter, however, can correspond to large angles in the center-of-mass (CM) system. To accomplish the required mass resolution, one needs to be able to quite accurately predict (i.e. simulate using computer programs) the *combined* effects of a number of independent experimental variables. This understanding became one of the major efforts in the work done for this thesis.

Let us begin by briefly outlining this problem.

5.1.1 Requirements of an isotope-spectrometer simulation

1. It is necessary to determine the acceptance characteristics of the spectrometer. Practically speaking, this means that a program is required which allows one to easily simulate changes in the fractional magnetic dispersion, $\Delta(B\rho)/B\rho$, which result from four sources:
   (a) varying the image/object (i/o) geometry of the solenoid ion-optical 'lens' (which is synonymous with changing the location of the entrance and focal-plane detectors and/or of the production target);
   (b) placing physical and/or software apertures in the device (either at the entrance, the focal plane, or inside the magnet's bore);
   (c) changing the size of the focal plane and entrance detectors; and

---

production energies are often found to be near 70 MeV/u, but may be as high as 100 MeV/u. These energies are attainable now at superconducting cyclotrons such as the NSCL in the US or GANIL at Caen, France and RIKEN in Japan. This energy regime is also used to study the nuclear equation of state and search for a liquid-gas and/or dynamical phase transition(s) in nuclear matter, for new collective modes of excitation of nuclear matter, etc. via multi-fragmentation reactions. Lastly, the high-energy regime generally implies relativistic energies. These are attained at nuclear facilities such as GSI at Darmstadt, or at RHIC at Brookhaven. The latter facility is particularly concerned with relativistic collisions which might reproduce early big-bang quark-gluon plasma phase transition conditions; the facilities at Darmstadt have recently produced many 10's of new neutron-rich isotopes via virtual-photon excited and nuclear-excited fission of U projectiles, and at least three new elements via HI fusion reactions.

   (d) changing the strength of the field by changing the supercurrent in the solenoid's coils.

2. In addition to simulating the solenoid's acceptance characteristics, the finite detector-system resolutions must be taken into consideration (the topic of the chapter "The Systematics of 2D Particle-ID Spectra with Magnetic Selection"). These too must be simulated, and the results convolved with the $\Delta(B\rho)/B\rho$ calculations, to obtain the particle-ID resolutions which a given setup of the spectrometer should produce.[2]

3. However, there is a further issue. There is a need to balance the benefit to

---

[2] Even if it were possible to attain perfect, "delta-function" detector resolutions, it would still not be possible to separate (identify) heavy ions that are produced over a continuum of kinetic energies and of emission angles for ions with Z's and A's above certain values. (The chapter, "The Systematics of 2D Particle-ID Spectra with Magnetic Selection" deals in detail with simulations of detector resolutions and magnetic selection.) For example, an unavoidable limit on the ability to resolve adjacent isotopes arises for ions with Z in the mid-20's when one employs an "MZ^2" identifier formed by multiplying $\Delta E \cdot E$. This can be readily seen in that above about $Z = 24$, the MZ^2 values of ions are no longer unique, but overlap (See especially the chart presented by [Goulding 1985]). Already, for ^{21}F and ^{17}Ne, the respective MZ^2 values of these two ions are essentially equal at 1701 and 1700 respectively. ΔE measurements or the MZ^2 identifier measurements are typically plotted against the ions' total energy, E, to produce a two-dimensional identifier. Z is 'resolved' along the ridges of these hyperbola. However, *most* isotopes generally will still lie in between the broad hyperbola ridges. Much of the data will fall in overlapping regions, and cannot be identified, especially if the ions are collected at lower energies where most isotopes will appear in a distribution of charge states.

One may also construct two-dimensional identifiers which incorporate time of flight and total energy [Coffin & Engelstein 1985]. Here the limit of resolution of adjacent masses depends on the ratio $l/\Delta t$, with l representing the length of the flight path between the timing-start and timing-stop detectors, and Δt representing the intrinsic timing resolution attainable by these detectors [Butler 1970] (See especially the chart of $l/\Delta t$ isoclines showing where isotopes of a given A are just resolved by [Butler 1970]. This is also reproduced in [Coffin and Engelstein 1985, p. 278]). Such limitations lead to the use of magnetic separators and spectrometers, especially for heavier isotopes which have progressively lower fractional mass differences between adjacent isotopes, and are more difficult to resolve.

The limits of using MZ^2 vs$E$ identifiers in conjunction with magnetic selection for the resolution of heavy ion masses were delineated by [Volkov 1985] (See, pp. 148-156, and especially Fig. 44 and the associated discussion.), in dealing particularly with very-neutron rich isotopes and multiple charge states (a combination eminently germane to the present investigation) where it was shown that the most neutron-rich, fully ionized ($q = Z$) isotopes fall in the same region of the 2D identifier as do higher–cross-section ions from the next higher atomic number $(Z + 1)$ in a $q = (Z + 1) - 2$ charge state. The result is that, to obtain mass resolution, one must employ all of the options: ΔE, E_{total} and time-of-flight (ToF) — together with magnetic selection.

> particle resolution from *low* beam rates and *small* apertures against the need, on the other hand, to obtain sufficient counting statistics in the run time which is available.

Calculations (computer programs) are required which can take into account all three of these effects: solenoid optics and acceptance, detector resolutions, and counting statistics. Repeated simulations of these factors are needed both before the fact (during the initial design of experiments) as well as for the optimal reduction and interpretation of data after the fact.

5.2 Preliminaries. Solenoidal field characteristics

BigSol has a highly linear current-to-field relationship. This is illustrated in Fig. 5.1. The data points in the figure represent current vs. magnetic field values (centroids) for the ions focused during eight experimental runs. These are selected because each of these resulted in good data, and because in each run beam was taken for statistically significant periods of time of from two to 14 hours. The continuously recorded field measurement signal was taken from a gaussmeter Hall probe at the edge of the solenoid's bore, near its entrance. The solenoid windings and resistances in the supply and control circuits comprise an LR circuit with a characteristic current decay-up or decay-down time whenever the power supply setting is changed. Aside from this approximately 20-minute transient, the field remains steady within the limits of measurement. The linear current-to-field behavior results from the complete lack of any ferrous yoke or other magnetic materials in the superconducting magnet's construction. This lack of hysteresis greatly simplifies the tuning of reaction products onto the focal plane and the changing of field settings between successive runs.[3]

---

[3] On the other hand, positive effects of an iron yoke on shaping the axial field were studied as part of the pioneering work on a solenoid device designed for studying nuclear reactions with light

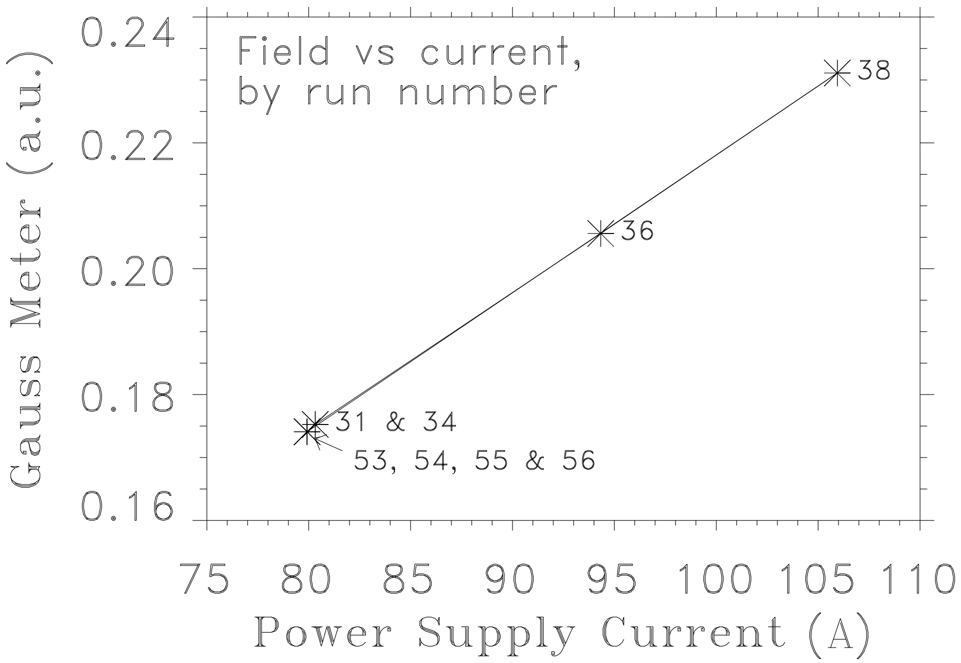

Figure 5.1: Field vs. current calibration for the UM 7-Tesla BigSol at NSCL during present experiments. Data points represent current vs. magnetic field values (centroids) as measured by a gaussmeter during each of eight major experimental runs. Beam was taken at each point for two to 14 hours. The field drift was insignificant once transient inductive delay of the coil had taken place. The linear behavior results from the complete lack of any ferrous yoke or other magnetic materials in the superconducting magnet's construction. The gaussmeter output was later calibrated against focused isotope groups of known magnetic rigidity.

The relative strengths of the computed axial and radial components of BigSol's field are shown in Fig. 5.2 for the actual physical extent of the spectrometer's flight-path. This is a vector-field plot which represents the magnetic field on a plane of constant azimuthal angle, ϕ, within a 3D-cylindrical coordinate system defined by (r, ϕ, z) where $\vec{B} = \hat{r}B_r(r,z) + \hat{z}B_z(r,z)$.[4] The rectangle overlaid on Fig. 5.2 represents the physical extent of the cryostat's bore (the radial direction has been exaggerated) through which ions pass. The quench limit for BigSol's superconducting coils is 171.25 A.

5.3 Field expression

Ion orbits through solenoids differ in several ways from the orbits of ions passing through dipoles, quadrupoles and other magnetic devices which have been much more commonly used in nuclear physics.

5.3.1 A variety of approaches

It is not possible to derive a closed-form expression for the magnetic field due to a current loop which holds at any arbitrary point in space [Montgomery 1980]. Previous authors have discussed an assortment of numerical and analytical approximations to solutions for these differential equations [Coslett 1969] [Montgomery 1980]. Many of these approaches predated modern computers and, generally, are limited in their application in that they apply only to certain zones of the field. A commonly used approach is the first-order Gaussian or paraxial approximation.[5] However, this the-

---

ion beams conducted at Orsay, France [Shapira 1984].

[4] There is no $\hat{\phi}B_\phi$ component, nor ϕ-dependence to the field, as this direction is parallel to the motion of the current carried by the coils. The relative strengths shown for the axial (B_z) and radial (B_r) components do not change as a function of the magnet's current.

[5] Comprehensive summaries of the Gaussian theory and its application to the *light* heavy-ion (HI) RNB transfer-reaction device, LilSol, at the joint UND-UM radioactive ion beam facility at UND, are given by [Stern 1987] and [Liu 1990].

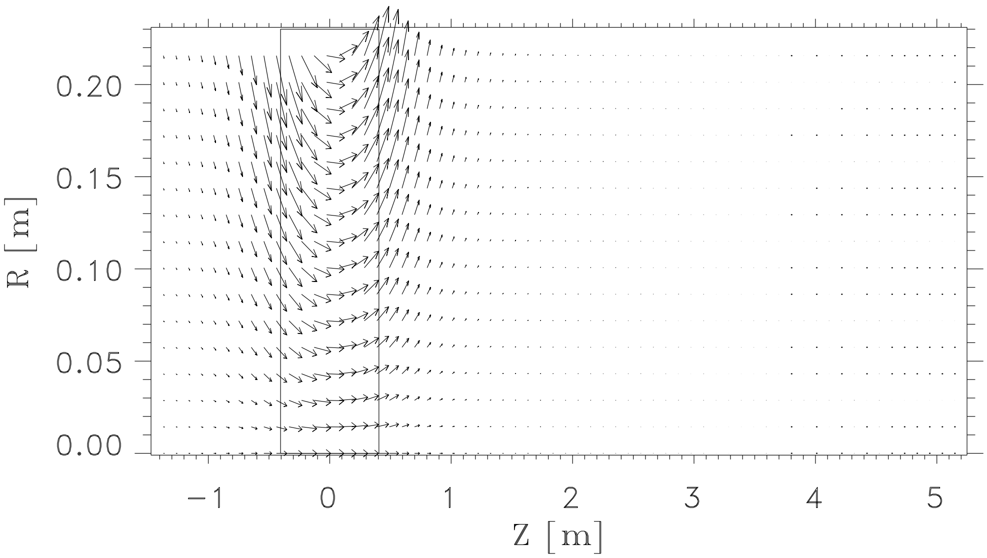

Figure 5.2: Vector-field plot representing the magnetic field over full extent of spectrometer flight path on a plane of constant azimuthal angle, ϕ. 3D-cylindrical coordinate system defined by (r, ϕ, z) where $\vec{B} = \hat{r}B_r(r, z) + \hat{z}B_z(r, z)$. There is no $\hat{\phi}$ component. The vertical rectangle represents the physical extent of the BigSol cryostat bore, through which ions pass. It is not shown to scale. The bore's true dimensions are $(Z, R) = (1.36, 0.30)$m. The field is shown over the full extent of the BigSol Isotope Spectrometer device: $-1.45 \leq Z \leq +5.45$m. Note that the radial component of the field, which is responsible for the major focusing effect, as well as the field's total magnitude, are largest at the greatest radial distance. The ratio of radial to axial components does not change with the field's magnitude.

ory does not reproduce the eight known solenoidal ion-optical aberrations, the effects of at least some of which are of interest to our present application.[6] These effects are only present when a third- or higher-order theory is used (owing to the cylindrical symmetry of a solenoidal field, there are no second or higher even-order field terms.)

The most general expressions – applicable to the field in all zones, whether inside or outside the physical extent of the solenoid coils themselves – can be given either for combinations of individual current loops of zero radii [Maxwell 1891] [Montgomery 1980], or for co-axial sheets of current [Garrett 1963], in terms of the complete elliptical integrals of the first and second kinds, K(Φ) and E(Φ) [op cit Maxwell, 1891]. If one is involved with specifying the design of the device itself, such a completely general expression is required to determine the mutual mechanical forces exerted on one another by the current-carrying superconducting-wire coils (so as to insure they are adequately restrained), and to determine the magnetic flux along the type-II superconducting wires comprising the coil (to insure this flux remains safely below the complete-penetration, quench-failure limit of the material [7]). However, if one is concerned exclusively with the field inside the bore of the solenoid (as is the case in so-called “MRI” (NMR) work [Nelson & Weaver 1964]), expressions in terms of Legendre polynomials and their derivatives are generally used [Garrett 1963] [Nelson & Weaver 1964] [Montgomery 1980], while beyond this zone, a similar expansion in powers of $1/r$ [Montgomery 1980] can be used.

---

[6] These are given by [Glaser 1952] [Garrett 1963] [Jiye 1986] as distortion, curvature of field, astigmatism, coma, spherical aberration, anisotropic astigmatism, anisotropic coma and anisotropic distortion. Of these, the important considerations are spherical aberrations. It can be shown [El-Kareh and El-Kareh 1970, op cit Stern 1986] that these are the only geometrical aberrations which do not vanish for a short solenoidal lens in which the ions are emitted from a point on the axis. Although we will not approach this problem in terms of aberrations per se, our treatment will, however, encompass these effects.

[7] For an overview of the characteristics of superconducting solenoid coils and various design and utilization characterists such as “training,” length-dependent type-II flux-penetration behavior, quench-failure modes, etc., see [Nelson & Weaver 1964].

In the present instance, we require a fairly general expression, as our ion orbits originate outside the solenoid, pass through its bore and are collected on detectors well beyond its physical extent. We may, however, make a significant simplification due to the cylindrical symmetry of the field and we need not be concerned with the complexities of ions which enter into or between the coils themselves. The following derivation is given, in different forms, by several authors [Garrett 1963] [Montgomery 1980] [Jiye 1986] [Szilagyi 1988] and leads to a power-series expansion for the magnetic field. We sketch the derivation in some detail to illustrate a basic simplification which arises from the field's cylindrical symmetry.

5.3.2 Derivation of power series expression

Following closely the modern notation, and the use of MKS units, by especially [Jiye 1986] and [Szilagyi 1988], one begins with the two of Maxwell's four equations [Maxwell, 1891] which concern the static magnetic induction

$$\nabla \times \vec{B} = \mu_0 \vec{j}_f \tag{5.1}$$

and

$$\nabla \cdot \vec{B} = 0, \tag{5.2}$$

where $\vec{B}$ is the magnetic induction, $\vec{j}_f$ the free-space current density and μ_0 is the permeability in vacuuo. According to Eqn. 5.2 the static field being considered has no divergence, thus we may write:

$$\vec{B} = \nabla \times \vec{A}, \tag{5.3}$$

where $\vec{A}$ is the magnetic vector potential. We choose to work in the Coulomb gauge, setting $\nabla \cdot \vec{A} = 0$. Substitution of Eqn. 5.3 into Eqn. 5.1 yields:

$$\nabla^2 \vec{A} = -\mu_0 \vec{j}_f \tag{5.4}$$

This, then, is a second order partial differential equation (PDE) for $\vec{A}$. However, in the case of BigSol, the presence of the reaction-product ions in or near its coil is relatively insignificant (a "beam" of at most one or several ions simultaneously passing through the magnet per any primary-beam burst), and we may set the free space current, j_f, to zero. The use of the Coulomb gauge will allow separation of variables, and hence reduction to a scalar potential. As a result, Eqn. 5.4 may be reduced to one dimension. Consider Laplace's equation, a homogeneous PDE for a *scalar* potential

$$\nabla^2 A = 0. \tag{5.5}$$

Cylindrical coordinates are most convenient for an axially symmetric solenoidal field. Laplace's equation is then

$$\frac{1}{r}\frac{\partial}{\partial r}(r\frac{\partial A}{\partial r}) + \frac{1}{r^2}\frac{\partial^2 A}{\partial \phi^2} + \frac{\partial^2 A}{\partial z^2} = 0. \tag{5.6}$$

Since this is periodic in ϕ, one normally proceeds by expressing the potential as a Fourier series and substituting partial derivatives of the series into Laplace's equation. However, being axially symmetric our potential cannot depend on ϕ and the odd (sine) portion of the Fourier series vanishes, and the even (cosine) portion collapses to its first term ($n = 1$), leaving simply its coefficients

$$\vec{A}(r, \phi = 0, z) = \sum_{m=0}^{\infty} a_m(r, z). \tag{5.7}$$

Back substitution produces the differential equations

$$\frac{\partial^2 a_m}{\partial r^2} + \left(\frac{1}{r}\frac{\partial a_m}{\partial r}\right) - \frac{m^2}{r^2}\frac{\partial^2 a_m}{\partial z^2} = 0 \tag{5.8}$$

for each value of m. Solutions can then be found as power series in r where the coefficients depend only on z

$$a_m(r, z) = \sum_{i=0}^{\infty} \alpha_m(z) r^{m+i}. \tag{5.9}$$

Again, by calculating partial derivatives, back substituting into the differential equation for a_m, and then examining the trend in the coefficients, the general expression [Szilagyi 1988, p. 5] [Jiye 1986, p. 18-19] eventually produced is

$$A(r,z) = \sum_{k=0}^{\infty} \frac{(-1)^k A^{(2k)}(z)}{(k!)^2} \left(\frac{r}{2}\right)^{2k} . \tag{5.10}$$

Finally, the expression for the field is obtained through the relationship of the axial flux density $B(z)$ to the scalar potential, which is now explicitly evaluated on axis to account for the current in the coils

$$B_0(z) = -\mu \frac{\partial A}{\partial z}\bigg|_{r=0} . \tag{5.11}$$

The power series for the components of the flux density (magnetic field)[8] are then

$$B_r = \sum_{k=1}^{\infty} \frac{(-1)^k B_0^{(2k-1)}(z)}{k!(k-1)!} \left(\frac{r}{2}\right)^{2k-1} \tag{5.12}$$

$$B_\phi = 0 \tag{5.13}$$

$$B_z = \sum_{k=0}^{\infty} \frac{(-1)^k B_0^{(2k)}(z)}{(k!)^2} \left(\frac{r}{2}\right)^{2k} \tag{5.14}$$

where

$$B_{0z} \equiv B(r=0,z). \tag{5.15}$$

5.3.3 Axially symmetric electro-magnetic fields are functions solely of the field on-axis.

The extremely important characteristic of this result is that the field in any region of interest is simply a function of the on-axis field, $B_0(z)$, and its derivatives with respect to z. The ability to express the field anywhere in space as a function of the axial field and its derivatives alone is actually a feature of *any* axially symmetric

---

[8] These expressions are good regardless of whether the B field is produced by currents [Szilagyi 1988, p. 60].

electrostatic field. The practical consequence here, is that if the solenoid's coil is wound precisely enough so that it may be assumed to be axially symmetric about the Z-axis, a model (or measurement) of the field along the axis will provide all the information needed to calculate the field in an ion-orbit ray-tracing code.

5.3.4 Consideration of the exact expression rather than a series-expansion

For completeness, we should consider the possibility of using an exact expression for the field in preference to the power series approach which, when coded to some finite power, is intrinsically an approximation. The exact expression for an axially symmetric (scalar) magnetic potential [9] can be shown in detail to be

$$A(r,z) = \frac{1}{\pi}\int_0^\pi a(z + \imath r\cos(\vartheta))d\vartheta \tag{5.16}$$

[Szilagyi 1988, p. 71] where ϑ is a variable of integration and $\imath$ is the complex number $\sqrt{-1}$. The complex function $a(z + \imath r\cos(\vartheta))$ is the axial potential distribution function. The difficulty here is in numerically evaluating this distribution function given its complex argument,[10] and, so, we will use the power series representation, but carrying terms to (at least) $k = 7$ in Eqns. 5.12-5.14.

The question remaining, then, is: What expression will provide a sufficiently accurate yet flexible model (we want derivatives of the on-axis field to about seventh order) for the on-axis field?

5.4 Axial-field expression

5.4.1 Thin-coil axial-field approximation

The geometry of BigSol, and, to a lesser extent, of its prototypical predecessor LilSol, is such that the thickness of the coil is relatively 'thin' vis-a-vis the large radial

---

[9] Modern derivations of which are simply an elaboration upon that given by [Maxwell, 1891] — whose succinct outline of this problem underlies all subsequent work.

[10] For a detailed discussion see [Szilagyi 1988, especially pp. 67-86].

size of the axial bore through the device. On this basis the on-axis field of LilSol was approximated from an infinitely-thin coil or current sheet [Stern 1987] [Liu 1990], as also was BigSol [Brown 1993] for the purposes of studying radioactive nuclear beams of light ions produced by transfer reactions. The expression is arrived at using Ampere's law which provides the expression for a single elementary current loop. This in turn is integrated over multiple such coils of identical radii to approximate a current sheet of elements. The on-axis field is then found to be

$$B(z, r=0) = \frac{\mu_0 NI}{2l} \left\{ \frac{z + l/2}{\sqrt{R^2 + (z + l/2)^2}} - \frac{z - l/2}{\sqrt{R^2 + (z - l/2)^2}} \right\} \tag{5.17}$$

where R is the radius of the idealized thin coil, l is its length, N is the number of wire turns and I is the current flowing through the wire.

The great advantage of this expression is that it is a simple matter to take successive derivatives and substitute these into Equations 5.12 and 5.14 to obtain the field. The results, to five terms in k, are

$$\begin{aligned} B_z = {} & \frac{\mu_0 NI}{2l} R^2 \frac{\sqrt{R^2 + (l/2)^2}}{l} \\ & \left\{ (r/2) \left[\frac{1}{(R^2 + (z + l/2)^2)^{3/2}} - \frac{1}{(R^2 + (z - l/2)^2)^{3/2}} \right] \right. \\ & \left. -3(r/2)^3 \left[\frac{4(z + l/2)^2 - R^2}{(R^2 + (z + l/2)^2)^{5/2}} - \frac{4(z - l/2)^2 - R^2}{(R^2 + (z - l/2)^2)^{7/2}} \right] \right\} \end{aligned} \tag{5.18}$$

where R is the radii of the idealized, thin coil and l is its length.

5.4.2 Exact, thick-coil axial-field expression

On the other hand, one can write an exact thick-coil expression by performing an additional integration of Eqn. 5.17 over the finite thickness of the three concentric elements which comprise the BigSol coils and arrive at the mathematically 'exact' expression

$$B(z, r=0) = \frac{\mu_0 NI}{2(r_2 - r_1)l}$$

$$\left\{(z+l/2)\ln\frac{r_2+\sqrt{r_2^2+(z+l/2)^2}}{r_1+\sqrt{r_1^2+(z+l/2)^2}}\right. \\ \left. -(z-l/2)\ln\frac{r_2+\sqrt{r_2^2+(z-l/2)^2}}{r_1+\sqrt{r_1^2+(z-l/2)^2}}\right\} \tag{5.19}$$

where r_1 is the radial distance from the z axis to the inner diameter of the coil, and r_2 is the radial distance to its outer diameter.

5.4.3 Comparison of thick- and thin-coil expressions

Putting aside for the present the technical questions of taking seven or more derivatives of Eqn. 5.19 and programming these into Eqns. 5.12 and 5.14, we first examine the difference in the on-axis profiles produced by the thin coil vs. the thick coil equations to determine which is appropriate for our purposes. Fig. 5.3 compares these on-axis profiles.

Fig. 5.3 overlays three profiles: the exact thick coil calculation, the thin coil approximation and a best-fit Gaussian-plus-constant approximation to the thick coil's profile. The calculations are performed at BigSol's maximum amperage of 171.25 A[11], and are shown for the region of -1.37m $\leq$ z $\leq$ 5.25m (the actual extent of the spectrometer from interaction target to focal plane). The physical extent of the BigSol coil is represented as a horizontal dotted line, and shows that the field at maximum amperage has fallen off to about 3.5 Tesla at the coil ends [12] It is apparent from this figure that while both the thick and thin coil profiles are nearly Gaussian

---

[11] This value immediately tells us that BigSol must have three separate, concentric coils, as indeed it does. This is because the maximum supercurrent carrying capacity for type II superconducting coils – as opposed to the "short sample limit" – is just over 57.25 A [Nelson & Weaver 1964]. Then $3 \cdot 57 = 171$ A. Beyond this value the coil will quench.

[12] A rule of thumb for solenoids is that the field at the end of the coil is about one-half of that at the center [Coslett 1954], as the coil can be pictured as being composed of two, equal-sized, half coils arranged end to end. The field in the center, then, is that due to the two coils whose ends meet there; the field at either end is taken as that of only a single half-coil's end, and so is about half that at the center. In reality, for finite length coils, of course some field intensity at the extreme ends is also to the presence of the more distant half-coil, and, thus, the end field is always a bit more than that due to a single half-coil taken alone. Nevertheless, this is a useful rule of thumb.

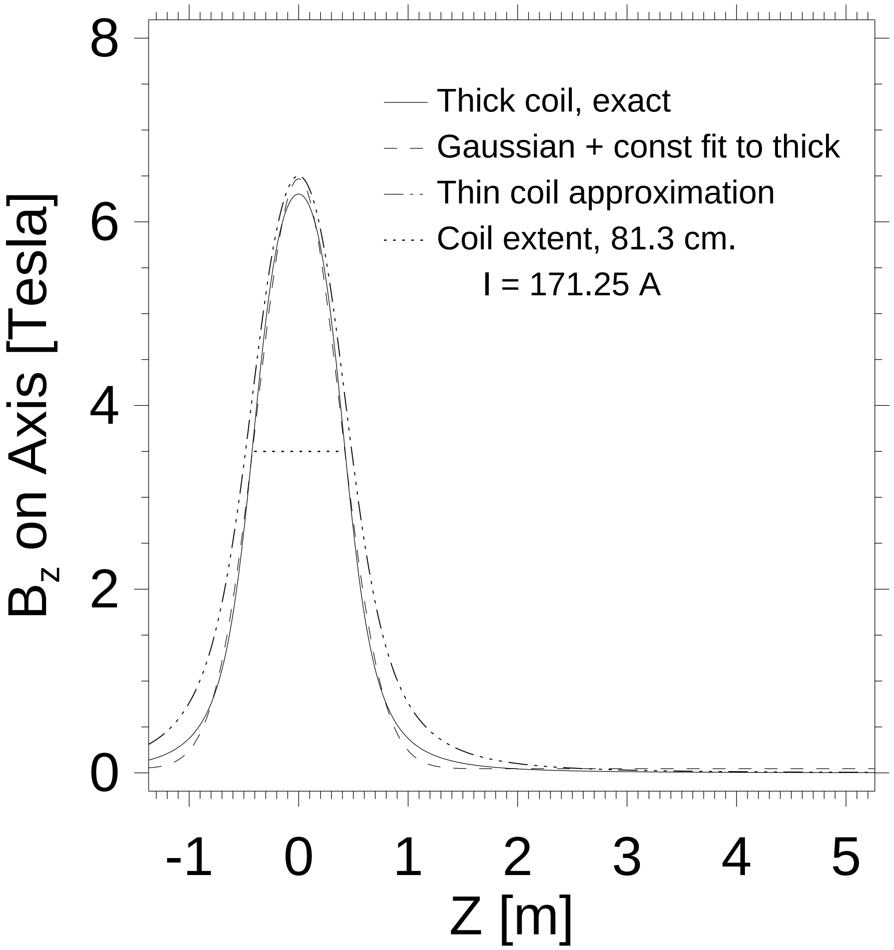

Figure 5.3: Difference between on-axis thick- and thin-coil field profiles

about the coil's center line, the thick-coil profile is somewhat flatter (platykurtic) as compared to that of the thin coil. In addition, the calculated (exact) field of the thick coil falls off faster, especially in the fringe field regions beyond the physical extent of the coil.

5.4.4 Calibration of the axial-field expression

A calibration performed by the manufacturer [Cryomagnetics^{R}, 1991] determined the field-to-current ratio for the BigSol coil to be 0.03796 T-m/A. [13] This calibration was performed by measuring the field at the center of the bore, i.e. $z = 0, r = 0$, while raising the current until the spontaneous quench limit was reached. However, in the ray-tracing code, it was found that when the value reported from this calibration was used, a thin-coil based program would not focus ions at the values of $B\rho$ (centroids) actually measured for ions focused with BigSol. By using the *rms radius* of the coil in a thin-coil axial-field program, rather than the mean radius, the situation was improved. The focused ions' rigidities then differed by about $1 - 2\%$ from the centroids of ions actually focused at the same amperage. In the case of the thick-coil formula, the focused ion's rigidity centroid was more straightforwardly reproduced using the actual inner and outer diameters of the coil bundle for the values of r_1 and r_2 in Eqn.5.19.

5.4.5 Sensitivity of ion-orbits to details of axial-field expression and calculation step size

As for the flattened field at the center of the magnet in the thick-coil model, this represents the theoretically expected behavior in that region.[14] However, as we shall

---

[13] Actually it was reported as 0.3796 T-m/A. We assume the decimal is misplaced as the field is reported to have quenched at 6.5T at 171.25A.

[14] That is, if one imagines a long coil in the thin-coil model, it is apparent that the field at $z = 0, r = 0$, and for some small distance about that point, would be expected to "saturate," near to a limiting value of $N\mu_0 I/l$.

see, the field near the center of the coil has relatively little bending (i.e. deflecting or "focusing") effect on ion orbits, as the field in this region is almost perfectly parallel to the axis and to the paths of ions passing through this region. In contrast, near the ends of the coil where the radial component of the field is large in proportion to the axial component (i.e., the "fringing field"), the orbit-bending, focusing effect is the greatest. It is often said that the focusing effect of solenoids (whether used for ion-optics or in electron microscopes) is achieved by their fringe fields, and this statement largely captures the truth of the matter.

Small differences in the model used for the on-axis field may have very large effects on the ion orbits and acceptance characteristics of the spectrometer. As a result orbital paths must be calculated on a particularly fine step size by any ray-tracing program because of this "high bending moment" region. We used 1mm generally as the step size for all orbit calculations shown here. One must run with successively smaller orbital step sizes until the results of the orbit-tracing program are shown empirically to converge to a fixed value for an ion's radial-hit position at the focal plane, else the results of the simulations will be incorrect. Generally a too-large step size underestimates the bending power of the solenoid. [15] The degree of sensitivity of orbit calculations to step-size implies a similar sensitivity to the expression for the field itself, For this reason, we judged it to be *very important* to use the "exact," thick-coil model of Eqn. 5.19 in all our simulation programs.[16]

---

[15] Using a small enough step size is particularly important if one is calculating orbits of ions through a gas-filled solenoid, where the ion is simulated to scatter off a tenuous gas after each step of the ray-tracing program. [We express our appreciation to, P. Fallon, LBNL Nuclear Division, for discussions on this issue] Such a solenoid is intended to focus multiple-charge-state ions as if all have some average, effective charge.

[16] In discussing approximation methods for the on-axis field to be used in calculations, the consensus of various authors is succinctly summarized by the statement: "Such formulas can only be used for rapid evaluation of the coil's properties." Since the thick-coil formula "is exact and relatively simple, it should always be used for the calculation of flux density distribution of finite-size coils." [Szilagyi, p. 108]

Returning now to the question which we had temporarily put aside earlier, we shall now require seven or more derivatives of the exact on-axis field profile, Eqn. 5.19, to be substituted in the power function representations of the field components, Eqns. 5.12-5.14. However, this results in an expressions (and code) which is quite cumbersome, and a simplification was sought.

5.5 Simplification of thick-coil axial-field derivatives

5.5.1 Far (dipole-like) field region

Fig. 5.4. This is a plot of the same thick- and thin-coil profiles shown previously, in Fig. 5.3, except they are now shown on a log-log scale.

The $B_z = z^{-3}$ line shown is that of a pure magnetic dipole: an inverse cube, which represents the expected behavior of the solenoidal field for z "very large." Indeed, the figure shows that, beyond only about 0.81m in the thick-coil case, and about 1.0m in the thin-coil case, the profiles of both fields appear to be perfectly parallel to the inverse-cube dipole field of the form[17]

$$B(r = 0, z) = \frac{a_4}{r^3}, \qquad\qquad z \geq |0.81|\, m. \tag{5.20}$$

5.5.2 Central (Gaussian-like) field region

Given this "large distance" behavior, now consider Fig. 5.5. This is similar to the previous figure, but now a profile of a best-fit Gaussian-plus-a-constant to the

---

[17] This assessment of BigSol is consistent with calculations shown by [Montgomery, p. 230]. It is the usual practise when designing solenoid ion- or electron-optical devices to parameterize the coil dimensions using $\alpha = r_1/r_2$ and $\beta = l/(2 \cdot r_1)$, where r_1, r_2 and l are as given in Eqn. 5.19. On this basis BigSol can be characterized by $\alpha = 1.27$ (0.3514/0.2794m or 14.0/11.0in) and $\beta = 1.454$ (0.8128/(2.0 x 0.2794 m or 32 inches long). Montgomery shows that two $\alpha = 3$ coils of $\beta = 2$ and 1 become pure-dipole like at a distance of $3 \leq z/r_1 \leq 4$. For BigSol $z = 0.81$ m translates to a $z/r_1 = 2.90$. In general, "The larger the coil, ... the larger z/r_1 will be before this blending" "of the calculated profile with the inverse cubic slope" [ibid.] takes place. Since the smaller α of BigSol, reflects the larger size of its coil, our determination of $z = 0.81$m. compares favorably with these examples.

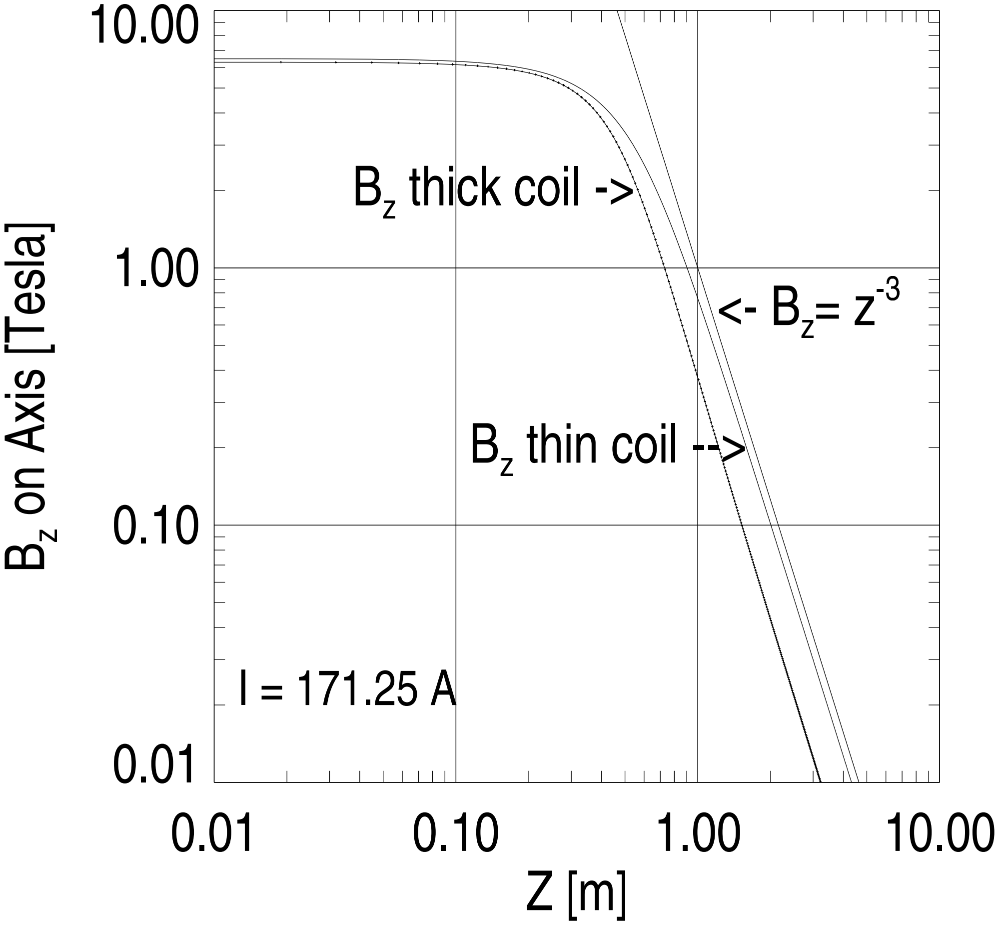

Figure 5.4: Log-log on-axis thick- and thin-coil field profiles showing inverse-cube magnetic dipole region

thick-coil axial field profile in the central region has been added. It represents an equation of the form[18]

$$y(z) = a_0 \exp\left[-\frac{1}{2}\left(\frac{z-a_1}{a_2}\right)^2\right] + a_3 \qquad |z| \leq 0.81m. \tag{5.21}$$

This approximation is similar to the approach taken by Glaser [Szilagyi 1988] [Coslett 1969] [Glaser 1952]. From Fig. 5.4 it is apparent that, while the Gaussian-plus-constant fit is not as platykurtic as the exact, thick coil profile, and while it does not fall off quite as fast as does the thick coil profile in the fringe field zones, it nevertheless clearly follows the exact thick coil profile much more closely than does the thin coil's approximation. And, so, the Gaussian-plus-constant approximation would be expected to much more closely reproduce the exact field's characteristics than would the thin coil approximation.[19]

5.5.3 Calculational scheme for computer simulation of acceptance

The solenoid field programs "`bfield.pro`," ion-orbit ray-tracing program "`orbit.pro`" and the solenoid-spectrometer acceptance program "`acceptance.pro`" code are reproduced in the Appendices. The overall process of calling these programs is done by the program `run_acceptance.pro`. Various 2D and 3D plotting and visualization routines are included in these programs for both single ion orbits and for the mapping of the radial-hit positions of multiple ion orbits (i.e. for mapping the spectrometer's acceptance) at the focal plane detectors for a range of rigidities ($B\rho$) and angles of emission (θ_{lab}). All computational code and

---

[18] Note that this approximation to the axial field is *not* what is meant by the "Gaussian" approximation in solenoid optics, which traditionally refers to a first-order approximation of the field in general, is restricted to the analysis of paraxial ion orbits, and does not reproduce higher-order aberrations. See especially [Stern 1987] for a detailed treatment of this type.

[19] Fits of the forms Gaussian- plus-linear and Gaussian-plus-quadratic, etc. were also tried, however, the best fit to the central region was produced by the Gaussian-plus-constant. The method of Glaser entails a Gaussian alone.

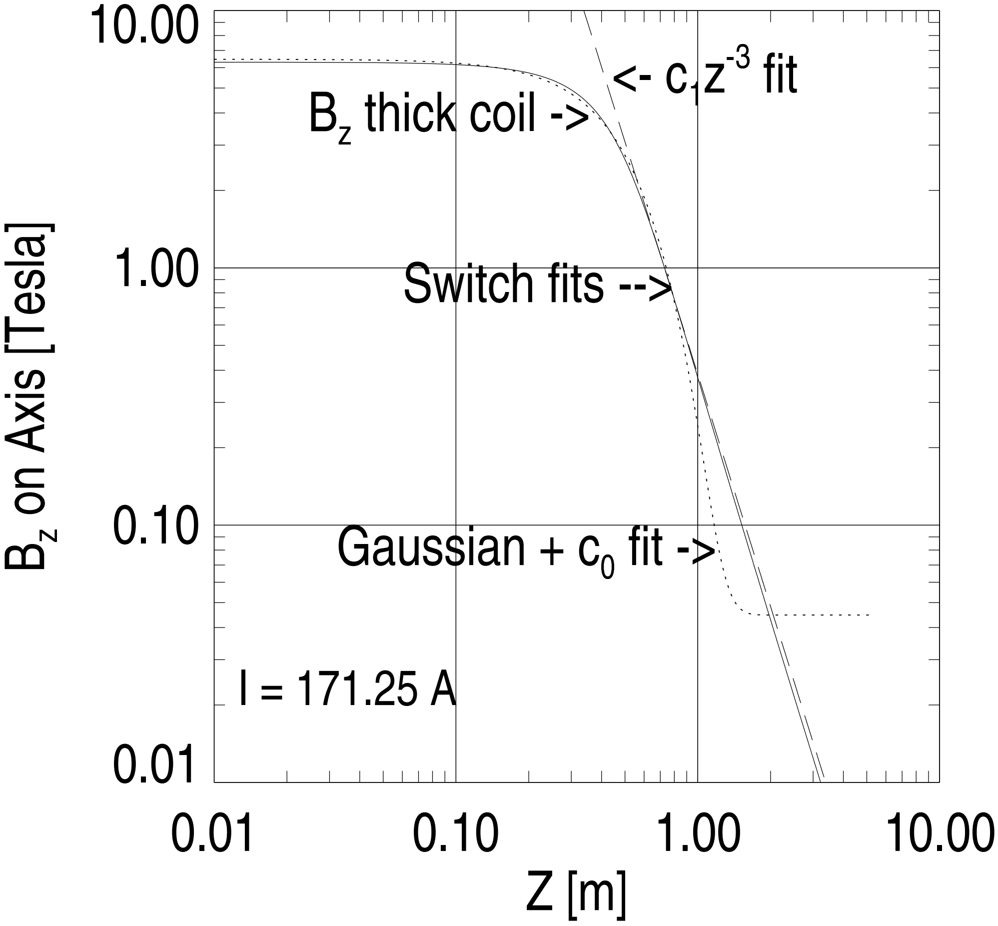

Figure 5.5: Like Fig. 5.4, but with a Gaussian+constant best-fit to the thick-coil's exact axial field profile.

visualizations were written in the IDL^{R} language. IDL code is operating-system (OS) independent.[20]

The calculational scheme is as follows:

1. The program `bfield.pro`:
    (a) calculates the exact (thick coil) on-axis field using Eqn. 5.19, at the amperage of interest;
    (b) finds the best-fit Gaussian-plus-quadratic to the on-axis field for the central region $B(z) \leq |0.81|$m. (This determines the constants a_0, a_1, a_2, and a_3 of Eqn. 5.21);
    (c) finds the best-fit inverse cubic to the on-axis field for the regions B(z)> $|0.81|$m. (This determines the constant a_4 in Eqn. 5.20);
    (d) calculates the field at the point requested using the derivatives of the axial field ($a_0, \ldots, a_4$) in the power function expression for the off-axis field.[21] `Bfield.pro` executes sufficiently fast that it is not necessary to make interpolations between calculated points or between points stored in a previously calculated lookup table. Interpolation is thus eliminated as a source of error, the field is calculated at each 1mm step of the orbit.

---

[20] The code has been run on both VMS and Unix systems, and should run under IDL for Windows, WindowsNT and Macintosh. Calls to the operating system (creating files, etc.) by the `run_acceptance.pro` program were written in a manner which automatically takes account of VMS/Unix OS differences. A full focal-plane mapping (acceptance calculation) as, for example, shown in the 2D wire-frame surface plots in this chapter, took approximately 45 minutes each using an alpha RISC processor. Each individual ion-orbit calculation performed is represented by a vertex on the wire frame. In turn each orbit was traced in 1mm steps over a flight path of 6.4m, and the field was calculated (not interpolated) at each step in the orbit. Much of this elapsed time is input/output (*i*/o) as the program was written using temporary file-storage of results rather than memory so as to permit running under the inexpensive "student version" of IDL which does not permit use of large memory arrays. This is intended to make the code accessible to persons without access to the full IDL programming and visualization package, but has not been fully tested in that environment.

[21] And these expressions for derivatives of *fits* to the exact axial field are *much simpler* in form than are the derivatives of the exact on-axis relationship itself.

2. The program `orbit.pro`:
   (a) calls `bfield.pro` to get the field at each new step in an ion orbit.
   (b) does the relativistically correct ion-optical ray-tracing calculations to increment the orbit until it hits the focal plane or the magnet's inner bore. It calculates the acceleration of the particle of atomic mass A and ionic charge q from the Lorentz force equation: $\vec{F}/A = (q/A)\vec{v} \times \vec{B}$.
   (c) determines the time-of-flight (ToF) needed to increment the orbit 1mm using the (constant) velocity of the particle, and
   (d) uses this ToF, together with the acceleration, velocity and present position as input to kinematic calculations which determine the new incremented location.

3. The program `acceptance.pro`:

   Repeatedly calls `orbit.pro` to map out the BigSol focal-plane acceptance (i.e., focal-plane-hit positions, r_{fp}), for a range of ion emission angles θ_{lab}, and $B\rho$'s. The user passes to the program the desired
   (a) current setting for the BigSol coils,
   (b) the i/o (image/object) geometry of the spectrometer setup,
   (c) the $B\rho$, the range of $B\rho$ values and $\delta(B\rho)$ step size,
   (d) the $\theta_{lab-min.}$, $\theta_{lab-max.}$ and the $\delta\theta$ step size

   over which to do the orbit calculations. The acceptance mapping of the focal plane is returned as the calculated radial hit-positions of ions at the focal plane, r_{fp}.

5.6 Characteristics of solenoid ion orbits

For our present purposes, it is sufficient to examine three characteristics of solenoidal ion orbits:

1. when used for $B\rho$ selection,*a solenoid is not a zero-degree device;*

2. for an ensemble of ions, all emitted at the same θ_{lab} and all arriving on the focal-plane detector at a ring of constant radius, r_{fp}, about the z- axis: *If these ion orbits are allowed to cross the field's symmetry axis n times* $\{n = 0, 1, 2, ...\}$, *this ensemble will be $(n+1)$-multiply valued in* $B\rho = B\rho(\theta_{lab}, r_{fp})$;

3. each time an ion orbit comes to a focus (crosses the symmetry axis) the ion orbit will have completed a loop through one turn within one quadrant of the plane perpendicular to the symmetry axis. That is, if the radial component of the orbit is projected onto the focal plane, it will appear to trace out one complete 'leaf' of a four-leaf clover during the process of traveling from the object position (target) on the z-axis and back again to the z-axis, at a downstream position.

The first characteristic listed above is rather straightforward and stands in contrast to the familiar behavior of dipole bending magnets. In a dipole field, ion orbits which enter at $\theta_{lab} \approx 0°$ will follow radii of curvature proportional to their individual values of p/q (momentum over charge state, see Eqn. 1.1). But, for a solenoid, ions emitted at $\theta_{lab} \approx 0°$ encounter no radial component of the field, (see Fig. 5.2) that is, no component perpendicular to its velocity. They will be undeviated and no magnetic selection takes place. This is unacceptable for a spectrometer. For this reason, in the present experiments, ions emitted at $\theta_{lab} \leq 0.7°$ were blocked by an on-axis aperture stop. [22]

The second and third characteristics of solenoid-ion orbits are illustrated by Figs. 5.6 and 5.7, which are 3D box representations of ion-orbit calculations.[23] The geometry used in these simulations is the same asymmetric i/o ratio as used in the present experiment, and the magnet's current setting in all four cases is 83 A — an intermediate current setting for BigSol. The walls of each 3D box plot show 2D projections of the simulated orbits onto the XZ, YZ and XY planes. The positive Z direction is taken to be along the symmetry axis of the magnet and in the direction of the primary beam, with the origin at the center of the solenoid. The XY plane in each case therefore shows a projection of the purely radial component of the orbits, and in each case they appear akin to one leaf of a four-leaf clover, illustrating characteristic number three listed above.

The second characteristic is the most important of the three listed above. In investigating this, it is useful to consider the behavior of $B\rho$ as a function of θ_{lab} and r_{fp}

$$B\rho_i = B\rho_i(r_{fp}, \theta_{lab}) \qquad\qquad i = (0, 1, 2, ...) \tag{5.22}$$

as well as its total derivative

$$d(B\rho) = \left.\frac{\partial(B\rho)}{\partial\theta_{lab}}\right|_{r_{fp}} d\theta_{lab} + \left.\frac{\partial(B\rho)}{\partial r_{fp}}\right|_{\theta_{lab}} dr_{fp}. \tag{5.23}$$

In Eqn. 5.22 i labels the multiple values possible for $B\rho$ depend on how many times the ion has crossed the axis. Here, for BigSol Spectrometer, the possibilities were restricted to $i = 0, 1$ only. We shall see that the two partial derivatives in

---

[22] This zero-degree behavior of a solenoid is quite analogous to the inability of a spherical optical lens to refract (separate) a ray of white light into its component colors when it enters the center of the lens at normal incidence (i.e. when it enters along its symmetry axis).

[23] All orbit and acceptance simulations were written in the Interactive Data Language^R (IDL) and are described in the appendices.

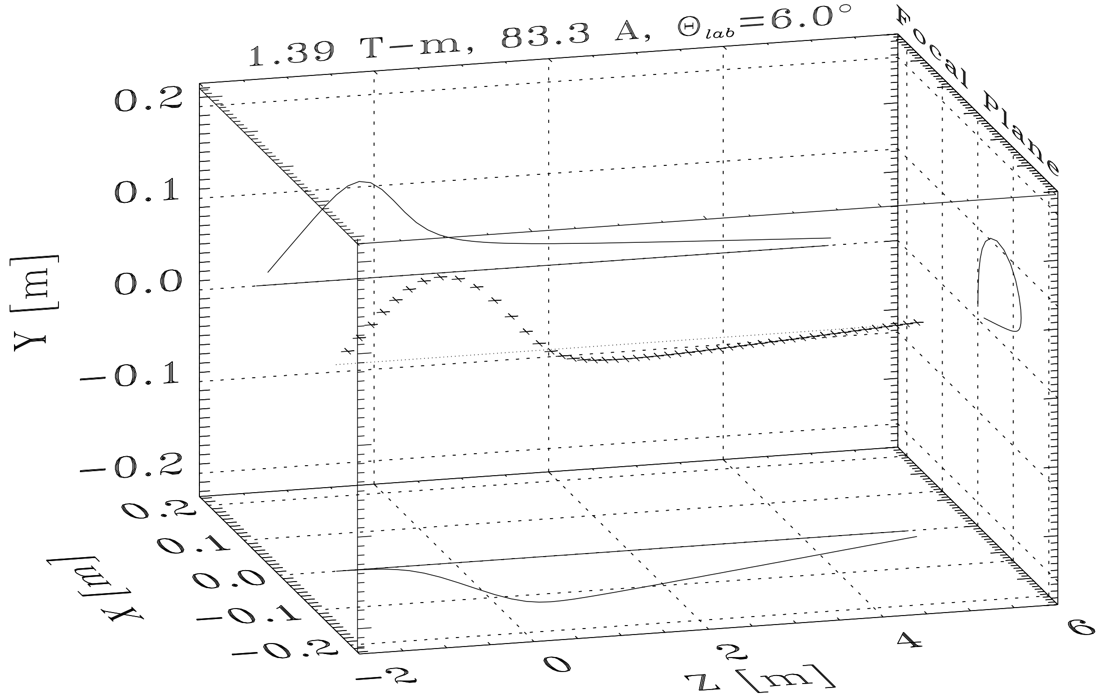

Figure 5.6: 3D box plot of simulated solenoid orbit. $\theta_{lab} = 6.0°$, $B\rho = 1.39$ T-m. Ion DOES cross axis yet reaches the SAME focal-plane position as for Fig. 5.7, illustrating double-valued $B\rho$ of solenoids as function of θ_{lab}.

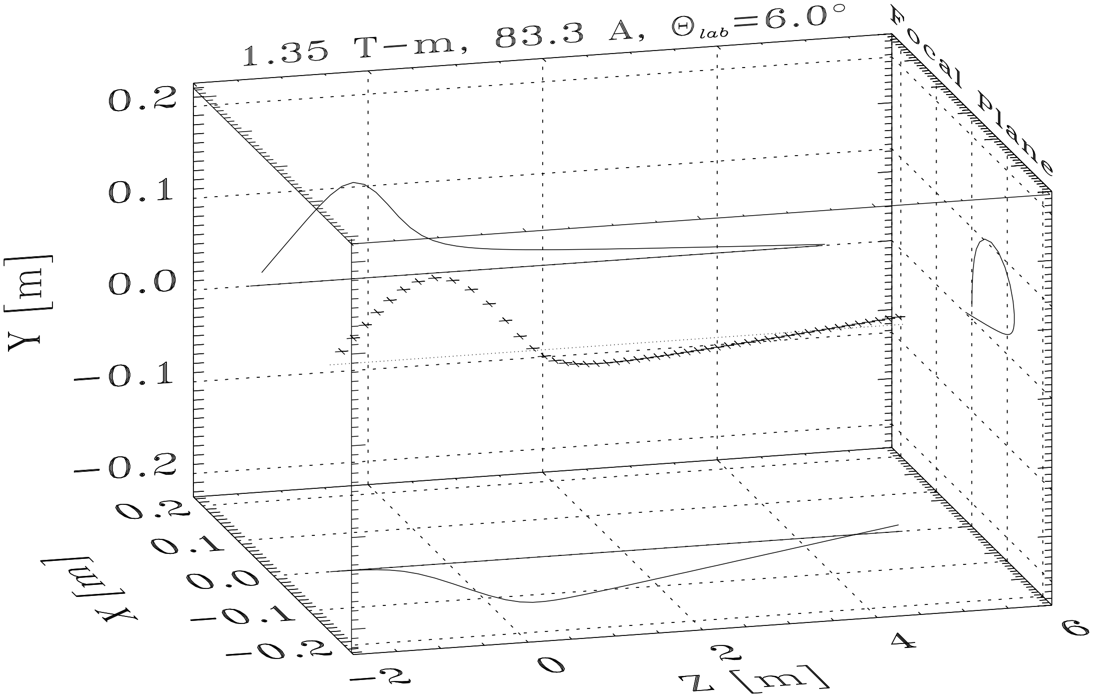

Figure 5.7: 3D box plot of simulated solenoid orbit. $\theta_{lab} = 6.0°$, $B\rho = 1.35$ T-m. Ion DOES cross axis to reach SAME focal-plane position as for Fig. 5.6.

Eqn. 5.23, designated as ∂_θ, and ∂_r, can be associated, respectively, with the effects of a focal-plane (image-location) aperture and of a target-plane (object-location) aperture. These two apertures are adjusted in hardware and/or software to limit the fractional dispersion $\Delta(B\rho)/B\rho$ so as to obtain acceptable isotopic resolution.

This second characteristic can be illustrated in two steps as discussed below.

5.7 Effect of entrance and focal plane apertures (∂_θ and ∂_r)

5.7.1 Double-valued $B\rho$ as function of θ_{lab} and focal-plane hit position r_{fp}

Consider once again Figs. 5.6 and 5.7 which represent ions emitted at the same angle: $\theta_{lab} = 6°$. In Fig. 5.6 an ion with a rigidity of 1.390 T-m strikes the focal plane at $r_{fp} = 18$ mm, with its path never crossing the Z-axis (In addition to the orbit, the z-axis is also projected onto the 2D walls of the box plot. Note that neither of the 2D projections of the orbit cross either Z-axis projection). On the other hand, Fig. 5.7 shows the orbit of an ion with a $B\rho$ of 1.349 T-m, which also strikes the focal plane at precisely the same radial position, $r_{fp} = 18$ mm, but, unlike the first orbit, this lower-rigidity ion is seen in the 2D projections to *have first crossed* the z-axis, near $Z = +4.5$ m.

Once one finds two such orbits ($B\rho_0$ and $B\rho_1$) connecting the same θ_{lab} and r_{fp}, one then knows that any ion emitted at this θ_{lab} and *inside* this rigidity interval (here $1.349 < B\rho < 1.390$ T-m), will hit the focal plane *inside* that radius (in this case inside $r_{fp} = 18$ mm). Any ion *outside* this interval (in the ranges of $B\rho > 1.390$ or $B\rho < 1.349$ T-m), which reaches the focal plane, will do so at a radius *outside* $r_{fp} = 18$ mm. This means that an annular aperture allowing ions emitted at $\theta_{lab} = 6°$ used in concert with an 18 mm radial aperture at the focal plane, would produce a "$B\rho$ bite" of $\Delta(B\rho) = 0.041$ T-m. This is a "fractional $B\rho$ dispersion" of about

3% (which is about 2x what is acceptable for the $B\rho$ dispersion, for the present experiment, if isotopes are to be resolved).

5.7.2 Limitations of single-ion-orbit simulations

The statement that r_{fp} at constant θ_{lab} has a minimum between $B\rho_{i=0}$ and $B\rho_{i=1}$, is based on the fact that the $r_{fp} = r_{fp}(B\rho, \theta)$ surface is concave. Single ion orbit plots such as Figs. 5.6 and 5.7 are of limited value for determining/visualizing issues of fractional dispersion and its implications for particle resolution—especially when one is focusing ≥ 200 different isotopes simultaneously during a single run (i.e. for any given $B\rho$ setting). It is much more useful to map out the *entire* $r_{fp} = r_{fp}(B\rho, \theta)$ surface for the particular i/o geometry and current setting being used. Figs. 5.8 – 5.10 are examples of such maps.

5.7.3 Comparing acceptance mapping of focal plane for different axial field models

In these wire-frame surface plots, the abscissa represents the $B\rho$ values of focused ions, the ordinate represents their θ_{lab} emission angles. The height of the surface represents the radial distance from the solenoid's axis at which the ion will hit the focal plane, r_{fp}. The first, Fig. 5.8 is a calculation resulting from using the simple Gaussian+constant fit to the field. The second, Fig. 5.9 is identical to the previous one, except that now the "far" field has been modeled using a best fit of an inverse-cubic curve to the on-axis exact field profile. The noticeably sharper appearance of the valley when the inverse-cubic far-field model is included is an indication of the significance of the portion of the orbit well beyond the extent of the solenoid itself. This is the model actually used for all acceptance and dispersion calculations which appear in this thesis. The valley running through its surface shows the characteristics

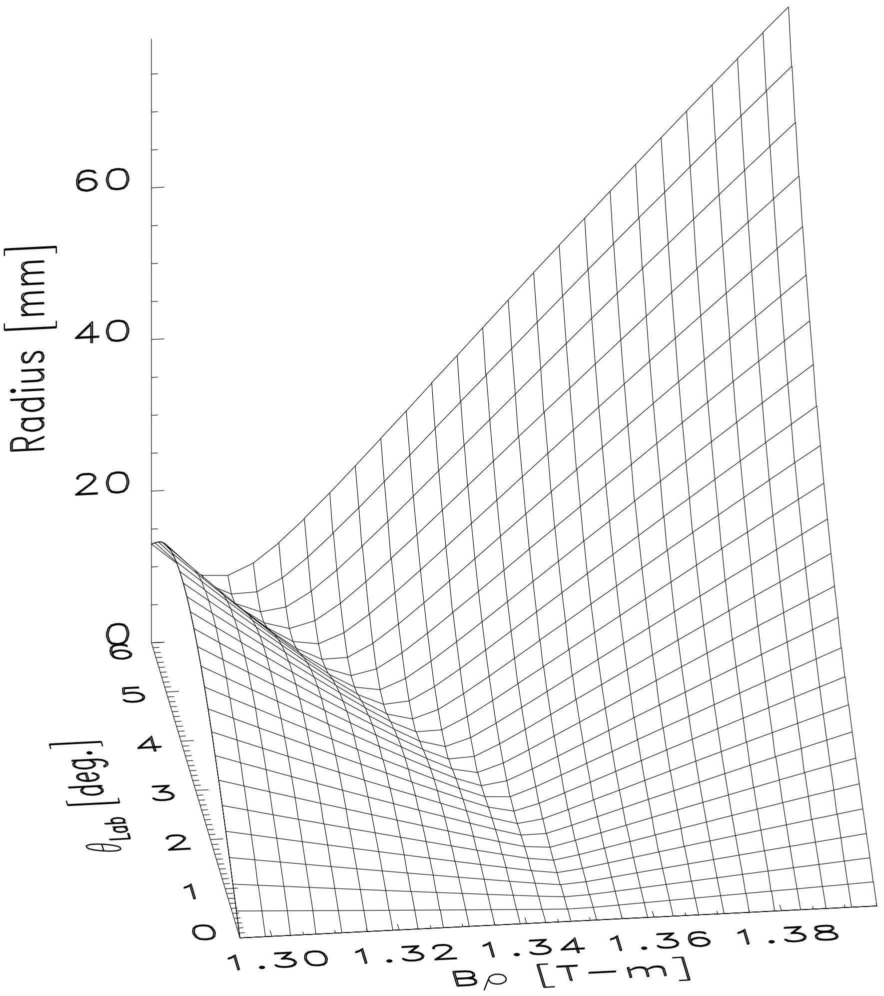

Figure 5.8: Acceptance map $r_{fp} = r_{fp}(B\rho, \theta)$ using a Gaussian-plus-a-constant fit to exact, thick coil. In this and the following wire-frame surface plots, the abscissa represents the $B\rho$ values of focused ions, the ordinate represents their θ_{lab} emission angles. The height of the surface represents the radial distance from the solenoid's axis at which the ion will hit the focal plane, r_{fp}.

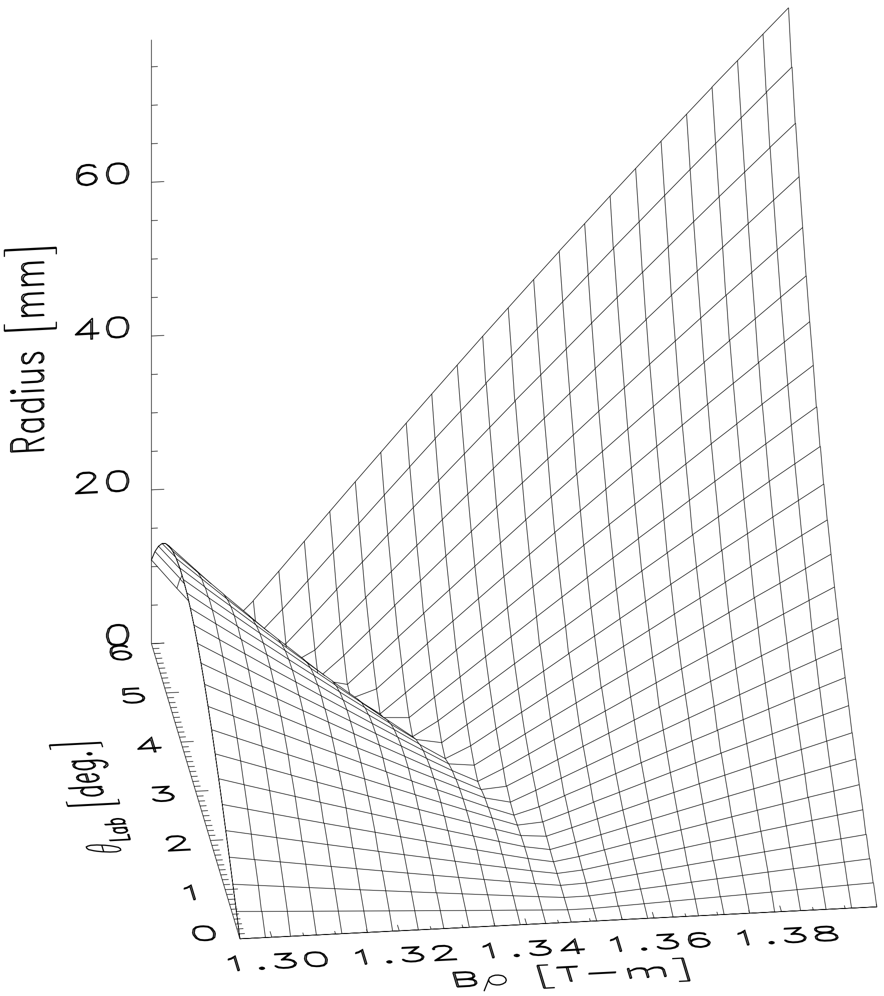

Figure 5.9: Acceptance map. Full thick-coil field model: Like Fig. 5.8 but with r^{-3} dipole-fit model for far field.

of the spectrometer's focal spot — which is quite evidently *not* constant in $B\rho$ as a function of θ_{lab}. Rather, there is considerable "chromatic" and spherical aberrations at the focal plane. The $B\rho$ values along the minima of this valley, at any given θ, is the magnetic rigidity value for which ions emitted at the θ will make the *closest* approach (radial-orbital apogee) to the center of the focal plane.

5.7.4 Characteristics of solenoid focal-plane acceptance maps (surfaces)

In general, it is significant that, for increasing θ_{lab}, at least four phenomena occur on the r_{fp} surface:

1. the walls of the valley become steeper (i.e. the $B\rho$ "bite" at constant theta gets smaller);
2. the minimum height at the center of the valley no longer goes to $r_{fp} = 0$ (i,e, above a certain θ_{lab}, ions can no longer be made to "focus" onto the center of the focal plane – *regardless* of their rigidity);
3. the focal-valley curves (meanders) to *lower* values of $B\rho$ (i.e. chromatic aberration occurs, where the rigidity of an ion is the magnetic analog of a photon's wavelength in an optical lens);
4. at very small angles, the valley broadens out until it disappears completely at $\theta_{lab} = 0^\circ$ (meaning that all ions emitted at or near to zero degrees will travel directly to the focal plane and no $B\rho$ selection will be imposed on them – the fractional $B\rho$ dispersion goes to 100%).

It is interesting at this point to consider Fig. 5.10. This is a surface plot made in a completely similar manner as Fig. 5.8, however, the infinitely-thin-coil approximation has been used for the axial field.

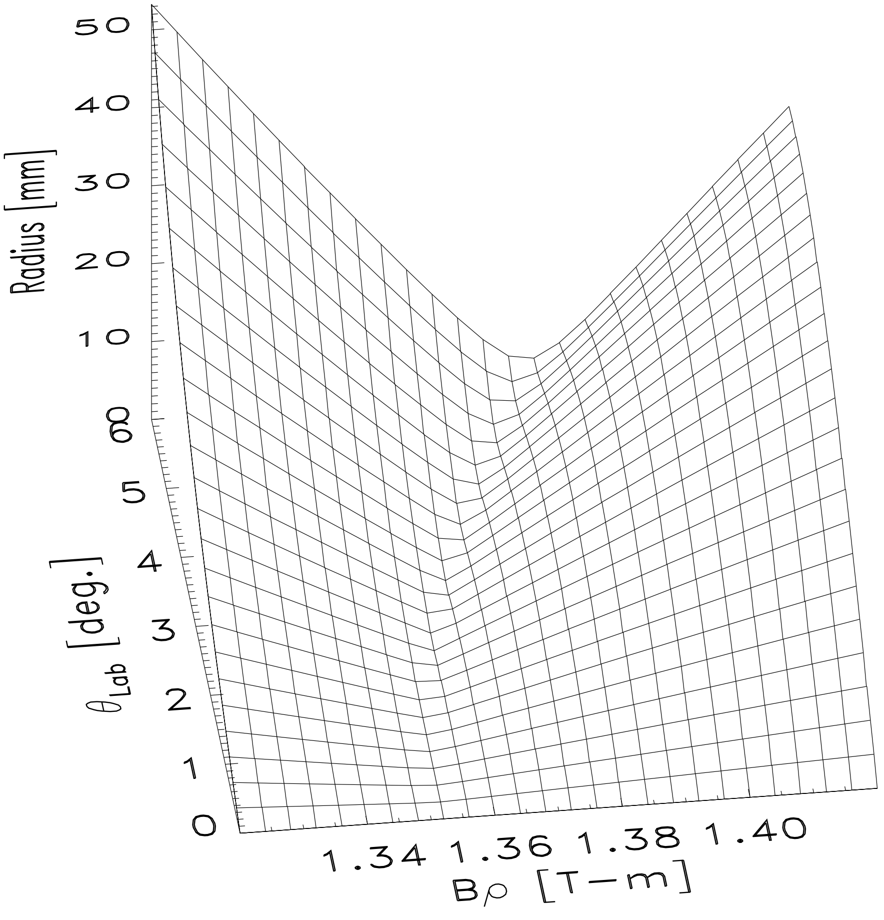

Figure 5.10: Acceptance map. Like Fig. 5.8 and 5.9 but using the inferior, infinitely thin-coil approximation. Note large discrepancy with "exact field" of Fig. 5.9.

If one then subtracts the calculation of Fig. 5.9 from that of Fig. 5.10, Fig. 5.11 results.

Further limitations to the thin-coil approximation are made apparent from this procedure. The difference plot surface shows that the thin coil approximation *underestimates* the degree to which focusing of higher θ_{lab} ions to small values of r_{fp} occurs. The meandering of its focal "valley" proceeds towards *higher* $B\rho$ – in the opposite direction from that predicted in the "exact" thick-coil calculation.

5.7.5 Determining cuts (apertures) required on the acceptance surface to achieve particle ID: Setting $\Delta(B\rho)/B\rho$

Returning to the thick-coil acceptance surface map, we know from the simulations shown in the chapter "The Systematics of 2D Particle-ID Spectra with Magnetic Selection," that a fractional $B\rho$ dispersion limited to about 1.7% must be imposed if ions in the region of interest are to be resolved. Fig. 5.12 shows implications of accomplishing this. The data shown here is identical to that of Fig. 5.9, however, it is now represented as a filled-contour plot. We wish to investigate what portion of this acceptance surface will have to be prevented from contributing to the ions collected at the focal plane, if the fractional magnetic dispersion is to be limited to no more than 1.5-1.7%.

To accomplish this, first, two horizontal lines have been drawn on the contour plot, along $\theta_{lab} = 0.7°$ and $3.1°$. This represents the effect of a software, or (in this particular case) hardware aperture having an annular shape and located at the entrance of the solenoid, just after the interaction target. This aperture only allows ions whose θ_{lab} falls between these two limits given above to enter the solenoid.

Next, a contour at $r_{fp} = 2$mm is highlighted in the figure. This particular isocline represents the effect of a hardware, or (in this particular case) a software aperture

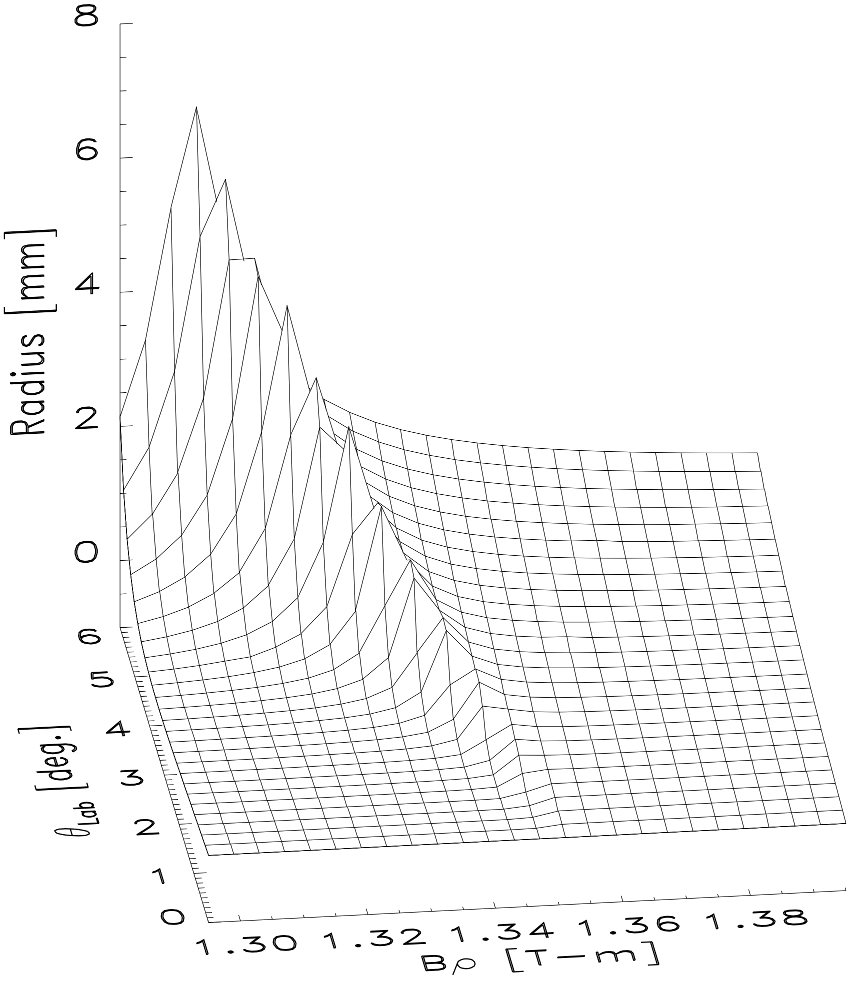

Figure 5.11: Difference of thin-coil minus thick-coil fields' acceptance-surface maps

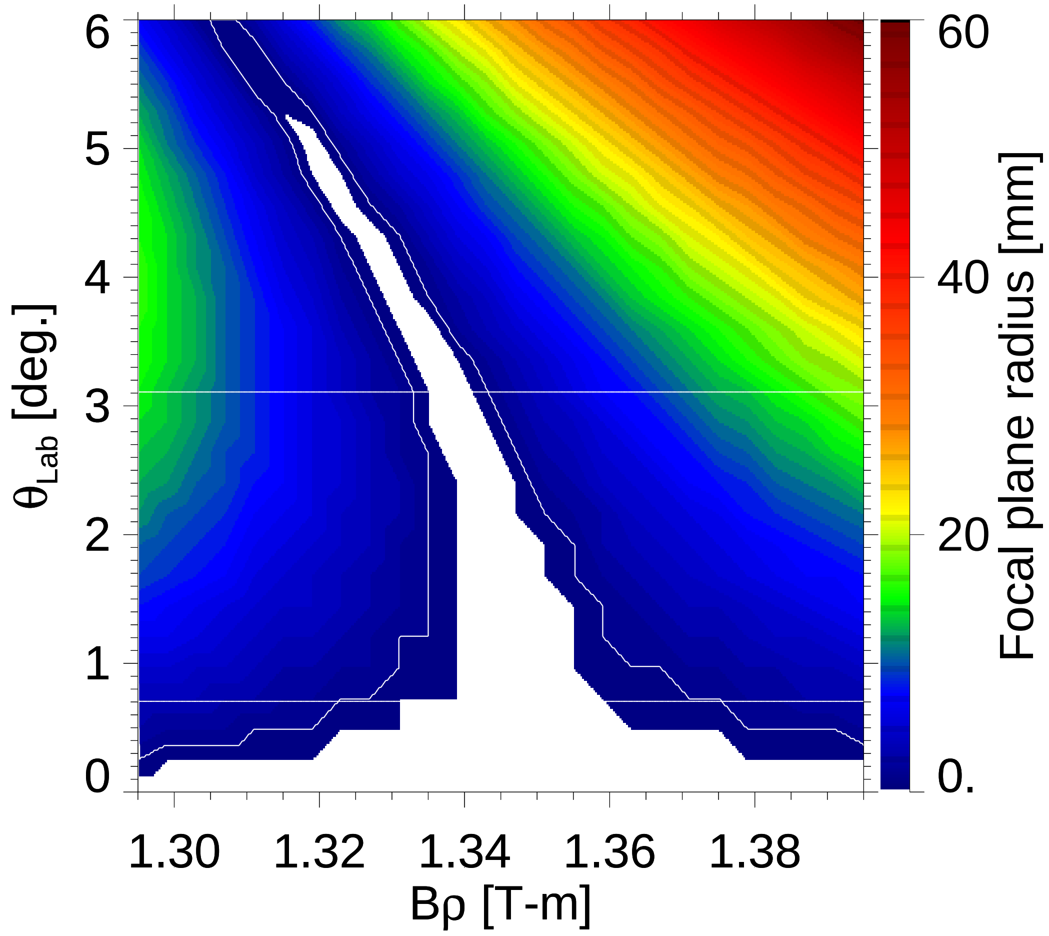

Figure 5.12: Contour map showing same information as in earlier wire-frame plot of Fig. 5.8, but now the radial-hit position of ions is represented by contours. Spectrometer acceptance for ideal, on-axis primary beam is shown together with the cuts caused by physical apertures (lines drawn at constant θ_{lab}) and cuts caused by software focal-plane apertures (lines drawn at constant-height contour). Acceptance is the INTERIOR region formed by these four aperture (cut) lines.

placed on the focal plane detector which excludes all events arriving at the focal plane at radial distances greater than 2mm from the central axis. This further restricts the portion of the acceptance surface which contributes ions to the focal plane spectra. The net result is that only ions whose $B\rho$ falls *within* the "acceptance polygon" defined by the limits of these r_{fp} and θ_{lab} apertures will be "$B\rho$ selected" by the spectrometer.

However, this one computed surface, Fig. 5.12, is not a sufficiently realistic model of the actual experimental acceptance. We must also consider the contribution to the acceptance of the spectrometer caused by the finite size of the primary beam. The size, and distribution of particles within the primary beam is often referred to as the "beam profile".

5.8 Effect of finite primary beam profile

Fig. 5.12 is the acceptance surface calculated[24] for a vanishingly "pencil-thin" beam of primary beam ions striking the target precisely at its center $r = 0$mm. In reality, the cyclotron beam in this experiment had a full width when measured at half of its maximum height (FWHM) of approximately 1mm.[25] To take into account consequences of the finite-width beam profile, three additional calculations of the same type as shown in Fig. 5.15 are carried out, but for beams with radial offsets from the target's centerline of 0.5, 1.0 and 1.5mm respectively. These locations are shown

---

[24] From here on all calculations are performed using the thick-coil formula, modeled using best fits of the forms Gaussian+constant in the near zone, and an inverse cube magnetic dipole in the far zone.

[25] This is a product of both the exactness of the cyclotron tune itself, and the tune of the subsequent beamline. A spurious beam "halo" which could not be fully eliminated by perfecting the tuning of the cyclotron or of the beam line did appear at the target. This was later determined to be a Sn isotope which is very nearly an exact q/A analog to the primary ^{136}Xe beam. This contamination problem was eliminated by a very small circular aperture placed just at the entrance to the target chamber. This aperture also insured that if the beam drifted off from its precise initial alignment, the count rate would fall rapidly and the problem would be quickly detected.

schematically in Fig. 5.13 superimposed over the profile of a 1mm FWHM Gaussian primary-beam envelope and shown in relation to the beam profile's σ (standard deviation). The distance, in standard deviations, of each beam, from the centroid of the Gaussian envelope to the central axis, will be used to determine the appropriate statistical weight for each beam in contributing to the total acceptance.

The results of two of these calculations are illustrated in Figs. 5.14 and 5.15 for 0.5 and 1.0mm beam-offset cases respectively.

These figures also have the same θ_{lab} and r_{fp}-sized gates drawn over them as were shown in Fig. 5.12, which showed the acceptance surface for the portion of the beam at zero offset from the z-axis. In each case it is instructive to observe the manner in which the acceptance polygon systematically deforms and translates for each of the different offsets for the primary beam envelope. Suffice it to say, that it is apparent from these these calculations that the details of the acceptance are a strong function of the beam profile at the target, and of the offset of the beam from the central axis of the device[26].

The results of these separate calculations are then collated in Figs. 5.16 through 5.19.

5.8.1 Projections of aperture-gated acceptance surface onto θ_{lab} and onto $B\rho$

Fig. 5.16 shows projections of the acceptance polygons of each surface plot on their *abscissa* ($B\rho$ axes) with *only* the $\mathrm{r}_{fp} = 2$mm software gate being imposed. In contrast, Fig. 5.17 shows projections of the acceptance polygons from each surface

---

[26] It should be stressed that here the effect of a a finite primary beam which is *parallel* to the axis is being simulated. It is of course possible that the primary beam may also be divergent to some degree when it first impinges on the production target. This is a more complicated situation, however, the programs used here are perfectly general and such beams may be specified and simulated in a manner similar to the present example. In general, careful beam alignment and tuning by the experimenters is required, though the relatively simple, straight-line geometry in aligning the solenoid's magnetic axis with the NSCL facility's beam pipe is not an unduly difficult constraint.

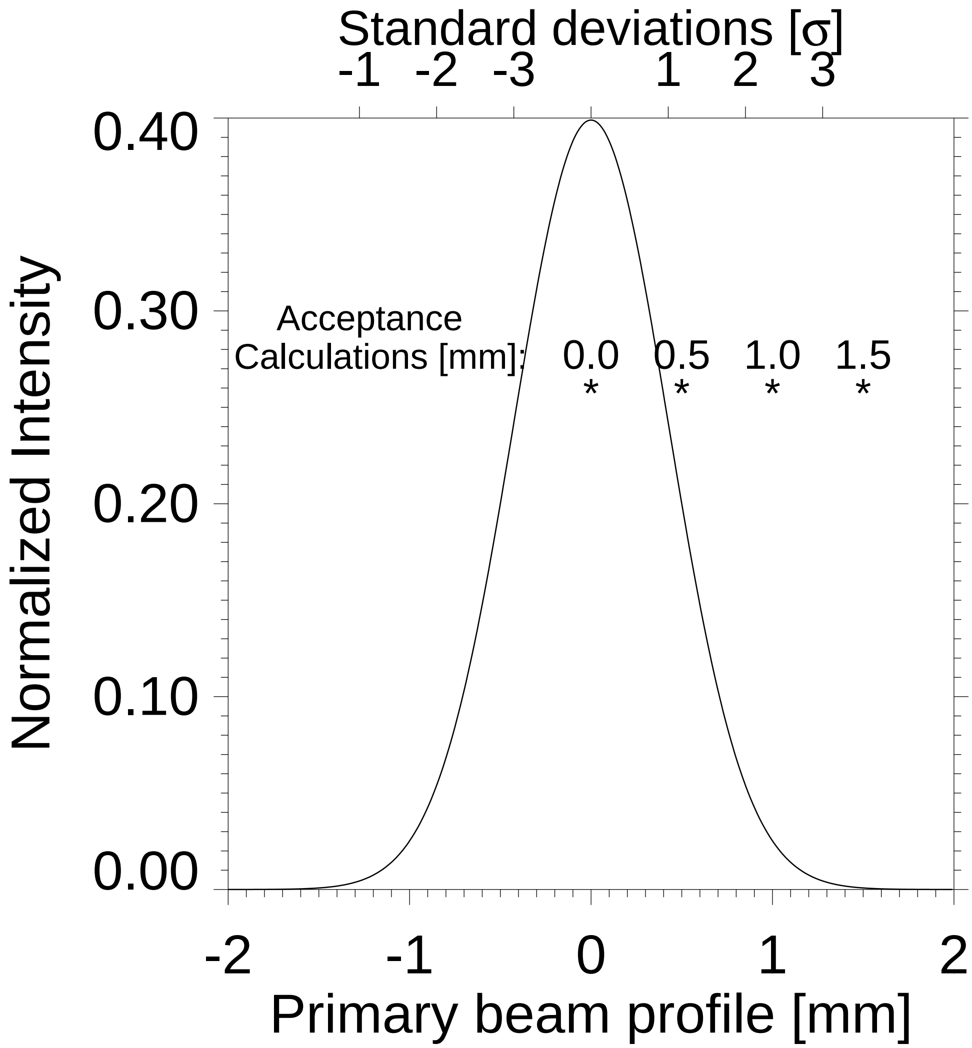

Figure 5.13: Model of 1mm FWHM, Simulation of finite Gaussian-shaped primary beam profile. Figure indicates locations of on- and off-axes calculations for "pencil thin" beams (*'s) performed in steps of 0.5mm. Each result was weighted by percentage of total Gaussian envelope's area near its location. Total of these calculations produces model of Gaussian-profile beam acceptance. See text.

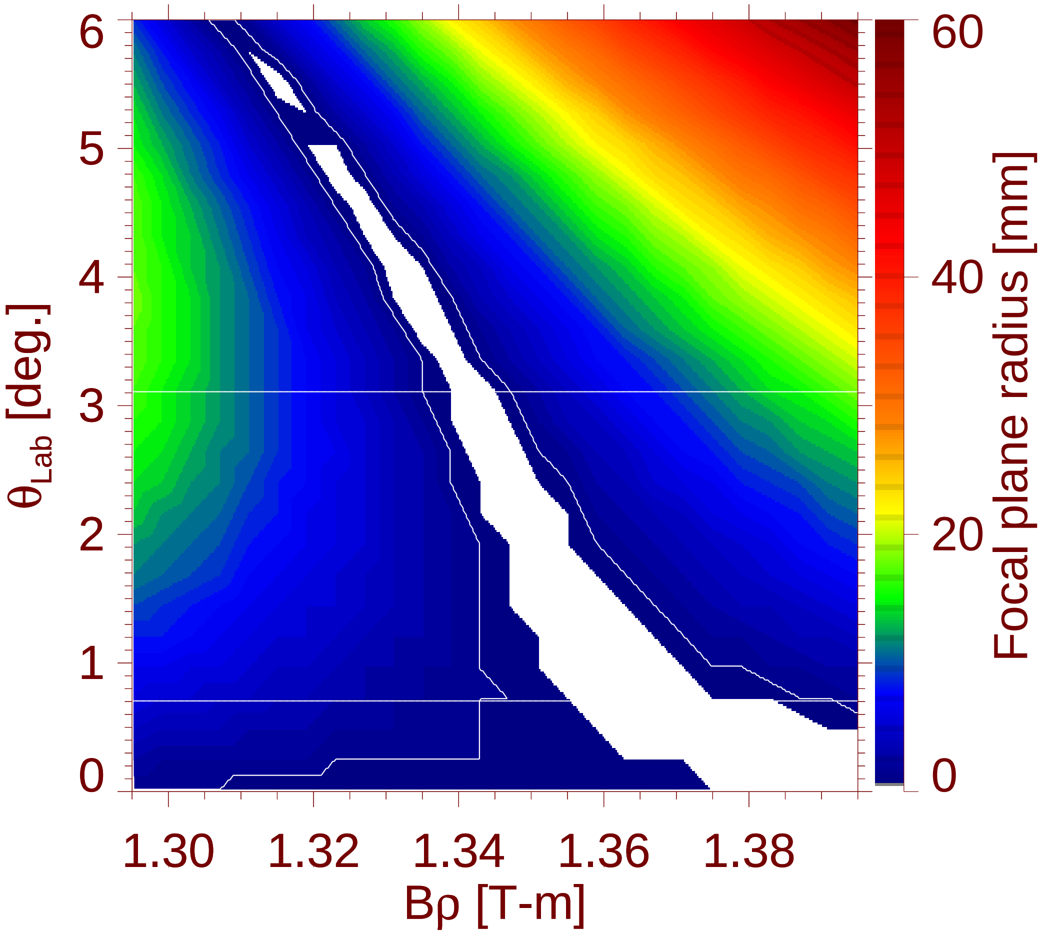

Figure 5.14: Like 5.12, but for “pencil-thin” primary beam offset by 0.5mm from Z-axis.

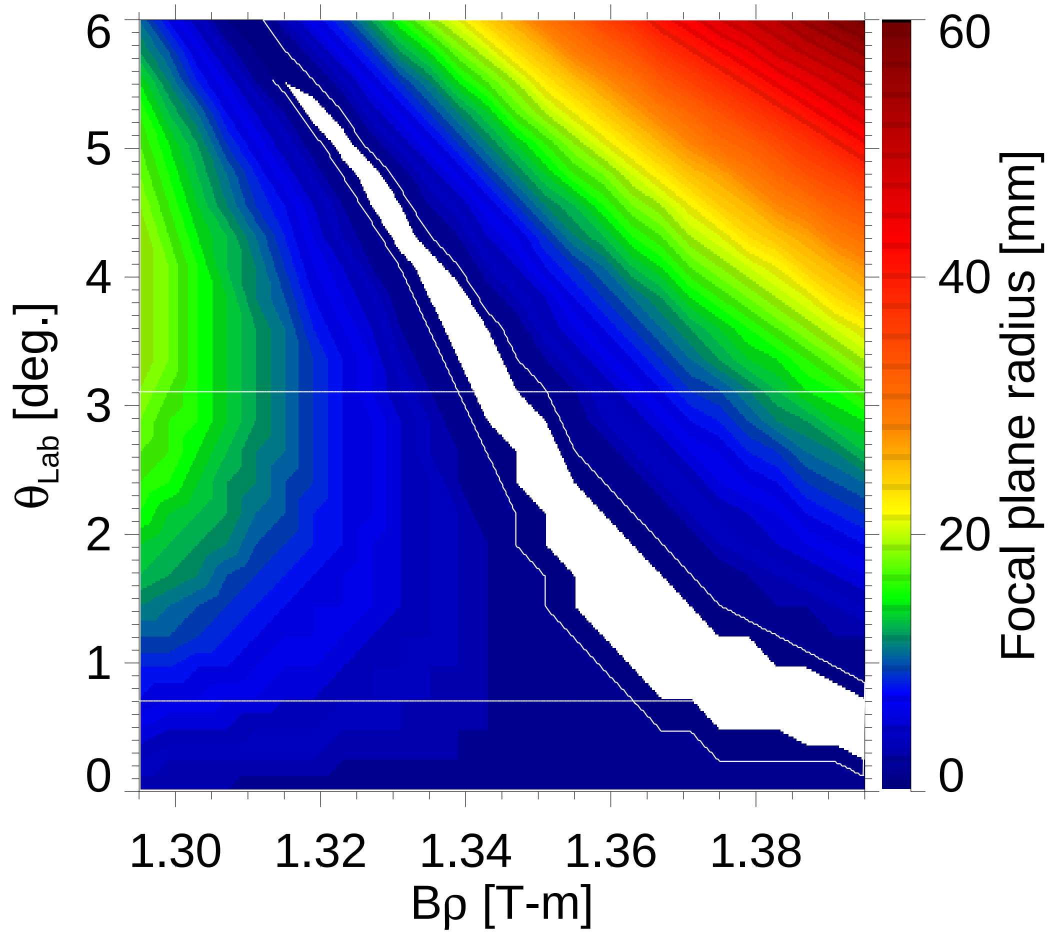

Figure 5.15: Like Fig. 5.12, but for "pencil-thin" beam profile offset by 1.0mm from Z-axis

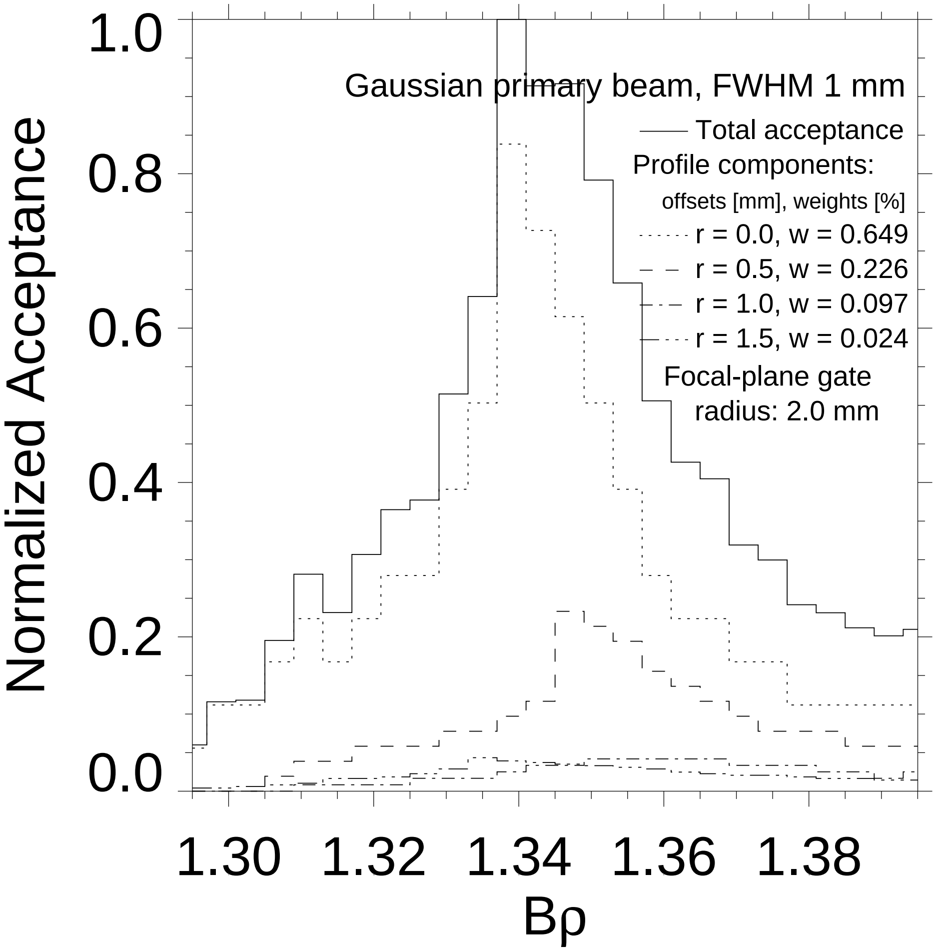

Figure 5.16: Projections onto $B\rho$-axis of the 2D acceptance polygons (no focal-plane cuts) of Figs. 5.12, 5.14 and 5.15, each weighted appropriately. Total shown is the complete acceptance.

plot onto their *ordinates* (θ_{lab} axes) under the identical focal-plane-gate-only condition. In each of these two plots, each projection shown has been weighted by the fraction of the area found under its portion of an ideal Gaussian-beam profile, and, the thick, solid, black line drawn above all the others is the sum of all the weighted constituents of the primary-beam profile.

It is immediately clear from these two results, that simply imposing a focal plane gate of 2mm is not a sufficient condition to restrict the $B\rho$ bite to $\Delta(B\rho)/B\rho)$ $\approx$ 1.6%, which is needed in the present experiments to accomplish sufficient isotopic resolution. Thus the θ-gated (using the *physical* entrance aperture) data from Fig. 5.16 is projected into a 1D histogram of $B\rho$ subject to the focal-plane software cuts: $0.7^\circ \leq \theta_{lab} \leq 3.1^\circ$ and $\mathrm{r}_{fp} \leq 2.3$mm. — producing Fig. 5.18. Finally, we arrive at a representation of the magnetic acceptance of BigSol as it was configured for these experiments. This model of the acceptance of BigSol *objectively* determines the size of the software gate needed on the position spectra in the focal plane in order to limit $\Delta(B\rho)/B\rho$ to about 1.7% to produce the desired mass resolution. This acceptance model also shows conclusively that it is *not necessary* to apply any (i.e. *software*) gate on the position of the particle in the *entrance* aperture in order to resolve the mass and atomic number of the ions. The $0.7^\circ \leq \theta_{lab} \leq 3.1^\circ$ *physical* aperture used at the entrance of BigSol was sufficient. Thus, the 2D-PPAC that was in the entrance aperture could be replaced with a fast timing detector, without the need of reconstructing the position in the entrace aperture (unless, of course, angular distributions are desired, which is a different experiment from that optimized to produce new, low cross-section neutron-rich nuclei).

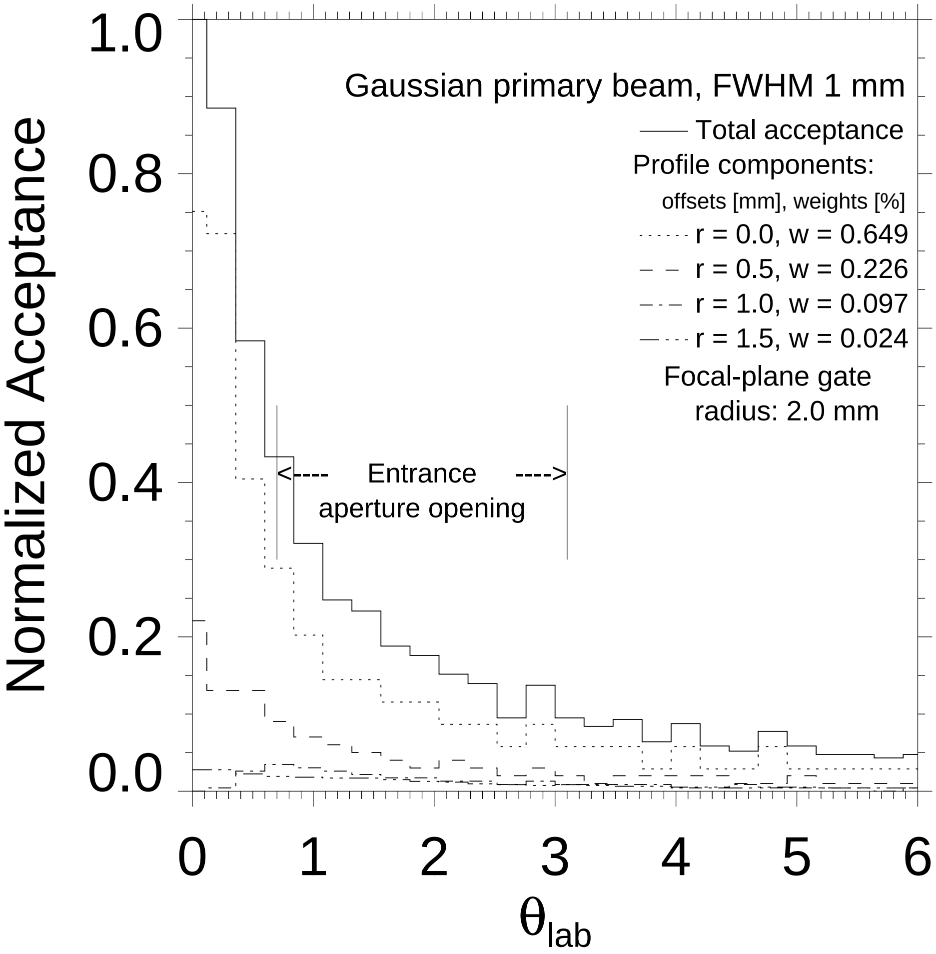

Figure 5.17: Projections onto θ_{lab}-axis of the 2D acceptance polygons (no focal-plane cuts) of Figs. 5.12, 5.14 and 5.15, each weighted appropriately. Total shown is the complete acceptance.

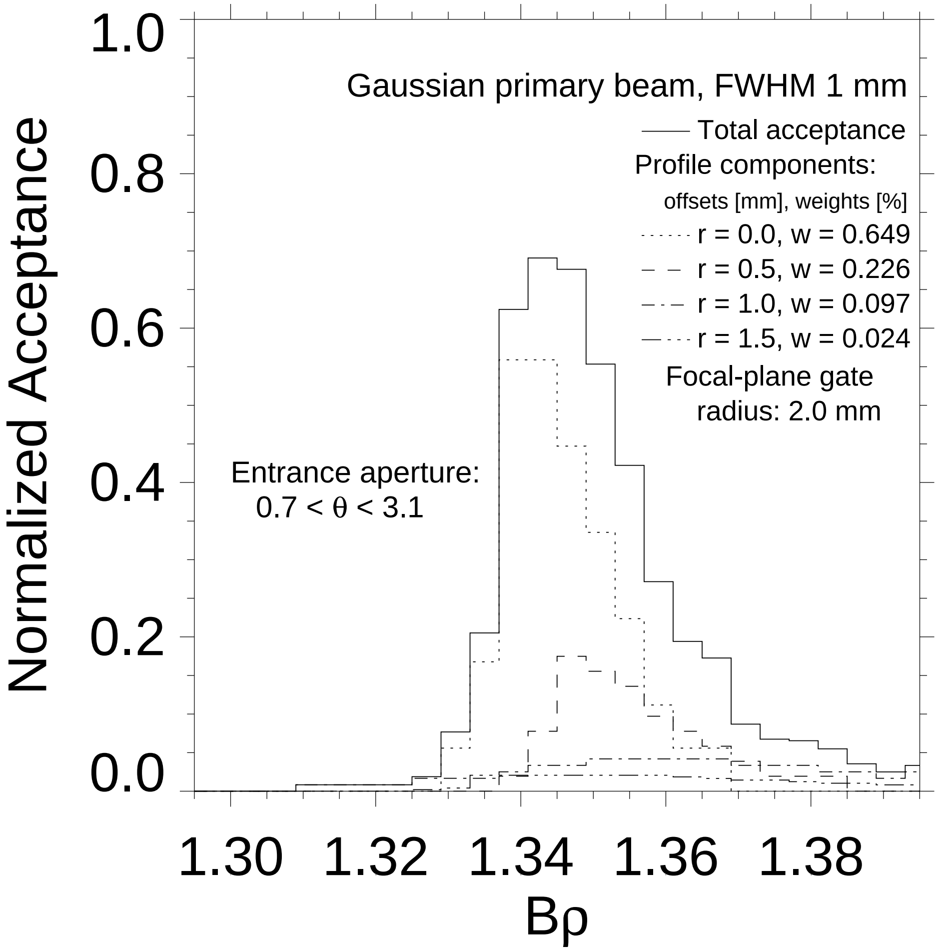

Figure 5.18: Like Fig. 5.16 but now with software focal-plane cuts applied to limit $\Delta(B\rho)/B\rho$. Total of separate calculations shown is final result of simulation for a 1mm FWHM Gaussian primary beam.

5.8.2 Interpretation of results

The interpretation of this figure is as follows: If a completely isotropic distribution of reaction products emerged from the production target over an area irradiated by the incoming, primary beam having a Gaussian intensity profile about the z-axis, and this isotropic distribution then entered the solenoid (and the solenoid had a supercurrent of 86.7 A in its coils), Fig. 5.18 would be the the $B\rho$ distribution of the yield observed at the focal plane detectors. In other words, if the *observed* experimental yield collected under exactly these conditions is divided by this computed isotropic yield, the observed yields can be corrected for the acceptance of the solenoid.

5.8.3 Quantitative results for $B\rho_0$ and $\Delta(B\rho)/B\rho$. Comparison to experiment.

Finally, it is necessary to attempt to quantitatively characterize the fractional magnetic dispersion of the products shown in Fig. 5.18 to see if, indeed, the requisite $\Delta(B\rho)/B\rho \approx 1.6\%$ constraint on achieving particle-ID resolution is accomplished. To accomplish this characterization, consider Fig. 5.19.

This figure shows a fit to the total (summed), calculated acceptance profile from Fig. 5.18 of the form Gaussian+linear. The fit has a centroid at 1.346 T-m and a fractional magnetic dispersion of 1.78%. This compares favorably (to about one part in ten or eleven)[27] with the effective fractional magnetic dispersion observed in the data after a detailed reduction process, as shown in [O'Donnell 1999] and the chapters, "Data Reduction Techniques for a Superconducting Solenoid Isotope Spectrometer" and "Results and Conclusions" below.

---

[27] Further improvement is principally dependent on detailed calibration of the model of the on-axis field profile from actual measurements — these are not as yet available.

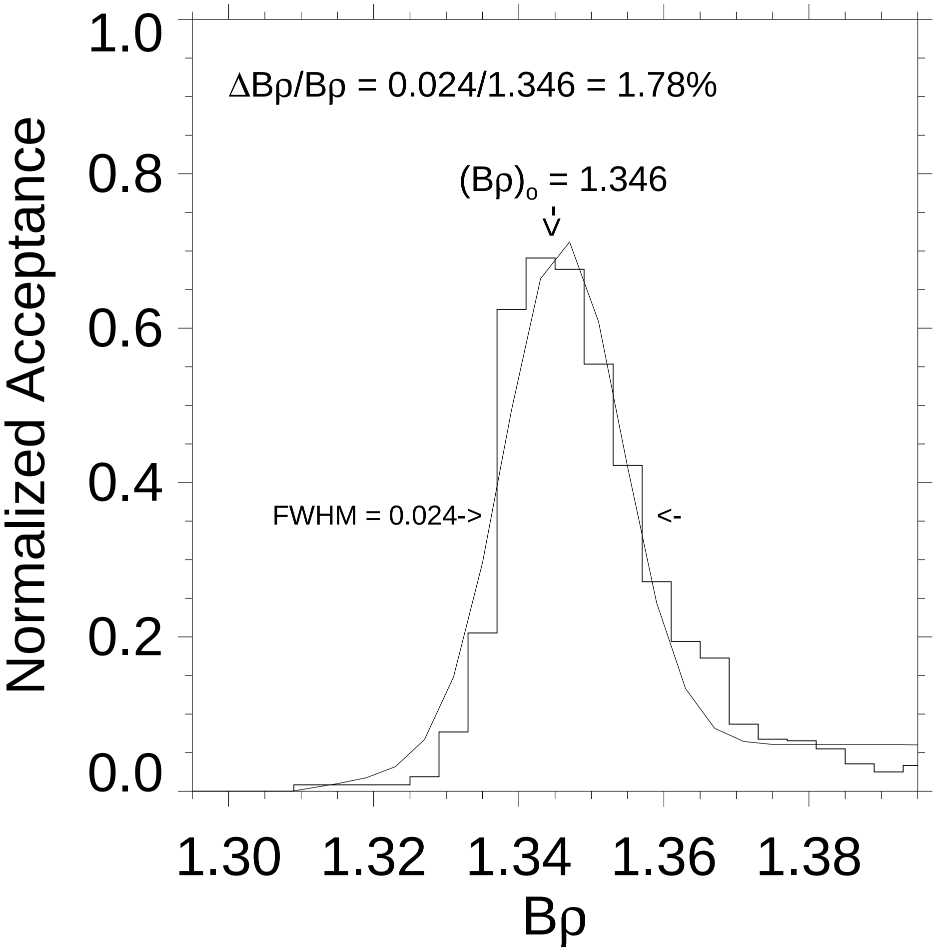

Figure 5.19: Fit to the calculated acceptance profile of Fig. 5.18 to determine $\Delta(B\rho)$. Result compares very favorably to actual experimental results in [O'Donnell 1999].

CHAPTER VI

“BigSol Isotope Spectrometer” Setup

Here we describe the device as shown schematically in Fig. 6.1 and in two renditions by an artist in Fig. 1.1 (page 5) and 1.2 (page 7). The apparatus is described starting from the beam-entrance end and moving towards the focal plane. Specifications of the experimental setup are given in Table 6.1.

6.1 Stopping-target considerations

In Fig. 6.1 the primary Xe beam is shown entering from the right to react in the target chamber. The specific aim of these experiments was the production and identification of neutron-rich isotopes in a region of the table of isotopes significantly below that of the primary beam. For this reason, the ^{nat}C target was chosen sufficiently thick (114 mg/cm^2) to stop both the primary beam as well as all other, extraneous heavy reaction products near the Z and A of the projectile. On the other hand, this target was still thin enough to allow the relatively lighter reaction products of interest to pass through it, albeit with their kinetic energies degraded. The necessary energy-loss and range calculations for ions passing through the target and detectors were accomplished using the TRIM program by [Ziegler & Biersack 1996].

The selectivity and energy losses imposed by the thick target somewhat com-

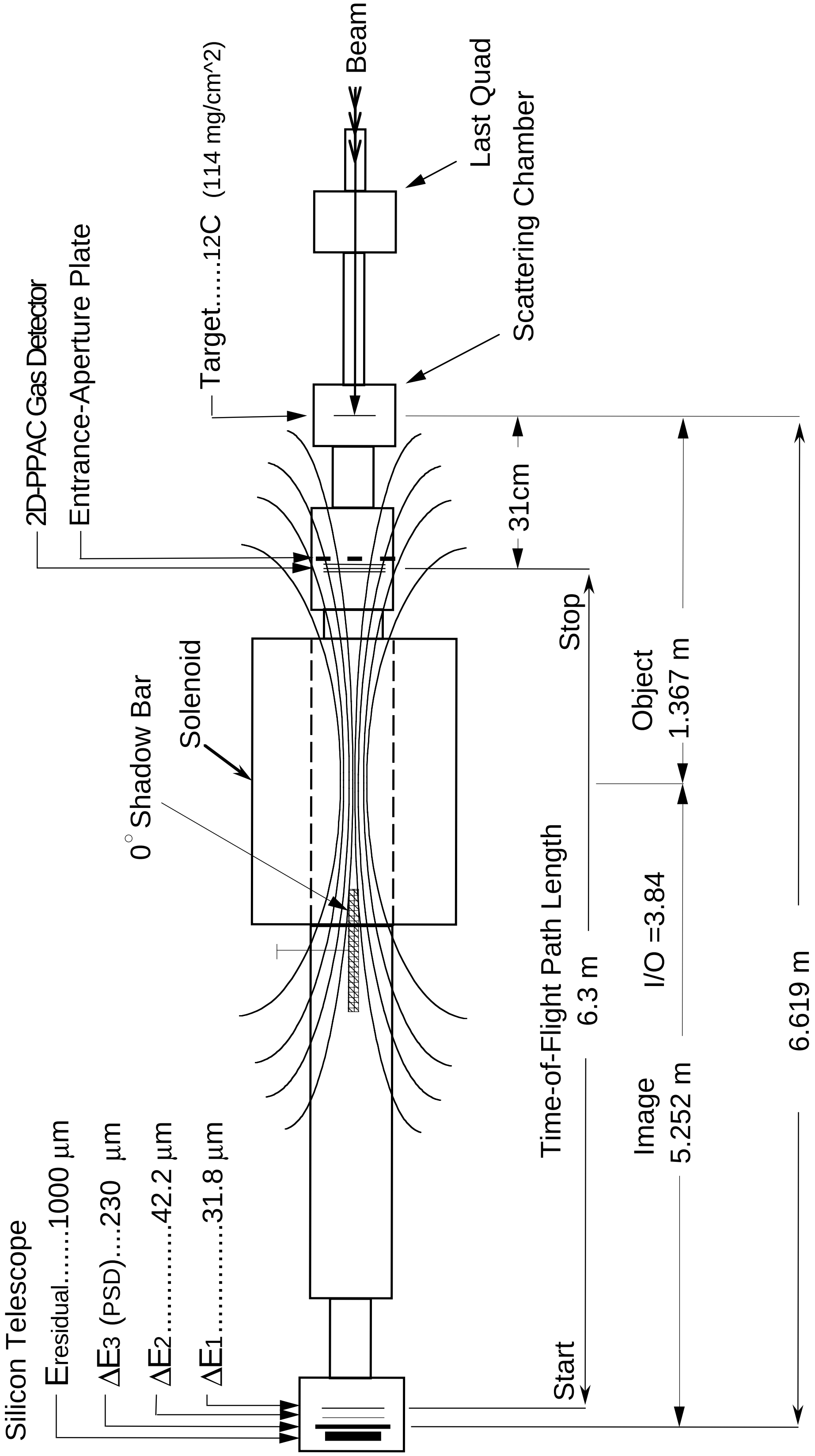

UM BigSol Isotope Spectrometer, NSCL

(Schematic, not to scale.)

Figure 6.1: (Page 136). UM BigSol Isotope Spectrometer. Schemtic of setup which was built and used for this thesis. The NSCL's K1200 cyclotron beam entered from the right-hand-side to react in the target chamber. Reaction products were focused through the solenoid ion-otical 'thick lens' onto the high-resolution silicon detectors at the far left for identification of possible exotic, neutron-rich (heavy) isotopes. The entrance- and focal-plane detector systems for energy, position and time-of-flight (ToF) measurements are shown.

plicate analysis of the overall reaction mechanism; investigation of the underlying reaction mechanism(s) would be facilitated by a thinner, less selective target.[1]

6.2 Entrance: 2D-PPAC-ToF detector and apertures

Fig. 6.1 shows an annular, mechanical aperture, which was placed 31 cm beyond the target. The mechanical aperture, in turn, is immediately in front of the position-sensitive, parallel-plate gas avalanche counter (2D-PPAC [Swan 1993]), which served as the solenoid's entrance detector. There were two differently sized aperture plates available to choose from. These plates were made of solid brass and each had a carbon stop affixed to its center. The carbon-plus-brass was sufficiently thick to stop any reaction products emitted at either $\theta_{\text{lab}} \leq 0.7^{\circ}$ in the one case, or at $\theta_{\text{lab}} \leq 2.2^{\circ}$ in the case of the other aperture plate. The open areas of the aperture plates, $\Delta\theta = \theta_{max} - \theta_{min}$ (see Table 6.1), were chosen so that the count rate of the 2D-PPAC was kept $\leq$ 35-50 KHz. The limiting criteria here is not the need to restrict $\Delta(B\rho)/B\rho$, since this can be adjusted with software apertures at the focal plane or in the 2D-PPAC spectra. Rather, the constraint here is the 35-50 KHz counting-rate

---

[1] With this in mind, and for future reference, a much thinner target with an areal density of 37 mg/cm^2 was tested briefly. From this test, the use of much-thinner targets was judged to be generally compatible with the experimental setup and methods developed for thick, stopping targets. However, the thin target required a lower primary-beam rate as heavy products were transmitted through it. It therefore required greater attention from the experimenters to insure the primary beam did not drift away from its alignment with the entrance-aperture plate's center-stop, which would rapidly cause radiation damage to the focal-plane Si detectors.

Table 6.1: University of Michigan ‘BigSol Isotope Spectrometer’ at NSCL.

• Beam	
Ion:	$^{136}\mathrm{Xe}^{24+}$
Kinetic energy:	30 MeV/u (4 GeV)
Intensity:	$\approx$ 4.6 enA (1.2e^{+09}particles/s), after attenuation by 10-100X
Accelerator:	K1200, National Superconducting Cyclotron Laboratory (NSCL).
• Target	
Material:	$^{\mathrm{nat}}$C in layered graphite foils.
Aerial Density:	114 mg/cm^2
• Solenoid field	
Current-to-rigidity:	80 amps $\approx$ 1.36 T-m ($\int \mathrm{B} \cdot \mathrm{dl}$)
Maximum Current:	170 amps
• Solenoid entrance (object)	
Apertures:	$0.7^\circ \leq \theta_{\mathrm{lab}} \leq 3.1^\circ$ or $2.2^\circ \leq \theta_{\mathrm{lab}} \leq 6.2^\circ$, and $\Delta\phi_{\mathrm{lab}} \approx 2\pi$
Timing-stop & θ_{lab} detector:	Position-sensitive parallel plate avalanche counter (2-D PPAC), iso-octane gas.
Counting rate:	$\leq 35 - 50$ kHz (PPAC)
• Solenoid focal-plane (image)	
$\Delta\mathrm{E}_1$ & time-start signal	31.8μm Si
$\Delta\mathrm{E}_2$:	42.2 μm Si
Si-PSD:	230 μm Si
$\mathrm{E}_{\mathrm{residual}}$:	1000 μm Si
Counting rate:	$\leq$ 500 Hz (at $\Delta\mathrm{E}_1$)
Logic:	Trigger and timing start on $\Delta\mathrm{E}_1$ event, timing stop on delayed PPAC anode signal.
• Spectrometer dimensions:	
Target to focal-plane distance:	6.62 m
image/object (i/0) distance:	5.25/$-$1.37 m (asymmetric mode)
Time-of-flight distance:	6.31 m

limitation of the 2D-PPAC detector itself. The 2D-PPAC was of a type routinely made by the NSCL Detector Laboratory, having an active area measuring 10x10 cm^2. Iso-octane gas at 7-10 Torr, and continuously renewed by flow, was used as the avalanche gas. The 2D-PPAC's XY-position signals were obtained by resistive charge division from cathode plates, one horizontally and the other vertically striped, located on either side of a central, solid anode plate. The plates were made of aluminized polyethylene sheets and the potential applied between them ranged from 600 to 650 Volts depending on the beam rate and the degree of detector aging.

The PPAC position signals were used principally to provide a measure of each reaction product's θ_{lab}. An intrinsic position resolution of about 1 mm at FWHM is typical for these PPACs when used for heavy-ion applications at the NSCL [Swan 1993], and was also evident in the present work. However, in this work, where the PPPAC was located very close behind both the target and an entrance aperture plate, two factors imposed additional limitations on position resolution: aperture slit-edge scattering and the occurrence of multiple hits by reaction products emitted simultaneously from moving, fissioning sources.

Although these PPACs are not generally intended for ToF measurements, in these experiments, the signal derived from the PPAC's solid anode plate, located between the two striped cathodes, was taken as a ToF-stop signal. Satisfactory timing resolution, in the range of 700-800 picoseconds was achieved for the lower-$B\rho$ (1.36 T-m) data sets. Exactly where the ToF resolution fell within this range depended on how ionizing the particular particle was, and on the counting rate being experienced by the detector. However, above about $B\rho = 1.7$ T-m, most lighter ions of interest (i.e., roughly $A \leq 40$) were insufficiently ionizing to be detected at the PPAC anode timing-stop. this was a significant limitation on the analysis of data collected at higher rigidities. ToF signals are especially {emphrequired to remove the charge-state ambiguities and establish particle identifications of the most neutron-rich data. (See [Volkov 1985] and Chapter VII, “Data Reduction Techniques for a Superconducting Solenoid Isotope Spectrometer.”)

It is apparent from Fig. 6.1, that the 2D-PPAC is positioned well within the fringe field near the entrance of the solenoid (field lines are shown schematically in the figure). However, data taken over a range of field strengths showed that the PPAC signals were unaffected by the solenoid’s fringe field. This fortuitous result is due to the fact that, at the PPAC’s location, the fringe-field lines of the solenoid are nearly normal to the plates of the detector. The PPAC preamplifiers, however, did need to be kept in a low-field region, and were placed about two meters from the PPAC in a direction perpendicular to the axis of the solenoid. The anode timing-pickoff preamplifier was close-mounted on the lexan cover of the PPAC-plus-aperture-plate vacuum chamber.[2]

6.3 Shadow bar and intermediate apertures

Additional beam blocks and apertures were placed within the solenoid itself, and in the extended ToF beamline beyond it. Inside the solenoid, a thin ‘neutron shadow bar’ (or, more accurately, a ‘higher-order-orbit blocking bar’) of diameter 3.8 cm and of length ≈ 1.25 m, was located along a portion of the axis just beyond the magnet’s center line (see Fig. 6.1). This bar both blocked energetic neutrons emitted near to $\theta_{lab} = 0°$ from reaching the Si focal-plane detectors, and, especially, blocked low-$B\rho$ ions’ orbits which may otherwise have crossed the axis multiple times before reaching

---

[2] A specially-built all-capacitive timing preamplifier was tried for the second, three-day experimental run at the NSCL. However, timing resolution was found to be inferior to that of the standard timing preamplifier used in the first three-day set of runs. Therefore the second set of experiments have timing information below what was needed to resolve isotopes.

the focal plane. Multiple-axis-crossing ions in a solenoid which is being employed as a *spectrometer* (as contrasted to being used simply as a RNB-*collector*) would cause an unacceptably large fractional-$B\rho$ dispersion, spoiling particle identification at the focal plane, without significantly improving acceptance.

The internal diameter of the solenoid and the ToF beamline beyond it have a radius of 20 cm. However, in general, this was not an issue as the ions collected in these experiments followed orbits within a few centimeters of the solenoid's axis. At the entrance to the focal-plane detector chamber, there was also a final, thick-brass ($\approx$ 7cm) annular aperture (not shown) to further reduce neutron and charged-particle background.

6.4 Focal-plane Si XY-ΔE-E-ToF detectors

A planar-Si ΔE-ΔE-E_{PSD}-$E_{residual}$ telescope was located inside the focal-plane chamber. For highly ionizing reaction products (collected at a higher $B\rho$ setting of 1.76 T-m), the signal from the Si $\mathrm{E_{PSD}}$ detector was added to that from the two thin ΔE detectors in front of it to make an optimal, thick-ΔExE identifier (an 'MZ^2 identifier'). At lower rigidities (1.36 T-m), however, an optimal identifier was constructed from taking either $\Delta E_1 + \Delta E_2$, or simply ΔE_1, as the ΔE signal. The general rule followed—the validity of which was clearly confirmed here—was that "...the optimum resolution is achieved when the ΔE and E signals are approximately equal." [Goulding 1985, p. 267].

The ΔE_1 detector was also used to provide a good-event trigger in the form of a ToF-start signal. The timing resolution of this thin, Si detector was about one order of magnitude faster than that of the 2D-PPAC anode plate, so that the PPAC was the resolution-limiting detector for the ToF measurements.[3] Count rates of particles

---

[3] While a gas detector's timing signal is generally faster than the timing signal from a thin Si

focused onto the focal plane, at ΔE_1, were typically $\leq$ 500 Hz—about 1.0-1.5% of the reaction-product rate found at the entrance PPAC.

The Si-PSD detector, which was the third element in the focal-plane detector stack, provided a high-resolution XY-position spectra. This spectra was used as the principal means to control in software the fractional $B\rho$ dispersion of the reaction products.

Further specification details of BigSol, its cryostat, current controls, etc. have been previously described elsewhere [O'Donnell 1994] [Becchetti2 1994].

---

detector, in the case of the PPAC, the parallel-plate geometry does not provide the steep field gradient and hence fast ion-collection ability which a cylindrical gas detector's field geometry provides. A thin, fast plastic scintillator at the entrance of the solenoid was also considered, but the strong solenoid fringe field and lack of position information for software entrance-aperture gating for a scintillator, favored the 2D-PPAC gas detector. Subsequent detailed analysis of the acceptance characteristics of a solenoid (see Chapter V, "Solenoid Ion Optics and Magnetic Dispersion"), however, show that the position sensitive detector at the entrance is not needed for particle ID. It is at the focal plane that position information is really crucial.

CHAPTER VII

Data Reduction Techniques for a Superconducting Solenoid Isotope Spectrometer

7.1 Introduction

In this chapter[1] a detailed explanation is given of the data reduction, analysis and visualization process developed to *eliminate the multiple-charge-state dependence of the present data* and achieve the particle-ID resolution for the neutron-rich nuclei reported in [O'Donnell 1999] and Chapter IX, "Results and Conclusions."

The process of data reduction presented several obstacles, some of which were peculiar to a solenoid-spectrometer, and others which were generic to lower-energy, massive-projectile fragmentation reactions. The reaction yielded over 200 separate isotopes in the focal-plane detector spectra, with each appearing in a distribution of ionic charge states. In light of these complications, the resolution achieved in these experiments is surprisingly good, especially in that only a *single* magnetic-element ion-optical device was employed. In addition, the very neutron-rich isotopes identified at $B\rho = 1.36$ T-m had insufficient kinetic energies to allow the use of multiple energy-loss detectors which would have provided much higher-resolution Bethe-Bloch ΔE signals.[2]

---

[1] This chapter was originally written as a private communication of the methods used to eliminate the multiple-charge-state dependence of the data and achieve the mass resolution shown in the paper [O'Donnell 1999]. The letter has been edited for inclusion in the present dissertation.

[2] In the higher-rigidity runs collected at $B\rho = 1.76$ T-m, however, it *was* possible to use multiple,

Several issues in the data reduction had to be examined in detail to eventually attain (and then optimize) mass resolution for at least a subset of the many experimental runs which had been recorded for later, off-line analysis.[3] These issues[4] included:

1. Optimal utilization/combination of data from the high-resolution all-silicon detectors at the focal plane, and from the PPAC-to-Si ToF system;

---

thick energy-loss detectors such that isotopic resolution was readily apparent. However, these higher-$B\rho$ ions were generally insufficiently ionizing to trip the PPAC-anode timing-stop detector. Hence, given that they appear in multiple charge states, their ToF information was insufficient for reliable particle-IDs. In reviewing the original proposal of our collaboration group for beam time at the NSCL, the expert reviewers offered fair warning as to the difficulties which would arise in the case of the present experiment from the combination of: massive projectile, relatively low beam energy and multiple charge states. These conditions are in contrast to the usually higher-energy, near-zero-degree sudden fragmentation reactions typically employed to produce exotic isotopes at the NSCL. This assessment was quite reasonable and was proven to be accurate. However, the goal of the experiment, from the physics point of view, was to explore precisely ***this*** specific type of reaction in the hope of opening up a mechanism to produce new, lower-Z ($10 \leq Z \leq 35$) neutron-rich isotopes at a time when continued progress was coming into question.

[3] Our collaboration was originally granted a single three-day experiment (72 hours of beam time) with a setup time which was effectively three months. BigSol was generally accessible regardless of other runs taking place at the NSCL because its N4 vault is at the end of a beamline, and beyond the A1200 beam analysis system used by most experimental groups. The director granted our collaboration a second three-day run which took place three months after the first was completed, as the first had been interrupted on its last day by an unrelated ^{14}C spill. The general hypothesis for this thesis was that we should collect/analyize reaction products as high in $B\rho$ as the detectors would allow, so as to single out products with the minimum of internal excitation energy. It was thought that this would be the best possibility of observing neutron-rich isotopes. However, above about 1.6 or 1.7 T-m, the energy-loss of most ions in the $Z = 20$'s and of some of the $Z = 30$'s, was insufficient to trigger a PPAC anode (timing) signal—though their position signals (derived from *integrated* energy signals) were satisfactory. Therefore, the runs with good timing are significantly lower in energy per nucleon: at about 1.36 T-m (and are the ones shown in the NIM conference paper [O'Donnell 1999]. Therefore, during the second three-day run, we tried placing a capacitive-only preamp the high B-field area, close mounted to the PPAC (on its vacuum chamber) so as to attain higher quality timing signals, and thus, allow a lower timing-signal-pickoff threshold. Unfortunately, this actually produced results which were worse than that of the original preamp and all subsequent runs of this second three-day set, even at lower $B\rho$ settings (e.g.: 1.36 T-m), do not have adequate timing resolution. At the time we were not fully aware that it would be inadequate, as it was only much later that the data reduction methods being described in this chapter were developed.

[4] An additional issue which will not be dealt with here in detail is that, for a large portion of the data taken, good ToF signals were not available because of a low signal-to-noise ratio for timing signals from the PPAC anode. Therefore, in an attempt to pick off timing stop signals for the most-energetic (highest $B\rho$), low-ionizing reaction products, a capacitive-only PPAC-anode timing preamplifier was tried during one-half of all data taking (viz.: the second, July, 1993 series). The idea was to obtain better signal-to-noise performance by placing the pre-amplifier directly on the PPAC chamber within the high B-field region. However, the timing attained with this preamplifier proved inferior to that from the standard preamplifier. In the process of data analysis, however, it became evident that this higher-energy data whose timing signals were below the pickoff threshold of the PPAC, a thick, multiple-ΔE vs. E_{total} identifier could be constructed using methods similar to those of [Volkov 1985]. Such an identifier, when formed using planar Si detectors, can resolve q, Z and A quite well. But, a charge state ambiguity for the most neutron-rich isotopes still cannot be removed without a timing signal. [ibid.]

2. Software position gating at the focal plane of the solenoid to provide detailed control of the solenoid's fractional $B\rho$ acceptance;

3. Overcoming systematic, correlated uncertainties in the absolute E and absolute ToF calibrations derived from cyclotron-analog calibration beams. The uncertainties in these quantities proved to be significantly larger than the intrinsic resolutions of the energy and time signals;

4. Finding appropriate A and Z identifiers which avoided (eliminated) the ubiquitous practice of placing thin, restrictive gates on Z bands in ΔE vs. ToF and/or in E vs. ToF 2D spectra so that *all* data was retained once the fractional-$B\rho$ acceptance gating is done;

5. In particular, calculating and, especially, forcibly integerizing q-state and mass assignments was avoided.

7.2 Software-aperture control of fractional magnetic dispersion with a solenoid

The chapter on solenoid ion optics explained the basis for setting the $B\rho$ "bite" by using hardware or software apertures at the solenoid's focal-plane and/or entrance. As shown in that chapter, the main issue regarding this experiment's acceptance bite is that the $B\rho$ of the ions collected is double-valued because the ions may have crossed the axis. Figs. 5.16- 5.18 illustrated the effect on the fractional $B\rho$ dispersion of applying apertures and gates of specific sizes.

A real-data example of a well-focused (centered) 2D Si-PSD spectra is shown in Fig. 7.1. In addition, an example of a 2D-PPAC spectra is shown in Fig. 7.2 for the case where the $0.7^\circ \leq \theta \leq 3.1^\circ$ entrance aperture was used, and where a software focal-plane aperture was set on the centroid of the focal spot (i.e., here the entrance

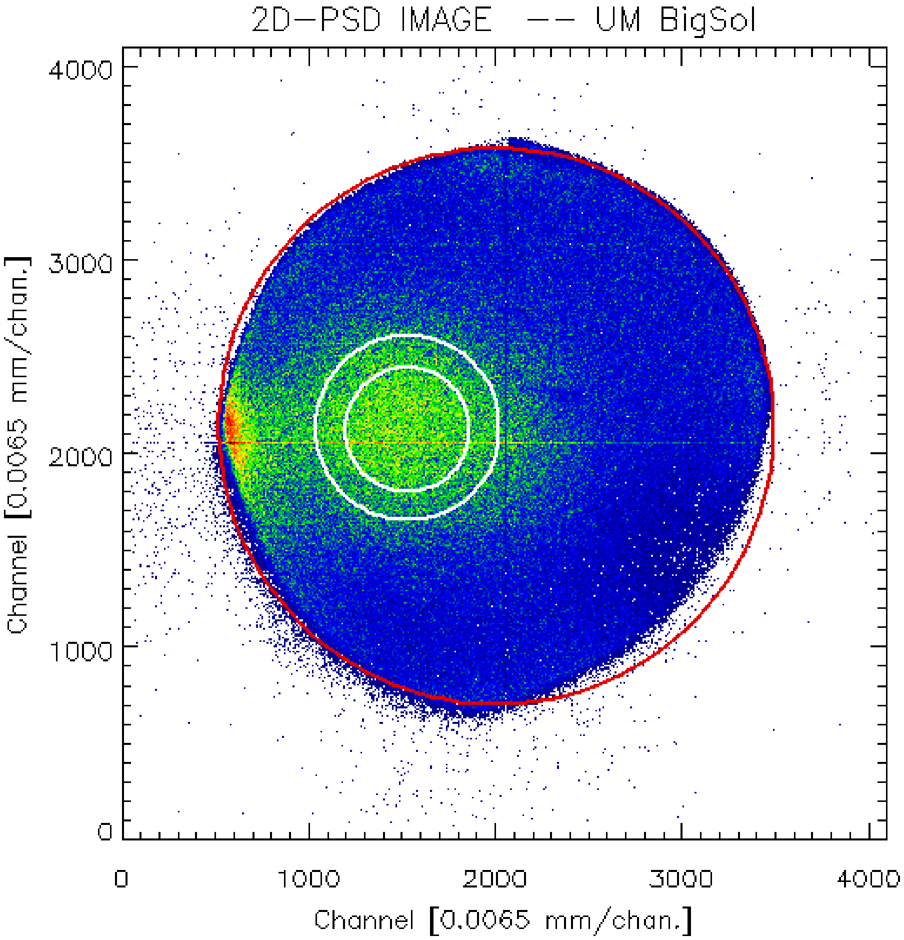

Figure 7.1: Typical 2D PSD image showing $B\rho$ selection software gates at solenoid focal plane. See text for details.

PPAC spectra is gated *by* the software gate in the 2D Si-PSD at the focal plane).

The PSD detector's active area measured 10 cm^2 (10^4 mm^2), but the red circle in Fig. 7.1 represents an area of only 300 mm^2. This smaller circle is the transmission area of the smaller of the two, round ΔE detectors located immediately in front of the PSD in the Si telescope. These detectors, then, effectively act as PSD apertures. The two, smaller, white circles on this figure represent *software* gates with radii of about $r_{fp} = 3.4$ and 2.2 mm about the centroid of the focal spot.

Indeed, these focal-plane gates encompass a rather small fraction of the available

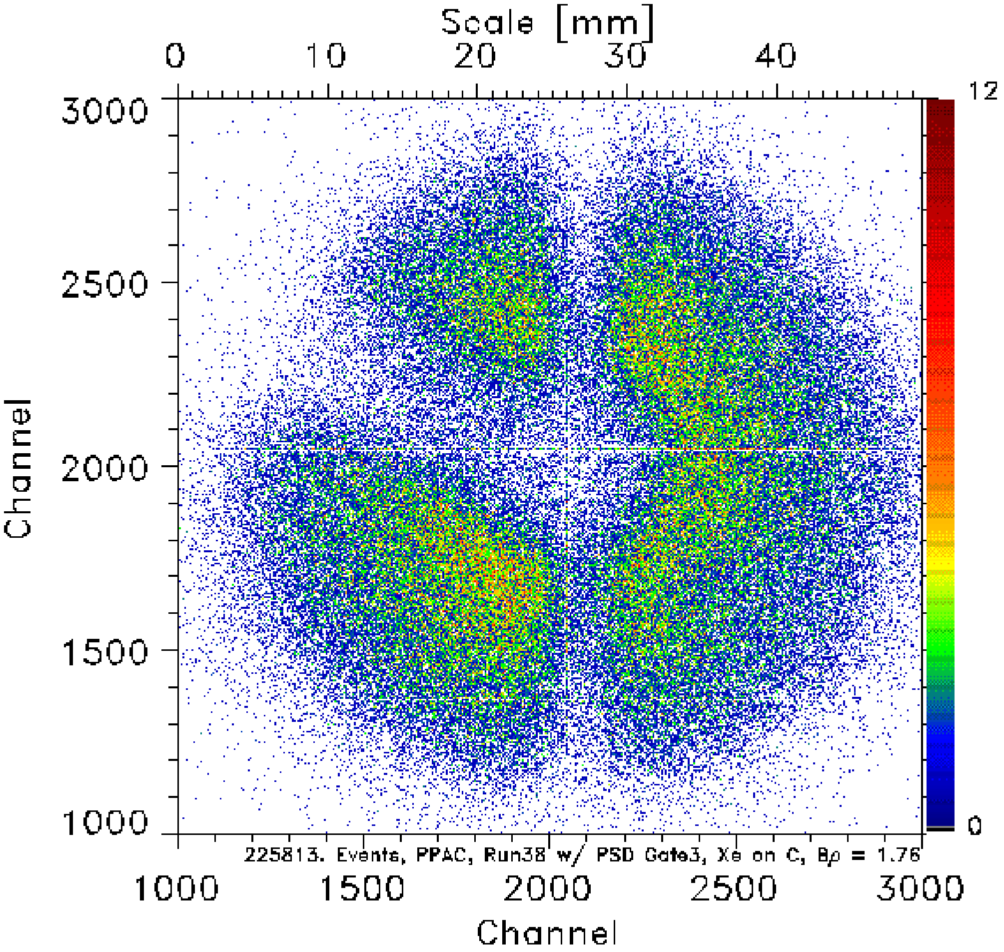

Figure 7.2: 2D entrance PPAC image with 0.7° − 3.1° aperture. PPAC spectra shown here has been gated by a software aperture on the Si-PSD *focal*-plane detector.

area of the detectors – roughly 10.6 and 6.8 mm^2 respectively out of the 300 mm^2 allowed by the first two ΔE detectors. Nevertheless, when the solenoid was properly focused and the entrance apertures and the focal plane detectors were carefully aligned with the cryostat-defined Z-axis of the solenoid[5] the central focal spot appeared as a Gaussian-like peak containing $20 \pm 10\%$ of all events. Nevertheless, the statistics could be maintained acceptably high because there was generally a surplus of beam available from the NSCL cyclotron such that the reduction of the active area of the detectors could be offset by increasing the beam current on target.

The relatively small area of this gated peak highlights the importance of having the ability to set a software vs. a mechanical aperture here. This ability is crucial. The relatively small size of this gate means that a slight misalignment of the primary beam would cause a mechanical aperture to entirely miss the relatively sharp focal spot. In the case of such a misalignment the simulations shown in the chapter, "Solenoid Ion Optics and Magnetic Dispersion" would be invalid, and all which follows in the present chapter with regards to obtaining particle resolution would be precluded.[6]

Once the $B\rho$-acceptance gating is properly done, a great deal of "structure" (in the statistician's sense) immediately appears in the 2D spectra (ΔE vs. E, ΔE vs.

---

[5] For example, in the first iteration of the experiments (April, 1993). this alignment was good to within ±1 mm. as measured by a precision surveying theodolite. Private communications, D. Roberts, U. Michigan BigSol collaboration.

[6] Two further possibilities should be noted: 1) It is also possible to analyze events falling onto the focal plane detectors at rather 'large' distances outside this gate – if they are analyzed in small fractional-$B\rho$ acceptance bites. One could in fact achieve reasonably good isotopic resolution from this off-focus data if another PPAC were placed just upstream of the focal plane to record whether each ion had crossed the axis or not and thus which of the double-valued $B\rho$ possibilities it belonged to. However, one has to be careful in assigning particle ID's to these off-focus events, as all these isotopes are shifted in energy and ToF (i.e., $B\rho$) from where they appear when they are optimally focused and identified with the analog calibrations beams. 2) Another possibility is a very thin, on-axis ion blocking bar throughout the solenoid which approaches quite close to the focal-plane detectors. This would allow ONLY non-axis-crossing ions to arrive at the focal plane and thus remove the double-valued-$B\rho$ problem altogether! This method may present significant promise for future solenoid spectrometer work. From their instrumental paper on the early solenoid device in use at Orsay, France in the 1980's [Schapira 1984] it appears that that device was designed to run in this mode.

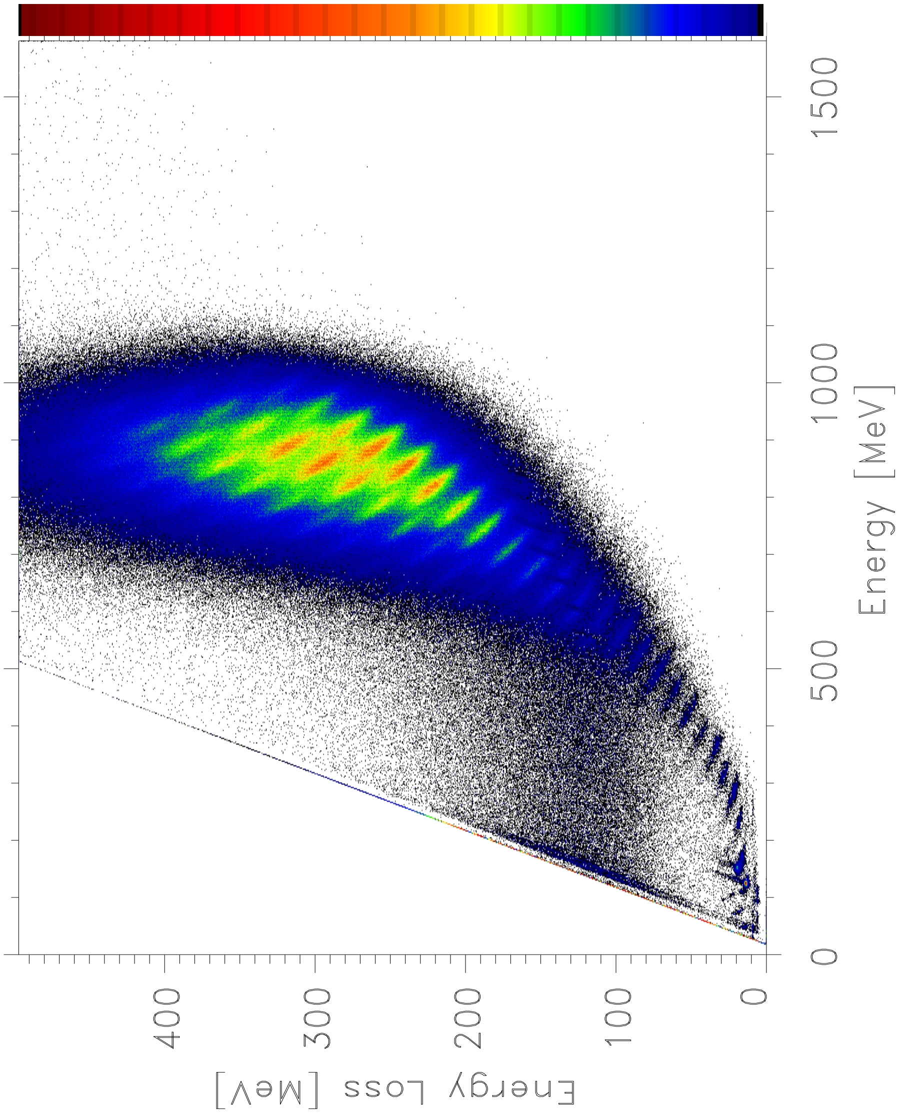

Figure 7.3: ΔE vs. E at 1.36 T-m. Full data, without software $B\rho$-bite restriction.

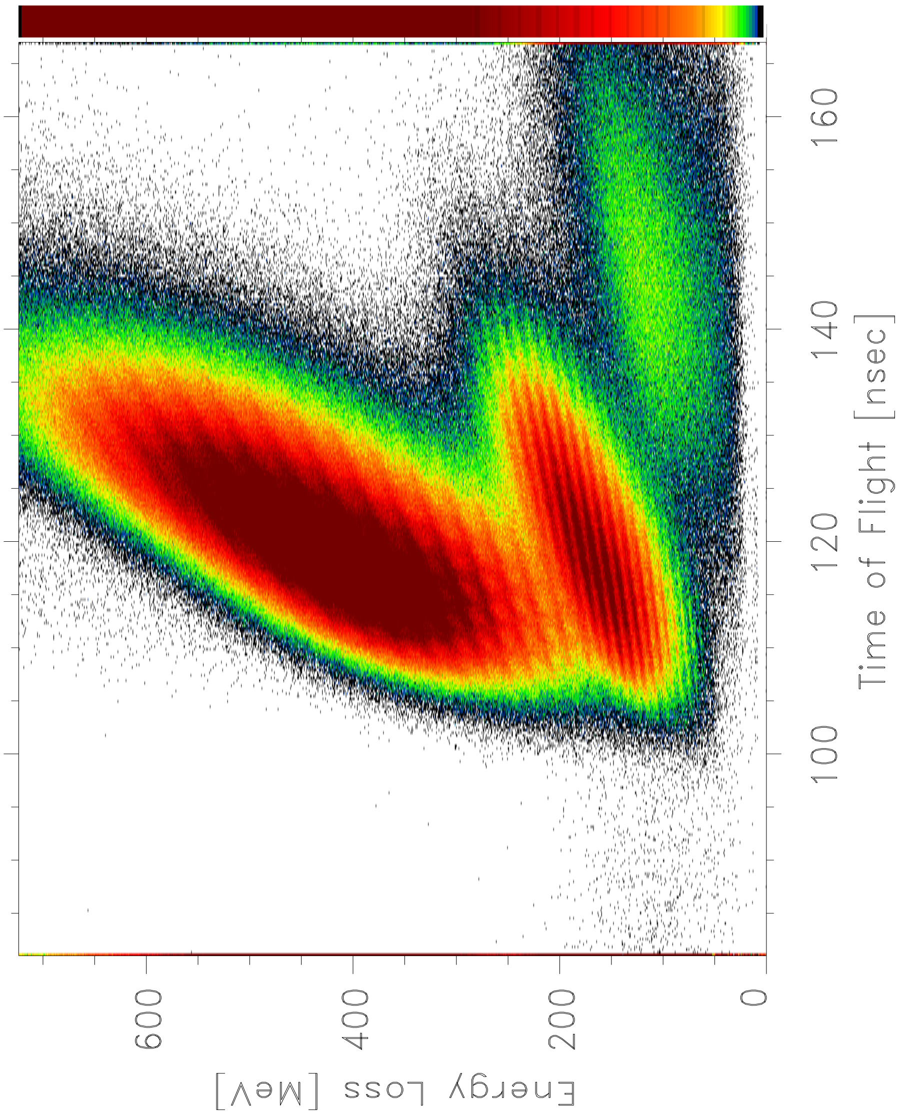

Figure 7.4: ΔE vs. ToF at 1.36 T-m. Full data, without software $B\rho$ bite restriction.

ToF, E vs. ToF, etc.). This structure represents the beginnings of resolution of the q-states, Z-bands and mass groups. As an illustration, "raw" spectra (for which there is good ToF information) are shown in Figs. 7.3 and 7.4. By "raw" we mean that this is the appearance of the data when events collected on the entire available open area of the Si-PSD are displayed. The only restriction on this data is that imposed by the presence of a $0.7^\circ \leq \theta_{lab} \leq 3.1^\circ$ physical aperture which was in place just before the 2D-PPAC. While some structure representing the characteristic Bethe-Bloch MZ^2 hyperbolae are evident in these spectra, adequate separation (resolution) is not evident for q-states nor, especially, for isotopic masses. Particle-ID resolution is precluded. In contrast, Fig. 7.5 and 7.6 show data from these same two spectra but where now a restrictive 2D-PSD $B\rho$ focal-plane gate has been imposed, allowing only data within a 1 mm radius of the peak to appear. Immediately, other sub-levels of structure have become apparent.

7.3 Data Reduction – statistical issues and particle identifiers

However, particle-ID resolution was still unsatisfactory, especially for the lower-energy (lower $B\rho$) data. There remained the problem of making explicit Z and A identifiers and of removing the q-state dependency in the spectra. However, as analysis proceeded along the lines one customarily follows, it appeared that the level of particle resolution intrinsically available in the data set was being partially lost.

7.3.1 Adding incommensurate-gain signals and eliminating aliasing of summed energy signals displayed at fine resolutions

The E signals from the four detectors in the telescope were originally binned and recorded into 2048 integer channels each. However, the $E_{residual}$ and PSD detectors were much thicker than the ΔE detectors (See Fig. 6.1), and so, required

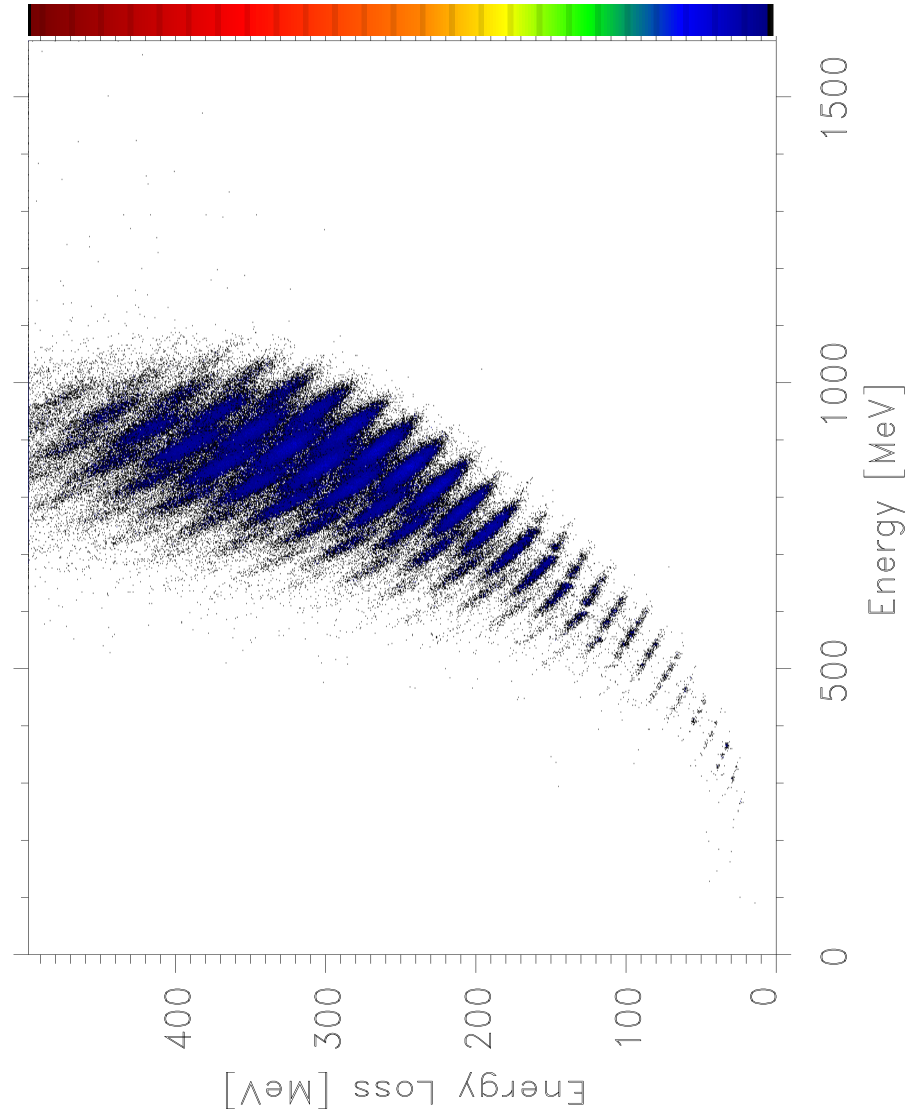

Figure 7.5: Same run as Fig. 7.3 but with a $B\rho \approx 1.7\%$ cut applied in 2D-PSD focal-plane spectra. Note emergence of structure.

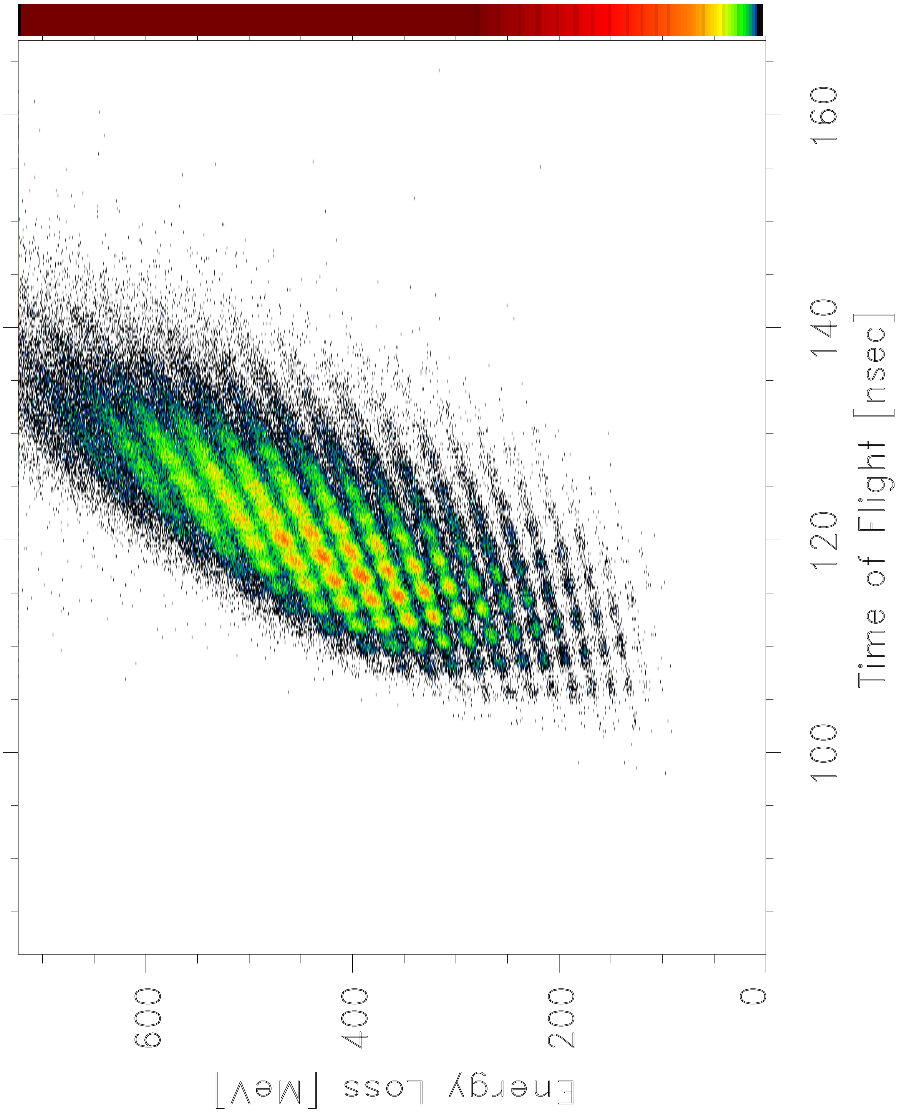

Figure 7.6: Same as Fig. 7.4 but with a $B\rho \approx 1.7\%$ cut applied in in 2D-PSD focal-plane spectra. Note emergence of structure.

pre-amplifiers with very different gains. The ratio of preamp gains for the E and E_{PSD} detectors as compared to the ΔE detectors was approximately 1/2.78. This difference in energy resolution presents an issue as to how to optimally combine such information/signals.

In order to add up the differently gained signals to construct a total energy signal, one typically fits pulser calibration data to obtain gains and offsets (expressed as floats) for *each* signal source *separately.* The primary acquisition, analysis and display system used in these experiments (XSYS[7]) would then separately fix these calibrated signals producing integer histograms. However, upon adding four such signals, one obtained a total-E signal and multiple-ΔE signals that were badly aliased [Plastock & Kalley 1986]. That is, spurious, digital-artifact patterns become apparent in the data at the fine 2D resolutions necessary for achieving particle-group separation/visualization.

It was found that this effect could be eliminated and much finer-resolution displays could be attained. This was achieved by finding the least common *integer*-multiple of the detectors' pulsar-derived gains. These least common *integer* multipliers were then used to calibrate the individual signal sources before adding them up. The important point here is that only integer, multiplicative math (as opposed to division) was performed on each channel before adding them to generate the energy-loss and total-energy values. Any further 'calibration' performed after this point, was always done via non-linear axis labeling only. The data binning itself is never

---

[7] Written originally at the Max Plank Institute, Germany, it has since been edited and developed at several other institutions. Our version was acquired from the Indiana Cyclotron Facility, U. Illinois, Urbana-Champaign, especially by Mr. Dick Yoder for VAX-VMS systems. The program was used as the de facto "on-line" acquisition system at the NSCL during these experiments by running it in so-called "off-line" (play-back mode) wherein the data buffers emanating from the NSCL's VME DAQ (data acquisition) system were transferred by means of ethernet to a VMS machine running XSYS and the XSYS program accepted these signals just as if they were emanating from tape or disc storage devices. The run-control tasks were performed then by the NSCL's usual DAQ system. This setup was engineered by Mr. Ron Fox, computing director of the NSCL.

altered.[8]

This method, of course, sacrifices somewhat the precision of the energy-deposited-to-signal-generated calibration in comparison to that usually attained from pulsar calibration of *individual* detectors. However, the trade-off of attaining smooth, non-aliased combined-signal sources is sufficient compensation. In fact further fine-tuning of the calibration using real particles is still necessary.[9]

This further fine-tuning of the absolute energy and energy-loss Si detector signals is accomplished using analog 'cocktail'[10] calibration beams sent through the entire stack of detectors. In an earlier test run[11] the Si detector energy and particle ID calibration was attempted by using alpha particles emitted from a ^{226}Rn source. This source emits the most energetic alpha particle attainable from radioactive calibration sources, having an energy of 8.78 MeV. However, even the 8.78 MeV alphas from this source penetrated only the first, thin ΔE detector in the stack, stopping in the second detector. This is inadequate as a calibration of the response of the stack-as-a-unit to energetic heavy-ion reaction products.

It was also possible to inject such particles into each detector separately, by im-

---

[8] If there had been a more sophisticated analysis/visualization package available (such as IDL) for these first-pass cuts from the data tapes and the initial calibrations of the data, it would have been possible to exclusively use float arrays for the calibrated and summed signals, and to somewhat simplify this initial process. The quest for such a package was not uneventful, requiring at least six months efforts consulting with experts at U Michigan's Institute for Technology Development (ITD) and others before being introduced to IDL at the University of Michigan Medical School's cyclotron laboratory for Positron Emission Tomography. In particular the assistance of Ms. Jenny Rogers, system manager and IDL programmer and the Director, Gary Hutchenson, PhD, was extremely valuable.

[9] The pulsar calibrations do not involve real, energetic ions hitting and passing through the detector stack. Instead, this initial calibration is accomplished by injecting several different calibrated amounts of charge, as the independent variable, into each preamp located immediately adjacent to its silicon detector. The output signal of the pre-ampliflier, cables, amplifiers and associated electronics, as registered in the DAQ computer, is then taken as the dependent variable. A calibration which results in a similarly linear relationship of charge injected to output signal is then attained by adjusting the gain settings of the NIM-style amplifiers. The result, then, of this charge-pulsar calibration is to calibrate the electronics only; the calibration of the Si detectors is accomplished later, in a separate process using real calibration beams.

[10] The meaning of 'cocktail beams' and cyclotron 'analog beams' is discussed in chapter, "Systematics of 2D Particle-ID Spectra with Magnetic Selection."

[11] November 1992

pregnating small pin-sized wires with the Rn-source daughters and then placing these "Rn pins" between the detectors in the stack. These alpha-particle (real particle) signals from the Si detectors are very useful to adjust various settings (e.g. pole-zero) in the NIM electronics modules during the pre-experiment setup period before live beam can be taken. However, the experience of the original test run and the advice of various experienced workers in the heavy-ion spectrometer field[12] strongly indicated the need to have ions of a similar energy and mass to those which would be encountered in the actual experiment penetrate the entire detector stack in order to achieve accurate energy and, especially, particle-ID calibrations.

That is to say, although some precision in the pulsar-gain matching was sacrificed, absolute energy calibrations were satisfactorily recovered with the cocktail calibration beams.

After this least-integer-multiple calibration procedure, one could display much finer E and ΔE resolutions in 2D spectra without the appearance of aliasing patterns. One MeV/channel was adequate to resolve this data with a $\approx 1.7\%$ fractional $B\rho$ spread. The *underlying* combined energy resolution of the detectors, however, was considerably better. This E-resolution quest actually becomes unproductive after a certain point, as the $B\rho$ dispersion bite becomes the limiting factor on resolution after reaching about a one MeV/channel level.

7.3.1.1 Higher $B\rho$ runs: without time of flight

Above a magnetic ridgity of $B\rho \approx (1.6 - 1.7)$ T-m, the energy-loss of most ions in the $Z = 20$'s and, to some extent, in the $Z = 30$'s, was insufficient to trigger a PPAC anode (timing) signal—though their position signals were acceptable. This

---

[12] We express our appreciation to J. Winger, D. Morrisey, G. Peasly (NSCL) and G. Wosniak (LBNL) whose advice in this regard is much appreciated.

dichotomy is due to the fact that T_oF signals are derived from a constant fraction rise time measurement (a 'pick off' derivative measurement) in hardware, while position is derived from finding a centroid of summed (integrated) signals. For this reason position measurements are always more robust against a drop in the signal-to-noise ratio. Therefore, the runs with good timing are, unfortunately, those collected at a lower $B\rho$ of about 1.36 T-m and are those shown in [O'Donnell 1999] with identified isotopes. At the higher-$B\rho$ runs, (at 1.76 T-m and above), there is indeed a sharply pronounced structure ("resolution") evident for A's, Z's and q's in the thick-ΔE vs. E_{total} spectra (where $\Delta E = \Delta E_1 + \Delta E_2 + E_{PSD}$). Nevertheless, it is not generally possible to positively identify the most neutron-rich isotopes without also having time-of-flight signals. This is because the most neutron-rich isotopes of the fully stripped ($q = Z$) charge state of a given element (Z) happen to fall in the same location as the isotopes of the third charge state ($q = (Z+1) - 2$) of the next higher element ($Z + 1$) band.[13]

Typical examples of the resolution achieved in these higher $B\rho$, multiple-ΔE vs. E spectra, are shown in Fig. 7.7, and in more detail in Fig. 7.8. Three different energy-degraded calibration beams of ^{40}Ar are shown laid over two spectra which were collected taken at two different $B\rho$'s.

7.3.1.2 Lower-$B\rho$ runs: with time of flight

For the lower-$B\rho$ data (at 1.36 T-m), where ToF information was available, there were still overlapping Z-bands in the ΔE vs. E spectra, and mass groups were not fully resolved in ΔE vs. ToF at this stage of the data reduction. This problem arises due to the ions' shorter ranges at this $B\rho$ which meant that one could only use a single-element ΔE detector. Previously shown Fig. 7.7 and 7.8 are typical of this

---

[13] See [Volkov 1985], though our results are perhaps not as problematic as Volkov indicates.

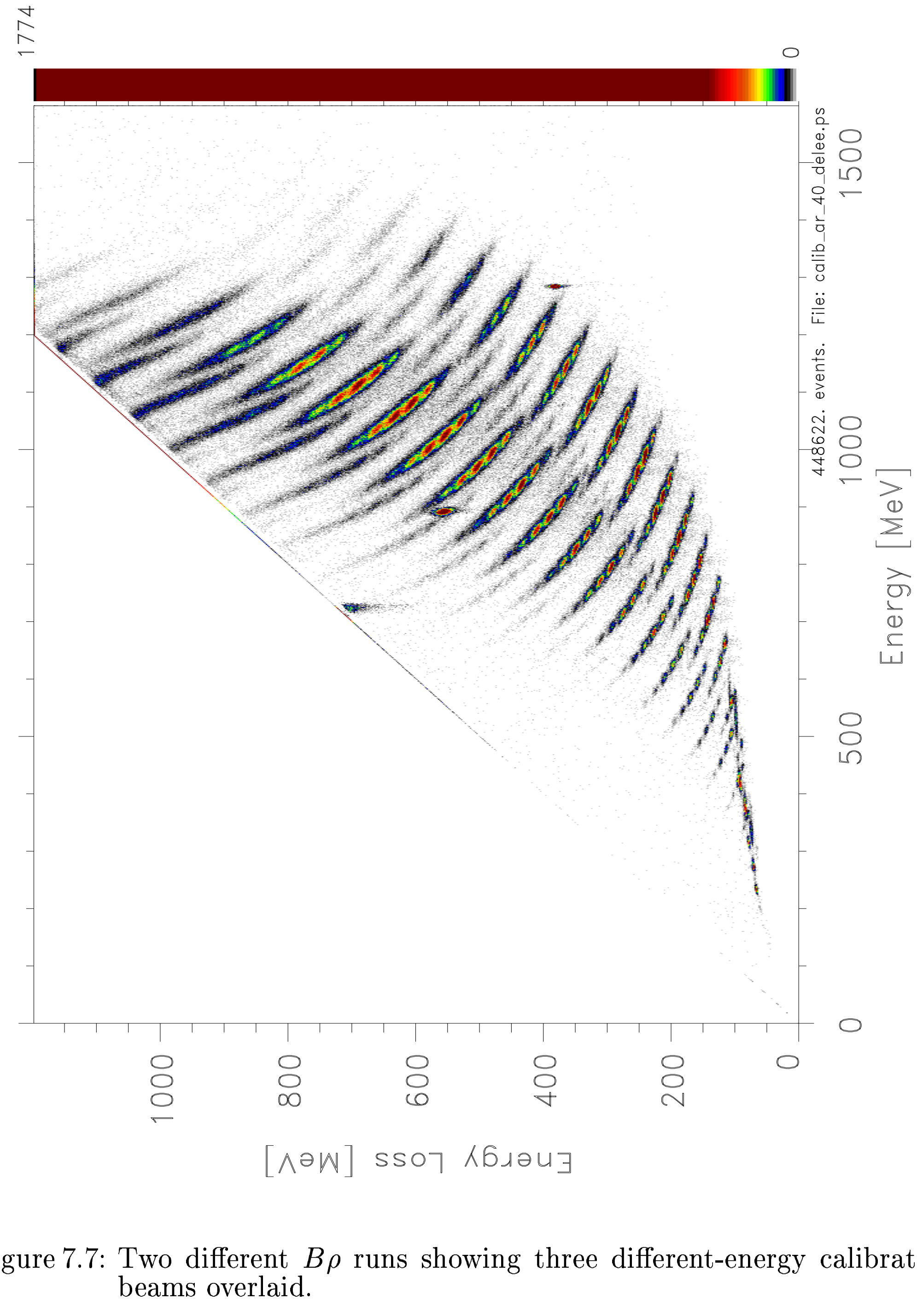

Figure 7.7: Two different $B\rho$ runs showing three different-energy calibration ^{40}Ar beams overlaid.

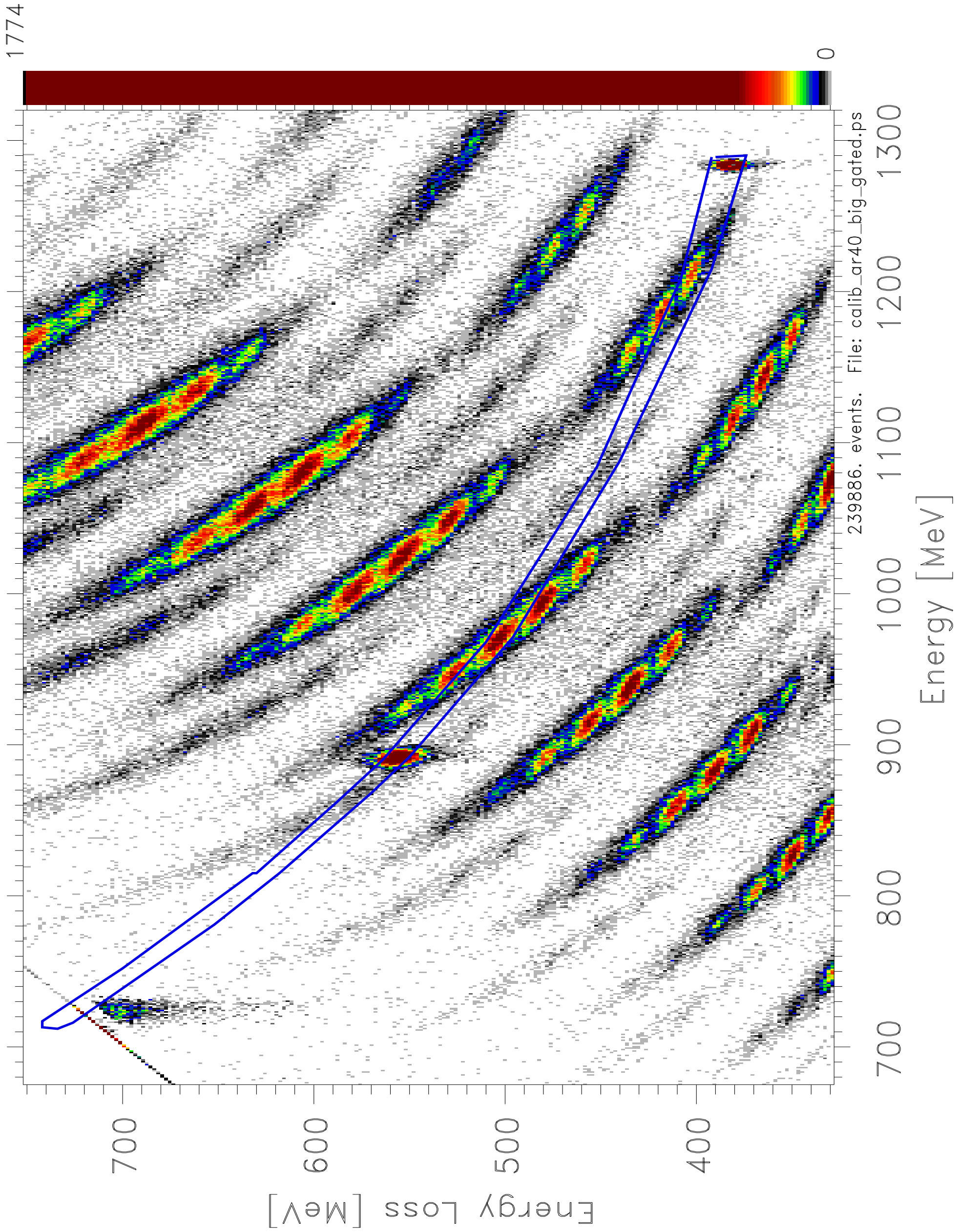

Figure 7.8: Blowup of Fig. 7.7 for ^{40}Ar MZ^2-band region. Two different magnetic-rigidity runs (about 1.36 and 1.76 T-m) are combined here to accomplish full tiling calibration.

type of data. The following describes the process of optimizing isotopic resolution of this data.

7.3.2 Retaining full data set (no gating) in constructing identifiers

Repeated attempts were made to gate on (make cuts on) individual q-states so as to analyze them separately. Drawing such gates is an *extremely subjective* and, thus, unsatisfactory process. There were concerns as to the methodological acceptability of this quite common process of drawing thin hyperbola-shaped gates ('banana' gates) along the central ridges of Bethe-Bloch Z-bands to 'separate' these into 'resolved' bins when viewed as projections into other signals' spectra. This was judged to be an unacceptably subjective process, seriously biasing the determination of relative yields (or cross sections), especially when multiple charge states are involved, as they are in our data.

Further, it was felt that the process of forcing integer charge-state and/or mass assignments, a procedure often followed this field, is indefensible from the viewpoint of current good-practise norms in statistical science. Integerization throws away information as to the uncertainty of the q-state assignments which should be propagated into the subsequent calculations that determine mass-assignments, etc.

It appeared that the problem of characterizing (quantifying) the number of counts of each isotope and properly assigning errors, could be interpreted as belonging to 'multiple-group discriminant analysis' [Flury & Riedwyl 1988] and [Sharma 1996]. There are two principals in accord with the standard practises of modern multi-dimensional data reduction which were consistently applied:

1. If at all possible, one should never 'throw away' (gate out) data, and

2. One should construct an identification scheme in an appropriate higher-dimensional

phase space which includes *all* possible parameters simultaneously, and

3. The 2D standard distance from a given isotope peak's centroid should be used as the measure of the error for assignment of an event as belonging to a particular A, Z group.

This implies that 'bad' data points should be *automatically* displaced by the identifiers to regions well separated from the 'good' data-of-interest. That is to say, one should never a priori, subjectively remove 'bad' data points (i.e., in nuclear science these include double hits, slit-edge scattered events, noise, and especially events residing in the overlap regions between particle groups). Rather, the *test* of the constructed higher-dimensional identifier's worth is not simply the degree to which it appears to resolve different isotopes into separated regions, but, precisely whether it *'automatically'* throws such 'bad' points into regions of the constructed identifier which are well separated from the data-of-interest [Flury & Riedwyl 1988].

Specifically, *a key goal here was to find particle identifiers which would combine signals in such a manner that q would be eliminated (be canceled out) from the calculations.* The (not immediately obvious) constructed space ended up being a fairly simple Z-identifier vs. an A-identifier.

7.3.2.1 Z-identifiers

For the Z-identifier, a number of different schemes found in the literature (e.g., [Cerny 1984] [Goulding 1984] [Leo 1987]) which involve optimizing exponents appearing in some reasonable approximation for the range of an ionized particle were explored. However, it became evident that these identifiers quite generally traded-off (sacrificed) *resolution* of Z groups to the *linearization* of Z. Eventually, it was found that a simple identifier involving the product of the signal sources: $\Delta E \cdot E_{total}$

(displayed against the E_{total} signal) produced Z-bands which were optimally well separated even though they were *spread out* in a *non-linear* fashion. The *key advantage* of forming this identifier is that it grouped the events according to Z alone—*independent of charge state.* There was then no need whatsoever to calculate q, to set gates or to otherwise determine charge states in order to determine an event's Z.

This Z-identifier is simply the well-known, 'MZ^2 identifier' scheme. This Z-identifier could be easily linearized later, with a square-root transformation algorithm if desired, but, even this process seemed to decrease the information content unnecessarily.

7.3.2.2 Isotope-identifiers

For the mass-identifier dimension, it was initially found that calculations of mass produced rather 'blunt' and poorly resolved projections into one-dimensional spectra. See Fig. 7.9 and 7.10, An example of a 2D spectrum of this type displayed against the Z-identifier found in the previous section is shown in Fig. 7.11. There are two groups besides the main group of ions in this figure. The group on the left-hand side and going up along the Z axis, are ToF 'accidentals' which are displaced by precisely one cyclotron-RF cycle from the main group. In subsequent spectra these accidentals had one cycle's time (about 85 ns) added to them, and they thus fell very satisfactorily into alignment with the main group. The smaller group, at low-Z and low-A in this 2D identifier, are light ions which were insufficiently ionizing to trigger the PPAC-anode timing-stop signal, and therefore have *no* time of flight. They are 'TDC time-outs' (TDC: time-to-digital converter, ADC: analog-to-digital converter). These Figures (Figs. 7.10, 7.9, and 7.11) were part of an early attempt to make a mass identifier from $E \cdot (ToF)^2$. The insets in these figures are Fourier transforms of the mass-identifier spectra (with the zeroth-order not shown). This transform was

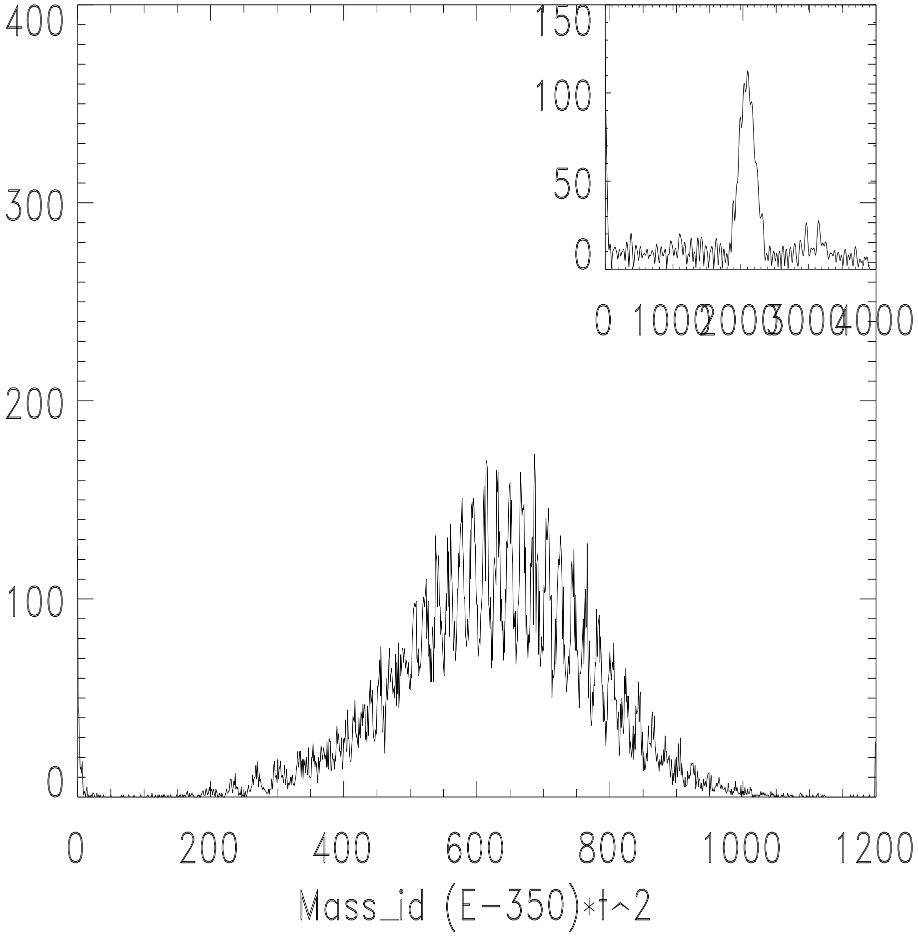

Figure 7.9: Projection of A-identifier and its Fourier transform used to objectively assess effect of parameter on resolution (here set to 350).

found to be useful to *objectively* characterize and compare the resolutions produced by various different identifier schemes.

The reader will also notice that Fig. 7.9 has 350 subtracted from 'E,' and that Fig. 7.10 has 300 subtracted. Note the difference in their appearance. This shows the sensitivity of the mass resolution to changes in the energy-offset calibration. When this and other attempted A-identifiers, were plotted (on the X-axis) against the Z-identifier, it appeared that the masses fell on slightly parabolic bands. In

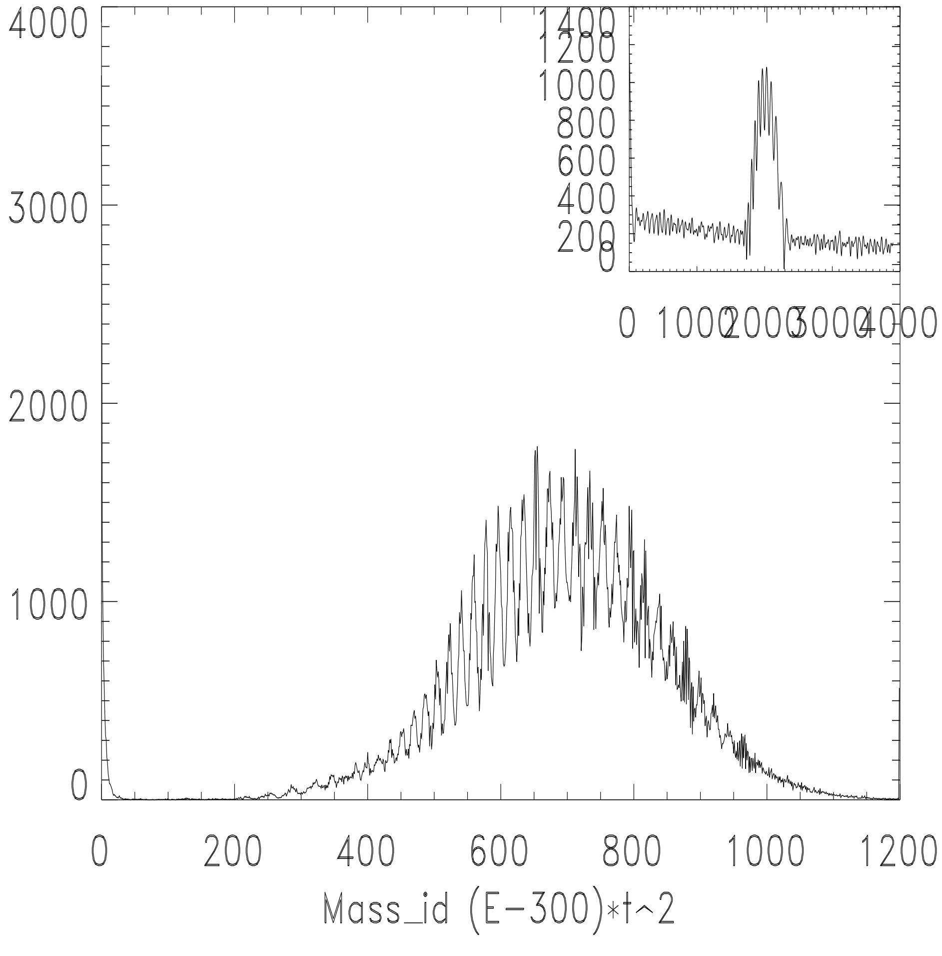

Figure 7.10: Projection of A-identifier and its Fourier transform used to objectively assess effect of parameter on resolution (here set to 300).

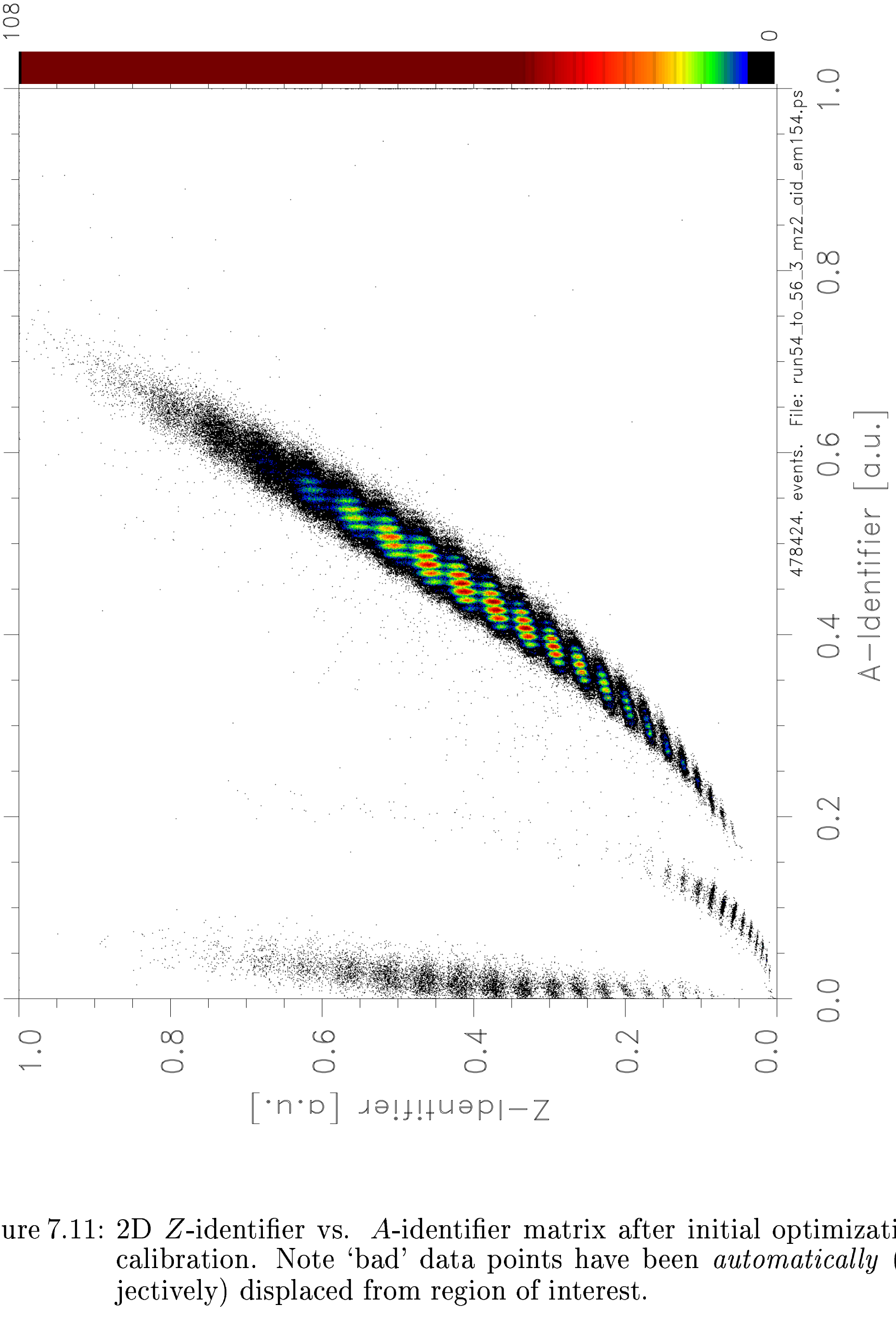

Figure 7.11: 2D Z-identifier vs. A-identifier matrix after initial optimization of E calibration. Note 'bad' data points have been *automatically* (i.e., objectively) displaced from region of interest.

other words, the projection onto the A-identifier axis was poorly resolved. It became evident (was deduced) that this distortion was the result of inaccuracies in the energy and time of flight calibrations.

7.3.3 Treating systematic, correlated energy and ToF errors in cyclotron-analog calibration beams.

We should digress a bit to explain how these energy-calibration errors are introduced. The top of Figs. 7.12 and 7.13 are ΔE vs. E plots of two sets of analog calibration beams from the K1200 cyclotron from the two sets of experiments which were conducted three months apart. These calibration beams were permitted to pass through the solenoid at $\theta_{lab} = 0^\circ$ without a magnetic field being present[14]. Below this, is a projection of gates set on these beams which select the highest-energy portion representing that part having undergone the least scattering and anomalous (Landau) straggling, and thus most suitable to establish energy calibrations. The top portions of Figs. 7.14 and Fig. 7.15 then show straight-line best fits to the channel numbers of these beams for the two sets of experiments, plotted against their expected energies. The bottom halves of these plots are the fits' residuals. These plots of the fit residuals reveal the *systematic* problem with the calibration beams. Fig. 7.16 shows a blowup of the calibration beams from the April, 1993 set. The small bumps at either side of the very large primary peak for each beam indicates that the highest populated peak is one of 2-3 in each case, and, not necessarily the maximum (expected) energy group.

---

[14] See chapter: "The Systematics of 2D Particle-ID Spectra with Magnetic Selection," explaining the process of using calibrations beams, which were too diffuse to be elastically scattered and thus could not be subjected to magnetic selection as a means to calibrate the spectrometer and detectors. These 'cocktail' beams therefore had to be taken through the spectrometer at zero degrees. This meant that the target, the annular entrance aperture with its thick center stop and the shadow bar inside the bore of the spectrometer had to be moved aside every time a calibration beam was needed. This, of course, was a rather time consuming process involving the cooperation of several experimenters, and, more importantly, can easily leave any of these elements mis-aligned when they are reinserted.

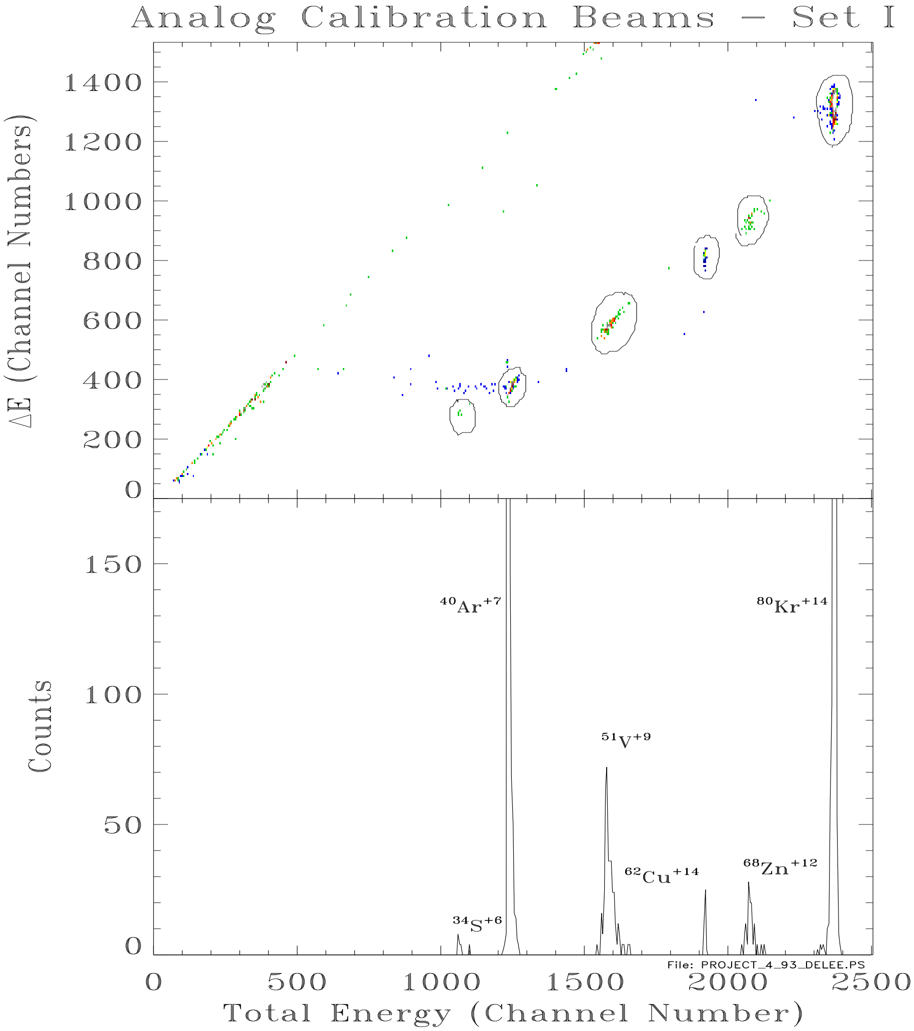

Figure 7.12: Top: ΔE vs. E plot of analog calibration beams experiment conducted April, 1993. Bottom: Projections of calibration beams with scattered beam gated out.

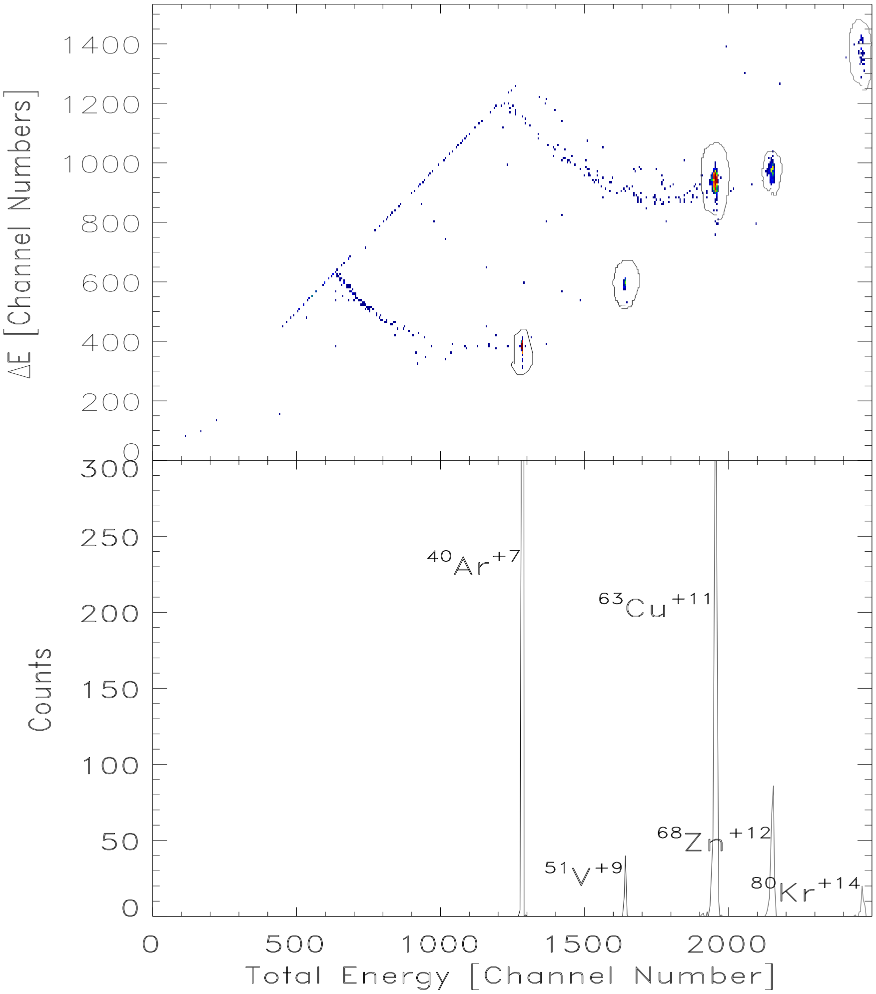

Figure 7.13: Top: ΔE vs. E plot of analog calibration beams experiment conducted July, 1993. Bottom: Projections of calibration beams with scattered beam gated out.

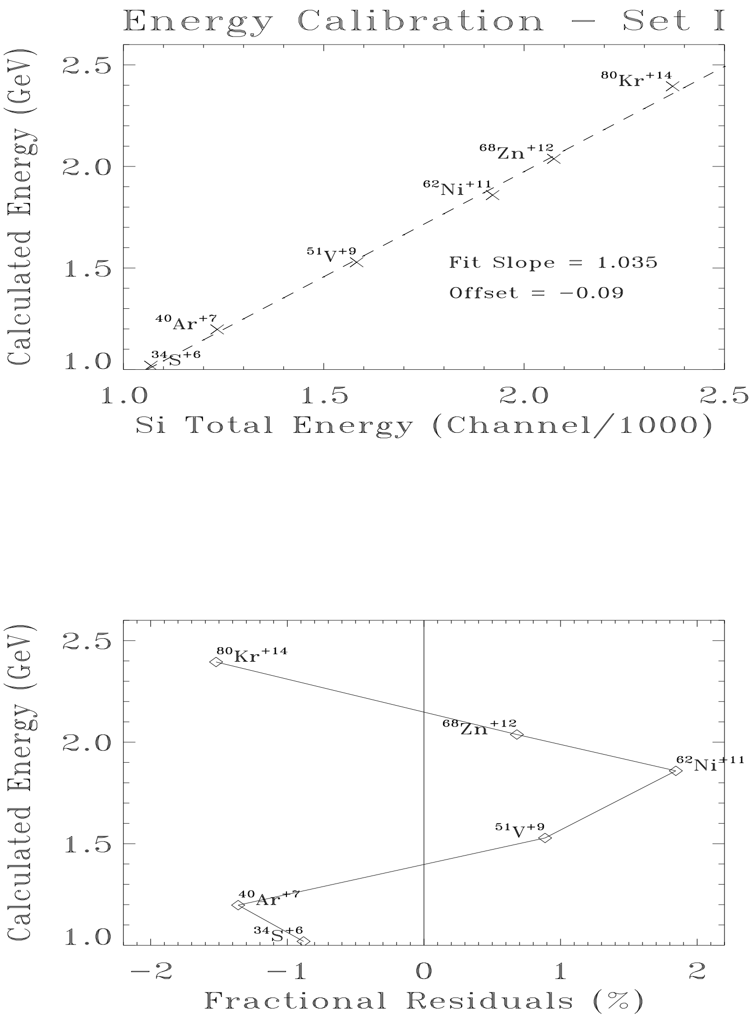

File: E_CALIB_FITS_4_93.PS

Figure 7.14: Top: Straight-line best fits of analog calibration beams' channel numbers against their calculated optimal-radii (turn) extraction energies. April, 1993 against their expected energies. Bottom: Fractional fit residuals. Systematics indicate problem with determining energy calibrations. See text.

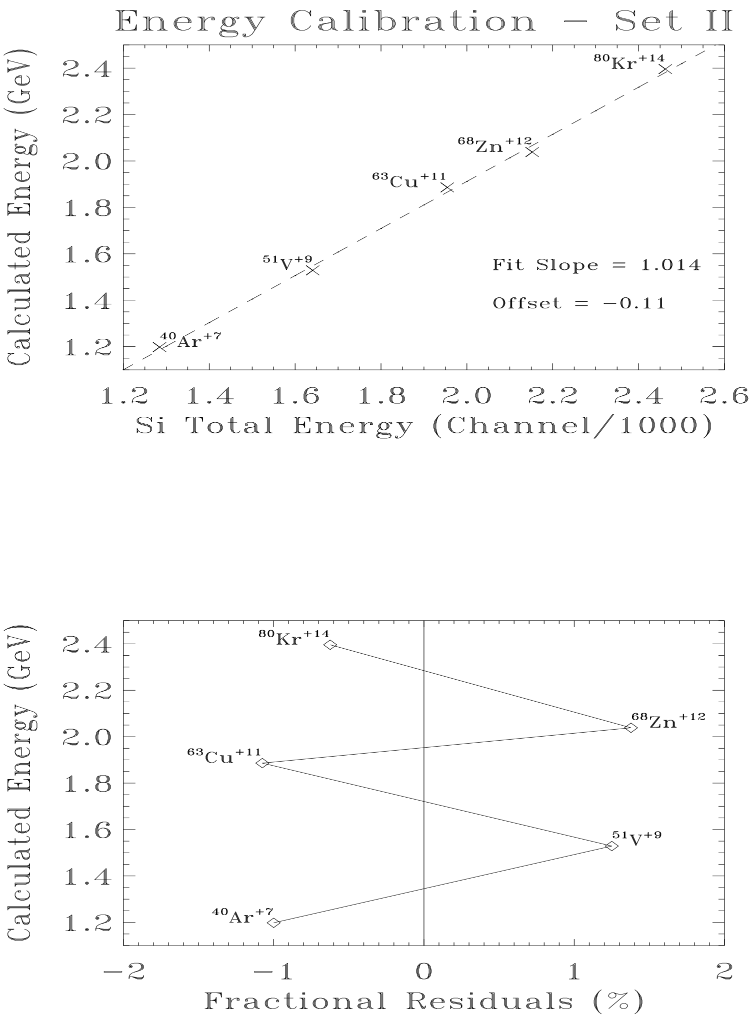

File: E_CALIB_FITS_7_93.PS

Figure 7.15: Top: Straight-line best fits of analog calibration beams' channel numbers against their calculated optimal-radii (turn) extraction energies. July, 1993 against their expected energies. Bottom: Fractional fit residuals. Systematics indicate problem with determining energy calibrations. See text.

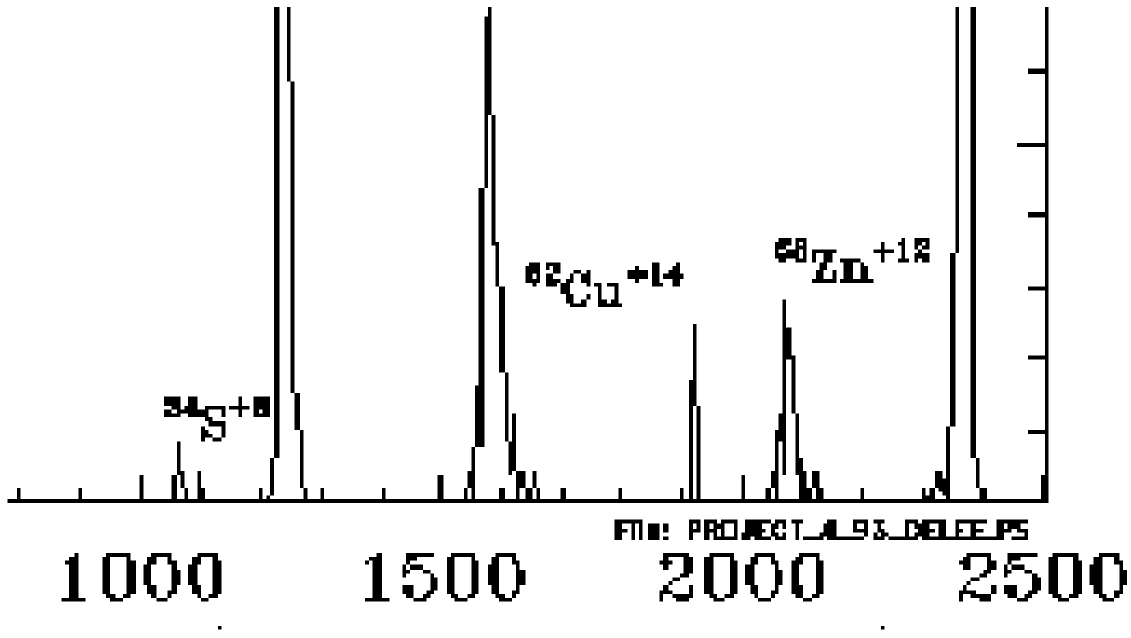

Figure 7.16: Blowup of Fig. 7.14 showing the main peak of each analog calibration beam is not necessarily the only (the expected) group for each isotope. Small, but fairly distinct ‘bumps’ are shown to the right or left of some peaks. April 1993 data shown.

That is to say, here the zinc (Zn) and vanadium (V) beams were produced from the cyclotron and its ion source *simultaneously*: as q/A (charge-to-mass) analogs of one another. They were collected as a single 'cocktail beam,' as were the argon (Ar) and krypton (Kr) beams, while the Ni beam was collected separately – i.e., not as a 'cocktail' (Note: the Ni is labeled as 'Cu' in of the projection of the gated calibration beams of Fig. 7.14). Shown in the bottom half of that figure we can see that, to the right of both the Zn and V beams, there is a small clump of data points just removed from each of the large main peaks, while, to the left of the Kr beam, there is also a similar small clump of data points.[15] Fig. 7.16 is a blowup of this region. From this and similar projections, it was concluded that the Ar/Kr cocktail pair was apparently a primary-turn-extracted cocktail beam, while the Zn/V set and the Ni beam were not primary-turn extracted cyclotron beams. (I.E., they were likely to have been extracted at some other *radii*, as an ion's energy is actually a function of its *radii* in the cyclotron, independent of the number of turns per se.) This explains why the energy-fit residuals of the Ar/Kr pair are systematically low, and the other sets have residuals which are systematically high. As a demonstration that this is not a fluke occurrence, examine Fig. 7.13 which contains similar calibration beams – only now Cu replaces Ni as a non-cocktail beam – which were collected during the Set II of our experiments, conducted three months later than Set I shown in the previous figures. A similar systematic shifting of cocktail sets is seen in the Set II experiment data.

The magnitude of the systematic error is significant. Judging from the fit residuals, the errors in the energy fits are between +1.5% of the Ar beam's kinetic energy of

---

[15] The ^{40}Ar calibration beam has a substantial amount of (slit-edge?) scattered beam to its left in the upper, 2D spectra in Fig. 7.14 – so we leave its projection out of this assessment as its interpretation is problematic.

1.2 GeV (i.e., +8 MeV) and -1.9% of the Ni beam's kinetic energy of about 1.85 GeV (i.e., about -10 MeV). From the residuals' pattern it can be deduced that this error effects only the *offset* of the linear fit, and that *within* each cocktail-isotope group, the slope of the fit is very nearly the same. The conclusion reached is that the slope of the fit, m_E (MeV/channel), is known sufficiently well, and that the parameter yet to be determined is the offset, b_E (MeV).

Similarly, in the timing spectra, we have accidentals from a number of beam bursts, which gives us the slope of the calibration, m_{ToF} (ns/channel) to high accuracy (as we know the cyclotron frequency to high precision). However, we need to determine the offset (time zero) for this calibration.[16] To accomplish this we need to know the exact (absolute) energy of the calibration beams and to use these in order to calculate the relativistically correct time of flight for each of these calibration beams. (Fig. 7.17 shows the ToF vs. E relationship for the flight-path length of the BigSol Spectrometer device (6.4 m)). To first order it can be assumed that the energy of the ions increases proportional to the number of orbits they have executed inside the cyclotron. Ions execute about 800 turns (orbits) and gain roughly constant energy per orbit. Their energies are a function of, not the number or turns *per se*, but their radii in the cyclotron. There is then an uncertainty as to their energies if it is not conclusively verified they are being extracted at the expected radius.

The calculations of the expected energies of the analog calibration beams for their last/single turn extraction *also* has, of course, a certain degree of uncertainty (per-

---

[16] A standard technique to determine the 'time zero' of the TDC spectra is to run two equal-length BNC (coaxial) cables to the preamplifier inputs of both the timing-start (Si ΔE_1 and the timing-stop (PPAC anode) detectors, and then wye these two cables into a pulse generator. This is intended to simulate an 'infinitely fast' particle passing through the ToF system and calibrate the TDC spectra's time zero. This was done in the present experiments during the initial setup. However, various settings and cabling were changed in the course of the experiment. In addition, this method does not take into consideration the characteristics of the detectors' responses. In any case this calibration proved inadequate.

haps 1%). If one looks at the energy-calibration's fractional-residuals in Figs. 7.14 and 7.15 (the X-axis shows percent-fractional-residuals, labeled % for the linear energy calibration fits), the distance between the extreme values translates into a spread of about 3.5%.[17]

In general, the precision of the calibration of the *absolute* energy and ToF is not as important an issue for the *qualitative* tiling calibrations (particle-ID calibrations) it *was shown to be very relevant* for obtaining the optimal particle-group resolution. The errors in determining the absolute energies of the analog calibration beams lead to an inaccuracy in calibrating the ToF offset and together these both distort the appearance of the isotope-ID ellipsoids in the 2D Z-identification vs. A-identification matrix.

As we have explained above, there is an accurate, independent method of determining the slope of the ToF spectra calibration, so the problem with determining the energies of the calibration beams modulo perhaps six-to-seven different extraction turns (radii), effects only the *offsets* of both the time and energy calibrations, which cannot be independently determined. These offsets are thus directly correlated.

Taking b_E (i.e., the offset of the E calibration) as a parameter, a program was written which calculated how the E and ToF calibrations would change as a function of this parameter. These E and ToF calibrations were then the input into a program which calculated the relativistically correct calibration of the A-identifier based on these E and ToF results and on the flight-path distance (d) of the analog calibration

---

[17] Other sources of error are present. Aside from the uncertainty in the calculations of the expected energies of the analog calibration beams for their last/single turn (optimal radius) extraction, so too, in passing through the initial PPAC detector, each calibration beam looses a certain amount of energy (perhaps a few tens of MeV), and this also introduces further uncertainty. Although, since, for example, a ^{40}Ar analog beam is used to calibrate where a ^{40}Ar reaction product appears in the spectra, this loss will be the same for both a calibration and reaction-product ion.

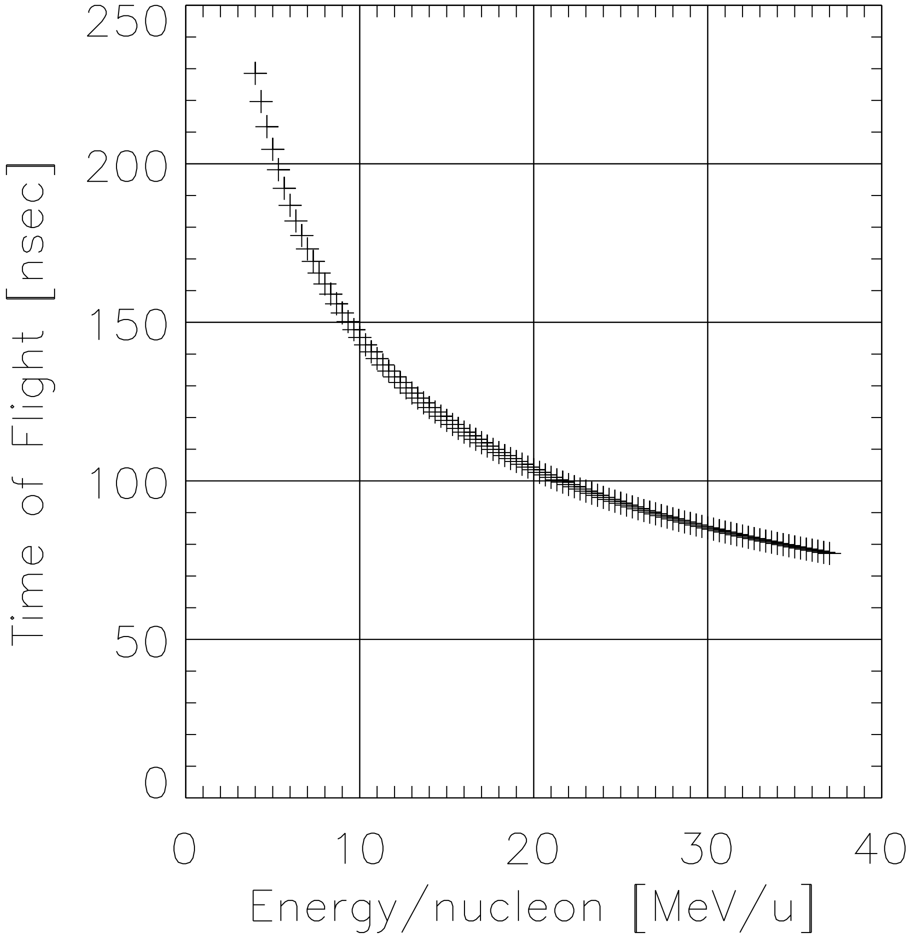

Figure 7.17: *ToF* through BigSol Isotope Spectrometer as a function of ion's E/A. Flight path is about 6.4 m.

ions through the solenoid.[18] This mass calculation consisted of

$$A = \frac{c^2}{m_0 E}(1+\gamma) \tag{7.1}$$

$$\begin{aligned} \text{where :} & \\ \gamma &= \frac{1}{\sqrt{1-\beta^2}} \\ \beta &= \frac{v}{c} \\ &= \left(\frac{d}{c \cdot ToF}\right). \end{aligned} \tag{7.2}$$

This programs was then run recursively over a range of b_E where

$$E = m_E \cdot E_{channel} + b_E \tag{7.3}$$

and

$$\gamma_i = \left(\frac{E_i}{A_i m_0 c^2} - 1\right) \tag{7.4}$$

where i in E_i and A_i refer to the different energies and masses of the analog calibration beams. From these γ_i's, a set of corresponding ToF_i's were calculated according to the relationship between γ and ToF shown in Eq. 7.2 above. Then, these new ToF_i values were used to determine the corresponding ToF signal calibration by fitting

$$ToF_i = m_{ToF} \cdot ToF_{channel} + b_{ToF}. \tag{7.5}$$

As the single b_E parameter was varied ('twiddled'), the 1D projections of the resulting A-identifier for each iteration were examined for its effect on the mass resolution. The trend can be seen in Fig. 7.18 which shows a series of results of this optimization process, and in Fig. 7.19 which shows a further refinement of the optimization process for the same identifier.

---

[18] The distance traveled was kept constant for all ions as ion-orbit ray tracing simulations showed that this should vary by only about 1 part in 10^4 for the orbits of adjacent-mass ion groups.

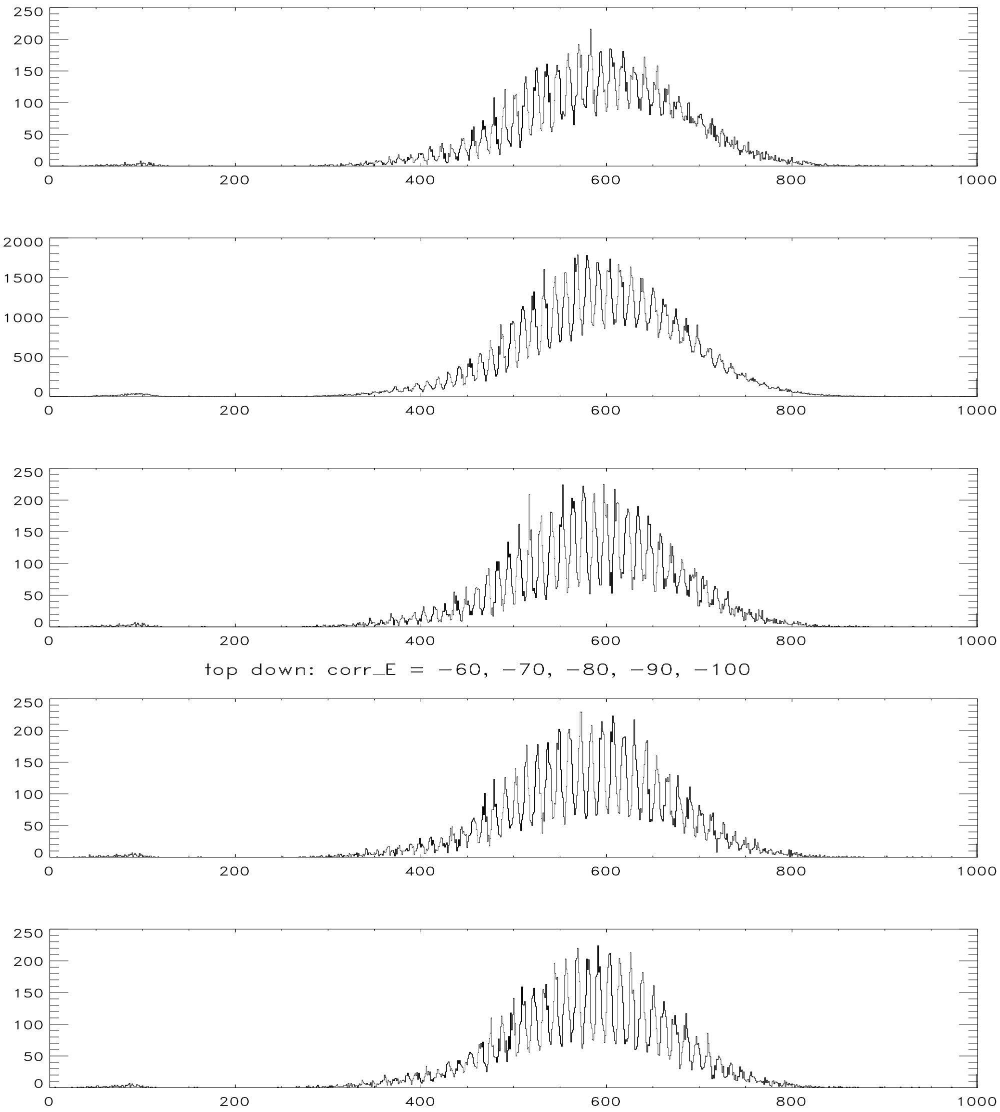

Figure 7.18: Effect on resolution of a *classical* calculation of A-identifier for small iterative changes in E-ToF calibration parameter. The values (top to bottom) tried here are: -60, -70, -80, -90, -100. See text.

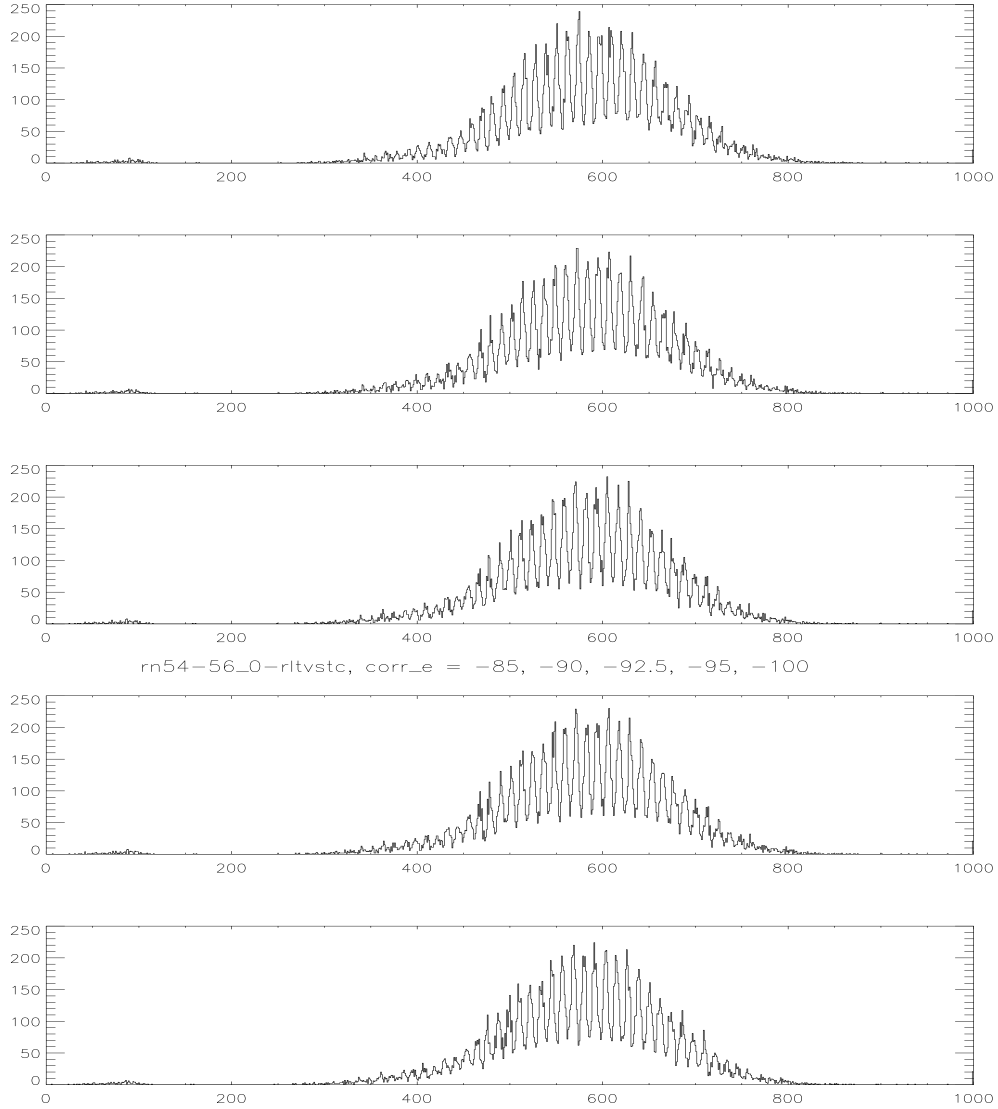

Figure 7.19: Effect on resolution of a *relativistic* calculation of A-identifier for small iterative changes in E-ToF calibration parameter. The values (top to bottom) tried here are: -85, -90, -92.5, -95, -100. See text.

The optimal mass-resolution setting for b_E turned out to be about -92.5 MeV.[19]

If we now look at the scale on which Fig. 7.15 is plotted, *this optimal correction would mean that the offset of the fitted line in the top figure would be shifted upwards by about 7.5 MeV, which strongly favors the Ar/Kr cocktail beam as having been in fact extracted at the optimal, final turn (radius) from the cyclotron.* The V/Zn pair then falls well below the fitted line, indicating that they are in fact lower in energy than what their calculated energy[20] should be if they would have been extracted at the final turn. This means that the V/Zn analog calibration pair were extracted *before* reaching their final-turn (radius).

This is how the mass resolution shown in [O'Donnell 1999], for the lower-$B\rho$ data which had usable ToF information, was achieved.

The particle-ID results of this parametric optimization are presented with in the final chapter, "Results and Conclusions." Histograms of neutron-rich yields, tables, and further discussion of the results are also presented there.

7.4 Summary

The resultant appearance of the Z-identifier vs. A-identifier is quite satisfactory, when one considers that it is derived from *all* the information contained in Figs. Fig. 7.5 and Fig. 7.6, with absolutely no restrictive gating having been used. In spite

---

[19] Which exceeded the apparently allowed limits. This presented a bit of a conundrum until it was eventually discovered that 103 channels had been added to each total energy channel in the original acquisition code(!) for technical reasons to do with displaying 'raw' summed 2D spectra in XSYS. If this gratuitous offset is corrected for, then -92.5 lies within the allowed correction range (this 'allowed' range is, of course, somewhat uncertain itself, as a number of factors contribute to it, as we discussed above.)

[20] To calculate the the expected single/last-extraction energies of these beams as delivered from the K1200 cyclotron, a program available to the cyclotron operator was used. This program has been adjusted over many years and takes into account relativistic effects and the alteration in mass of nuclei depending on their electronic binding energies consistent with their ionic charge-states. This later mass correction must not be ignored. Nevertheless, it should be assumed that the results are accurate to only about ±1% in energy. This later mass correction must not be ignored. These results were then scaled, in order to calculate the energies one would expect from each ion if it were to be extracted at its expected cyclotron orbit (radius).

of any particular isotope being present in up to several charge states in those 2D spectra, its charge states fall satisfactorily into the *same* mass bin. We believe this result is significant.

In addition, the data points lacking proper values for any one of the signals (such as those light, fast isotopes which failed to trigger the PPAC and therefore are TDC 'time-outs') are automatically (i.e., read: *objectively*) thrown far away from the area of interest on the final identifier. This is a fundamental criteria in statistical science for judging whether the identifier is suitable. [Flury & Riedwyl 1988][21]

Ideally the data would then also be de-convolved using the solenoid acceptance calculations of the chapter "Solenoid Ion Optics and Magnetic Dispersion." However, one must remain mindful that those acceptance calculations remain un-calibrated. These experiments were to a large degree *developmental/feasibility-test runs* for a novel solenoidal isotope spectrometer. The acceptance calculations are also extremely sensitive to beam-alignment assumptions.[22]

7.5 Signal source issues

7.5.1 General comments on ToF and timing resolution

The time-of-flight (ToF) system had a good-event start trigger at the focal plane of the solenoid consisting of a thin ΔE detector (the first detector in the stack), while a delayed PPAC (anode) signal was used as the ToF stop. Also, we were able to use an all-silicon detector stack at the focal plane, as opposed to plastic+Si, or similar,

---

[21] Further analysis steps on this data include 2D multiple-group discriminate analysis identification procedure as discussed above, to extract yields, plus errors in terms of 2D standard distances. Ideally this is the procedure which should be performed rather than to make 1D Z-band-gated projections as was done in the NIM paper binning [O'Donnell 1999]. However, such projections are frequently practised in experiments performed in nuclear physics to determine the counts of (n- or p-rich) nuclei. This practise *does not assign errors* explicitly to statements that this or that isotope has been 'made.' We feel such statements should be accompanied by *quantified* confidence levels.

[22] It is important to note that, unfortunately, we do not have elastic scattering data (e.g., C on C) for the solenoid with which to calibrate my acceptance simulations to the actual solenoid device. Therefore, we report 'yields' as opposed to cross sections. In addition, any future experiments of this type must accomplish entrance-detector (PPAC) position calibrations.

which was, of course, advantageous for obtaining good energy resolution.

It has been said 600 ps is a reasonable number for our optimal timing resolution, but this statement should be qualified. It is an estimate made from the cyclotron-analog calibration beams sent down the axis of the solenoid. (They are generally too tenuous to scatter elastically and so are not $B\rho$ selected by the solenoid). One then puts thin gates in energy on these beams and observes how they spread in the time spectra. This is, however, inaccurate theoretically as a determination of timing resolution. In addition, it is not known how much of the energy (time) spread observed in the calibration beams' signals is due to the beams' spread, and how much is due to intrinsic resolution of energy (time) by the detectors. Complicating matters further is the uncertainty as to the beams' multiple-turn extraction characteristics (which turn are we getting?). Their energies are also spread in going through the first detector (the PPAC), etc.

These issues not only make it difficult to say exactly what the detectors' resolutions are, but, more importantly, they contribute to significant, systematic inaccuracies in calibrations of absolute energy – which in turn cause a correlated inaccuracy in the time of flight calibrations. This proved to be important for particle-group resolution, as described in the preceding section. Other means were also pursued to characterize the timing resolution, with mixed results.[23]

---

[23] We also attempted to determine the ToF resolution using alpha particles from a ^{228}Th source while scanning the magnet through $B\rho$, and bringing one line into focus after another. But, the acceptance of the magnet while scanning enters the picture (as opposed to acceptance at constant $B\rho$) and the angular spread of the alpha particles being emitted from the source must be understood (a mask having small holes, again, was not used over the PPAC). The result is that this data is complicated to interpret (unreliable) for determining timing resolution.

7.6 Calibration of ΔE signals

The calibration of the ΔE signal to MeV is accomplished by assuming that any ions on the 'stopping line'[24] in the ΔE vs. E spectra should have deposited precisely equal energies in in both these constructed signal sources. Accordingly, once the total E calibration was accomplished using the analog beams, the ΔE scale was calibrated by fitting events on the stopping line in ΔE to the values they have in the calibrated E spectra. This "self-consistent" calibration was also important for the resultant MZ^2 identifier's appearance.

7.7 The Bethe-Bloch Energy Loss Relation

7.7.1 Si-telescope analysis and dynamic range

As these were largely 'shakedown' runs for using BigSol as an isotope *spectrometer* – a quite different process from using it as an RNB collector – the run plan included taking data at more than one magnetic rigidity. However, small changes in $B\rho$, of as little as three tenths of a T-m, cause relatively large changes in the ranges.[25] As compared to photons (e.g. X-rays) whose energy loss along their range is largely an elimination process described by an exponential fall off of the photon beam's intensity with distance traveled, the energy loss of energetic ions is characterized by the Bethe-Bloch equation, often also referred to as the *stopping power* equation or, yet more directly, as an energetic ion's '$\frac{dE}{dx}$.' This equation[26], not electrons. In the

---

[24] The 'stopping' line appears at $\Delta E = E$ for ions with insufficient energy to penetrate the ΔE detector(s) and so they have no $E_{residual}$ signals. The 'punch-through' region of a ΔE vs. E spectrum is where ions which are very penetrating have passed through the entire detector stack without being stopped, and therefore the signal they produce in the $E_{residual}$ detector is actually a ΔE signal. The 'stopping line' can be seen in all the simulations presented in the chapter, "The Systematics of 2D Particle-ID Spectra with Magnetic Selection."

[25] In nuclear physics, by the "range" of an energetic ion in a detector (e.g. in Si, Ge, gas, etc.) or other material (e.g. in air, aluminum, or, in radiation biology in skin, muscle, bone, etc.) is meant the distance traveled by an ion, neutron, electron, photon, etc. in the material before coming to rest.

[26] This exposition follows closely that of [Leo 1987, p. 24]. The expression for the energy loss of a charged particle passing through a material was first performed classically by Niels Bohr.

latter case modifications are necessary due to the light mass of electrons. is central to any experiment in nuclear physics, as well as any in elementary particle, and, frequently, to solid state physics experiments as well. In full, it has the form

$$-\frac{dE}{dx} = 2\pi N_a r_e^2 m_e c^2 \rho \frac{Z}{A}\frac{Z^2}{\beta^2}\left[\ln\left(\frac{2m_e\gamma^2\nu^2 W_{max}}{I^2}\right) - \beta^2\right]. \tag{7.6}$$

where

$$2\pi N_a r_e^2 m_e c^2 = 0.1535\mathrm{MeVcm}^2/\mathrm{g} \tag{7.7}$$

r_e: classical electron radius= $2.817X10^{-13}$

m_e: electron mass

N_a: Avogadro's number = $6.022\mathrm{X}10^{23}$ mol^{-1}

I: mean excitation potential

Z: atomic number of *absorbing* material

A: atomic weight of *absorbing* material

ρ: density of absorbing material

Z: atomic number of incident particle

β: ν/c of the incident particle

γ: $1/\sqrt{1-\beta^2}$

W_{max}: maximum energy transfer in a single collision

Here W_{max} is the greatest possible energy transfer which can take place in an ion-electron collision: a *knock-on* collision. From the kinematics of such a collision for an ion having mass M we have

$$W_{max} = \frac{2m_e c^2\eta^2}{1 + 2s\sqrt{1+\eta^2} + s^2}, \tag{7.8}$$

An outline of this derivation is given in [Jackson 1975, Chapt 13.]. Later Bethe, [Livingston & Bethe 1937], Bloch and others performed the quantum-mechanically correct derivation. This is the formula presented here. Further corrections for the *density effect* of the medium, and an electron *shell* closing correction for the medium are often added. Note that we give the the version of the Bethe-Bloch equation for {ions where $s = m_e/M$ and $\eta = \beta\gamma$. Equation 7.6 can be written in a somewhat more transparent form [Goulding 1984, pp. 228-229] as

$$-\frac{dE}{dx} = 4\pi n(e^4/m_e)(q_{eff}/v^2)\,ln\left[\frac{2m_e v^2}{I(1-\beta^2)} - \beta^2 - S - D\right]. \tag{7.9}$$

n:	number of electrons/cm^3 in in the absorber
e:	charge of an electron
q$_{eff}$:	effective, rms charge of the ion in units of e
v:	the ion's velocity
S:	correction for different ionization potential of shells
D:	density correction factor

If one assumes that the ions are moving ‘sufficiently’ fast (i.e., the ionization potential reaches a maximum when the velocity of the ion matches the Bohr velocity of the outermost electron in its ‘orbital’ motion), they will be completely stripped and $q_{eff} = Z$, the atomic number of the ion. If we also neglect the shell and density corrections, the form of the Bethe-Bloch equation is simplified from Equation 7.9 to:

$$-\frac{dE}{dx} = k_0 Z^2(c^2/v^2)\,ln\left[\frac{k_1 v^2}{c^2 - v^2}\right] \tag{7.10}$$

with k_0 and k_1 constants. If the energetic ion is non-relativistic, we can write $v^2 = 2E/M$, and the logarithmic term will relatively slowly as a function of E leading, finally [Goulding 1984, p. 29], to the very well-know approximation to the Bethe-Bloch equation[27]

$$\frac{dE}{dx} \propto MZ^2 \tag{7.11}$$

---

[27] However, these approximations are not strictly necessary to produce the MZ^2 result. This can be seen by expanding the logarithmic term in Equation 7.6 in a Taylor series in powers of γ by first making a change of variable $(1-X)$ =(the argument of the logarithm). If one then expands γ in terms of β, and proceedes to at least four terms in the expansion keeping, in each case, the terms linear in β ...the result, when this is re-substituted into Eqn. eq:bethe-bloch, is indeed $\propto MZ^2$.

Clearly, then, a 2D scatter plot of all events' energy losses through, for example, one or a number of initial Si detectors, plotted against the total energy which the ion deposits in all detectors as it is brought completely to rest, should produce a spectra of parabolic bands for each MZ^2-valued ion. Quite reliable programs and published volumes with tabulated stopping powers for different materials and species of energetic ions are available for the Bethe-Bloch formula. In particular, the compilations of by Ziegler, and especially the programs "TRIM" and "SRIM" [Ziegler & Biersack 1996] are widely used to calculate the stopping powers and ranges of ions in detectors, targets and other materials.

One of the consequences of this model is that, while energy is transferred essentially continuously along an ion's path to the electrons of the material, a large portion of the ions' energies are ultimately deposited in a short interval just before the ion comes to rest. This sharp rise in energy loss at the end of an ion's range is called the Bragg peak. The practical consequence of this behavior here is that the quite thick, stopping Si detectors at the back of the Si telescope stack will receive a large pulse of energy owing both to their thickness and to the Bragg peak energy deposition occurring there. This can easily cause non-linearities along an ion's path through the Si semiconductors resulting from local saturation effects when the ion's energy deposition exceeds the material's locally available electron-hole pair creation potential (the so-called "pulse-height defect" characteristic of heavy ions). Saturation effects can also occur from overloading the detectors' electronics, especially the Si detectors' preamplifiers. It was to correct such preamp saturation that specially constructed low-gain preamplifiers were used in these experiments on the Si PSD energy signal and the final, thick stopping Si detector. of the reaction products within the Si detectors. That is to say, "big" in that the ratio of the magnitudes of the multiple-ΔE-to-$E_{residual}$ signals changed by perhaps $20 - 40\%$ for a given isotope as the $B\rho$ setting of the spectrometer was changed over a range of only $3 - 4$ tenths of a Tesla-meter. This effect was found to be quite significant in that this is an amount sufficient to shift the optimal multiple-detector combination for constructing the ΔE signal. In fact it was found that the optimal multiple detector combination for constructing the ΔE signal in these experiments can be different even for the higher-Z vs. lower-Z ions within the *same* run.[28] The general rule followed in these experiments – with considerable success – was based on an article by [Goulding 1984] and the statistical consequences of the central limit theorem [Leo 1987]. That is, to obtain the maximum information (optimal resolution) one should strive to have signals of equal magnitude from the (multiple) ΔE detector(s) on the one hand, and from the $E_{residual}$ detector(s) on the other. In fact, without relatively thick Si ΔE there was no hope of resolution. It should be noted that this approach differs from much of the extant practise in the heavy-ion field where quite thin ΔE detectors are often used as this insures a highly linear response. However, the crucial issue is optimal *separation* (resolution) of isotope groups, and linearization of well-resolved though non-linear Bethe-Bloch identifiers can be easily attained in software with 2D spectra "warping" algorithms which are now widely available.

---

[28] A resolution of this difficulty would require that several thin, pre-calibrated ΔE detectors should be available during a run which could be easily slid into or removed from the Si telescope. This would be done as is needed to optimize the ratio of the ΔE to $\mathrm{E}_{residual}$ signals as the penetrability of the reaction products varies with the $B\rho$ setting of the device.

CHAPTER VIII

The Systematics of 2D Particle-ID Spectra with Magnetic Selection

8.1 Overview

Of utmost importance in the production and study of exotic isotopes is establishing positive isotopic identification. One must be able to establish the (A, Z) of every isotope produced. This is not a simple matter.[1]

We show this process in two steps.

1. We explain the systematics of a typical ΔE vs. E spectra under the constraint of magnetic selection and give the formulas describing these systematics. In particular we will show the structures which emerge with the progressive narrowing of the fractional-$B\rho$ bite. These structures will be shown to represent:
   (a) Bethe-Bloch Z-band hyperbolae;
   (b) q-states within each Z-band;
   (c) An identical series of isotopic masses repeated within each q-state of a given Z-band.

---

[1] In this thesis, more time was expended on this problem and, in particular, on eliminating charge-state ambiguities, than any others.

2. A step-by-step outline of the process of establishing isotopic identifications for a particular experimental data set will be discussed.

It should be noted that there is an analogous procedure which was followed to interpret ΔE vs. ToF spectra. This will not be traced out in detail, but example spectra showing the results are given. These types of spectra are also discussed in [Bazin 1990] for fully stripped ions.

8.2 Relations due to magnetic selection

We are concerned in this dissertation with 2D ΔE vs. E spectra where there are multiple charge (q) states and the spectra is subjected to a restrictive magnetic selection, $\Delta(B\rho)/B\rho$.

Figs. 8.1 and 8.2 are simulations of ΔE vs. E while Figs. 8.4 and 8.5 are ΔE vs. ToF simulations under precisely uniform conditions. The calculation of Bethe-Bloch ΔE values are performed using a simple MZ^2/E approximation to the full equation, as here *resolution* is our primary interest, and this depends only on differences in ΔE, not absolute values.[2] The simulation also takes the ΔE detectors to be sufficiently thick such that approximately equal energy depositions occur in the ΔE detectors and the $E_{residual}$ detectors. This situation should produce the optimal particle resolution as a consequence of the central limit theorem. [Leo 1987] [Goulding 1985] In all the simulations which follow, the same constant cross section as a function of energy (a flat excitation function) has been input into the calculations. In addition, the ΔE, E and ToF detector simulations have each been convolved with Gaussian response functions having widths which are representative of the fractional resolutions of the actual detectors used in these experiments. These resolutions have been

---

[2] A full discussion of the Bethe-Bloch equation and approximations to it for the energy loss of ions in detectors is given in Section 7.7.

described in the chapter on data reduction, above.

8.2.1 ΔE vs. E: $\Delta(B\rho)/B\rho \approx 100\%$

The upper left plot in Fig. 8.1 shows a ΔE vs$E$ simulation with no magnetic selection performed (i.e. $\Delta(B\rho)/B\rho = 100.0\%$). There is no resolution whatsoever of Z, q or A apparent in this plot although it contains simulated Bethe-Bloch Z hyperbolae for $16 \leq Z \leq 19$. Each Z hyperbola has two q states,[3] the charge-state distribution between which has been calculated using the formulas of [Baron 1990] and, within each q-state, the *same* six isotopes are present having values

$$A = 2Z + n \qquad n = (0, 1, ..., 5). \tag{8.1}$$

8.2.2 Magnetic selection relationships for particle-ID spectra

The set of relations we need are as follows:

- For energy loss in a detector (approximation to the full Bethe-Bloch equation)

  $$\Delta E \quad = \quad k\frac{MZ^2}{E}, \tag{8.2}$$

  (where k is proportional to the detector thickness).

- The magnetic selection criteria

  $$B\rho \quad = \quad \frac{p}{q} \tag{8.3}$$

  or, as a function of the kinetic energy

  $$B\rho \quad = \quad \frac{\sqrt{2AE}}{q}. \tag{8.4}$$

---

[3] Actually, the simulation was performed for up to four charge states. However, only the first two are significantly populated at these kinetic energies. Hence, throughout we refer to "the two charge states" in the spectra.

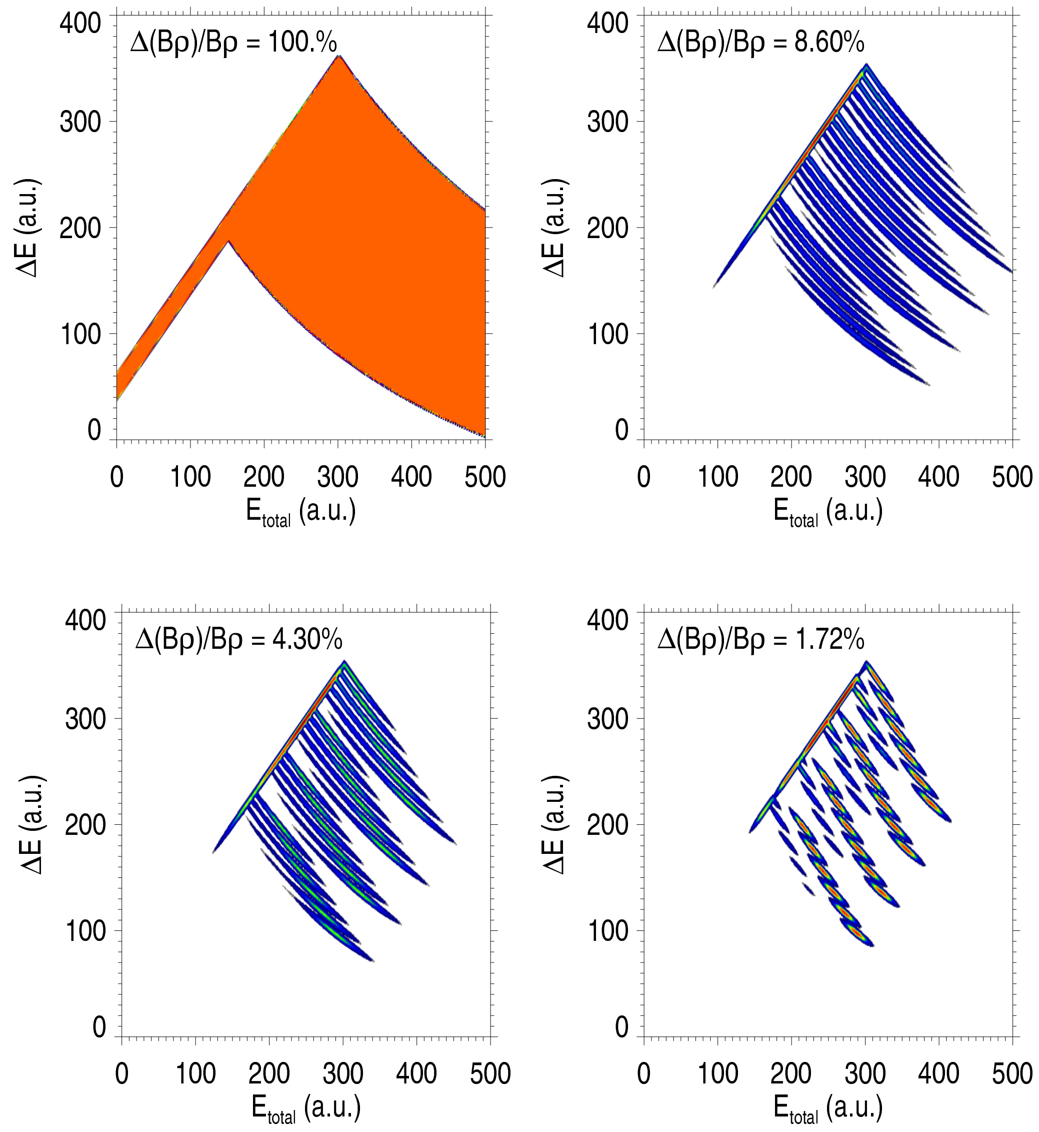

Figure 8.1: Simulated ΔE vs. E spectra with detector thicknesses and energies similar to present experiments. The effect of progressively more restrictive $B\rho$ selection is illustrated as indicated in each plot. Bottom right plot shows resolution of six isotopes in two charge states for each of four Z bands. Isotopes range from $A = 2Z$ to $A = 2Z + 5$ for elements $16 \leq Z \leq 19$.

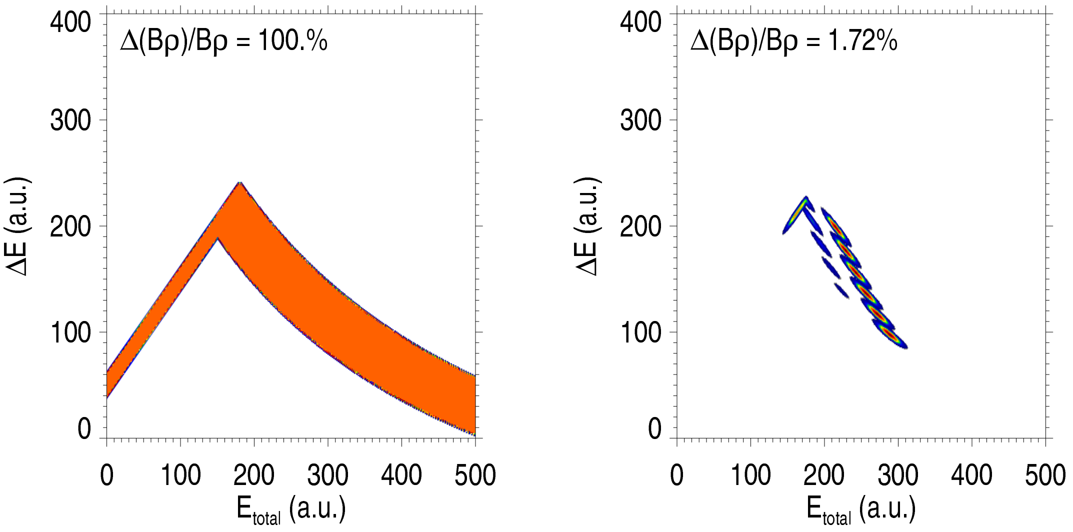

Figure 8.2: Like Fig. 8.1 but showing portion representing a single-Z hyperbola: $Z = 16$, having two q-states: $q = Z$ and $q = Z - 1$. Six isotopes are shown in each q-state: $A = 2Z$ to $A = 2Z + 5$. Note what portions of left-side plot (no magnetic selection) are lost in going to the right-hand plot (narrow magnetic selection) in order to achieve particle-ID resolution.

- Rearranging for E

$$E = \frac{(B\rho)^2 q^2}{2A}. \tag{8.5}$$

Eqn. 8.3 we may also be written

$$\begin{aligned} B\rho &= \frac{p}{q} \\ &= \left(\frac{d}{ToF}\right)\frac{A}{q}, \end{aligned} \tag{8.6}$$

- Hence, for time of flight (ToF)

$$ToF \propto \frac{A}{q}. \tag{8.7}$$

- Finally, for spectra subject to a constraint of magnetic selection, we substitute Eqn. 8.5 for E into Eqn. 8.2

$$\begin{aligned} \Delta E &= k\frac{2}{(B\rho)^2}\left(\frac{AZ}{q}\right)^2 \\ &\propto \left(\frac{AZ}{q}\right)^2 \end{aligned} \tag{8.8}$$

  where we have let $M \to A$ for consistency.

There are two implications of these relations in which we have an immediate interest. To begin with, Eqn. 8.2 tells us that there should be a family of Z hyperbolae parameterized by M (curves of constant MZ^2) on our plot, and this behavior can be seen in the upper-left plot in Fig. 8.1. However, the hyperbolae overlap,[4] so much so that there is no hope of resolving individual Z's, q's or A's in this spectra as it now appears.

Let us look at this issue in more detail. Eqns. 8.5 and 8.8 tell us how E and ΔE change as a function of Z, A and q. In both these equations, E and ΔE are

---

[4] See Chapter III on non-uniqueness of MZ^2 identifiers.

proportional to $[\mathcal{F}(Z, A, q)]^2$. In both cases the proportionality constant is $2/(B\rho)^2$, or its inverse. Physically, if a continuum of $B\rho$ values are allowed, then an ion with a particular (Z, A, q) will be found at a continuum of E and ΔE values—i.e., all along its Bethe-Bloch hyperbola. This is indeed what we see in the upper-left plot of Fig. 8.1.

However, if we had some way to independently restrict the range of $B\rho$ values which appear in the spectra, then any particular (Z, A, q)-valued ion could only appear within a restricted range of E and ΔE values. The size of this restricted range would be in proportion (or inversly proportional) to the range of allowed $(B\rho)^2$ values. Further, if the range of $B\rho$ values is made 'small enough,' then the range of E and ΔE values over which any isotope can appear may be so small that no two isotopes' ranges will overlap. If the value of $\Delta(B\rho)/B\rho$ can be made *this* small, then all isotopes will be 'resolved'—we would be able to reliably identify every isotope.

One major utility of a magnetic spectrometer is that it is precisely such a device capable of restricting the ions which reach its focal plane according to their $B\rho$ values. The details of how this is accomplished by a single dipole or quadrupole magnet, or by a highly complex, multiple-magnetic-element 'doubly achromatic' magnetic-ion-analysis device such as the 1200[5] device at the NSCL—or by a single solenoid like BigSol[6]—will vary. In addition, all magnetic spectrometers may not be able to operate at the same magnetic rigidities and not be able to accomplish equally fine control over $\Delta(B\rho)/B\rho$, etc. *But*, the effect of a given $\Delta(B\rho)/B\rho$ selection, if it

---

[5] The A1200 is being upgraded to an 'A1900' analysis system to match the new, coupled cyclotron upgrade currently underway a the NSCL. This upgrade involves coupling the K500 cyclotron to (inject into) the K1200 superconducting cyclotron, achieving higher charge state heavy ions which are accelerated to higher energies. Much higher beam intensities and many new exotic beams will also be available.

[6] For a detailed analysis, see the chapter "Solenoid Ion Optics and Magnetic Dispersion" in this dissertation.

can be accomplished, would be the same, independent of the spectrometer which imposed the selection on the spectra.

The question, then, is 'How small is small enough?' How small must $\Delta(B\rho)/B\rho$ be made in order to resolve *our* simulated data?[7] Before answering this question, there is one more important systematic relationship predicted by the above equations:

Note that Eqn. 8.8 has a term $(Z/q)^2$. This means that, for a given isobaric multiplet (i.e., for constant A, across Z's), all of the isotopes which are completely stripped of electrons (i.e. whose q is equal to their Z) will have $Z/q = 1$. Hence this term can then be ignored in Eqn. 8.8. This means that ions with the same A and which are fully ionized will appear at the same, constant value of ΔE independent of Z. *All fully stripped ions of the same atomic mass, A, should fall on the same horizontal line under magnetic selection.* (See [Volkov 1985].)

8.2.3 ΔE vs. E: $\Delta(B\rho)/B\rho$ small

Now we return to seek an answer to our question: 'How small is small enough?' We will answer this question empirically, by simply subjecting our simulated spectra to successively more restrictive magnetic selections and observing the results.

Consider once more Fig. 8.1. Proceeding from left-to-right across the top of this figure, and then from left-to-right across the bottom of the figure, these plots show the effects of subjecting the identical set of data to the following progressively more restrictive constraints:

$$\Delta(B\rho)/B\rho \;=\; 100\%,\ 8.6\%,\ 4.3\% \text{ and } 1.72\%.$$

The reader will notice that as the $B\rho$ 'bite' becomes more restrictive in Fig. 8.1, fewer of the total data points (events) appear in the spectra. But, progressively

---

[7] Which is very close in its characteristics to our actual experimental data.

more *structure* emerges in what remains.

8.3 Identifying the Z, q, A structures in magnetically selected 2D spectra

To see what the various structures represent in these plots, consider first Fig. 8.2. The left-hand plot here shows only one Z-hyperbola, the $Z = 16$ band, before any magnetic selection is imposed on the data, out of the four Z-hyperbolae, $Z = 16-19$, shown in the upper-left-hand plot of Fig. 8.1. This demonstrates what portion of each plot in Fig. 8.1 corresponds to a single-Z Bethe-Bloch hyperbola. The right-hand-side plot in Fig. 8.2 is the same, single $Z = 16$ band as is shown in the plot to its left, *after* it has been subjected to the magnetic selection: $\Delta(B\rho)/B\rho = 1.72\%$.

Now, let us assume that we know, somehow[8], that, in Fig. 8.2, the diagonally descending band to the right-hand side, whose end is located near to energy channel 300, is the $q = Z$, fully stripped charge state. The less-intense, diagonally descending band just to its left must then be the $q = Z-1$ charge state of $Z = 16$ (the $q = Z-1$ charge state is not as fully populated as is the fully stripped one at this energy).

That the q-band on the left-hand side of a given Z band must be the lower q state, is required by Eqn. 8.5. The reason can be seen as follows: Hold A, Z and $B\rho$ constant, then the *lower* q-state appears at a *lower* total energy. In a similar vein, from Eqn. 8.8 we see that as one goes from $q = Z$ to $q = Z - 1$ at constant Z and $B\rho$, to keep A constant requires this A to be found at *higher* ΔE than it was found to be in the fully-stripped q state.

Now let us focus on the fine-structure *within* each q-band. Within both the fully stripped and the $q = Z + 1$, $Z = 16$ band, there are small ellipses evident. These

---

[8] In practise this information has to be obtained from calibration beams which are analogs of the cyclotron's primary A/q tune. This process is discussed below.

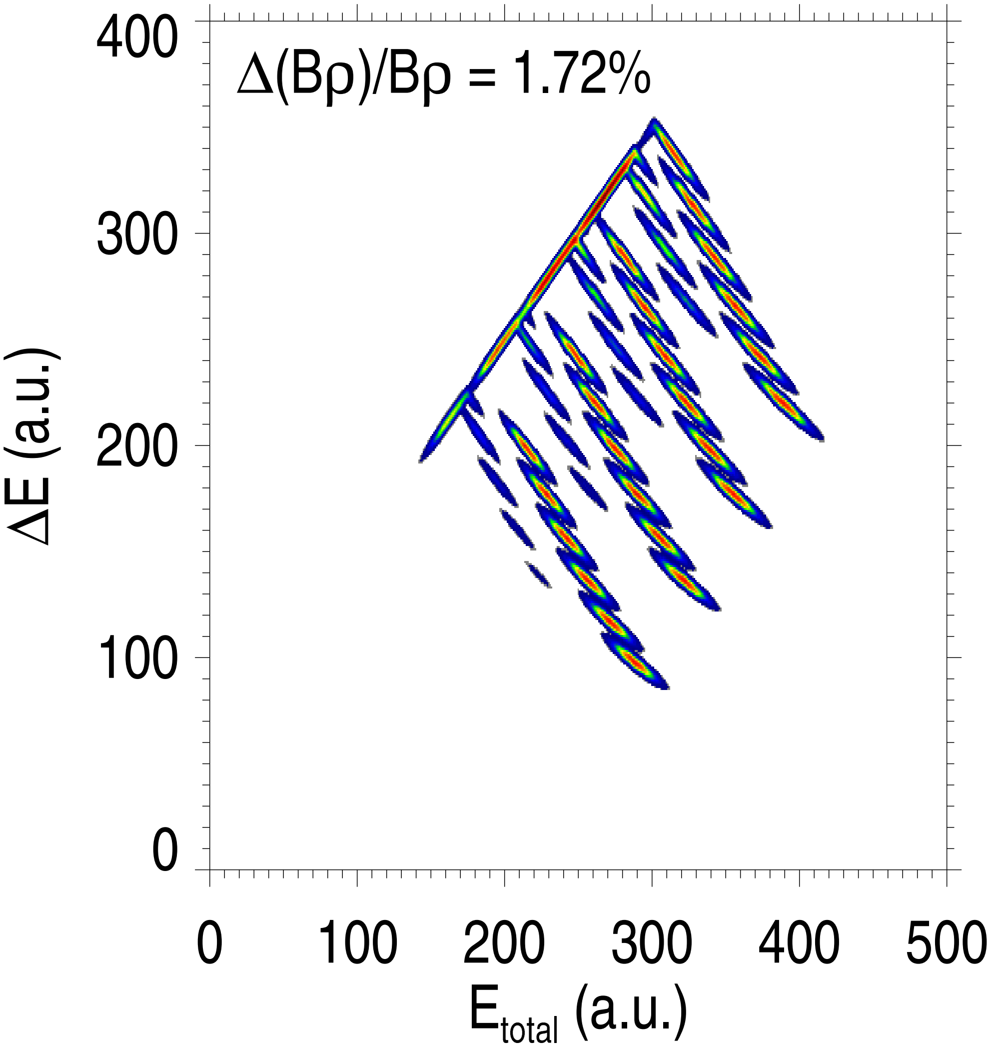

Figure 8.3: Blowup of lower-right plot in Fig. 8.1, showing isotopic resolution in ΔE vs. E for $\Delta(B\rho)/B\rho = 1.7\%$, $(16 \leq Z \leq 19)$, $(Z \leq q \leq Z-1)$ and $(2Z \leq A \leq 2Z+5)$. See text for an explanation of particle-ID systematics.

oval-shaped structures correspond to the separate isotopes of element $Z = 16$. From Eqns. 8.8 and 8.5 it is apparent that at $q = Z =$ constant, the heavier (more n-rich) isotopes go in steps towards *lower* energy and *higher* ΔE.

Fig. 8.3 is an enlarged version of the bottom-right-hand plot in Fig. 8.1. By comparison with the right-hand plot in Fig. 8.2, the reader should now be able to identify which portion of each Z band in the large Fig. 8.3 represents fully-stripped isotopes, and which portion of each represents the $q = Z - 1$ portion. In particular, locate the ($Z = 19$, $q = Z$) band in Fig. 8.3. Now, say we have somehow ascertained that the isotope farthest right on this band is the $A = 2Z + 0 = 38$ isotope of potassium (i.e.: ${}^{38}_{19}\mathrm{K}^{+19}$). Recall that we said above that all A's in fully stripped q-states should fall on perfectly horizontal lines in ΔE under magnetic selection. If such a horizontal line is drawn across the plot from right-to-left, starting at the ${}^{38}_{19}\mathrm{K}^{+19}$'s peak, this line will intersect, in order: ${}^{38}_{19}\mathrm{K}^{+19}$, ${}^{38}_{18}\mathrm{Ar}^{+18}$, ${}^{38}_{17}\mathrm{Cl}^{+17}$, and, as expected, ${}^{38}_{16}\mathrm{S}^{+16}$ does not appear in our simulation as the simulation was performed over a mass range from $2Z$ to $2Z + 5$, which, for sulfur, includes only $32 \leq A \leq 37$.

So too, (referring still to Fig. 8.3) one can determine isotopic identifications for events on the not-fully-stripped ($q = Z - 1$) bands of each element using Eqn. 8.8—but here the $(Z/q)^2$ term does not cancel out. Now one must use the squares of rational fractions for the successive values of this term as one goes across the spectra. The constant-A events are no longer on a horizontal line, etc.

In short, the lesson here is: Once a SINGLE ISOTOPE can be positively identified, ALL ISOTOPES can be identified ... *if* one understands the systematics and *if* a sufficiently small fractional $B\rho$ selection can be imposed by the spectrometer.[9]

---

[9] Of course, if the underlying *detector* resolution is too poor, the fractional $B\rho$ restriction will not achieve particle resolution. The fractional detector resolutions *must* be *better* than the fractional $B\rho$ resolution imposed on the spectra. The fractional detector resolutions are independent of the spectrometer's fractional $B\rho$ setting. Consequently, one combines these in quadrature to find the

8.4 Extensions of the particle-ID systematics

It should be stated that there are also similar systematics which can be used for the *vertical* alignments of the isotopes on various Z and $q = Z - n$ hyperbolae. We made a table and tried permutations of ion identification assignments until we could *simultaneously* satisfy Eqn. 8.5 AND Eqn. 8.8.

There are other systematics which must also be checked. One requirement is to insure that the odd-even effect due to the pairing term (viz.: as in the Semi-Empirical Mass Model) is satisfied consistent with the isotopes which are identified to be even-A and odd-A. Additionally, in the case of the present experiments, with a very mass-asymmetric reaction (massive beam and light, ^{nat}C target) one expects a significant yield of carbon, especially as there should be 'knock-outs' from the target. If indeed the isotope identified as ^{12}C is one of the most intense (or THE most intense), this is another confirmation of the accuracy of the systematics of the isotopic mass assignments.

In particular, it would be extremely important to verify the absence of isotopes identified as having $A = 8$ and $A = 5$ as an important consistency check. However, in the present experiments, isotopes in this lower portion of the spectra are very penetrating and punched through the silicon detector stack. That is, the dynamic range of the detectors did not permit this check to be accomplished and this made isotope identifications significantly more difficult.

For completeness, we include Figs. 8.4 and 8.5 which are like Figs. 8.1 and 8.2, but show ΔE vs. ToF. These additional figures show the same simulated data subjected to exactly the same magnetic selections as that shown in the previous ΔE vs. E simulations. All simulations shown here were written and visualized in the

---

resulting isotopic resolution.

IDL^{R} language.[10]

8.5 Cyclotron analog ('cocktail') calibration beams

8.5.1 General procedure

To accomplish calibrations of kinetic energy (E), time-of-flight (ToF) and, most importantly, for isotopic (A and Z) calibrations, a method developed by [McMahan 1986] working at the NSCL[11] was adapted to the peculiarities of a solenoidal device.[12] These isotopic calibrations are often called 'tiling' calibrations for reasons which will soon become apparent.

The calibration procedure entailed first tuning the K1200 cyclotron and the beam line to optimize the delivery of the ${}^{136}_{54}\mathrm{Xe}^{+24}$ ($A/q \approx 5.67$) primary beam. The cyclotron RF was then slightly de-tuned to optimize the extraction of each of several isotopes which were both:

1. Nearly exact mass-to-charge (A/q) 'analogs' of the primary Xe beam, and
2. Of utility as calibration beams due to their atomic number (Z) and atomic mass (A) falling in or near to the region of interest for the experiment's reaction products.

In these experiments the NSCL's room-temperature electron cyclotron resonance (ECR) ion source was used.[13] Such analog beams do not necessarily require the

---

[10] Interactive Data Language, Research Systems, Inc. (RSI), 777 29th Street, Suite 302, Boulder, CO, 80303. (303)786-9900.

[11] which is similar to a method used by [Becchetti 1976] to calibrate plastic scintillators.

[12] Our thanks especially to Gordon Woszniak of Lawrence Berkeley Laboratories for suggesting the procedure, to Graham Peasley of the NSCL (currently at Hope College, Michigan) who assisted with the choice of calibration beams to attempt and Nicolo Moretto with the group from Catania, Italy who, together with G.P. gave valuable hands-on assistance to our group in the early morning hours.

[13] There is also a superconducting ECR available at the NSCL. However, for our primary beam and the beam rates we were able to take, the room temperature source was adequate. The assistance of Dallas Cole of the NSCL ECR ion source group is greatly appreciated for obliging our special requests and for being available at odd hours to reload the ^{40}Ar and ^{80}Kr gasses.

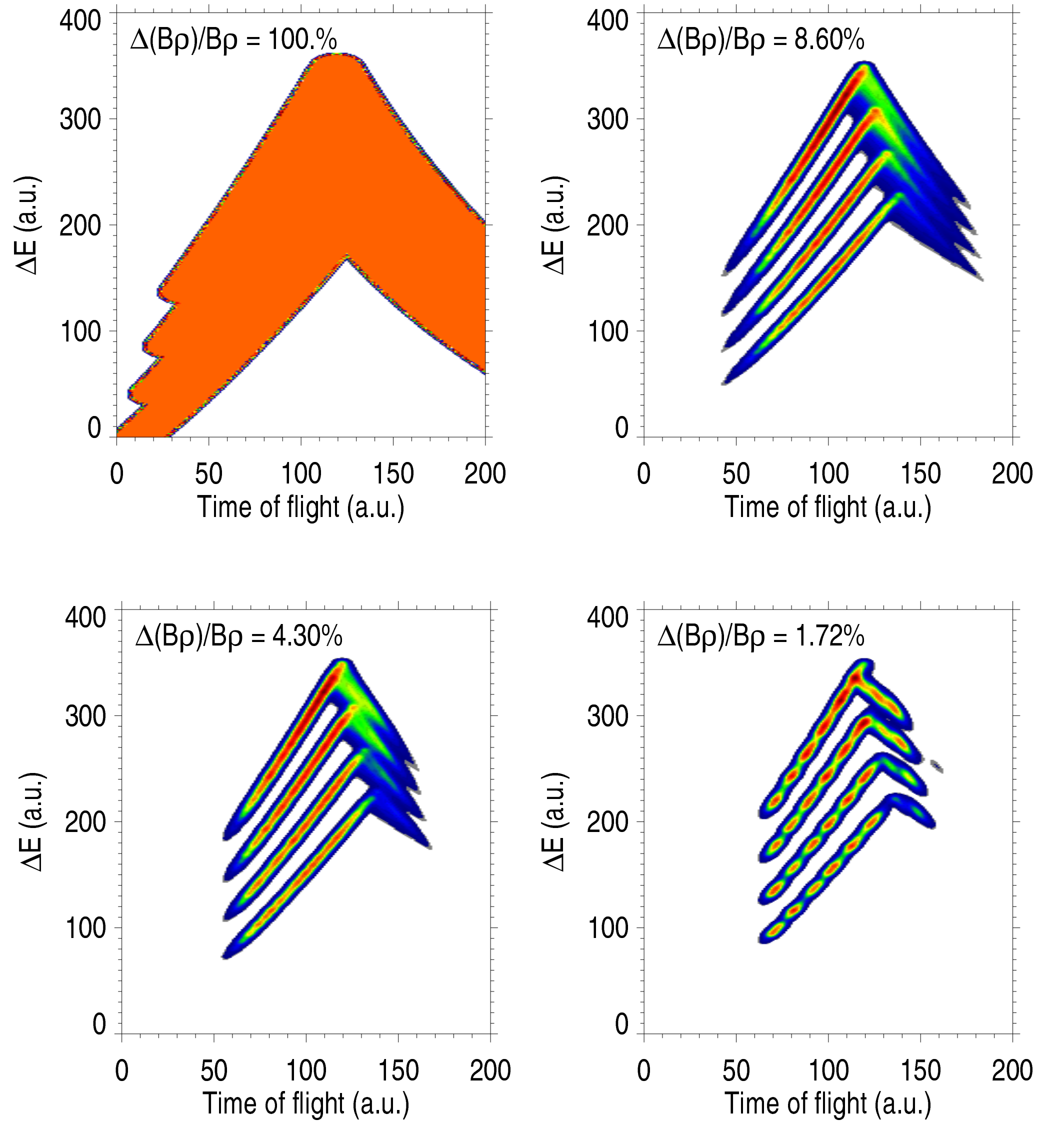

Figure 8.4: Simulated ΔE vs. ToF spectra with detector thicknesses and energies similar to present experiments. The effects of progressively more restrictive $B\rho$ selections are illustrated from one plot to the next. Bottom right plot (see Fig. 8.3 for expanded view) shows resolution of six isotopes in two charge states of each of four Z bands when $\Delta(B\rho)/B\rho$ is finally restricted to about 1.7 T-m. Note, the diagonal bands seen here are *not* bands having data from only one Z (atomic number) group. These bands mix Z. Isotopes shown range from $A = Z$ to $A = 2Z + 5$ for elements $16 \leq Z \leq 19$. Nota Bene: about eight isotopes are present in each band shown here, whereas the simulaton has only six isotopes per atomic number. This partially illustrates the 'charge-state ambiguity' as to mass-identification in such multiple-q-state spectra.

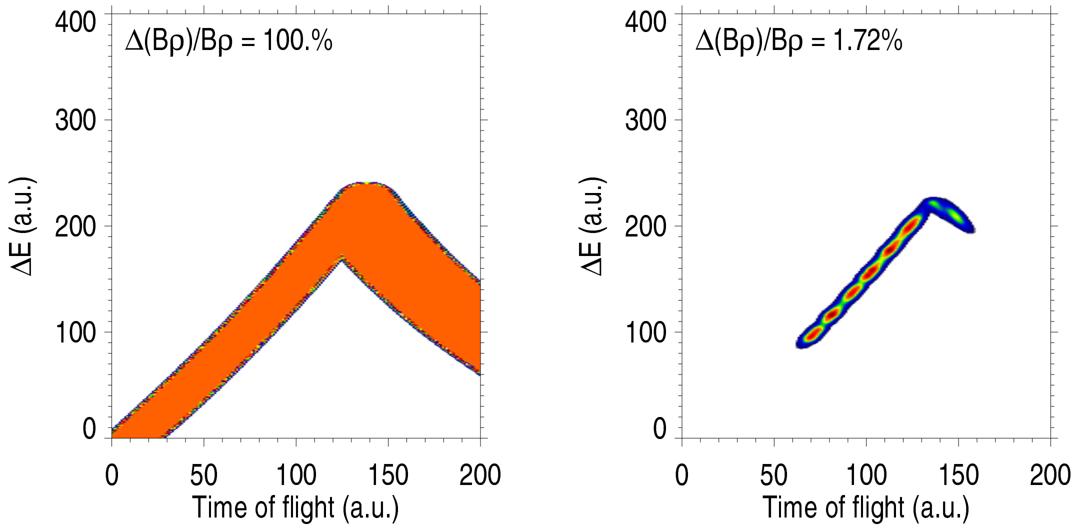

Figure 8.5: Like Fig. 8.4 but showing portion representing a single element: $Z = 16$, having two q-states: $q = Z$ and $q = Z - 1$. Six isotopes are shown in each q-state: $A = 2Z$ to $A = 2Z + 5$. Note what portions of left-side plot (no magnetic selection) are lost in going to the right-hand plot (narrow magnetic selection) in order to achieve particle-ID resolution.

introduction of new material into the cyclotron's ion source. As long as the isotopes happen to be present in its the ECR's construction materials, or were loaded as a primary beam in the recent past, they are generally found to be available as contaminants ('dirt') in the ion source.

To accelerate and deliver the analog calibration beams, the cyclotron must be fine tuned ('tweaked') away from its primary-beam setting to the exact RF dee-frequency at which calculations predict an analog will be found. Once the correct frequency is found, the result will typically be a 'beam' of A/q analog ions delivered to the experimental area at a rate of anywhere from several counts to several thousands-of-counts per second.[14] This is quite adequate for calibration of the silicon detector stack as the efficiency of the Si stack is close to 100% for detection of heavy ions.

Different types of ions are available as calibration beams. An important calibration beam in these experiments was the 'cocktail' mix of two nobel gases which were simultaneously delivered through the cyclotron and beam line: $^{40}_{18}\mathrm{Ar}^{+7}$ and $^{36}_{80}\mathrm{Kr}^{+14}$. Unlike the many metals which are always to be found in in the ion source, these nobel isotopes will rather quickly dissipate from the source and won't normally be found there. However, because the $^{40}_{18}\mathrm{Ar}^{+7}$ and $^{80}_{36}\mathrm{Kr}^{+14}$ analogs could provide a valuable isotopic calibration, a slight amount of each was bled into the ion source by the ECR operator *along with* the primary ^{136}Xe gas charge.

---

[14] We should make clear that the process of finding and tuning in these analog calibration beams is as much an art as a science, and requires close coordination between the cyclotron operators at the NSCL control room and the experimenters watching for tenuous events. To do this in a reasonable amount of time per each calibration beam requires a skilled operator, otherwise it may not be possible to find/tune the required beams at all. The farther one has to go away from the primary tune to find an analog, the less accurate is the calculation of its optimal frequency. In addition, unexpected analog beams are often found, perhaps even quite close to the tune of the analog beam being sought. Care and much cross checking is required to insure one is not fooled by a misidentified, unexpected A/q analog beam. (See chapter: Data Reduction, for a detailed discussion of the methods used to verify the identities of the cyclotron-analog calibration beams.)

8.5.2 Difficulties with analog beams

By using calibration beams which are analogs of the primary beam, the need to retune the cyclotron and the beamline—procedures taking approximately four- and two-hours respectively—is avoided. Precisely because they are analogs of the primary beam, and the cyclotron's magnetic field remains unchanged when they are tuned for extraction, they are delivered at very nearly the same energy per nucleon as is the primary beam (viz.: here 30 MeV/u primary, and 30.0 ± 0.5 MeV/u for the analogs). While this is crucial for saving limited beam time, the kinetic energies of the analog beams present a problem in that the reaction products from the breakup of the primary beam—especially when a thick target is used as here—will be produced at some *fraction* of the energy of the primary. As a result, although these analogs will provide precise absolute kinetic energy and time-of-flight calibrations, they are not immediately appropriate for isotopic-identification ('tiling') calibrations.

Compounding this difficulty is the fact that the calibration beams must be allowed to pass through the solenoid along the axis (i.e. at $\theta_{lab} \approx 0°$) and therefore do *not* undergo magnetic selection. This is because, as they are very low count-rate beams, it is not practical to use them to calibrate the magnetic-rigidity field settings ($B\rho$) of the solenoid. To calibrate the spectrometer's rigidity would require that the beams be elastically scattered away from $\theta \approx 0°$ with a thin target, focused one at a time through the solenoid and onto the silicon detectors at the focal plane. (Recall that a solenoid is *not* a 'zero-degree' device—there is no focusing or magnetic selection of ions passing along its axis *parallel* to the $\vec{B}$ field.)

Therefore, the positions of the calibration beams in the 2D spectra: ΔE vs. E, ΔE vs. ToF, etc., only show the one, particular spot on the Bethe-Block energy-loss hyperbolae where an ion of *that* particular A and Z and of *that* specific energy is located. It does not, however, reveal the *overall* shape of that ion's Bethe-Bloch hyperbola as a function of its kinetic energy. Therefore, from this calibration-beam information alone, it is not possible to accurately identify where that same isotope will be located on the 2D spectra when it is collected at some *other* energy. In addition, it is extremely important to note that under conditions of magnetic selection—an ion's q-state will also become very important in determining where it will appear on the 2D spectra.

We should make it clear that most of these problems are routinely avoided in exotic isotope production experiments at, for example, the A1200 system at the NSCL[15], the LISE system at GANIL[16] and at other state-of-the-art fragment separators. This is because these devices are based on exploiting a different reaction mechanism—projectile fragmentation (see Chapter II) and they are almost *always* operated at sufficient energies to insure that the reaction products of interest are *completely* stripped of electrons. In this case there is no ambiguity as to Z identifications (i.e. $Z = q$ when an ion is fully stripped), and therefore there is no A/q charge-state ambiguity in the mass identifications.

To resolve the difficulty arising from a difference in energy between the calibration beams and the reaction products which needed to be particle-identified, a series of thin targets were introduced during the latter run, in July of 1993, to stepwise degrade the analog beams in energy. This can be quickly accomplished once the analog calibration beam is tuned through the cyclotron, and, although the calibration beams are still transported through the solenoid at $\theta_{lab} \approx 0°$, this procedure maps out a number of points on each analog isotope's 'MZ^2/E' hyperbola. If a sufficient number of these calibration-beam 'spots' are collected in this manner, a smooth hyperbola may

---

[15] National Superconducting Cyclotron Laboratory, E. Lansing, MI.

[16] Grand Accelerateur National D'Ions Lourds, Caen, France

be drawn through them to identify the location of that particular calibration-beam's (that isotope's) MZ^2/E hyperbola. This method can indeed provide a reliable tiling calibration for both atomic number and atomic mass identification—however there are still many pitfalls encountered to correctly establish both the quantitative energy calibrations and the qualitative isotope-ID calibrations of the data. These are elaborated in detail in Chapter VII, "Data Reduction Techniques for a Superconducting Solenoid Isotope Spectrometer."

CHAPTER IX

Results and Conclusions

“One is always a long way from solving a problem until one actually has the answer.” **— Stephen Hawking**[1]

This thesis consisted of a number of projects, all contributing to a common goal of producing and studying exotic, neutron-rich isotopes in the region of $11 \leq Z \leq 30$ in the Table of Isotopes. These can be isolated as separate instrument-development, data-reduction, data-calibration, particle-identification and physics projects. We briefly comment on each.

9.1 Overview

These experiments were conducted in 1993[2] to investigate the feasibility of using a simple, single-element superconducting solenoid as an isotope spectrometer to produce and identify new, very neutron-rich isotopes. A very mass-asymmetric, “fission-like” reaction was planned, with fragments observed at and beyond the classical grazing angle ($\approx 0.7^\circ_{lab}$ in this case)—as opposed to a measurement at zero-

---

[1] *Op Cit*, National Superconducting Cyclotron Laboratory’s weekly “Green Sheet,” 30 July, 1999

[2] A short-flight-path test run was conducted in November, 1992, while the reconfiguration of BigSol into the new isotope spectrometer mode was still underway.

degrees. A solenoid device is particularly well-suited for such an experiment.

The isotopes listed in Table 9.1 are the most neutron-rich which were collected in our 1993 “BigSol Isotope Spectrometer” experiments, at $B\rho = 1.36$ T-m. They include many isotopes which were not previously reported at the time they were collected. (The 15 figures shown below are experimental results showing where these numbers originate.) Some of these isotopes had been previously produced in 1991 in an experiment by a group at the GSI Institute[3], using the FRS fragment separator and these results were reported in [Bernas 1994]. Others were produced in a 1995 GSI experiment reported in [Bernas 1997]. The isotopes observed in 1993 with the BigSol Isotope Spectrometer were finally confidently identified in 1997-1998, and subsequently reported at a conference in May of 1998 [O’Donnell 1999] as part of this thesis work.

The plan for these experiments was to collect the fastest “fission-like” (i.e., non-projectile-fragmentation) products, near to the reaction’s classical grazing angle, and thus, in effect, make a cut on the least-internally excited fragments—those which should be most likely to retain a fortuitously high neutron excess. The major motivation for this investigation was the perception being expressed by several workers in this field that “pure” projectile-fragmentation reactions[4] performed with progressively heavier and faster projectiles—were not proving to be as fruitful as they had previously in producing new, neutron-rich isotopes. For example, note the projectile-fragmentation studies aimed at producing heavier neutron-rich isotopes which were summarized by [Bazin 1991].[5]

---

[3] Gesellschaft für Schwerionenforschung, Darmstadt, Germany

[4] Specifically we mean reactions with projectiles *above* the nuclear Fermi-motion energy, with the fragments selectively observed at $\theta_{lab} = 0°$ *and* at the velocity of the projectile-beam.

[5] This paper’s abstract stated that it: “Discusses the success of projectile fragmentation for the production of light nuclei far from the valley of stability. However, *attempts to extend this method to heavier masses (around 80) do not exhibit the same promising behaviour.* Cross sections of nuclei

Table 9.1. Yields of the most neutron-rich isotopes from 'BigSol Isotope Spectrometer.' (See caption, following page.)

Isotope	*Z*	*N-excess*	*Counts*
^{45}Ar	18	9	3
^{48}K	19	10	2
^{52}Ca	20	12	1
^{55}Sc	21	13	1
^{56}Sc	21	14	3
^{56}Ti	22	13	4
^{57}Ti	22	13	1
^{61}V	23	15	2
^{62}V	23	16	1
^{66}Cr	24	18	1
^{66}Mn	25	16	1
^{67}Mn	25	17	1
^{68}Mn	25	18	1
^{68}Fe	26	16	1
^{69}Fe	26	17	1
^{70}Co	27	17	1
^{71}Co	27	17	2
^{73}Ni	28	17	2
^{76}Ni	28	20	1
^{76}Cu	29	18	1
^{78}Cu	29	20	2
^{80}Cu	29	22	1
^{78}Zn	30	18	2
^{81}Ga	31	19	2
^{81}Ge	32	17	2

Table 9.1: (Page 208)Yields of the most neutron-rich isotopes produced by "BigSol Isotope Spectrometer" with ^{136}Xe on a thick, primary-beam stopping C target at 30 MeV/u. The "Counts" column shows the event count after a 3.3 hour run, with a total integrated beam of $\approx 1.4\text{x}10^{13}$ Xe ions producing $5.8\text{x}10^{6}$ events at the focal plane. A total of $2.8\text{x}10^{5}$ events passed the focal-plane software gate limiting $\Delta B\rho/B\rho$ to about $1.6 - 1.7\%$ at $B\rho = 1.36$ T-m, needed to achieve particle ID. The main limitation which prevented taking the full 4.6 enA (electrical nanoamperes) beam then available at the NSCL was the $\leq$ 50k counting rate limit of the entrance PPAC-anode timing-stop detector. The lack of an axis-crossing blocking bar along the solenoid's axis makes it difficult (but not impossible) to analyze the remaining 90% of the collected focal-plane data. Such an on-axis bar would prevent the double-valued $B\rho$ of ions collected away from the central beam spot on the focal-plane detector. See section: "Future BigSol Improvements."

---

far from stability are very dependent on the excitation energy deposited in the precursor of the projectile-like fragment". ... "the authors report on two experiments performed at the GANIL and SATURNE facilities, aimed at studying the isotopic and velocity distributions of fragments produced in the reactions ^{86}Kr at 44 MeV/u on ^{27}Al, ^{103}Rh and ^{197}Au targets, and ^{84}Kr at 200 MeV/u on a ^{197}Au target. The results are compared to various models and show that in this mass and energy range the simple abrasion-ablation+evaporation picture is no longer valid and cannot account for the observed yields." (Emphasis added - T. O'D.)

The identifications of our 1993 BigSol isotopes only become possible when:

1. Data reduction methods traditionally practised in this subfield of nuclear physics were set aside in favor of developing more statistically defensible, multi-dimensional methods consistent with current, good-practise norms of statistical science.

2. A reliable method was developed of utilizing multiple cyclotron-analog beams (which, for technical reasons, could not be magnetically-selected when using a solenoid) to overlay magnetically selected reaction-product spectra and provide particle IDs.

3. A detailed analysis of the systematics of the absolute energies and flight times of the cyclotron analog beams was carried out to discern the principle extraction-turn orbit (radius) of each and compensate for the resultant systematic errors in the absolute energy and (correlated to this) the time-of-flight (ToF) calibration offsets.

4. It was shown that the intrinsic precision of the absolute energy and time-of-flight calibrations attainable from the analog calibration beams was inferior to the resolution inherently present in the E, ΔE and ToF spectra and that this resolution could be recovered by systematically varying a parametric representation of the discrepancy until the optimal structural regularity appeared in the 2D atomic-number vs. atomic-mass identification matrix.

5. Most importantly, it was demonstrated that it is possible, with sufficient restriction of $\Delta(B\rho)/B\rho$, to totally avoid calculating the ionic charge states of the data. Rather, Z-identification and A-identification derived from combinations of signal sources are possible such that the ionic charge state (q) *drops out*

Element:	*AMU:*		
	BigSol	GSI'94$_{Max}$	GSI'97$_{Max}$
${}_{18}$Ar	45	-	-
${}_{19}$K	48	-	-
${}_{20}$Ca	52	52	56
${}_{21}$Sc	55-56	57	58
${}_{22}$Ti	56-57	57	61
${}_{23}$V	61-62	51	64
${}_{24}$Cr	66	64	67
${}_{25}$Mn	66-68	66	69
${}_{26}$Fe	68-69	69	72
${}_{27}$Co	70-71	72	75
${}_{28}$Ni	73,76	76	78
${}_{29}$Cu	76,78,80	79	80
${}_{30}$Zn	78	81	82
${}_{31}$Ga	81	84	85
${}_{32}$Ge	81	86	87

Table 9.2: Neutron-rich isotopes produced by "BigSol Isotope Spectrometer" at low beam energy (30 MeV/u) compared to GSI, Darmstadt data at relativistic energies (750 MeV/u). The "BigSol" column gives the highest neutron-number isotope(s) for each element. Yields for this short run are small, as given in Table 9.1. The most neutron-rich isotope produced at GSI for each element overlapping with the BigSol data is shown in the column "GSI'94$_{Max}$" from [Bernas 1994]. The column "GSI'97$_{Max}$" shows the maximum neutron-rich isotope reported for each element in [Bernas 1997]. In the second GSI experiment a dose of 10^{10} ions was obtained at a rate of $2x10^7$ ions/s.

of the equations, and is thus *exactly* removed. As a result ALL charge states of each (Z, A) isotope collected fall within one and only one 2D-ellipsoidal Z-A identifier-region— independent of their charge states while passing through the spectrometer.

6. The merit of this multi-dimensional particle identifier scheme was *objectively* assessed based on whether it *automaticly* displaced so-called "bad" data far from the region of interest (ROI) for identified ions. Data lacking proper timing (i.e. "accidentals" off by one beam burst in time and some light, fast ions[6]) are *automatically* segregated from the A-Z ROI in the 2D identifier. This allows *objective* recovery of events which suffer from "missing data" and whose exclusion would otherwise skew statistical measures of cross sections, etc.

7. We emphasize: *The extremely "messy" multiple-charge-state data, consisting of some 200 separate isotopic species, were resolved and their q-state ambiguity completely removed without any gates or cuts whatsoever being set on the data,* with the exception of the initial software $\Delta(B\rho)/B\rho$ aperture at the focal plane.

In both the present thesis work and that of others which produce such spectra, the identification of multiple charge-state isotopes has presented a formidable technical challenge not present at higher, and especially not at relativistic, energies. For example, at relativistic energies one finds full-electron stripping of products and essentially 100% collection efficiency from kinematic focusing. A major contribution to the objective reduction and particle-identification of traditionally problematic multiple-charge-state, low-energy, heavy-ion data has been made in the present thesis. This advance is a necessary prerequisite to the routine exploitation of these

---

[6] Which lack timing signals because their energy loss was below the level that could reliably trigger the PPAC-anode hardware threshold in the constant fraction discriminator.

low-energy neutron-rich reaction products as RNBs.

Although the data analysis methods used in the present thesis were tedious to develop and implement, we are convinced that they are dictated by the current norms of good, multi-dimensional statistical practise. And, furthermore, since this data *could not be analyzed without these practises*, these methods are *dictated by the physics.* If we are to explore reactions in this energy, and A-Z regime, to understand them, and, furthermore, exploit them for their potential to reveal the secrets of the limits of nuclear binding, we must be able to interpret the data which nature presents to us.

9.2 Spectra of neutron-rich isotopes with yields

Here we present a number of spectra from which the yields for neutron-rich isotopes listed in Table 9.1 were extracted. Some spectra illustrate the general character of the data collected with BigSol Isotope Spectrometer, while other spectra illustrate the calibration-beam particle-identifications. Detailed explanations of these methods have been given previously in this thesis.

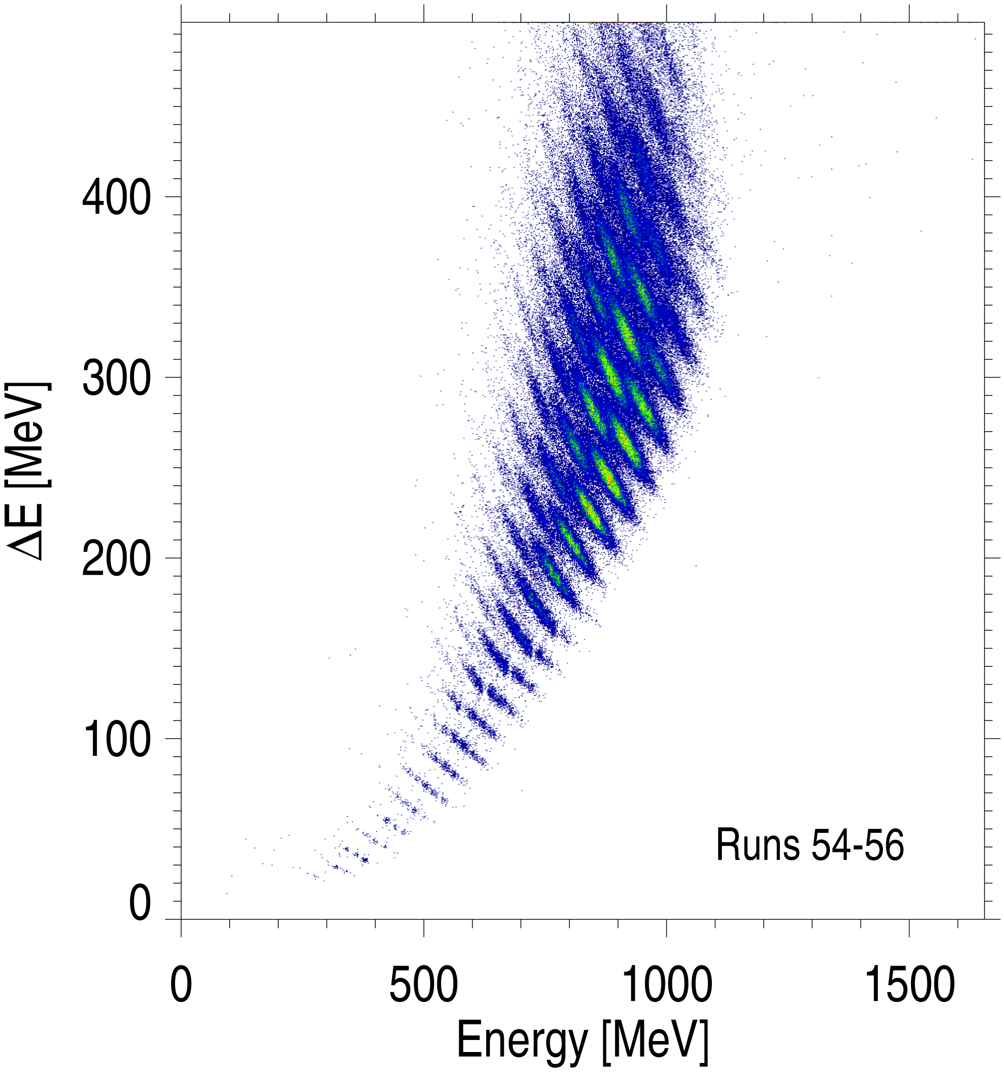

Figure 9.1: ΔE vs. E_{total} at 1.36 T-m. $\Delta(B\rho)/B\rho \approx 1.7\%$ for $0.7^\circ \leq \theta_{lab} \leq 3.1^\circ$. A single ΔE detector is used here as the ions are not as penetrating as with data at 1.76 T-m. This 1.36 T-m data, however, does have timing signals (the higher $B\rho$-data was generally below the PPAC-anode time-pick-off threshold, but was sufficiently penetrating to use multiple ΔE detectors of about 320 μm thickness, and therefore has superior resolution in ΔE). Time of flight is needed to remove charge-state ambiguities and thus the 1.36 T-m data was used for this thesis. The trend, however, is such that for each element examined, the relative isotopic yields in the *higher* magnetic rigidity data are peaked at higher neutron numbers.

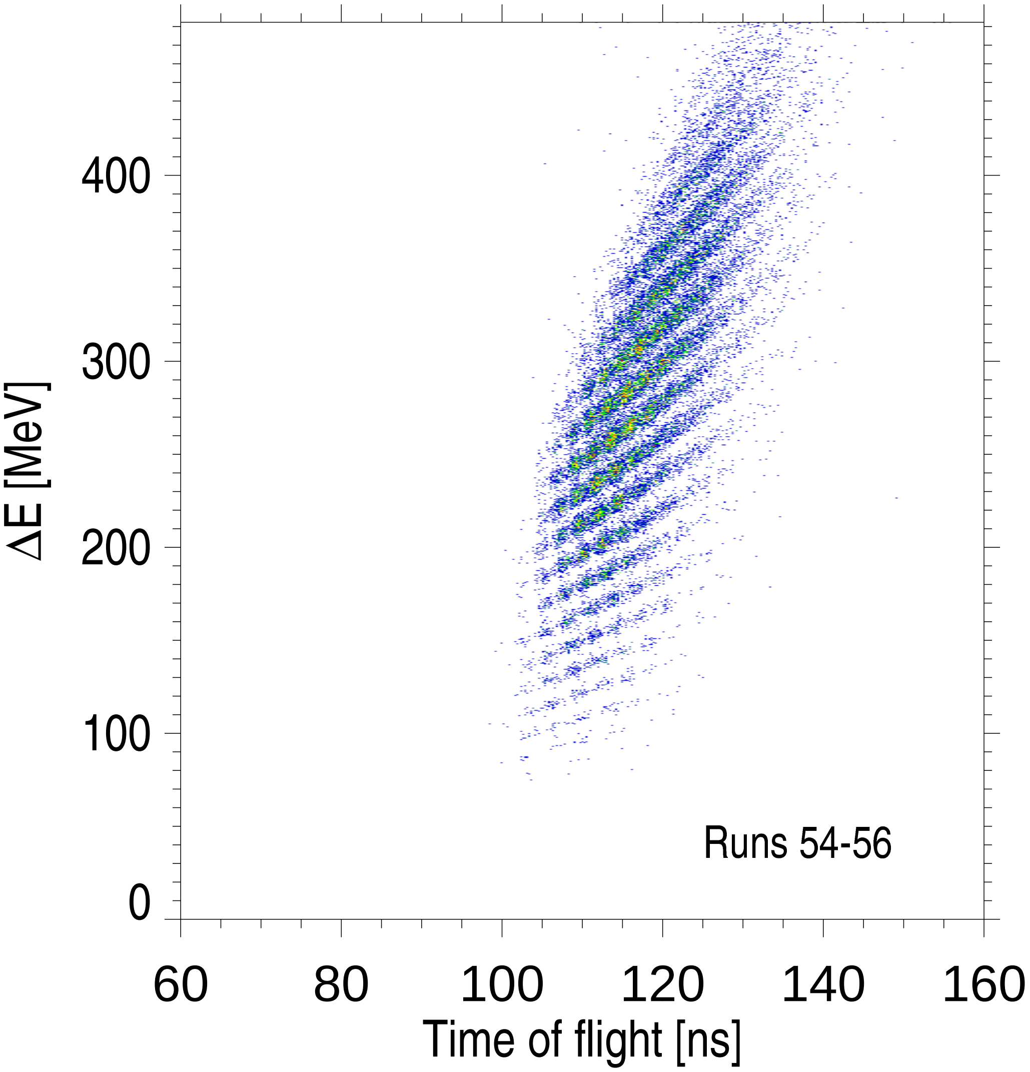

Figure 9.2: ΔE vs. ToF, at 1.36 T-m. Events shown here are identical to those shown in the immediately previous Fig. 9.1 which showed ΔE vs. E_{total}. Event-by-event time of flight shown here was measured between a thin SiSB timing-start detector (ΔE_1) in the the focal plane Si telescope, and a delayed timing-stop signal taken from the anode of the parallel-plate avalanche detector (2D-PPAC) at the solenoid entrance, just after the reaction target.

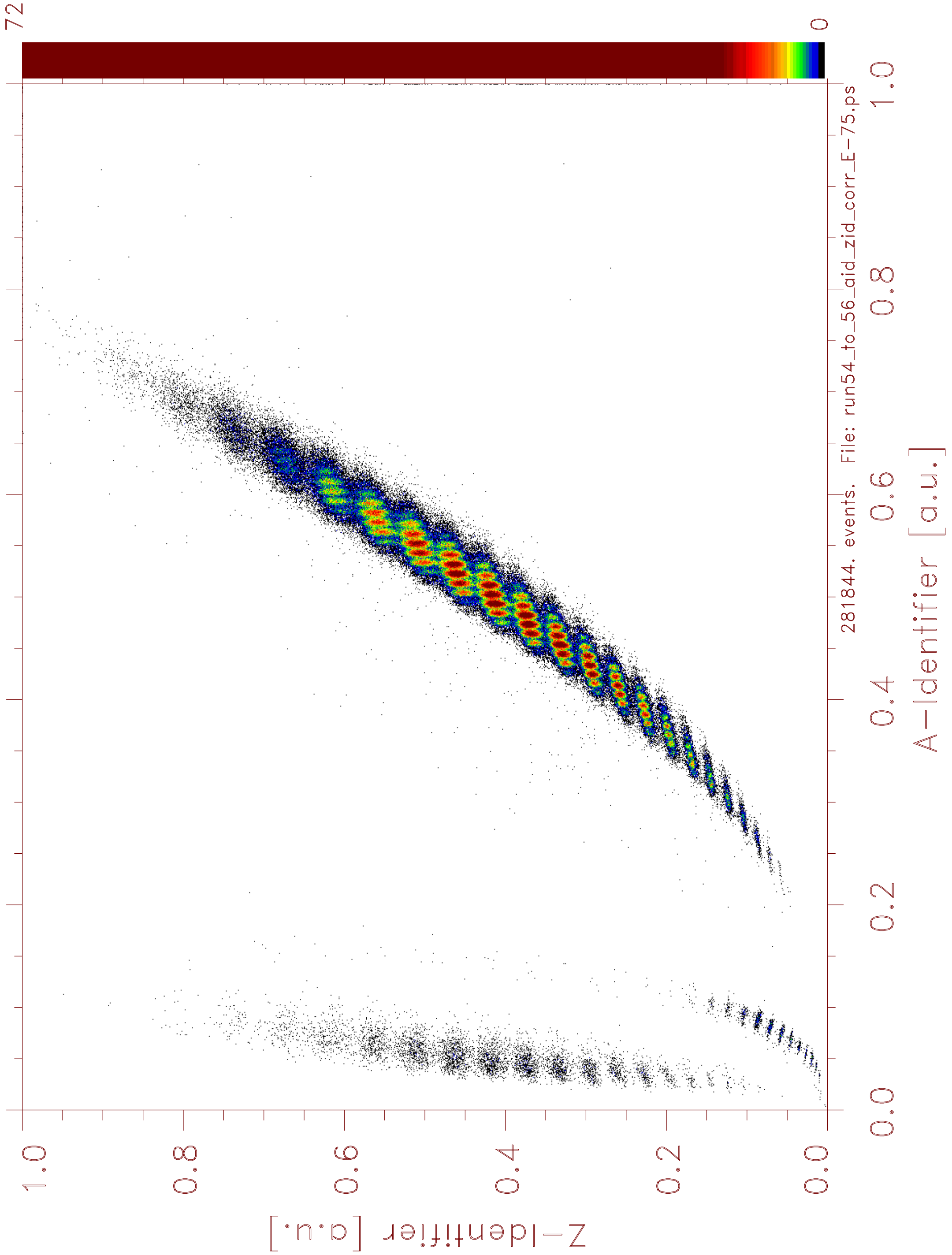
72
0
281844. events. File: run54_to_56_aid_zid_corr_E-75.ps
A−Identifier [a.u.]
Z−Identifier [a.u.]
0.0
0.2
0.4
0.6
0.8
1.0

Figure 9.3: (Page 216) Lower-energy run 2D Z-identifier vs. A-identifier with charge-state dependencies completely removed from both dimensions. Note that TDC (time-to-digital-converter) signal "fold-over" events (along y-axis on left) and low-ionizing light particles which did not trigger the PPAC-anode detector (displaced downward in E_{total}), are *automatically* displaced far from the particle-ID region of interest (ROI)—an indication of a satisfactory identifier. No restrictive cuts were placed in the data except in the focal-plane software aperture to restrict $\Delta(B\rho)/B\rho \approx 1.7\%$. Data shown is the same as that in Figs. 9.1 and 9.2, collected at $0.7^\circ \leq \theta_{lab} \leq 3.1^\circ$.

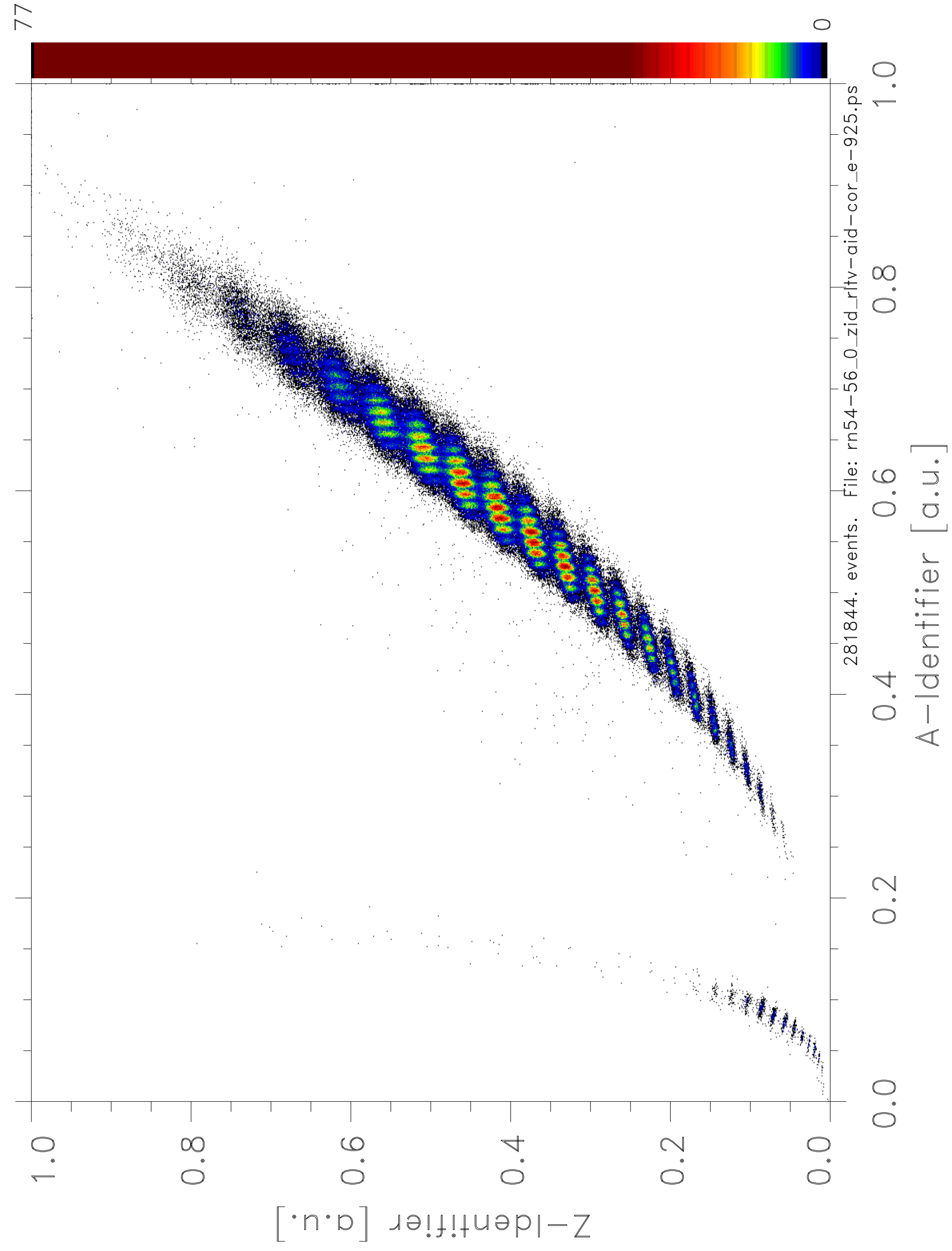
77
0
281844. events. File: rn54-56_0_zid_rltv-aid-cor_e-925.ps
A-Identifier [a.u.]
0.0
0.2
0.4
0.6
0.8
1.0
Z-Identifier [a.u.]
0.0
0.2
0.4
0.6
0.8
1.0

Figure 9.4: (Page 218) 2D Z-identifier vs. A-identifier, identical to Fig. 9.3 except here the A-Identifier is from a relativistic calculation of atomic mass while in Fig. 9.3 the calculation is classical. Also, here TDC “fold-overs” seen along y-axis in Fig. 9.3 have had precisely one cyclotron RF cycle-time added to bring them properly into main particle-identifier group. Note relatively low level of background in region of the most neutron-rich isotopes.

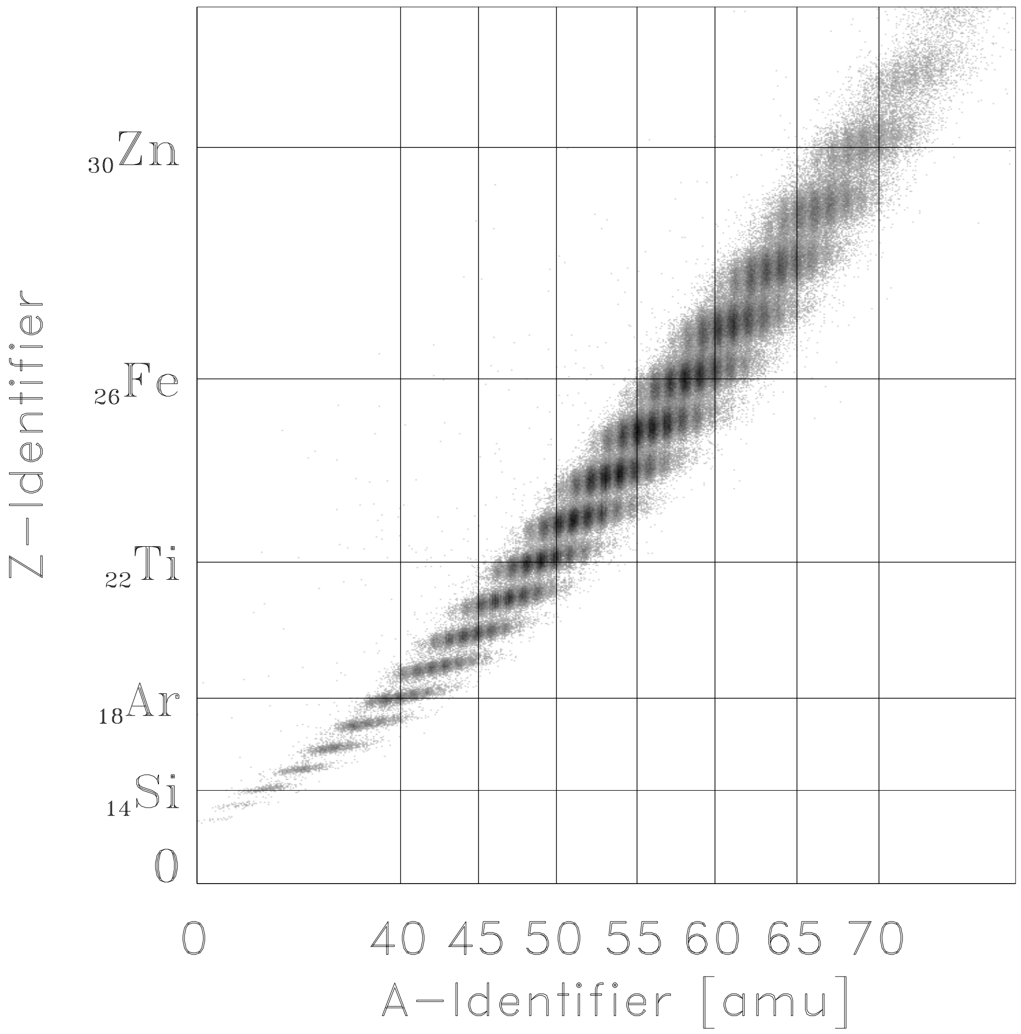

Figure 9.5: 2D Z-identifier vs. A-identifier. Identical to Fig. 9.4 but grey scale and having absolute, calibrated values of Z-identifier and A-identifier shown. Data from 4-5 charge states are positively identified by Z and A values—independent of their q-states. Data includes neutron-rich nuclei up to and beyond the most n-rich produced at the time of this experiment.

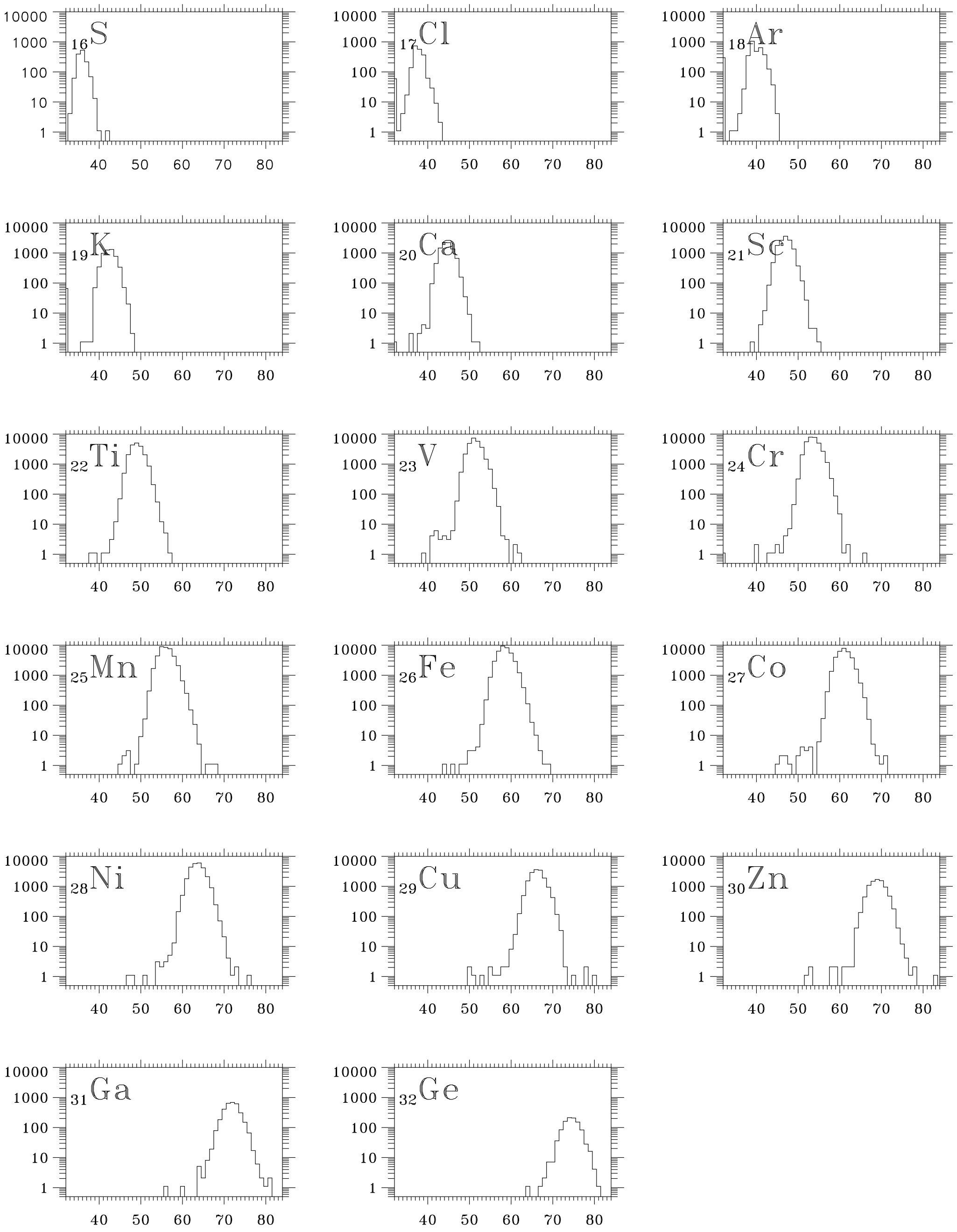

file = rn54–56_gang_plot_a_z_log.ps –28apr98

Figure 9.6: Yields (summed, binned histograms) of neutron-rich isotopes for elements from sulfur to germanium at 1.36 T-m. Obtained from Z-identifier vs. A-identifier of Fig. 9.3. $\Delta(B\rho)/B\rho \approx 1.7\%$. See also Table 9.1.

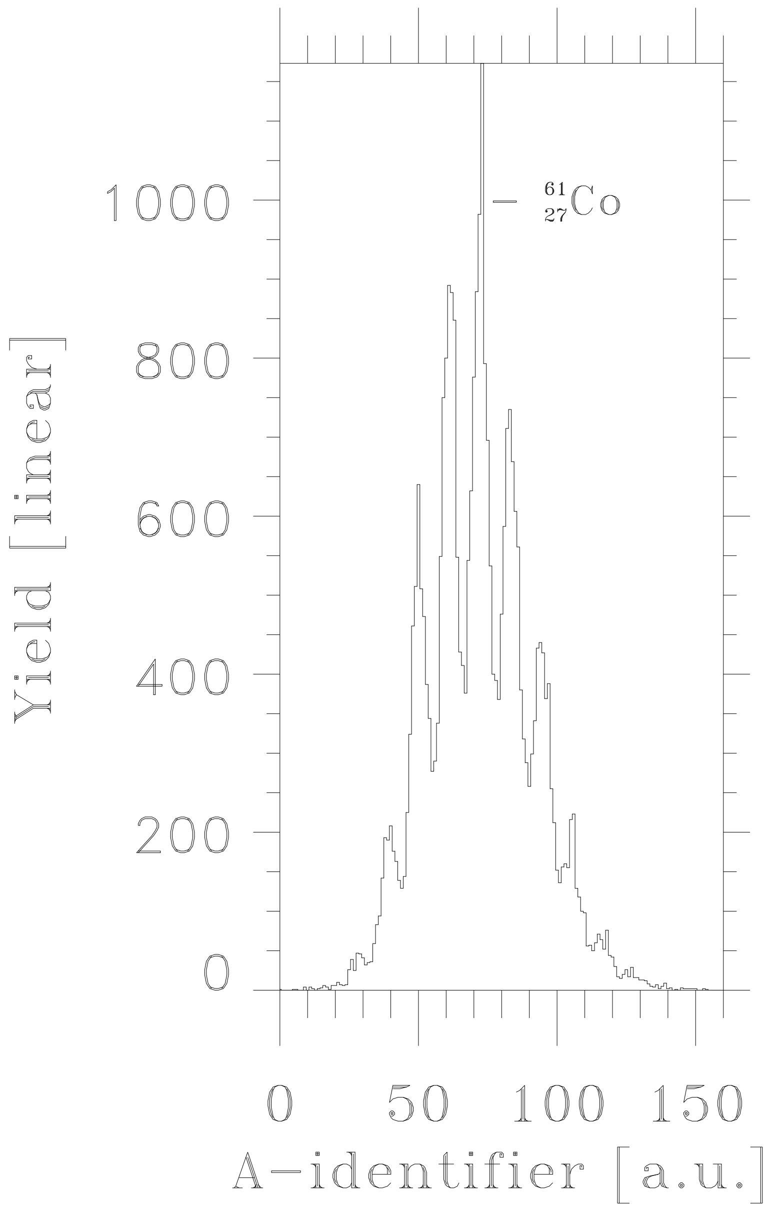

Figure 9.7: One-dimensional projection (histogram) of resolved cobalt-isotope Z-band from 2D Z-identifier vs. A-identifier shown in Fig. 9.4. Scale is linear, showing counts per channel.

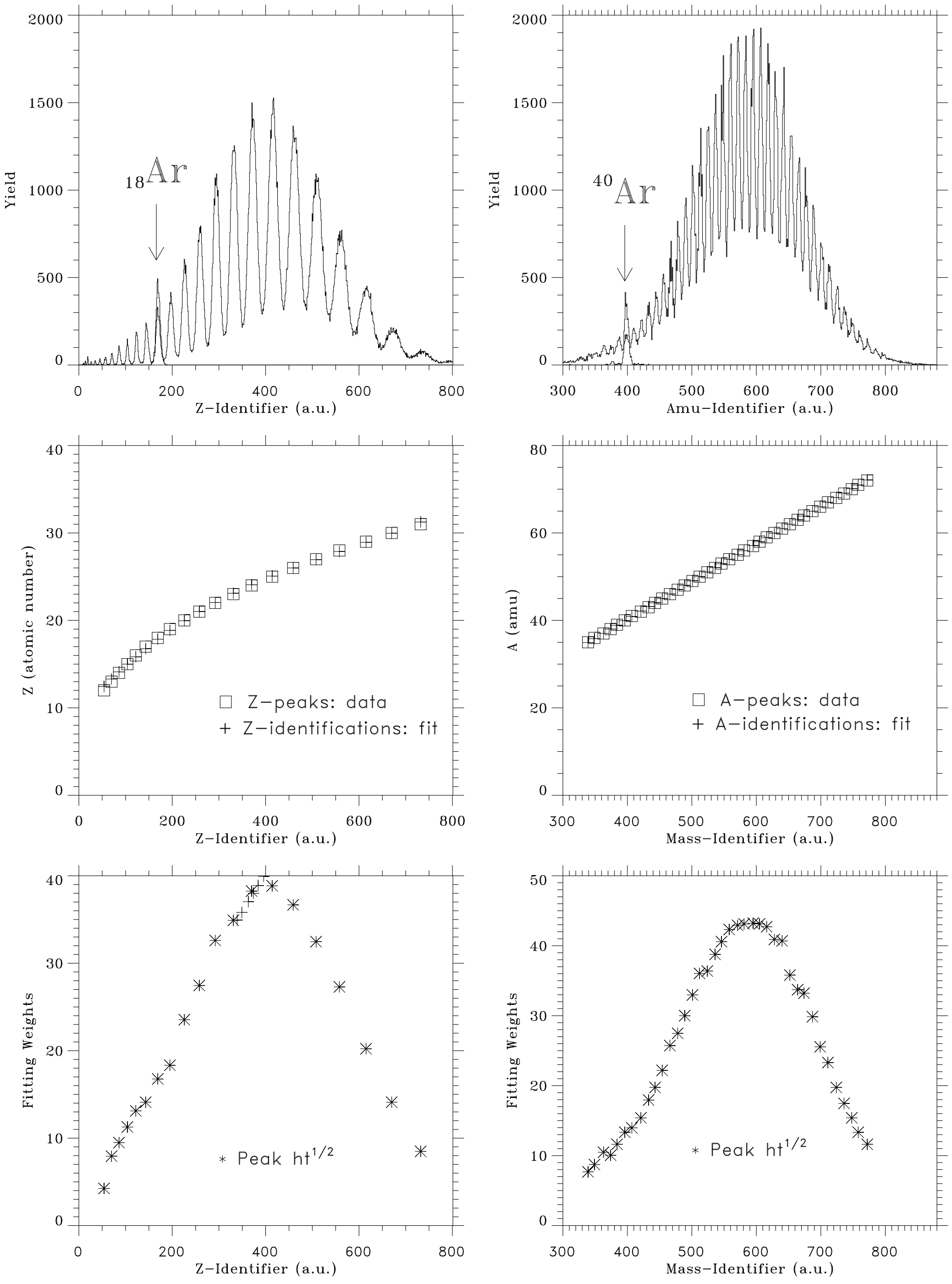

Figure 9.8: Lower-energy run. Top row: One-dimensional projections from 2D Z-identifiers and A-identifiers shown in Fig. 9.5, with $^{40}_{18}$Ar cyclotron-analog calibration beam overlaid to illustrate particle identifications. Middle row: Fits to centroids of Z- and A-identifiers' peak locations. Bottom row: Statistical weights used in multiple-peak fitting to Z- and A-identifiers' peaks.

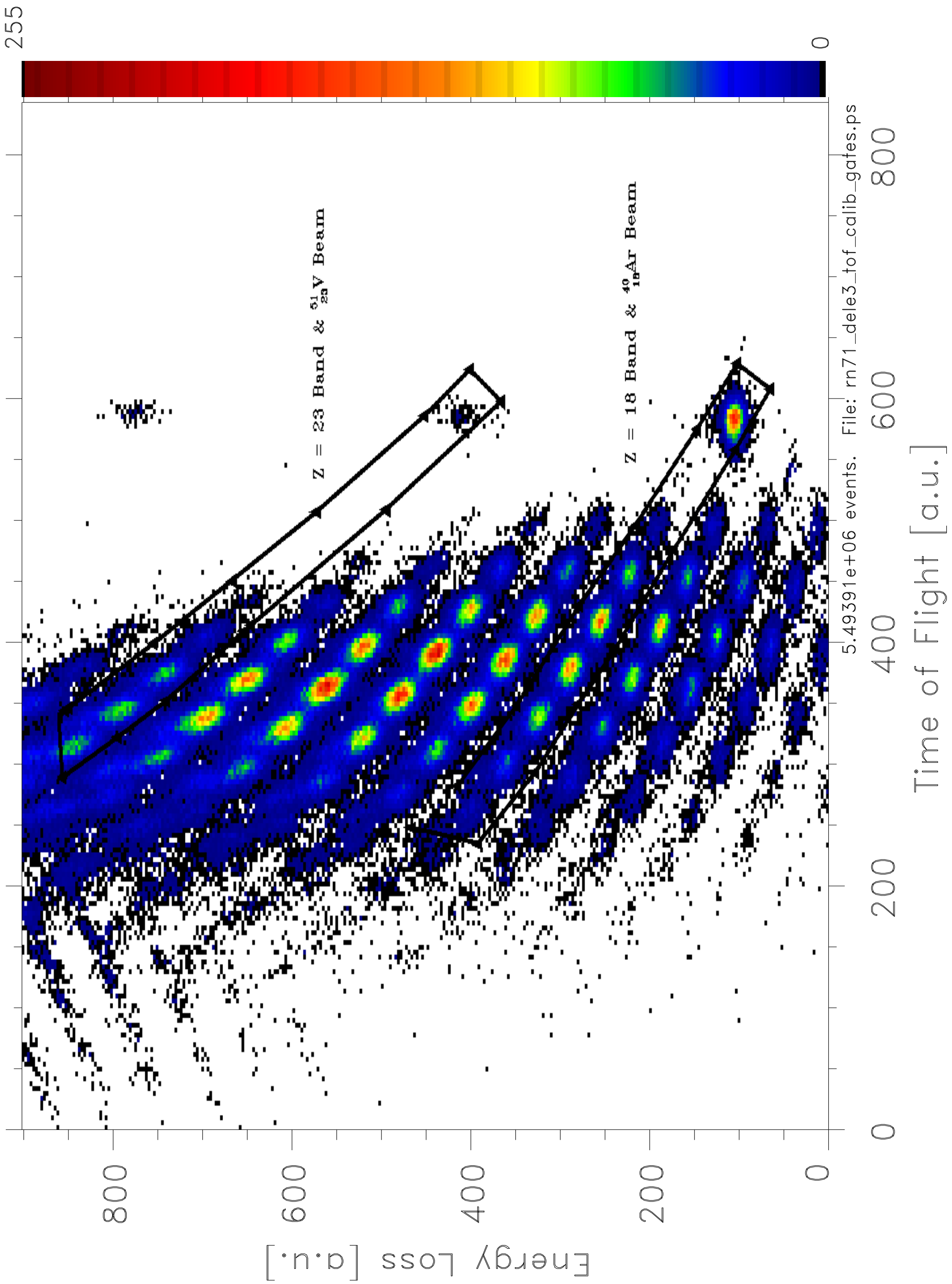
Z = 23 Band & $^{51}_{23}$V Beam
Z = 18 Band & $^{40}_{18}$Ar Beam
Time of Flight [a.u.]
Energy Loss [a.u.]
0
200
400
600
800
0
200
400
600
800
0
255
5.49391e+06 events. File: rn71_dele3_tof_calib_gates.ps

Figure 9.9: (Page 224) Higher-energy run multiple (330 μm) ΔE vs. ToF ($B\rho \approx 1.8$ T-m) with cyclotron-analog beams overlaid.

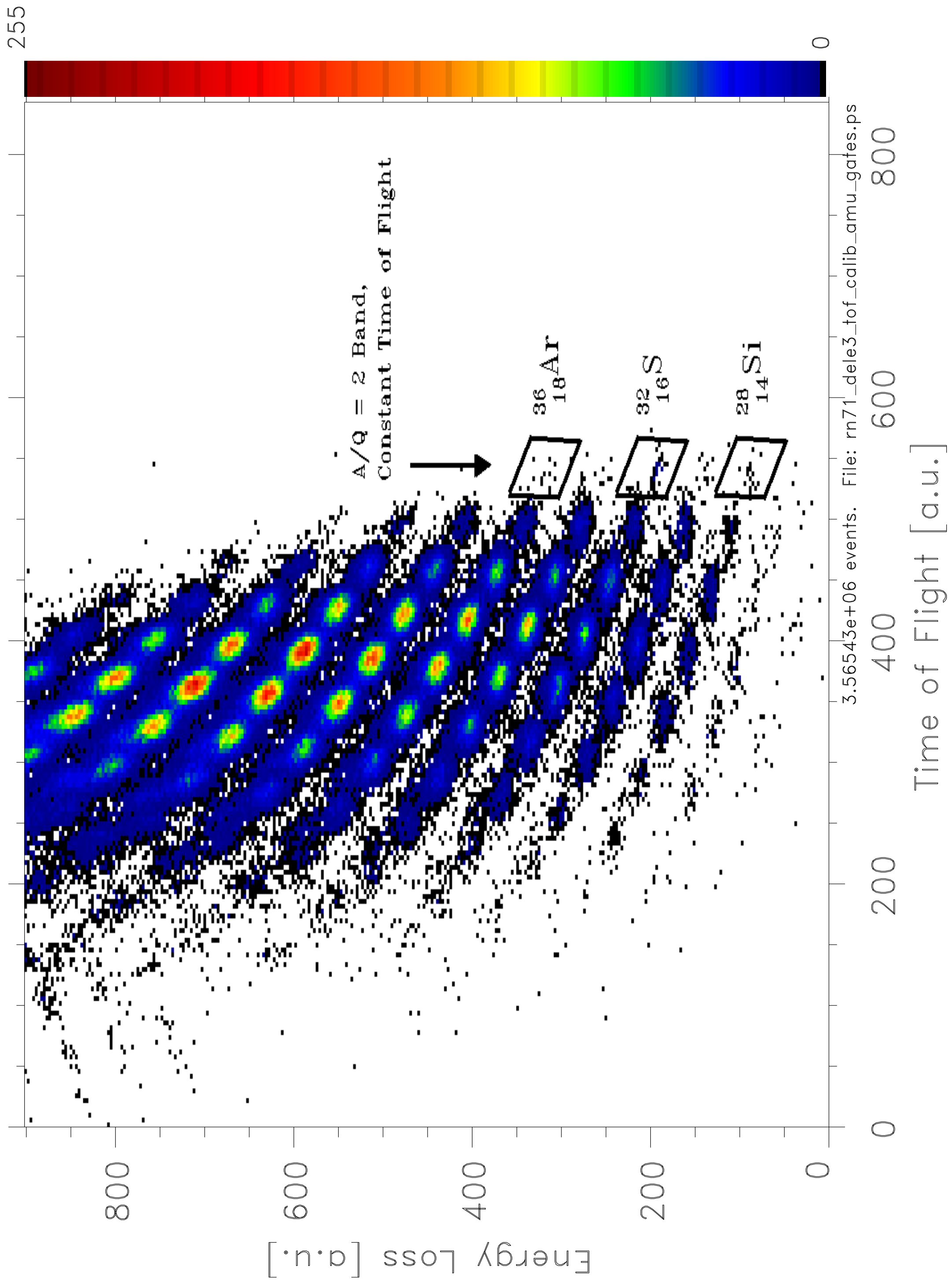
255
0
A/Q = 2 Band,
Constant Time of Flight
$^{36}_{18}$Ar
$^{32}_{16}$S
$^{28}_{14}$Si
0
200
400
600
800
Time of Flight [a.u.]
Energy Loss [a.u.]
3.56543e+06 events. File: rn71_dele3_tof_calib_amu_gates.ps

Figure 9.10: (Page 226) Like Fig. 9.9. Having the Z-band identifications established previously by calibration beams in Fig. 9.9, the location of the straight, vertical $A/q = 2$ line at constant ToF now establishes the atomic-mass identifications as indicated.

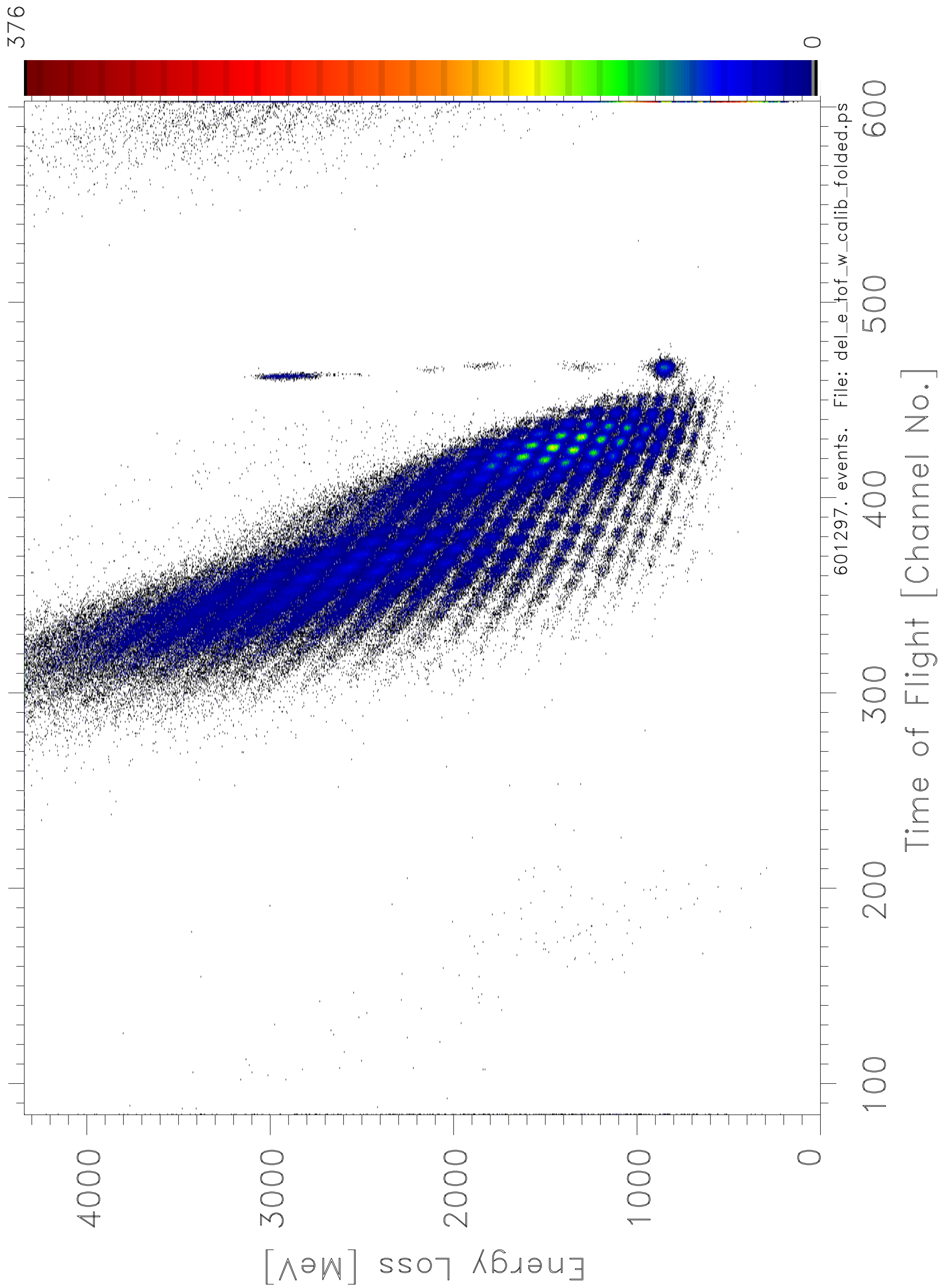
376
0
Energy Loss [MeV]
4000
3000
2000
1000
0
Time of Flight [Channel No.]
100
200
300
400
500
600
601297. events. File: del_e_tof_w_calib_folded.ps

Figure 9.11: (Page 228) Lower-energy run is overlaid (to the left of) higher energy run in ΔE vs. ToF to transfer atomic number (Z) calibrations established in Fig. 9.9 to lower-energy run spectra. Atomic mass calibrations are then established for lower-energy run in same manner as shown in Fig. 9.10 for isotopes of higher-energy run.

9.3 Comparisons with other experiments

The particular experimental run which produced the results shown in Table 9.1 lasted for about 3.3 hours and is among many dozens collected under differing experimental conditions. The total counts of the most neutron-rich isotopes listed here are therefore quite small, but represent only a subset of the data collected. Results from two other research groups should be compared to and contrasted with the results of this thesis.

As mentioned above, a group working at the GSI in Darmstadt, produced and identified in 1991 [Bernas 1994] and 1995 [Bernas 1997] many of these and other new isotopes (some 100 in total) in elegant experiments conducted at relativistic energies (750 MeV/u) with ^{238}U on Pb, and later on Be. The reaction mechanisms of the GSI work consist of electromagnetic-fission and peripheral nuclear reactions leading to fission[7] of a relativistic ^{238}U projectile at low internal excitation. In a later, significant development, a much-lower energy (20 MeV/u) experiment—conducted at the NSCL in 1996—consisting of ^{238}U on ^{238}Pb [Souliotis 1997] reproduced many of the new n-rich isotopes first reported by the GSI group. These *low-energy* isotopes are consistent with sequential fission following a quasi-elastic or deep-inelastic nuclear collision. These isotopes populate a region of higher-Z than the isotopes which are reported in the present thesis work. This result is anticipated as this thesis utilized thick-target suppression of heavy reaction fragments and of unreacted primary beam to selectively study lower-Z reaction products with a minimum of background.

---

[7] A multi-fragmentation component is also identified, and is likely responsible for producing the lower-Z neutron-rich isotopes (which overlap with the data shown in this thesis) according to [Bernas 1998], though "Such a large n-excess is not compatible with the image of a dense excited piece of nuclear matter which would be formed in head-on collisions." [ibid., p. 670]. Note that the lightest binary *fission* fragment ever identified is ^{68}Fe, and the heaviest ternary fragment is ^{34}Si [ibid., and references therein.]

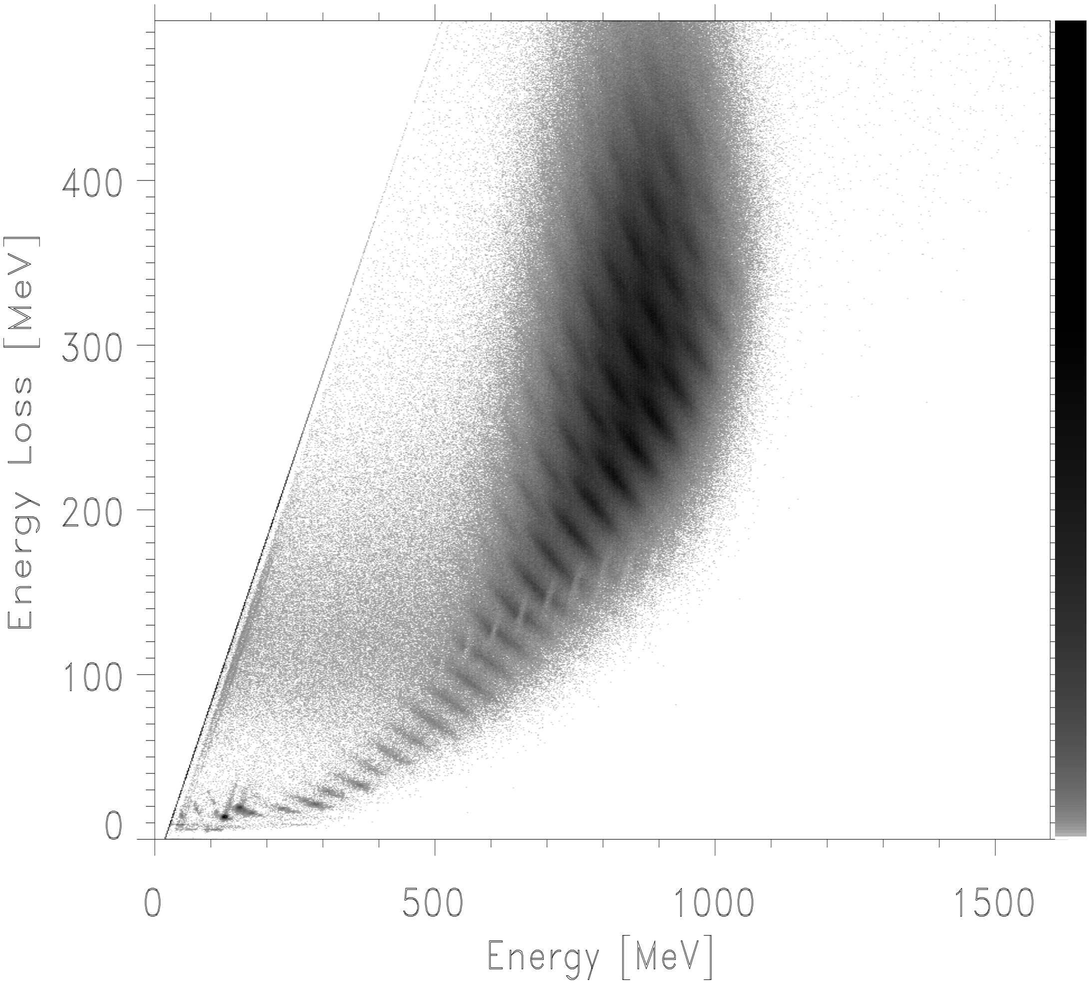

Figure 9.12: Lower-energy run ΔE vs. E before application of restrictive focal-plane software-gate setting $\Delta(B\rho)/B\rho \approx 1.7\%$.

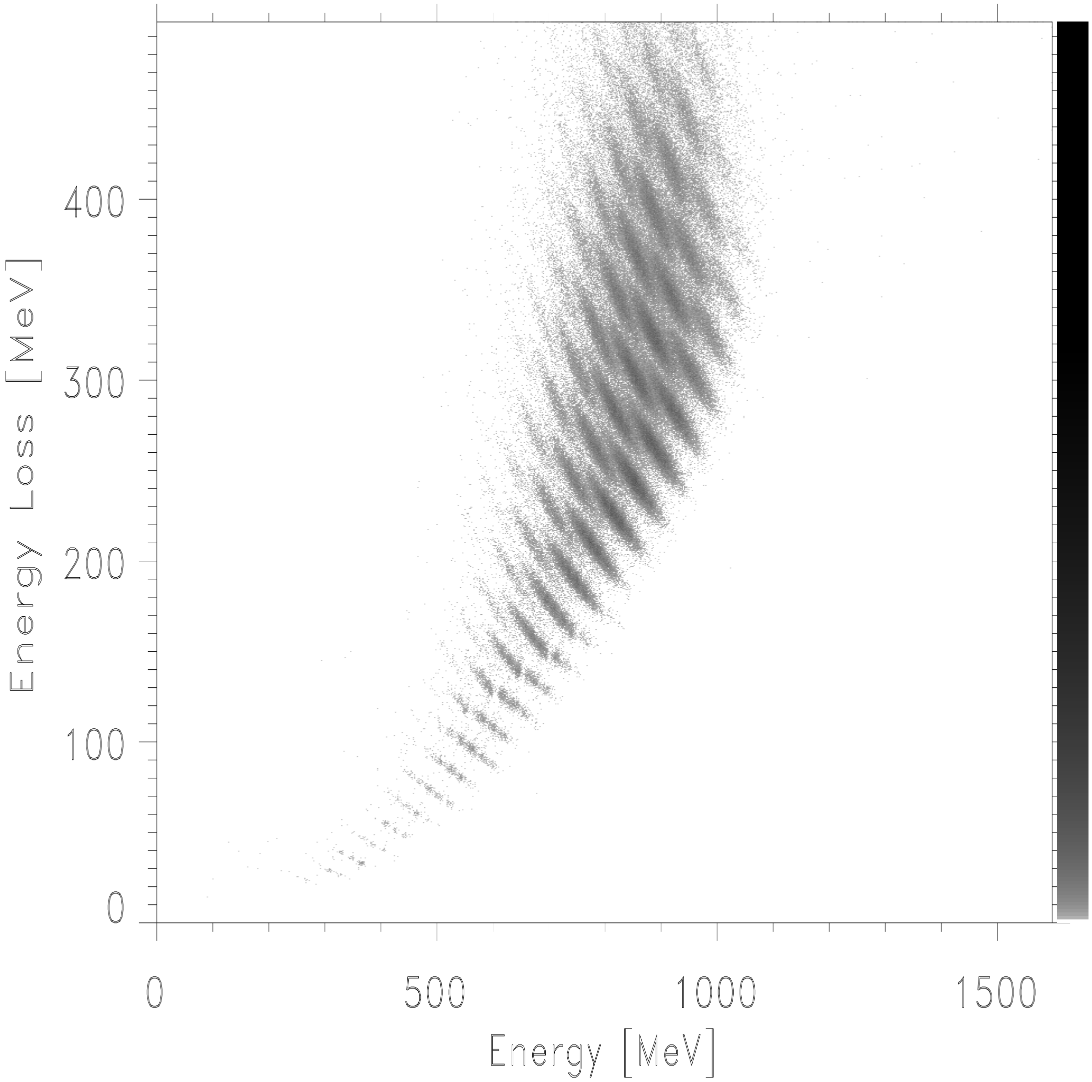

Figure 9.13: Lower-energy run ΔE vs. E after application of restrictive focal-plane software gate setting $\Delta(B\rho)/B\rho \approx 1.7\%$.

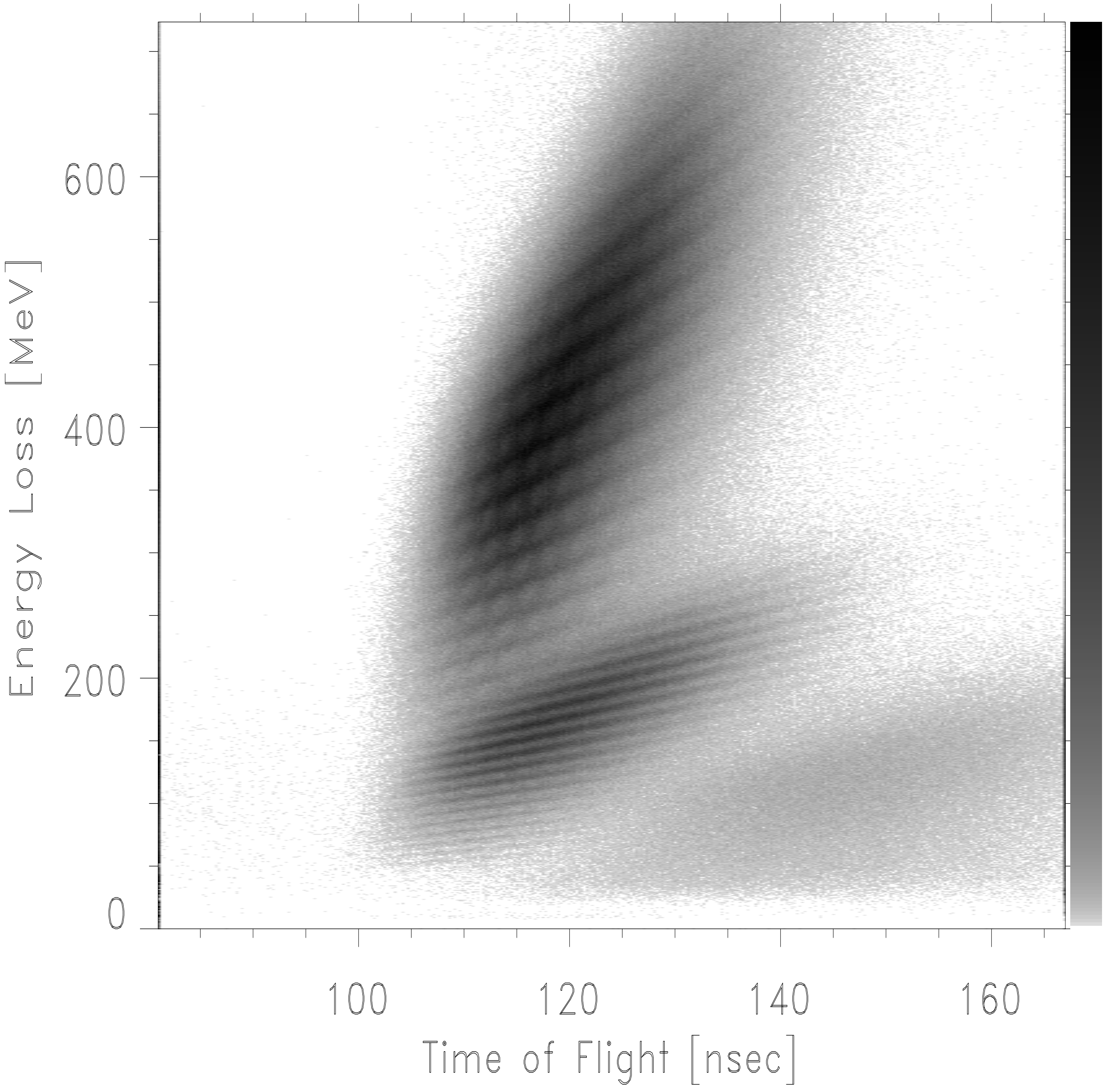

Figure 9.14: Lower-energy run ΔE vs. ToF before application of restrictive focal-plane software gate setting $\Delta(B\rho)/B\rho \approx 1.7\%$. Note y-axis is mislabeled: maximum ΔE is 500 MeV as per other plots of this low-energy data.

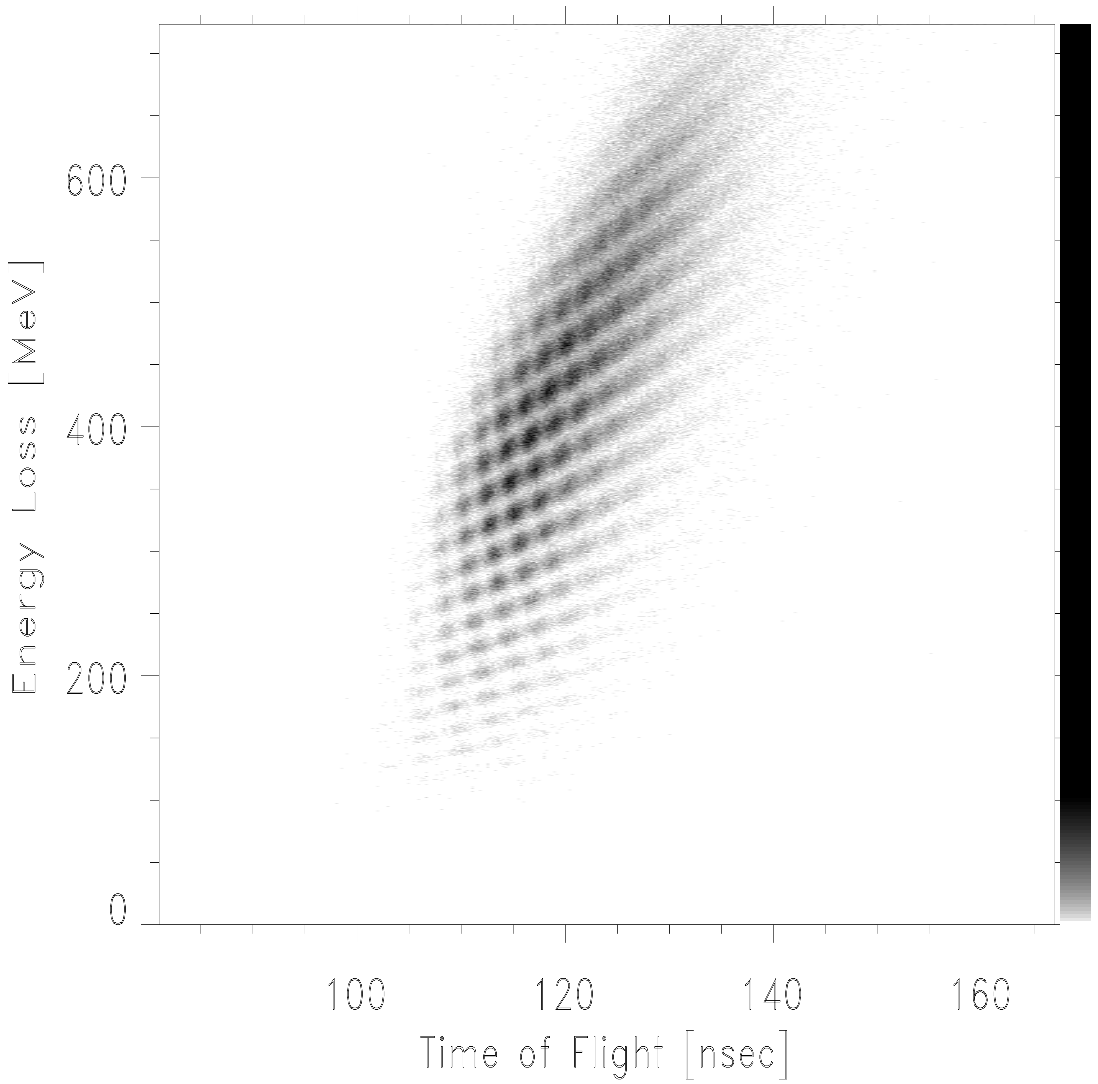

Figure 9.15: Lower-energy run ΔE vs. ToF after application of restrictive focal-plane software gate setting $\Delta(B\rho)/B\rho \approx 1.7\%$.

9.4 Future possibilities for new neutron-rich RNBs

In our estimation, it is reasonable to expect that very neutron-rich isotopes that were first produced at, and/or reported from, relativistic collisions at Darmstadt can also be produced in copious numbers in *low-energy*, massive-projectile experiments such as has been done by [Souliotis 1997] and in the present thesis work. Reproducing these isotopes at low energies is significant in that this opens up the possibility that many existing low-energy accelerator facilities, which generally can produce quite high beam currents, may be able to produce neutron-rich RNBs. Half life measurements and the structure of nuclei along the astrophysical r-process path could be investigated, as could new, possibly exotic, structures at the limits of particle stability. The latter may include short-lived nuclear isomeric states, the study of which is particularly well-suited for solenoid-based measurements owing to the short flight path [Brown 1993] [Brown2 1995].

9.5 Future studies of reaction mechanisms

Another issue raised by the present results is the necessity of understanding the reaction mechanism in more detail. This study is ongoing and will eventually include comparison of the present data to the systematic Xe reaction studies of [van Veldhuizen, 2000], [Hanold 1993], and others.[8]

9.6 Summary of instrumental developments

1. BigSol, the 7-Tesla University of Michigan superconducting solenoid magnet which had been previously configured for *light* heavy-ion radioactive nuclear

---

[8] Our thanks to Walter Loveland, Oregon State University, Corvallis for advice in further investigations of the reaction mechanism.

beams (RNB's), at the National Superconducting Cyclotron Laboratory, was reconfigured as the BigSol Isotope Spectrometer device.

2. This device was optimized for fragmenting a massive beam (^{136}Xe) at intermediate energy (30 MeV/u).
3. A light (C), thick (114mg/cm^2) target was used.
4. Products emitted at small angles ($0.7° \leq \theta_{lab} \leq 6.0°$), and at
5. The highest momenta possible (1.36 and 1.76 T-m) given the available silicon focal-plane telescope array were collected.
6. Fractional magnetic dispersion $\Delta(B\rho)/B\rho$ was limited to $\approx 1.7\%$.
7. Position-sensitive entrance and focal-plane detectors were used, the data were analyzed with offline software analysis (XY-position resolutions of ≤ 1 mm).
8. Signals collected included time of flight over a distance of ≈ 6.2 m between the entrance-2D PPAC (position-sensitive parallel-plate gas avalanche counter) and a thin ΔE silicon surface barrier (SiSB) detector at the focal plane.
9. Other signals included energy loss through thick, multiple, SiSB ΔE detectors (total thickness about 320 μm) and Si $E_{residual}$ (≈ 1 mm) signals with resolutions of about several parts in 10^4.
10. Software particle identifiers were sought, and developed , which eliminate (cancel out) the q-state structure in the data for both Z-identifiers and A-identifiers. Thus the multiple q-states and the charge-state ambiguity as to mass-ID of isotopes are *exactly* eliminated.

9.7 Future BigSol improvements

In any future experiments using a similar reaction, the following improvements should be undertaken:

1. Looking at the highest-rigidity reaction products, and in particular, rigidities well above the beam velocity, should be most productive in collecting highly neutron-rich isotopes.

2. Significantly thicker energy-loss and, especially, residual-energy silicon detectors should be available to allow higher-energy reaction products to be studied. Small changes in the magnetic rigidity of the products being focused translates into rather large changes in the range of the products in the focal-plane telescope. Optimization of ΔE thickness vs. $E_{residual}$ thickness needs to be maintained across different reaction-product energies. The ideal circumstance is roughly equal energy deposition in the ΔE and $E_{residual}$ detectors. Therefore a number of pre-calibrated detectors should be available for remote insertion into the detector stack as needed.

3. The double-valued magnetic rigidity of isotopes arriving at the focal plane away from its center (focal spot) makes it difficult to analyze events not near the center of the focal plane position-sensitive detector. Therefore, a thin, "detector-shadowing bar" along the magnet's axis and extending as close to the focal-plane detectors as possible, should be used to stop axis-crossing-fragment orbits.

4. The entrance acceptance of the solenoid is not the important variable in controlling the fractional magnetic ridgity. The position-sensitive aspect of the

entrance detector (2D-PPAC) can be eliminated in favor of a mechanical apertures. In the previous experiments the primary beam rate had to be limited, to prevent the PPAC from exceeding a rate of about $50,000$ events/second. By removing the PPAC at the entrance aperture a larger primary beam current may be used, resulting in a better collection rate of isotopes in the focal-plane.

5. It is vital to achieve timing for the most energetic fragments. The entrance timing-stop-signal detector consisting of a PPAC-anode signal should be replaced with another appropriate detector having a lower *threshold*. Possibilities of a fast-timing include a channel plate, or a thin plastic scintillator. The problem here was generally *not* poor timing resolution, but that the fastest (highest rigidity) fragments we attempted to collect ($B\rho \geq 1.7$ T-m) were not sufficiently ionizing to trigger the PPAC-anode-timing pickoff. However, the ΔE vs. E signals' resolution for the faster ions—analyzed using about 332 μm of ΔE detectors—was excellent. The timing signal is needed to remove charge-state ambiguity for the most neutron-rich isotopes which are overlapped in ΔE vs. E by low-charge-state ions among the next-higher-Z fragments.

6. Lastly, and perhaps most importantly, it is extremely time-consuming to setup this device at the NSCL. Perhaps $3 - 4$ months of setup time were required for each of three iterations of this experiment. A permanent set-up of the BigSol Isotope Spectrometer is necessary to conduct systematic studies over a period of time. This would permit a scientific program of investigation of exotic, neutron-rich nuclei based on this device.

APPENDICES

APPENDIX A

The `bfield.pro` program

```
;==========================================================================
; This is:  bfield.pro
; This module is based on:
; "Solenoid Magnet Design"
;   by D. Bruce Montgomery, 1969, reprinted w/ corr. 1980,
;   Robt. E. Kreiger Publishing Company, Inc., Huntington,
;   N.Y., copyright 1969 John Wiley & Sons, inc.  See esp.
;   Chapter 8.
;  And M. Lee (private communications) for specs. of TwinSol.
;  This program calculates a solenoidal B field at ONE
;   point using expansion to third order (there are no
;   second or higher-even-order terms).  It is called
;   repeteadly along the ions path calculated by the program
;   orbits.pro.
; NOTE: All paramaters are preset to UM BigSol dimensions - unless
; /twin keyword set, then to TwinSol dimensions.
; Calling: Called from acceptance.pro. See that program.
; Language: IDL.
; By: T. O'Donnell U of Michigan Nuclear Group  28Aug1997
; email tom.odonnell@umich.edu
; Edited:  -02Sept97/03Sept97/06Sept97-def. of 'A'/
; -11jul98 added (again) /twin keyword for it's B(I) calib'n.
; -17jul99 added /thick_coil option, for a more realistic,
;  thick coil (other option has been for a thin, zero
;  thickness, cylindrical coil approximation per Liu,'90 and
;  Stern, '87.) Ref: Szilagyi, Miklos, Electron and Ion Optics,
;  Plenum Press, London & NY, 1988,  For Stern/Liu coil, see
;  p. 106, Eqn. 3-261 - 3.263.  For thick coil (exact) calc.
;  see p. 107-8, Eqn. 3-269 and 3-270.  NOTE this option
;  ONLY returns the Z-axis field profile.
; -20jul99 Added power series for thick coil. To get
;  exact thick_coil along z axis set /thick_coil, /exact.
;  To get full thick coil, using power series with
;  on-axis and its derivatives taken from gaussian plus
;  quadratic fit to exact thick coil, set /thick_coil.
; -20jul99 Now /thick_coil must be the coefficients of
;  a gaussian-plus-quadratic FIT to the EXACT thick coil
;  expression AT THE AMPREAGE OF INTEREST (i.e. 6 terms)
;  which are obtained from plot_alongzr.pro.
```

```
; -21jul99 Major reworking of the keywords controlling
;  whether will calculate /thick_coil (using fit to /exact
;  on-axis field for the I_amps of interest, and derivatives
;  of the fit), or /exact (to obtain the profile and fit), or
;  the default thin coil approximation.
;  NOTE: /THIN and /EXACT are mutually exclusive now.
;=============================================================================
function bfield, position, I_amps,  $
     debug = debug, printB = printB, $
     input_cartesian = input_cartesian,  $
     twin = twin, thick_coefs = thick_coefs, $
     exact=exact
; Cylindrical coor. system: (rho, phi, z) with MKS units: (m, rads, m).
;   unless /input_cartesian is set with MKS units: (m, m, m).
if keyword_set(exact) and keyword_set(thick_coefs) then begin
    print, "       ERROR       ---- bfield.pro ----- "
    print, "       /thick_coefs & /exact are mutually exclusive keywords"
    print, "       EXITING ........                              "
    goto, very_end
endif
if keyword_set(exact) ne 1 then begin
  if keyword_set(thick_coefs) then begin
    fit_coefs = 1. ; Must be a 'named variable.'
    hhand = handle_info(fit_coefs, /first_child)
    handle_value, hhand, zcoefs ; Retrieve and assign to a var ('zcoefs' here).
    if n_elements(zcoefs) ne 8 then begin   ; 7th is coeff. in dipole approx'n
     ; at 'large' dist. from coil, 8th is the z value of this position.
     print, " ERROR      ---- bfield.pro -----
     print, "  For THICK COIL calculation (use of the expansion  "
     print, " for symmetric fields), you must pass the    "
        print, " coefficients of a quadratic-plus-gaussian fit (le "
print, " (le 6 terms) to the EXACT thick on-axis thick-coil"
     print, " field, which has been computed at the magnet    "
        print, " amperage of interest.  These are  obtained from   "
        print, "       or from plot_alongzr.pro or from a similar    "
        print, "       program included in the orbit.pro file.   "
     print, " EXITING ........   "
        goto, very_end
    endif
  endif
  if keyword_set(input_cartesian) then begin
    p = position
    p(0) = sqrt(position(0)^2 + position(1)^2)
    p(1) = atan(position(1), position(0))
    position(0:1) = p(0:1)
  endif
endif ; /exact ne 1's endif
if keyword_set(twin) eq 1 then begin
    L_sol     = 0.6177  ; Coil Length  24.32".  See: Precision Cryogenics
              ;  Systems, Inc., Dwg #1280, 4-29-91.
    R_sol     = 0.2123  ; For TwinSol this is RMS rad.
      ; Coil inner Radius 8.3583".  Ibid.
    Del_R_sol = 0.    ; Makes R_sol the rms.; Coil winding thickness: "
      ; Ibid
    ;Cryo_stat=  ; Outer dimension: total cryostat length.
    Cryo_rad  = 0.225425; Inner I.D./2.: Radius of cryostat vacuum tube.
                        ; R_sol is rms radius of coil
endif else begin        ;This is for BigSol (default):
```

```
                         ; Parameters (characteristic of BigSol):
    L_sol     = 0.812800; Coil Length 32".  See: Precision Cryogenics
;   Systems, Inc., Dwg #1280, 4-29-91.
    R_sol     = 0.279400; Coil inner Radius 11".  Ibid.
    Del_R_sol = 0.0762000;Coil winding thickness 3.0".  Ibid
    ;Cryo_stat= 3.65760 ; Outer dimension: total cryostat length.
    Cryo_rad  = 0.225425; Inner I.D./2.: Radius of cryostat vacuum tube.
endelse
;if (position(0) ge Cryo_rad) then begin
;    print, "ion hit cryostat inner diamater... "
;endif
;============================
; Our calibration (UM & T.O'D) differs from that given by Cryomagnetics Inc.
;  (current name of manufacturer of BigSol).  Both are presented here:
;
;(1) Our calibration:
;  To calibrate dB/dI, the B field as a function of the power supply setting
;  (I) for BigSol, we take data from the gauss meter and the power
;  supply and find the slope of the (very) straight line found there.
; To access these data, run these lines of IDL code on PNAXP::[odonnell}:
; >RESTORE,filename= $
; >        "[odonnell.calibrations.magnetic]magnetic_field.dat", /verbose
; >k_field = (gauss_m(3)-gauss_m(1))/(i_sol(3)-i_sol(1)) ; = 0.00217955 kgauss
; However, this gauss meter reading is off axis, on the end of the
;  cryostat at a point just beyond the bore-tube radius;
;  i.e. at about:  position = [0.225425,0,1.82880] in cyl. coors.  One needs
;  to verify the units of the gauss meter.  They are taken as kilogauss
;  here.  It can be shown that the field at the end of a solenoid
;  is about 1/2 (assuming coil is not wound with gaps between windings...)
;  the max field at the center of the coil on the symmetry (z) axis. [Mont-
;  gomery, op cit].  Thus:
; B_max_bigsol =approx= 2.*k_field*I_amps  (Note factor of 2.)
; Using the val for k_field above we calculate:
; B_max_bigsol =about=  7.4649589 tesla and about 0.044270206
; at the location where gauss meter probe was affixed with 171.25 ampheres.
;
;(2) Cryomagntics BigSol manual reports the following values:
; Coil inductance = 265 henries
;  k_field = 0.3796 "tesla-meter/amphere" (sic.) for "field to current ratio."
;  [Note: must mean 0.03796 tesla/amphere.] during Max field test @4.2K giving
;  6.57 tesla-meter @ 171.25 amperes.  The magnet was reported quenched
;  twice in this condition.
; Using the val for k_field above we calculate:
;  B_max_bigsol =about=  6.5006499 tesla (good agreement with original
;  design) and about 0.042050563 at the location where gauss meter probe
;  was affixed.
;=======================================================================
; NOTE CRYOMAGNETICS CALIBRATION WILL BE ADOPTED. UM calibrations suffer
;  some uncertainity from being collected at end of solenoid.
;========================================================================
; UM calibrations from solenoid's end:
;k_field= 0.00217955d+1         ; Tesla. (kilogauss * 10^1  = tesla)
;Bmax   = 2. * k_field * I_amps ; Note: factor of 2. because our calibrations
    ; were taken at END of solenoid, not CENTER
    ; as were Cryomagnetics. tesla
; Cryomagnetics, Inc. calibrations from solenoid's center:
k_field = 0.03796
if keyword_set(twin) then begin
    k_field = 0.03636 ; (Ref. M. Lee, Private Communication.)
```

```
endif else begin
    k_field = 0.03796 ; Ref: Cryomagnetics, Inc. calib'n at z = 0.
    Bmax = k_field * I_amps ; [Tesla]
endelse
; Thin cylindrical coil option (default):
if keyword_set(thick_coefs) ne 1 and keyword_set(exact) ne 1 then begin
    ; Independent Variables:
    r05 = position(0)/2.
    A   = (position(2)+ L_sol/2.)
    B   = A - L_sol
    if keyword_set(debug) then begin
        print, " A & B => ", A, B
        print, "rho = ", r05
    endif
    ; Derived factors:
    R_sol = sqrt(R_sol^2 + (R_sol + Del_R_sol)^2) ; Using an rms equivelant.
    R2      = R_sol^2
    R_05    = R_sol/2.
    R_052   = R_05^2
    R_053   = R_05^3
    RL      = sqrt(R2 + (L_sol/2.)^2)/L_sol
    B_field  = dblarr(2)
    A2      = A^2
    R2_A2   = sqrt(R2 + A2)
    R2_A2_3 = (R2_A2)^3
    R2_A2_5 = (R2_A2)^5
    R2_A2_7 = (R2_A2)^7
    B2      = B^2
    R2_B2   = sqrt(R2 + B2)
    R2_B2_3 = (R2_B2)^3
    R2_B2_5 = (R2_B2)^5
    R2_B2_7 = (R2_B2)^7
    BRL     = Bmax * RL
    ; The B_field = B_field(1) component of the field:
    B_field(1) = BRL * (A/R2_A2 - B/R2_B2) $
        - (r05)^2. * 3. * BRL * R2 * ( B/(R2_B2_5) - A/(R2_A2_5) )
    B_field(0) = (BRL * R2) $
        * ( (-r05 * ( 1./(R2_A2_3) - 1./(R2_B2_3)) ) $
     + r05^3 * 3. * ( ((4.*A2 - R2)/R2_A2_7) - ((4.*B2 - R2)/R2_B2_7) ) )
endif else begin     ; if /exact or /thick_coefs
    r1 = r_sol                  ; Ref: Fig 34, Szilagyi, M, 1988
    r2 = r_sol + del_r_sol
    z0      = position(2)
endelse
if keyword_set(exact) then begin
    B_field = dblarr(2)
    ; Ref: Eqn. 3-269 Vs 3-261, Szilagy, M.
    ; NOTE this is a calc. of ONLY the Z (on axis) component, albeit EXACT
    ; NOTE, we have k * I_max = B_max(0,0) from Cryomagnetics for BigSol.
    ;  How is their k defined? We see empirically it is: k = mu * N,
    ;  where N is the number of turns. The on-axis field of an infinite
    ;  solenoid is: Bz = mu * N * I, thus it would be: Bz = k * I.
    ; Calculation of Bz, thin coil and exact thick coil:
    ;IDL> print,  z00(1), z00_tc(1)   ; at: 171.25 Ams
    ;       6.5006499      6.3032689
    ;IDL> print, z00(1)/z00_tc(1)
    ;       1.0313141   -> but actually we want 6.57/b_ex
    ; Calculation of Bz for thick coil on axis using power fn expn:
    ; th = bfield_thickcoil( [0, 0, 0.], 171.25, /input_c, /thick)
    ; IDL> print, th
```

```
    ;       0.00000000      6.4672344
    ln_num1 = r2 + sqrt(r2*r2 + (z0 + l_sol/2.) * (z0 + l_sol/2.))
    ln_num2 = r2 + sqrt(r2*r2 + (z0 - l_sol/2.) * (z0 - l_sol/2.))
    ln_dnm1 = r1 + sqrt(r1*r1 + (z0 + l_sol/2.) * (z0 + l_sol/2.))
    ln_dnm2 = r1 + sqrt(r1*r1 + (z0 - l_sol/2.) * (z0 - l_sol/2.))
    fact_a  = (z0 + l_sol/2.) * alog(ln_num1/ln_dnm1)
    fact_b  = (z0 - l_sol/2.) * alog(ln_num2/ln_dnm2)
    B_field(1) =  (bmax/(2. * del_r_sol * l_sol)) * (fact_a - fact_b)
endif
if keyword_set(thick_coefs) then begin
     Bz    = dblarr(4)
     Br    = dblarr(4)
     ; NB: The program plotting_alongz.pro for a /thick_coefs w/ gaussian
     ;   plus quadratic fit to the thick-coil on axis field gives params.
     ;   (i.e., thick = plot_alongzr(0.0, 171.25, /input_car, /gauss, $
     ;   ,/thick, /oplot_gauss):
     a = zcoefs ; values of zcoefs from IDL handls fit_coefs above.
                ; The 7th element (c3) of a is s.t. c3/z^3 matches gaussian
                ;   fit at at z = +0.80 m.
     ; i.e.: A fit to exact B(0,z) at I_amps is used, passed
     ;  by the keyword: thick_coefs
     ; The coefficients at max amperags (171.25 A) are:
     ; a =  [6.3735356, -6.4373293e-09, 0.37420800, 0.11223847, $
     ;    -3.5286557e-10, -0.0092698317, (dipole fit coeff: c3),$
     ;      (z where switch: set in orbit.pro, probably z = +0.80 m)]
  case 1 of
  (z0 lt a(7)): begin ; Switch to dipole approx'n when z ge a(7) m
     ; Now calc. B_z(r,z) to 4 terms in the power series:
     r_2 = position(0)/2.
     u = (z0 - a(1))/a(2)
     u2 = u^2 & u3 = u2 * u & u3 = u3 * u & u4 = u3 * u & u5 = u4 * u
     u6 = u5 * u & u7 = u6 * u
     expn  =  a(0) * exp(-(u2/2.))
     Bz(0) =                 expn + a(3) + a(4) * z0 + a(5) * z0^2
     Bz(1) =       - r_2^2 * expn/a(2)^2 * (u2 + 1) + 2 * a(5)
     Bz(2) =   0.5 * r_2^4 * expn/a(2)^4 *         (u4 -  6*u2 +  3)
     Bz(3) = - 1/6.* r_2^6 * expn/a(2)^6 * (u6 - 15*u4 + 45*u2 - 15)
     Br = dblarr(4)
     Br(0) =     r_2   *(expn/a(2)   * u + a(4) + 2 * a(5) * z0)
     Br(1) = - 0.5 * r_2^3 * expn/a(2)^3 *                      (u3 -   3 * u)
     Br(2) =  1/12.* r_2^5 * expn/a(2)^5 *          (u5 -  10 *  u3 +  15 * u)
     Br(3) =-1/144.* r_2^7 * expn/a(2)^7 * (u7 - 21 * u5 + 105 * u3 - 105 * u)
     b_field = [total(br(*)), total(bz(*))]
     ; NOTA BENE: The fitted profile's SHAPE is strictly a fn. of
     ;   geometry of the coil (like alpha and beta in Coslett, 1950).
            end ; End of not-dipole-approx'n case.
  else: begin
     r_1   = position(0) &  r_2 = r_1 * r_1 &  r_3 = r_2 * r_1
     r_4  = r_3 * r_1    &  r_5 = r_4 * r_1 &  r_6 = r_5 * r_1
     r_7  = r_6 * r_1
     z3    = 1./(z0 * z0 * z0) & z4 = z3/z0 & z5 = z4/z0 & z6 = z5/z0
     z7    = z6/Z0        & z8 = z7/z0 & z9 = z8/z0 & z10= z9/z0
     Bz(0) =  1.        *  z3
     Bz(1) = -3.        * r_2 * z5
     Bz(2) =  45/4.     * r_4 * z7
     Bz(3) = -52.5      * r_6 * z9
     Br(0) =  3/2. * r_1 * z4
     Br(1) = -15/4. * r_3 * z6
```

```
     Br(2) =  105/16. * r_5 * z8
     Br(3) = -9.84375 * r_7 * z10
     b_field = a(6) * [total(br(*)), total(bz(*))]
   ; a(6) coeff. taken from handle passed from orbit.pro.
        end   ; End of dipole-approx'n case
  endcase
endif ; /thick keyword's endif
if keyword_set(printB) then print, b_field
return, b_field
very_end:
end
```

APPENDIX B

The `orbit.pro` program

```
;===========================================
; To calculate and plot field strength and its
;  components on-axis, using bfield.pro
; IDL Code T.O'D. 30aug97
; Directory=> ::pnaxp[odonnell.sol_simulation]
; Edited:   17jul99 to calc. old code's thin
; cylindrical shell approx'n and new
; thick shell (exact) on-axis B field.
; Ref: Szilagyi, M, 1988. Added /thick_coil
; which calls bfield.pro
; -NOTE: Using cryomagnetics' k value * I (amps) gives
; the field at center off by about 3% for thick coil.
; Thick coil also falls off faster than thin coil approx.
;       - 17jul99: added a gaussian + quadratic (6 coefficient)
; fitting routine. Since it is v. difficult to calc. all
; the higher-order derivatives for the off-axis thick-coil field's
; components as a fn of derivatives of on-axis.  We will fit
; it with a Gaussian + quadratic, and THEN take derivatives of this
; much simpler on-axis expression. This is similar to the aprox'n
; of GLASER. Ref: ...
; -When /gaussian invoked, the returned array is dblarr(zpoints, 4),
; where ret(*,0) is zaxis labels, ret(*,1) is B_z values along axis,
; ret(*,2) is the best-fitted gaussian+quadratic, and ret(*,3)'s
; first 6 are the fit coefficients (see IDL's gaussfit.pro function.)
; -19jul99 Make overplotting of the gaussian fit a keyword option
; called: /oplot_gauss
; -20jul99 added /exact to modify /thick_coil: see bfield.pro
; -20jul99 added /noplot to enable being called by bfield, orbit, etc.
; -22jul99 changed bfield.pro's /thick_coil to /thick_coefs due to
;   errors in passing keywords w/ same name between programs.
;===== First included function =========================================
; Purpose:  Calculate exact thick coil field at I_amps, do gaussian-plus-
;       quadratic fit to it and return the six fit coefficients to
;       the main program orbit.pro, above.
; Template: plot_alongzr.pro program
; Returns:  Six coefficients of the fit.
; Date:     22jul99
;-----------------------------------------------------------------------
function on_axisthick, I_amps, min_z, max_z
print, '----- on_axisthick.pro --- fitting to exact on-axis field ----
print, '                I_amps = ',I_amps
```

```
print, ’ min_z  = ’,min_z
print, ’ max_z  = ’,max_z
print, ’       zrange = ’,max_z - min_z
tmp =  max_z - min_z
zlength = (max_z - min_z)
zpoints = 1024                  ; Insure max in(*,0) is just beyond max_z:
zlength = zlength + (zlength/float(zpoints))
zaxis      = (dindgen(zpoints) * zlength/(zpoints-1)) + min_z
z_exact = dindgen(zpoints, 2)
for i = 0, zpoints-1 do begin
    z_exact(i,*) = bfield([0.0, 0.0, zaxis(i)],  $
        I_amps, /input_cartesian, /exact) * 1.03 ;<- empitical 3% calib’n
endfor
; -- Gaussian-plus-quadratic fitting code:
zfit    = zaxis - zaxis
nnterms = 4; 5 6 Avoid NEG linear term.; Must be declared before call gaussfit.
zret    = dblarr(nnterms)
zfit    = gaussfit(zaxis, z_exact(*,1), zret, nterms = nnterms)
; Take the value at 0.8 m of the fit and make that the point where
;   the fit will shift from gaussian -> c3/z^-3 dipole approx. We determine
;   c3 to accomplish this:
p3 = min(where(zaxis ge 0.8))
z3 = zaxis(p3)
v3 = zfit(p3) ; Value of fitted curve at about +0.81 m
c3 = v3 * z3^(3.) ; Require: v3 = c3/z^3. Find c3.
print, p3, z3, v3, c3
     ; Make sure returned vector is 6 terms to comply w/ orbit.pro,
     ;   no matter how many fitted coefficients (always are le 6).
zdum = dblarr(8) ; 7th element wll be c3, 8th is z3.
zdum(0: n_elements(zret)-1) = zret
zdum(6:7) = [c3, z3]
zret = zdum
print, ’    fit coefficients  = ’, zret
if n_elements(zret) ne 8 then begin
 print,’ ------- ERROR -------- orbit.pro ----------------------- ’
 print,’ ------- n terms in zret not six, but: ’, n_elements(zret)
 print, ’ ’
endif
     ; Store results of fit in an IDL handle (dynamic memory, similar
     ;   to a common block or pointer). Ref: p. 11-19 IDL User Guide:
; Creates a top-level handle if first time running the program:
fit_coefs = 1. ; Needs to be a declared var.
if handle_info(fit_coefs) eq 0 then fit_coefs = handle_create()
junk = handle_create(fit_coefs, value=zret)  ; Creating a handle.
if handle_info(fit_coefs) then                   $
    print, "  ----- Valid handle ’fit_coefs’ created."
; Debug print, ’ -----the fit coefficients are: ’, zcoefs
if !d.name eq ’x’ then begin
    plot, zaxis, zfit, charsize = 2, psym = -1,  $
     symsize = 0.2, xstyle = 1, ystyle = 2
    oplot, zaxis, z_exact(*,1)
    window, !d.window + 1
endif
; Steps in other programs to retrieve the handle’s variable:
; hhand = handle_info(fit_coefs, /first_child)
; handle_value, hhand, tmp ; Retrieve and assign to a var (’tmp’ here).
; print, " ----- new value is  = ", hhand
return, zret
```

```
end
; === Begin main function: orbit.pro ==========================
function orbit, r, phio, min_z, E, amu, $
    qo, phi_vo, theta_vo, max_z, Del_x,  $
    I_amps, postscript = postscript,  $
    encapsulated = encapsulated,  $
    save_file = save_file, no_plot = no_plot, $
    focal_position = focal_position, twin = twin, $
    thick_coil=thick_coil
print,'  ---- orbit.pro ---- thick_coil [t, f] = ' , thick_coil
if keyword_set(thick_coil) then begin
     ; Get the gaussian-plus-quadratic coefficients for B(0,z)
     ;   at THIS I_amps:
    gaussfits = 1
    ffits = dblarr(6)
    ffits = on_axisthick(I_amps, min_z, max_z)
    ; Results are stored in handle (IDL dynamic memory as 'fit_coefs'.)
endif  else begin
    gaussfits  = 0
endelse
mydevice = !d.name
; Note: focal_position keyword doesn't write any files, just saves final
;   position of the ion at z_max (focal plane) in the array which is
;   returned.  This is especially for use when this fn is called by
;   sol_acceptance.pro.
atomic_no = qo
z = min_z
if keyword_set(twin) then begin
    Cryo_rad = 0.125 ; id is .15, but pipe is .125 m
endif else begin
    Cryo_rad = 0.225425
endelse
phi      = phio * !dtor ; Convert degrees to radians
phi_v    = phi_vo *!dtor ;    "       "    "     "
theta_v  = theta_vo * !dtor ;    "       "    "     "
q        = qo * 1.60217733d-19 ; Coulombs * ion's (pos.) charge state.
F        = dblarr(3) ; Magnetic force
V        = dblarr(3) ; Velocity ith step
V1       = V  ; Velocity i+1th step
Vel      = beta(E, amu) * 2.998792458d+8
     ; Returns [m/s]. beta.pro = user fn
mass     = amu * gamma(E, amu) * 1.6605402d-27
     ; gamma.pro = user fn.  Ion mass
     ; (amu*gamma*u) is in kilograms.
if Vel ne 0.0 then begin
    Del_t = Del_x/Vel
endif else begin
    Vel   = Vel + 0.000000000000001
    Del_t = Del_x/Vel
endelse
P  = dblarr(3)            ; Position(s)
P1 = P                   ; Note: [phi, r, z] is IDL's default
     ;  ordering.  Now, convert to cartesian:
P    = [r * cos(phi), r * sin(phi), z]  ; P = [Px, Py, Pz]
V(0) = Vel * sin(theta_v) * cos(phi_v)  ; V_x = ...
V(1) = Vel * sin(theta_v) * sin(phi_v)  ; V_y = ...
V(2) = Vel * cos(theta_v) ; V_z = ...
if (keyword_set(focal_position) ne 1) then begin
```

```
    openw, u, 'orbit.dat', /get_lun
    printf, u, p
endif
r_ = r ; Set r_ for First pass through while
     ;  loop to test radial distance.
;=======================
; Insert code here to represent physical obstructions which would
; obstruct the ion's orbit.  Included is:
; 1) Cryostat ID,  2) "Neutron shadow bar along z-axis,
; 3) Brass aperture ring at entrance of rear chamber.
;-----------------------
s_bar = [0.515, -0.09, 0.01905] ; [z_max, z_min, r] of BigSol shadow bar.
if keyword_set(twin) then s_bar = [-40., 40, -1. ]
       ; Can put faraday cup dimensions also...
increments = 1.    ; Count increments till hit focal plane
       ;   to get total flight path at constant
       ;   velocity -> time of flight.
while (r_ le cryo_rad)   and $ ;1 Cryostat limit
   (P(2) le max_z) $ ; <-EITHER this line in OR next 4 lines
   ; (P(2) le max_z)   and    $ ;2 Focal plane limit
   ;(P(2) ge min_z)      and    $ ;3 Stops doubled-back orbits
   ; (((P(2) le s_bar(0)) and  $ ;4 Shadow bar limits
   ;   (P(2) ge s_bar(1)) and  $ ;
   ;   (r_ le s_bar(2))) ne 1) $ ;Note: r on 1st pass is the starting;
    do begin   ; r, thereafter calc'd below.
    ; Neutron shadow bar references:
     ; Logbook #1 of 3 & 4,1993 p. 109 for radius
     ; Ibid. p. 80 for length
     ; Ibid, p. 29 for position)`
     ; Test is "while...NOT inside shadow bar..."
    ;=======================
    if keyword_set(twin) then begin
        Bo = bfield(P(*),I_amps,/input_cartesian, /twin)
    endif else begin
        Bo = bfield(P(*), I_amps, /input_cartesian, thick_coefs = gaussfits)
     ; Setting keyword /thick_coefs tells bfield,pro to
     ;  retrieve dynamic-memory handle 'fit_coefs' value.
    endelse  ; Two-element Bo = [Bo(r), Bo(z)], as Bo(phi) d.n.e.
    p_theta = atan(P(1), P(0))
    B = [Bo(0) * cos(p_theta), Bo(0) * sin(p_theta), Bo(1)]
    F(0) =  q * (V(1)*B(2) - V(2)*B(1)) ; |Units=> Coulomb-m/s-Tesla
    F(1) = -q * (V(0)*B(2) - V(2)*B(0)) ; |      = Coul-m/s-N/(mI)
    F(2) =  q * (V(0)*B(1) - V(1)*B(0)) ; |      = N
    for i = 0, 2 do begin
        V1(i) = V(i) + (F(i)/mass) * Del_t
        P1(i) = P(i) + V(i) * Del_t + 0.5 * (F(i)/mass) * Del_t^2
    endfor
    V = V1 & P = P1 ; Update for next iteration.
    if (keyword_set(focal_position) ne 1) then begin
     printf, u, p ; No file written if only want focal_pos'n
    endif
    r_ = sqrt(P(0)^2 + P(1)^2) ; To be used in while conditions above
    increments = increments + 1
endwhile
if (keyword_set(focal_position) ne 1) then begin
    free_lun, u ; Closes file and deallocates file unit.
    print, 'The file - orbit.dat - has been written.'
    if keyword_set(save_file) then begin
```

```
     dummy = read_data('orbit.dat',/save_file)
    endif else begin
     dummy = read_data('orbit.dat')
    endelse
endif
if keyword_set(no_plot) or keyword_set(focal_position) $
    then goto, skip_plot
if keyword_set(postscript) or keyword_set(encapsulated) then begin
    make_ps,'orbit.ps'
    if keyword_set(encapsulated) then begin
     device, /encapsulated
    endif else begin
     device, encapsulated = 0
    endelse
    device, /portrait
    device, ysize = 4.0, /inches
    !p.color = 1
    print, "IDL postscript !p.color set to:", !p.color
endif
plot_3dbox,dummy(*,2),dummy(*,1),dummy(*,0), $
    /xy_,/xz_,/yz_, $
    psym = 1,  $
    az =  15, ax = 35, $
    charsize = 2.1, /save, $
    yrange = [-cryo_rad, cryo_rad], $
    zrange = [-cryo_rad, cryo_rad],  $ ;[-0.2, 0.2], $
    xrange = [min_z, max_z],  $
    ystyle = 1, zstyle =  1, $
    ;2-9-98    title = 'UM BigSol - Simulation',$
    xtitle = '!17Z !6[m]!17', $
    ytitle = '!17X !6[m]!17', $
    ztitle = '!17Y !6[m]!17'
    ;xtick_get = vx, ytick_get = vy, ztick_get = vz
zaxis = fltarr(150,3)
for i=0,149 do zaxis(i,2) = (i*(max_z-min_z)/150.)
usersym ,[-.05, 0,.05], [0,0,0] ; Small dashes on symmetry axis
plot_3dbox, zaxis(*,2)+min_z, zaxis(*,1), zaxis(*,0), /noerase, /t3d, $
    psym = 8, $
    /xy_,/xz_,/yz_, $
    az = 15, ax = 35, $
    charsize = 2.1, /save,                      $
    yrange = [-cryo_rad, cryo_rad], $
    zrange = [-cryo_rad, cryo_rad],  $ ;[-0.2,0.2]
    xrange = [min_z, max_z],                    $
    ystyle = 1, zstyle =  1,                    $
    ;2-9-98    title = 'UM BigSol - Simulation',$
    xtitle = '!17Z !6[m]!17',                   $
    ytitle = '!17X !6[m]!17',                   $
    ztitle = '!17Y !6[m]!17'
;2-9-98 xyouts,0.40,-0.02,isotope_name_q(amu,fix(atomic_no),   $
;2-9-98    fix(qo)),/norm,charsize = 2.5, /t3d
;2-9-98str = strtrim(strmid(strtrim(e/amu,2),0,4)+' MeV/u'+', '  $
;2-9-98      +strmid(strtrim(theta_Vo,2),0,4)+'!9%!3',2)
;2-9-98str1 = strmid(strtrim(I_amps,2),0,4)+' Amps'
;2-9-98  xyouts,0.52,-0.02, strtrim('!5'+str), /norm, charsize = 2.5, /t3d
;2-9-98  xyouts,0.52,-0.02, strtrim('!5!C'+str1), /norm, charsize = 2.5, /t3d
```

```
;2-9-98 begin addition:
; Add axes in front to keep box plot from looking inside-out:
zz = strarr(10)   ; Make plenty-long blank strings
zz(*) = ' '      ; to make blank axes tick names.
axis, -2., -0.22, 0.22, zaxis = 1, zticknamee = zz, zstyle = 1, /t3d
axis, -2., -0.22, 0.22, yaxis = 0, ytickname = zz, ystyle = 1, /t3d
axis, -2., -0.22, 0.22, xaxis = 0, xtickname = zz, xstyle = 1, /t3d
str0 = strmid(strtrim(theta_Vo,2),0,3)+'!9%!17'
str0 = strtrim('!7H!I!17!8lab!17!N='+str0)
str1 = strmid(strtrim(I_amps,2),0,4)+' !17A'
str2 = round(convert_Eqa_brho(E, qo, amu) * 100.)/100.
str2 = strmid(strtrim(str2,2),0,4)+'!17 T-m'
xyouts, 2.0, 0.225, strtrim(str2+', '+str1+', '+str0,2),$
    Z = 0.24, /data, alignment = 0.5, $
    charsize = 1.9, text_axes = 1, /t3d
    ; Warning: XYZ in the 3d_box plot routine is not same as our
    ;   XYZ axes' labels. Note Text_axes = 0 is xy plane
xyouts, 6., 0.0, '!17Focal Plane',  $
    Z = 0.24, /data, alignment = 0.5,               $
    charsize = 2.5, text_axes = 5,  $
    orientation = -90, /t3d
if keyword_set(postscript) or keyword_set(encapsulated) then begin
    device,/close
    set_plot, mydevice
endif
skip_plot:
close, /all ; I.E.: Close all opened files.
if keyword_set(focal_position) ne 1 then begin
    print, ' ---------------------------------------------------- '
    print, '--> Nothing is returned unless /focal_position (it is '
    print, '     not now set), or /save_file is set. Then data    '
    print, '     will be in the file                              '
    print, '     orbit.dat.                        <orbit.pro>  '
    print, ' ---------------------------------------------------- '
endif
Vel = beta(E, amu) * 2.998792458d+8
p   = [p, float(increments), del_x, Vel]
      ; p is the last point in the orbit
      ;  in cartesian coors: [x,y,z] in [m]
      ;  Return this and total orbit steps,
      ;  meters/step, and ion (relativistic)
      ;  velocity.
return, p
end
;---------------------------------
```

APPENDIX C

The `acceptance.pro` program

```
;==========================================================================;
This is acceptance.pro
; This is a [.accept_nim] version which
; calls orbit.pro
; - 01mar99
;
; This program repeatedly calls orbit.pro over a range of
;  values of theta_vo (initial angle of emission of an ion, of
;  its initial velociry vector) and for a range of Br (B-rho)
;  values for a constant geometry (image distance Z_obj, object
;  distance Z_img, and magnet cryostat bore inner radius R, etc.)
;  and constand field setting, amps.
; The initial azimuthial angle-of-emission phi_vo will be held
;  constant as well, in result of which the final position phi
;  of the particle at the focal plane represents delta_phi of the
;  ion through its orbit.
; The purpose of this program is to produce the focal plane radial
;  position of a particle as a fn of B_rho and theta_vo so that the
;  solenoid's data can be calibrated to cross sections, or,
;  conversely, so that data generated from models can be filtered
;  throught this and compared to actual data.
;====================================================================
; Language: IDL 4.*.*
; By:     T. O'Donnell  UMichigan Nuclear Group   08Sep1997
; email: tom.odonnell@umich.edu
; Changes:  12nov97: allow command line def'n of steps_x and steps_y,
; esp. for lookng at focal spot closely; and twin added
; keyword to use UM/UND TwinSol paramaters Vs. BigSol
; defaults.
;     05jul98: added second file below to run same b-rho, vary
; theta:  acceptance_brho_c_thet_v.pro
;     11jul98 repaired 'bug' where /twin not in enough cases
;     01mar99 This now calls orbit.pro to produce
; arrays for NIM BigSol Spectrometer paper.
; Re-activated the shadow-bar condition there...
;     02mar99 Removed all but one case needed to end bug
; which was returning empty arrays ...
;     -21jul99 Added keyword /thick_coil to conform with new
;     bfield.pro option.  See bfield.pro code for explanation.
;====================================================================
function acceptance, ro, phio, z_obj, z_img, Br_min, Br_max,       $
      q, amu, phi_vo, theta_min, theta_max, del_x,  $
```

```
      steps_x, steps_y, I_amps, info = info,         $
      no_plot = no_plot, twin = twin,  $
      thick_coil = thick_coil
; This will produce a square matrix r = r(theta, Brho) of radial
;  position at the focal plane.
if (keyword_set(info) ne 1) then info = string('no_name_supplied')
     ; Info is returned as a string
     ;  used for naming files, etc.
if keyword_set(thick_coil) then tthickcoil = 1 else tthickcoil = 0
arr = dblarr(steps_x +1, steps_y +1, 3) ; To hold orbit.pro output
     ;  as fn of Theta, Brho.
tof = dblarr(steps_x +1, steps_y +1)
steps_x = float(steps_x)
steps_y = float(steps_y)
theta_step = (theta_max - theta_min)/steps_y
theta = (findgen(steps_y + 1) * theta_step) + theta_min
     ; Theta_min ;theta values to go through
Br_step = (Br_max - Br_min)/steps_x
Br = (findgen(steps_x + 1) * Br_step) + Br_min; Brho values to go through.
for i = 0, steps_x do begin
    for j = 0, steps_y do begin
        Ti =  convert_brho_eqa(Br(i), q, amu)
                orb_ = orbit(ro, phio, z_obj, Ti, amu, q, phi_vo,  $
                        theta(j), z_img, del_x, I_amps, /no_plot, $
                        /focal_position, thick_coil = tthickcoil)
    arr(i, j, *) = orb_(0:2)
         ; orb_(N_elements(orb_(*,0))-1, *)
                            ; Save ion position at end of orbit:
                            ;  i.e., at focal plane unless hit
                            ;  the cryostat bore radius.
    tof(i, j) = orb_(3) * orb_(4)/orb_(5) ; steps*(m/step)/velocity
    endfor
endfor
arr1 = create_struct('foci',arr,'tof',tof,'theta',theta,'brho',Br,'info',info)
return, arr1
end
;---------------------------------------------------------------------
; This is: acceptance_brho_c(onstant)_thet_v(ariable).pro
; Added 05jul98, see notes above.
; NOTE arguments are same but some no longer operative.  I.E.:
; br_min, & steps_s (i.e. no. of steps of Brho to compute).
; Whereas Br_min is now the ONE Brho calculated at several
; Thetas.
;---------------------------------------------------------------------
function acceptance_brho_c_thet_v, ro, phio,         $
      z_obj, z_img, Br_min, Br_max,              $
                         q, amu, phi_vo, theta_min, theta_max, del_x, $
                         steps_x, steps_y, I_amps, info = info,       $
                         no_plot = no_plot, twin = twin
if (keyword_set(info) ne 1) then info = string('no_name_supplied')
                                 ; Info is returned as a string
                                 ;  used for naming files, etc.
arr = dblarr(steps_x +1, steps_y +1, 3) ; To hold orbit.pro output
                                 ;  as fn of Theta, Brho.
tof = dblarr(steps_x +1, steps_y +1) ; To return time of flight.
;steps_x = float(steps_x) ; Only one step in Brho here.
steps_y = float(steps_y)
```

```
theta_step = (theta_max - theta_min)/steps_y
theta = (findgen(steps_y + 1) * theta_step) + theta_min
                                ; Theta_min ;theta values to go through
Br = x_step
    for j = 0, steps_y do begin
        Ti =  convert_brho_eqa(Br(i), q, amu)
        if keyword_set(no_plot) then begin
           if keyword_set(twin) then begin
                orb_ = orbit(ro, phio, z_obj, Ti, amu, q, phi_vo,  $
                        theta(j), z_img, del_x, I_amps, /no_plot,      $
                        /focal_position, /twin, thick_coil = tthickcoil)
           endif else begin
                orb_ = orbit(ro, phio, z_obj, Ti, amu, q, phi_vo,  $
                        theta(j), z_img, del_x, I_amps, /no_plot,      $
                                /focal_position, thick_coil = tthickcoil)
           endelse              ; Ends choice of BigSol Vs TwinSol.
                arr(i, j, *) = orb_(*)
        endif else begin        ; Ends no_polot choice.
           if keyword_set(twin) then begin
                orb_ = orbit(ro, phio, z_obj, Ti, amu, q, phi_vo,  $
                        theta(j), z_img, del_x, I_amps, /twin,  $
     thick_coil = tthickcoil)
           endif else begin
                orb_ = orbit(ro, phio, z_obj, Ti, amu, q, phi_vo,  $
                        theta(j), z_img, del_x, I_amps,  $
     thick_coil = tthickcoil)
           endelse
     endelse
        arr(i, j, *) = orb_(N_elements(orb_(*,0))-1, *)
                                ; Save ion position at end of orbit:
                                ;  i.e., at focal plane unless hit
                                ;  the cryostat bore radius.
     tof(i, j)    = orb_(3) * orb_(4)/orb_(5) ; steps*(m/step)/velocity
    endfor
;endfor ; Only one Brho step now
arr1 = create_struct('foci',arr,'tof', tof,'theta',theta,'brho',Br,'info',info)
return, arr1
end
```

BIBLIOGRAPHY

BIBLIOGRAPHY

[Allatt 1998] R. Allatt et al, in [ENAM 98], p. 570-71.

[Anne 1987] R. Anne, D.Bazin, A.C.Mueller, M.Langevin, J.C.Jacman, Nucl. Inst. Meth. A257 (1987) p. 215.

[Anne 1996] Nucl. Inst. Meth. B. Vol. 126, No. 1-4 (Apr. 1996), pp. 279-283.

[Arnold 1989] M. Arnold, in *The First International Conference on Radioactive Nuclear Beams*; ed. W.D. Meyers, et al, (Singapore; World Scientific; 1989) p. 209.

[Audi & Wapstra 1995] G. Audi, O. Bersillion, J. Blochot, A. H. Wapstra, Nucl. Phys. A 634 (1997) p. 1.

[Balbes 1995] *"Cross Sections and Reaction Rates of d+^{8}Li Reactions Involved in Big Bang Nucleosynthesis,"* M.J. Balbes, M.M. Farrell, R.N. Boyd, X. Gu, M. Hencheck, J.D. Kalen, C.A. Mitchell, J.J. Kolata, K. Lamkin, R. Smith, R. Tighe, K. Ashktorab, F.D. Becchetti, J. Brown, D. Roberts, T.F. Wang, D. Humphreys, G. Vourvopoulos, and M.S. Islam, Nucl. Phys. A584 (1995) pp. 315-334.

[Bai 1998] *"Mass measurement in the fp-shell using the TOFI spectrometer,"* Y. Bai, D.J. Vieira, H.L. Seifert & J.M.Wouters, in [ENAM 1998], pp. 90-93.

[Baron 1995] E.Baron, J. Gillet, M.Ozille, Nucl. Inst. Meth. A. Vol. 362 (Aug. 1, 1995), pp. 90-93.

[Bazin 1991] *"Intermediate energy heavy ion reactions and the production of nuclei far from stability,"* D.Bazin, D.Guerreau, R.Anne, D.Guillemaud-Mueller, C.Grunberg, A.C.Mueller, M.G.Saint-Laurent, L.Tassan-Got, D.Bachelier, C.D.Bacri, R.Bimbot, B.Borderie, J.L.Boyard, F.Clapier, C.Donzaud, T.Hennino, M.F.Rivet, P.Roussel,D.Disdier, B.Lott, N.Bauer, J.Kapusta, *Proceedings of the 7th Winter Workshop on Nuclear Dynamics.* Advances in Nuclear Dynamics. 26 Jan.-2 Feb. 1991; Key West, FL, USA, World Scientific, Singapore; 1991; xii 326 pp. 60-70.

[Bazin 1990] Bazin et al, Nuclear Physics A515 (1990) pp. 349-364.

[Becchetti & Kolota 1997] *"Proceeding fo the 14th International Conference on the Application of Accelerators in Research and Industry,"* F.D. Becchetti, & J.J. Kolata, Denton, Texas, USA, November 1996, AIP conference prod. No. 392 (1997) pp. 369-375.

[Becchetti & Kolata2 1997] *“Low-Energy Radioactive Beam Experiments using the UMD-UND Solenoid RNB Apparatus at the UND Tandem: Past, Present and Future,”* F.D. Becchetti and J.J. Kolata, Proc. 14th Int'l. Conf. on the Application of Accelerators in Research and Industry, Denton, Texas, November 1996, J.L. Duggan and I.L. Morgan, editors, AIP Conference Proceedings 392 pp. 369-375 (AIP Press, Woodbury, New York, November 1997).

[Becchetti2 1994] *“Installation and In-Beam Tests of a Large-Bore 7T Superconducting Solenoid Reaction-Product Collector,”* F.D. Becchetti et al., Nucl. Instr. Meth. B79 , (1994) pp. 326-329.

[Becchetti3 1989] *“A Radioactive Beam Facility using a Large Superconducting Solenoid,”* F.D. Becchetti, J.J. Kolata, W.Z. Liu, D.A. Roberts, and J.W. Jänecke, Nucl. Instrum. Meth. B40/41, (1989) p. 503.

[Becchetti4 1990] *“Production and Use of Radioactive ^{7}Be beams,”* F.D. Becchetti et al, Nucl. Instrum. Methods A294, (1990) pp. 26-30.

[Becchetti5 1990] *“Total Nuclear Reaction Probabilities and Average Cross Sections for 16 to 23 MeV ^{6}Li in Silicon,”* F.D. Becchetti et al, Nuclear Physics A516,(1990) pp. 416-428.

[Becchetti6 1991] *“Production and Use of ^{6}He, ^{7}Be, ^{8}Li, ^{12}B and Metastable Nuclear Beams,”* F.D. Becchetti et al, Nucl. Instrum. Methods, B56/57, (1991) p. 554.

[Becchetti7 1992] *“Reaction rates for ^{8}Li(p,α) and ^{8}Li(p,n,α) and their Effect on Primordial Nucleosynthesis,”* F.D. Becchetti, J.A. Brown, W.Z. Liu, J.W. Jänecke, D.A. Roberts, J.J. Kolata, R.J. Smith, K.L. Lamkin, A. Morsad, R.E. Warner, R.N. Boyd, and J.D. Kalen, Nucl. Phys. A550, (1992) pp. 507-516.

[Becchetti8 1993] *“^{2}H Induced Reactions on ^{8}Li and Primordial Nucleosynthesis,”* F.D. Becchetti, M. J. Balbes et al., Phys. Rev. Lett. 71 (24)(1993) p. 3931.

[Becchetti9 1993] *“Systematics of ^{8}Li-Induced Radioactive Beam Reactions: $E = 13$–20 MeV,”* F.D. Becchetti et al., Phys. Rev. C 48 , (1993) pp. 308-318.

[Becchetti10 1999] *“Production of Exotic (or Polarized) Low-Energy Radioactive Beams via Two Successive Nuclear Reactions: Tertiary Beams,”* F.D. Becchetti, M.Y. Lee, T.W. O'Donnell, D.A. Roberts, J.J. Kolata, V. Guimarces, D. Peterson, and P. Santi, Nuclear Instruments and Methods in Physics Research A 422 (1999) pp. 505-509.

[Becchetti11 1999] *“CoulEx-NucleEx Interference in ^{8}Li RNB Inelastic Scattering near the Coulomb Barrier,”* F.D. Becchetti et al, presented at Centennial Meeting of the American Physical Society, BAPS Vol.44, No.1, Part I (1999) p. 259.

[Becchetti12 1976] *“Response of Plastic Scintillator Detectors to Heavy Ions, $Z < 35$, $E < 170$ MeV,”* F.D.Becchetti, C.E.Thorn and M.J.Levine, Nucl. Instrum. Methods 138, 93-104 (1976) pp. 93-104.

[Becchetti & Greenless 1969] F.D. Becchetti Jr., and G.W. Greenless, Phys. Rev. 12, 1190 (1969) pp. 1190-1240.

[Bertsch 1972] G. F. Bertsch, *"The Practitioner's Shell Model,"* (New York: North-Holland/American Elsevier, 1972).

[Bernas 1994] *"Projectile fission at relativistic velocities: a novel and powerful source of neutron-rich isotopes well suited for in-flight isotopic separation."* M.Bernas, S.Czajkowski, P.Armbruster, H.Geissel, P.Dessagne C.Donzaud, H.R.Faust, E.Hanelt, A.Heinz, M.Hesse, C.Kozhuharov, C.Miehe, G.Munzenberg, M.Pfutzner, C.Rohl, K.H.Schmidt, W.Schwab, C.Stephan, K.Summerer, L.Tassan-Got, B.Voss, Phys. Lett. B331, (1994).

[Bernas 1997] *"Discovery and cross-section measurement of 58 new fission products in projectile-fission of* $750{\cdot}A\ MeV\ {}^{238}U$*,"* M. Bernas, C. Engelmann, P. Armbruster, S. Czajkowski, F. Ameil, C. Bvckstiegel, Ph. Dessagne, C. Donzaud, H. Geissel, A. Heinz, Z. Janas, C. Kozhuharov, Ch. Miehi, G. M—nzenberg, M. Pf—tzner, W. Schwab, C. Stiphan, K. S—mmerer, L. Tassan-Got and B. Voss, Phys. Lett. B415 (1997), pp. 111-116.

[Bernas 1998] M. Bernas, in *Exotic Nuclei and Atomic Masses, Bellaire, MI, 1998;* ed. B.M. Sherrill, D. J. Morrissey & C.N. Davids, (Woodbury, NY: AIP Conference Proceedings, 1998), pp. 664-671.

[Bethe & Bacher 1936] H.A.Bethe and R.F.Bacher, Rev. Mod. Phys. 8 (1936) p. 82.

[Bjorken & Grotch 1987] *"Quantum Electrodynamics,"*, in "Nuclear and particle physics source book," pp. 301-307, S.P.Parker, Ed., (New York: McGraw-Hill, 1987).

[Black 1996] C,T.Black, D.C.Ralph and M.Tinkham, Phys. Rev. Lett 76, 688 (1996),

[Bohr & Klackar 1937] N. Bohr, F. Kalckar, Kgl. Danske Videnskab. Selskab, Mat. fys. Medd. 14, 10 (1937).

[Bohr, Mottelson & Pines 1958] A. Bohr, B.R. Mottelson, and D. Pines, Phys Rev. 110, 936 (1958); A. Bohr, & B.R. Mottelson, vol. 1, (1958).

[Bohr & Mottelson 1969] A.Bohr and B.Mottelson, *"Nuclear Structure,"* Vol. 1 and 2, Benjamin, Reading Mass, (1969).

[Boyd, 1993] R.N.Boyd, in [RNB 1993], pp. 445-451.

[Bromley 1985] D.Allan Bromley, *"Treatise on Heavy-Ion Science,"*(New York: Plenum Press, 1985).

[Brown 1993] J.B. Brown, unpublished thesis, University of Michigan, Ann Arbor, MI 1993.

[Brown2 1995] *"Proton Scattering from an Excited Nucleus* ($^{18}F^m$, $J\pi = 5^+$, $E_x = 1.1$ *MeV) Using a* γ *Ray Tagged Secondary Isomeric Nuclear Beam,"* J.B. Brown, F.D. Becchetti, J. Jänecke, D.A. Roberts, D.W. Litzenberg, T.W. O'Donnell, R.E. Warner, N.A. Orr, and R.M. Ronningen, Phys. Rev. C 51 (1995) pp. 1312-1319.

[Brown3 1992] *"Coulomb Excitation of* ^8Li*,"* J.A. Brown et al, Phys. Rev. Lett. 66, (1992) p. 2452.

[Burcham 1979] *"Introduction to Nuclear Physics,"*W.E. Burcham, Longman Inc., New York, (1979).

[Burge 1988] *"Atomic Nuclei and their Particles",* E. J. Burge (2nd Ed. , Oxford Press; 1988).

[Caussyn 1993] *"Cross Sections for the Primordial Reaction* $^8Li(p,n)^8Be_{g.s.}$ *at* $E_{c.m.} = 1.5$ *MeV,"* D.D. Caussyn, N.R. Fletcher, K.W. Kemper, E.E. Towers, J.J. Kolata, K.L. Lamkin, R.J. Smith, F.D. Becchetti, J.A. Brown, J.W. Jänecke, D.A. Roberts and L. Gay, Phys. Rev. C 47 pp. 387-391.

[Carey 1987] *"The Optics of Charged Particle Beams,"* D. C. Carey, (Harwood Academic Publishers, New York; 1987).

[Cerney 1984] J. Cerney in *Treatise on Heavy-Ion Science;* ed. by A. Bromley (New York: Plenum Press; 1984).

[Chadwick 1932] Chadwick, J., Proc. R. Soc. A136 (1932) p. 692.

[Cockcroft & Walton 1932] J.D. Cockroft, and E.T.S. Walton, Proc. R. Soc. A129, 477 (1930) and Proc. R. Soc. A137 (1932) p. 229.

[Coffin and Engelstein 1985] *"Time-of-Flight Systems for Heavy Ions,"* J.P. Coffin, P. Engelstein, in *"Treatise on Heavy-Ion Science,"* Vol. 7; ed. D. Allen Bromley (New York: Plenum Press; 1985)pp. 275-327.

[Coslett 1950] *"Introduction to Electron Optics,"* V.E. Coslett, (Oxford: Clarendon Press; 1950).

[de Broglie 1923, 1924] L. de Broglie, Nature 112 (1923) 540; *Thesis*, Paris, 1924, Ann. Physique (10) (1925) 2.

[deShalit & Feshbach 1974] *Theoretical Nuclear Physics*, A. deShalit $ H. Feshbach, Vol. 1: Nuclear Structure (New York: Wiley Classics Library; 1990).

[DeYoung 1998] *"Fusion of a neutron skin nucleus: The* $^{209}Bi(^6He,4n)$ *reaction,"* P.A. DeYoung et al, Phys Rev C58 (6) (1998) pp. 3442-3444.

[Einstein 1905] *"On the Movement of Small Particles Suspended in a Stationary Liquid Demanded by the Molecular-Kinetic Theory of Heat,"* A. Einstein, Ann. d. Phys., 17,(1905) p. 549.

[Einstein2 1906] *"On the Theory of the Brownian Movement,"* A. Einstein, Annalen der Physik (4), 19, (1906), pp. 371-381.

[Einstein3 1906] *"A New Determination of Molecular Dimensions,"* A. Einstein, Annalen der Phusik (4), 19, (1906), pp. 289-306.

[Einstein4 1907] *"Theoretical Observations on the Brownian Motion,"* A. Einstein, Zeit. für Elektrochemie, 13, (1907), pp. 41-42.

[Einstein5 1908] *"The Elementary Theory of the Brownian Motion,"* A. Einstein, Zeit. für Elektrochemie, 14, (1908), pp. 235-239.

[Enge 1966] *"Introduction to Nuclear Physics,"* H.A. Enge, (Reading, MA: Addison-Wesley Publishing Co; 1980).

[El-Kareh & El-Kareh 1970] *"Electron Beams, Lenses and Optics,"* A. B. El-Kareh, and J.C. J. El-Kareh,(New York: Academia Press; 1970).

[Evans 1955] R.D. Evans, *"The Atomic Nucleus,"* R.D. Evans, (New York: McGraw-Hill; 1955), op. cit. Burcham, (1979), p. 197.

[Fermi 1949] *"Notes on Thermodynamics and Statistics,"* E. Fermi, (Chicago: University of Chicago; 1966) pp. 154-158. (Reprinted from Fermi's handwritten lecture notes from 1949.)

[Feshbach Porter & Weisskopf, 1953] H. Feshbach, C.E. Porter and V.F.Weisskoff Phys. Rev. 99, 166 (1953).

[Foldy 1951] L.L. Foldy, Phys. Rev. 83, (1951), op cit, [deShalit & Feshbach, 1974], p. 9.

[ENAM 1998] *"Exotic Nuclei and Atomic Masses,"* Bellaire, MI, 1998; ed. B.M. Sherrill, D.J. Morrissey & C.N. Davids, (Woodbury, NY: AIP Conference Proceedings; 1998).

[Flury & Riedwyl 1988] *"Multivariate Statistics, a Practical Approach,"* B. Flury and H. Riedwyl, (London: Chapman and Hall; 1988.)(See especially the discussion of two-group linear discriminant analysis (pp. 106-114) and chapter 8 on *"identification analysis,"* both of which can be generalized to the multiple- ion groups characteristic of nuclear spectra.)

[Garrett 1951] *"Axially Symmetric Systems for Generating and Measureing Magnetic Fields, Part I,"* B. Garret, J. App. Phys., 22, 9, September, (1951).

[Garrett 1963] *"Calculation of Fields, Forces, and Mutual Inductances of Current Systems by Elliptic Integrals,"* B. Garret, J. App. Phys., 34, 9, September, (1963).

[Garvey & Kelson 1966] G.T. Garvey & I. Kelson, Phys. Rev. Lett. 16, 197 (1966).

[Garvey & Kelson 1969] G.T. Garvey W.J. Gerace, R.L. Jaffe, I. Talmi & I. Kelson, Rev. Mod. Phys, 41 S1 (1969).

[Glaser 1952] *"Grundlagen der Elektronenoptik,"* W. Glaser, (Vienna: Springer-Verlag; 1952).

[Goulding 1985] *"Heavy-Ion Identification Using Detector Telescopes,"* F.C. Goulding *Treatise on Heavy-Ion Science*, vol. 7; ed. D. Allan Bromley, (New York: Plenum Press; 1985) pp. 227-270.

[Green & Engler 1953] A.E.S. Green & N.A. Engler Phys. Rev. 911(1953)40 op cit [Bohr & Mottelson, 1969].

[Gross 1993] D.H.E.Gross, Nucl. Phys. A553 (1993) 605 .

[Gu 1995] *"The ^{8}Li (p,n) Reaction and Primordial Nucleosynthesis,"* X. Gu, R.N. Boyd, M.M. Farrell, J.D. Kalen, C.A. Mitchell, J.J. Kolata, K. Lamkim, K. Ashktorab, F.D. Becchetti, J. Brown, D.A. Roberts, K. Kimura, I. Tanihata, and K. Yoshida, Phys. Lett. B343 (1995) pp. 31-35.

[Hamilton 1980] *"Future Directions in Studies of Nuclei Far from Stability,"* J.H.Hamilton et al, eds., (Amsterdam, Netherlands: North-Holland; 1980).

[Hanold 1993] *"Transition from complete to incomplete fusion in asymmetric heavy ion reactions,"* K. Hanold L.G. Moretto, G.F. Peaslee, G.J. Wozniak, D.R. Bowman, M.F. Mohar, D.J. Morrissey, Phys. Rev. C48, 2, (1993); p. 723-734.

[Hanold 1995] *"Heavy residues from very mass-asymmetric heavy-ion reactions,"* K. A. Hanold, D. Bazin, M. F. Mohar, L. G. Moretto, D. J. Morrissey, N. A. Orr, B. M. Sherrill, J. A. Winger, G. J. Wozniak, and S. J. Yennello, (1995) pp. 1462-1483.

[Hansen 1995] P.G. Hansen, A.S.Jensen, B.Jonson, Ann. Rev. Nucl Part. Phys. 45 (1995) p. 591.

[Harss, 1990] *"Production of radioactive ion beams using an in-flight technique,"* H.Harss, R.C.Pardo, K.E.Rhem, R.Borasi, J.P.Greene, R¿V¿F¿Janssens, C¿L¿Jiang, J.M.Paul, J.P.Schiffer, R.E.Segel, J.Specht, T.F.Wang, P.Wilt. and B.Zabransky, Preprint, Argonne National Laboratories, Nuclear Division, 1999

[Haustein 1988] *Atomic and nuclear data tables,"* P.E.Haustein, Special Editor, vol 39, no. 2, July, 1988.

[Haxel, Jensen & Suess 1949] O. Haxel et al, Phys. Rev., Letters, April 18, (1949).

[Haxel, Jensen2 & Suess 1949] O. Haxel, J. H. D. Jensen and H. Suess, Phys. Rev. 75 (1949) p. 1766.

[Heisenberg 1932] Heisenberg W., Z. Phys. 8, 156 (1932).

[Hussein et al 1998] *"RIBRAS: Radioactive Ion Beams in Brasil,"* M.S. Hussein, A. Lepine-Szily, R. Lichtenthaler, A. C. C. Villari, V. Guimaraes. (Internal Report, University of Sao Palo, Brasil, IFUSP-DFN/98-012; 1998).

[Jackson 1975] *"Classical Electrodynamics,"* J.D. Jackson, (New York: John Wiley & Sons; 1975) chapt. 13.

[Jänecke & Masson 1988] J. Jänecke, P.J. Masson, Atomic Data and Nuclear Data Tables 39, 185-271 (1988), and 39, 273-280 (1988).

[Jiye 1986] *"Aberration Theory in Electron and Ion Optics,"* X. Jiye, (New York: Academic Press, Inc.; 1986).

[Kelley 1995] J. Kelley et al, Phys. Rev. Lett. 74 (1995) 30.

[Kolata 1998] *"Exotic Nuclei and Atomic Masses,"* Bellaire, MI, 1998 Paper G3, J.J. Kolata; eds. B.M. Sherrill, D. J. Morrissey, & C.N. Davids, (Woodbury, NY: AIP Conference Proceedings; 1998).

[Kolata2 1998] *" $^{6}He + {}^{209}Bi$ Fusion-Fission Reaction,"* J.J. Kolata, V. Guimarces, D. Peterson, P. Santi, R. White-Stevens, J. von Schwarzenberg, J.D. Hinnefeld, E.F. Aguilera, E. Martinez-Quiroz, D.A. Roberts, F.D. Becchetti, M.Y. Lee, and R.A. Kryger, Phys. Rev. C57 1 (1998) pp. R6-R9.

[Krane 1988] *"Introductory Nuclear Physics,"* K.S. Krane, (New York: John Wiley & Sons; 1988).

[Landau & Lifshitz 1976] *"Course of Theoretical Physics, vol. 5," Statistical Physics* 3rd Ed. Part 1, L.D. Landau & E. M. Lifshitz, (Oxford: Pergamon Press; 1980.) (original Russian version, 1959 from 1976 revised edition) pp. 517-518.

[Laurent 1979] H. Lauren, & J. P. Schapira, Nucl. Instr. and Meth. 162 (1979) 181-192.

[Lawrence 1931] E.O. Lawrence, and M.S. Livingston, Phys. Rev.37, 1707 (1931), and Phys. Rev. 40, 19 (1932).

[Lee 1997] *"Proceeding fo the 14th International Conference on the Application of Accelerators in Research and Industry,"* Denton, Texas, USA, M. Y. Lee, November 1996, AIP conference prod. No. 392, (1997); pp. 397-400.

[Lee2 2000] M.Y. Lee, unpublished thesis, University of Michigan, Ann Arbor, MI 2000.

[Lee3 1998] *"Proceedings of the Workshop onthe Experimmental Equipment for and Advanced ISOL Facility (LBNL-42138);"* ed. I. Y. Lee (1998).

[Leo 1987] *"Techniques for Nuclear and Particle Physics Experiments,"* W. R. Leo, (New York: Springer-Verlag; 1987) p. 24.

[Liu 1990] *"Production and Use of Radioactive Ion Beams for Measurements of Nuclear Reactions,"* W.Z. Liu, unpublished thesis, University of Michigan, Ann Arbor, MI (1990).

[Liu2 1989] *"Measurements of Discrete Nuclear Reactions Induced by a Radioactive* ^{8}*Li Beam,"* W.Z. Liu, D.A. Roberts, J.W.Jänecke, J.J. Kolata, A. Morsad, X.J. Kong, and R.E. Warner, Phys. Rev. C 40, (1989) R1104.

[Mathews 1990] *"Proc. Workshop on the Science of Intense Radioactive Ion Beams,"* LA-11964-C, G.J. Mathews; ed. J. B. McClelland and D.J. Viera, (1990) p. 213.

[Maxwell 1891] *"A Treatise on Electricity and Magnetism,"* third ed. vols. 1 & 2, J.C. Maxwell, (New York: Dover Publications, Inc.; 1954.) (Reprint of third edition of Clarendon Press, 1891).

[Mayer 1948] M. Mayer, Phys Rev. 74 3 (1948).

[Mayer 1949] M.G. Mayer, Phys. Rev. 75 (1949).

[Mayer & Jensen 1955] *"Elementary Theory of Nuclear Shell Structure,"* M.G. Mayer & J.H.D. Jensen, (New York: Wiley; 1955).

[McMahan 1986] *"Using a cyclotron plus ECR source for detector evaluation and calibration,"* M.A. McMahan, G.J. Wozniak, C.M. Lyneis, D.R. Bowman, R.J. Charity,Z.H. Liu, L.G. Moretto, W.L. Kehoe, A.C. Mignerey, M.N. Namboodiri, Nucl. Instr.& Meth. in Phys. Res. A, Vol.A253, no.1; (1986) p. 1-9.

[Mittig 1997] *"Mass measurements far from stability,"*W. Mittig, A. Lipine-Szily, and N. A. Orr, Annu. Rev. Nucl. Part. Sci. 1997 47: 27-66.

[Möller & Nix 1995] P. Möller, and J.R. Nix, Atomic Data and Nuclear Data tables 59, 185 (1995).

[Montgomery 1980] *"The Magnetic and Mechanical Aspects of Resistive and Superconducting System,"* D.B. Montgomery, (New York: Kreiger Publishing, Co.; 1980) p. 237.

[Mueller 1998] *"Status of RNB Facilities in Europe,"* A.C. Mueller in *Exotic Nuclei and Atomic Masses, Bellaire, MI, 1998* eds. B. M. Sherrill, D. J. Morrissey & C. N. Davids, (Woodbury, NY: AIP Conference Proceedings; 1998), pp. 952-959 and citations therein.

[Mueller2 1993] *"On the Capabilities of Present Radioacive Beam Facilities,"* A.C. Mueller, p.8, in [RNB, 1993].

[Mueller & Sherrill 1993] *"Nuclei at the Limits of Particle Stability"* Annu. Rev. Nucl. Part. Sci. 1993 43: 529-584.

[Myers & Swiatecki 1966] W.D. Myers, and W.J. Swiatecki, Nucl. Phys 81(1966) 1. op cit, [Feshbach & de Shalit, 1990] p. 126.

[Nazarewicz 1998] *"Exotic nuclei from a theoretical paerspective,"* W.Nazarewicz, in [ENAM 1998], pp. 381-390.

[Nelson & Nelson 1964] *"Nuclear Magnetic Resonance Spectroscopy in Superconducting Magnetic Fields,"* Science, vol. 146, (1964), pp. 223-232.

[Newton 1687] *"Philosophiae Naturalis Principia Mathmatica (The Principia),"* Sir Issac Newton, 1687; (Tr. A. Motte, Amherst, NY: Prometheus Books; 1995).

[Nolan 1998] *"Status of RNB Facilities in North America,"* J. Nolan in *Exotic Nuclei and Atomic Masses, Bellaire, MI, 1998;* eds. B. M. Sherrill, D. J. Morrissey & C. N. Davids, (Woodbury, NY: AIP Conference Proceedings, 1998), pp. 952-959 and citations therein.

[O'Donnell 1994] *"Mass Separator Using a Large Solenoid 'Lens' with Time of Flight,and Position-Sensitive Detectors,"* T.W. O'Donnell, E. Aldredge, F.D. Becchetti, J.A. Brown, P. Conlan, J. Jänecke, R.S. Raymond, D.A. Roberts, R.S. Tickle, H.C. Griffin, J. Staynoff, and R. Ronningen, Nucl. Instrum. Meth. A353 (1994) pp. 215-216.

[O'Donnell 1999] *"Isotope yields with a solenoid-based fragment mass analysis system—prospects for exotic isotope studies in the* $10 \leq Z \leq 30$ *range."*T.W.O'Donnell, F.D. Becchetti, J.Brown, J.W.Jänecke, M.Y.Lee, R.S.Raymond, D.A.Roberts, R.S.Tickle, R.M.Ronningen, Nucl. Instr. and Meth. in Phys. Res. A (1999).

[Ogloblin & Penionzhkevich 1984] *"Very Neutron-Rich Very Light Nuclei,"* in *Treatise on Heavy-Ion Science*, vol. 8; ed. D. Allen Bromley, (New York: Plenum Press; 1985), pp. 227-270.

[Oppenheimer & Phillips 1935] J.R. Oppenheimer and M. Phillips, Phys. Rev. 48, 500 (1935).

[Pardo 1998] *" Proceedings of XIX Intern. Linac. Conf.,"* R.C. Pardo et al, Chicago, IL, August 23-28, (1998) .

[Perey & Perey 1976] A.M. Perey & F.G. Perey, Atomic Data and Nuclear Data Tables 17 (1976) 1.

[Plastock & Kalley 1986] *"Theory and Problems of Computer Graphics,"* R.A. Plastock and G. Kalley, Schaum's Outline Series, (New York: McGraw-Hill, Inc.; 1986) pp. 69-71.

[Rossignoli 1998] R.Rossignoli, N.Canosa and P.Ring, Phys. Rev. Lett, 80, 1853, (1998).

[Roberts 1995] *"Unusual Energy Dependence of the Total Nuclear Reaction Cross Section for a Secondary Isomeric Nuclear Beam,"* D.A. Roberts, F.D.Becchetti, J.B. Brown, J. Jänecke, K. Pham, T.W. O'Donnell, R.E. Warner, R.M. Ronningen, and H. Wilschut, Nucl. Phys. A588 (1995) pp. 247c-252c.

[RNB 1993] , *"Proceedings of the Third International Conference on Radioactive Nuclear Beams,"* Michigan State University, East Lansing, Michigan, USA, 24-27 May, 1993; ed. D.J. Morrissey, (Gif-sur-Yvette Cedex, France: Editions Frontieres; 1993).

[Ryder 1985] *"Quantum Field Theory,"* L.H. Ryder, (Cambridge: Cambridge University Press; 1985) pp. 13 and 108.

[Sagan 1980] *"Cosmos,"* C. Sagan, (New York: Random House; 1980) p. 30.

[Sarazin 1998] Sarazin, F, et al in [ENAM, 1998], p. 44-49.

[Schapira 1984] Schapira et al, Nucl. Instr. and Meth. 224 (1984) 337-346.

[Sharma 1996] *" Applied Multivariate Techniques,"* S. Sharma, (New York: John Wiley and Sons, Inc.; 1996)., See especially Chapter 8, *"Multiple- Group Discriminate Analysis."*

[Sherrill 1991] B.M. Sherrill et al, Nucl. Instrum. Meth B56/57, 106 (1991).

[Siemens & Jensen 1987] *"Elements of Nuclei, Many-Body Physics with the Strong Interaction,"* P.J. Siemens and A.S. Jensen, (Addison-Wesley Publishing Company, Inc.; 1987).

[Simon 1998] H. Simon, Ph.d. Thesis unpublished, TU Darmstadt, (1998).

[Smith 1990] *"Elastic and Inelastic Scattering of* ^{8}Li *from* ^{12}C*,"* R.J. Smith et al., Phys. Rev. C 43 , 2346.

[Smith2 1991] *"Scattering of* ^{6}He *from* ^{197}Au*,* ^{nat}Ti*,* ^{27}Al*,* ^{nat}C *and* ^{9}Be *at E=8-9 MeV,"* R.J. Smith et al., Phys. Rev. C 43 , 761.

[Souliotis Loveland, 1997] Souliotis, G.A., W.Loveland, W. et al, Phys. Rev. C Rapid Comm. 55, 5 (1995).

[Stern 1987] *"Design and Utilization of an Air Core Superconducting-Solenoid Nuclear Reaction Product Spectrometer,"* R. Stern, unpublished thesis, University of Michigan, Ann Arbor, MI (1987).

[Swan 1993] *"A simple two-dimensional PPAC,"* D. Swan, J. Yurkon, D.J. Morrissey, Nucl. Instr. and Meth. A, Vol. 348, No.2-3; (1994), p.314-17.

[Symons 1979] T.J.M.Symons, Y.P.Viyogi, G.D.Westfall, P. Doll, D.E.Greiner, et al, Phys. Rev. Lett. 42: 40-43 (1979).

[Szilagyi 1988] *"Electron and Ion Optics,"* M. Szilagyi, (New York: Plenum Press; 1988).

[Tanihata 1992] I. Tanihata, D. Hirata, T.Kobayashi, S. Shimoura, K. Sugimoto, H. Toki, Phys. Lett. B 28 (1992) p. 216.

[Tobocman 1959] W. Tobocman, Phys. Rev. 115, 98 (1959).

[Van de Graaff 1931] R. J. Van de Graff, Phys. Rev. 38, 1919 (1931).

[Vanderbosch & Huizenga, 1973] *”Nuclear Fission”,* R.Vanderbosch and J.Huizenga, Academic Press, New York, 1973.

[van Veldhuizen 2000] *“Fusion-like residues and fission in energetic nuclear collisions from 25 to 400 MeV/nucleon,”* E.J. van Veldhuizen, A. Kuznetsov, W. Loveland, L. Westerberg, K. Aleklett, F. Bismarck and V. Lyapin, preprint, dated January, 22, (2000).

[Viera 1989] *“Annual Review of Nuclear and Particle Science,”* S. Viera V. 39, (1989) pp. 407-465.

[Volkov 1985] *“The Production of Nuclei Far from Stability,”* V.V. Volkov, in *Treatise on Heavy-Ion Science*, vol. 8; ed. D. Allen Bromley, (New York: Plenum Press; 1985), pp. 101-195.

[Wagoner, Fowler and Hoyle 1967] R.V.Wagoner, W.A.Fowler, and F.Hoyle, Astropys. Journal 148, 3, 1967.

[Wallace & Woosley 1981] R.K. Wallace & S.E. Woosley, APJS, 45, 389 (1981).

[Warner 1995] *“Elastic Scattering of 10 MeV* ^{6}*He from* ^{1}*2C,* ^{nat}*Ni, and* ^{197}*Au,”* R.E. Warner, F.D. Becchetti, J.W. Jänecke, D.A. Roberts, D. Butts, C.L. Carpenter, J.M. Fetter, A. Muthukrishnan, J.J. Kolata, K. Lamkin, M. Belbot, M. Zahar, A. Galonsky, K. Ieki, and P. Zecher, Phys. Rev. C 51 (1995), pp. 178-181.

[Warner2 1998] *“Reaction Cross Sections in Si of Light Proton-halo Candidates* ^{12}*N and* ^{7}*Ne,”* R.E. Warner, H. Thirumurthy, J. Woodroffe, F.D. Becchetti, J.A. Brown, B.S. Davids, A. Galonsky, J.J. Kolata, J.J. Kruse, M.Y. Lee, A. Nadasen, T.W. O’Donnell, D.A. Roberts, R.M. Ronningen, C. Samanta, P. Schwandt, J. von Schwarzenberg, M. Steiner, K. Subotic, J. Wang, and J.A. Zimmerman, Nucl. Phys. A635/3 (1998) pp. 292-304.

[Westfall, 1979] G.D.Westfall, T.J.M.Symons, G.D.Greiner, H.H.Heckman, P.J.Lindstrom, et al, Phys. Rev. Lett. 43: 1859-62 (1979).

[Wigner 1955] E.P. Wigner, Am. J. Phys. 23, 371 (1955), and references therein.

[Wöhr 1998] A. Wöhr, et al, p. 456,in [ENAM 1998], p. 456.

[Wollnik 1987] *“Optics of Charged Particles,”* H. Wollnik, (New York: Academic Press, Inc.; 1987).

[Ziegler 1989] J.F. Ziegler,"Transmission and Range of Ions in Matter (TRIM) computer program," J.F. Ziegler, IBM Research, Yorktown, NY (1989).

[Ziegler & Biersack 1996] *"Stopping and Range of Ions in Matter (SRIM) computer program,"* J.F. Ziegler (IBM) and J. P. Biersack (Hahn-Meitner), IBM Research, Yorktown, NY USA; Hahn-Meitner Inst. 1 Berlin 39 Germany.